

UNIVERSITY OF CALIFORNIA

Santa Barbara

Traveling-wave Amplifier-Photodetectors

A Dissertation submitted in partial satisfaction of the
requirements for the degree Doctor of Philosophy
in Electrical and Computer Engineering

by

Daniel Lasaosa

Committee in charge:

Professor John E. Bowers, Chair

Professor Daniel Blumenthal

Professor Larry Coldren

Professor Nadir Dagi

September 2004

The dissertation of Daniel Lasosa is approved.

Daniel J. Blumenthal

Larry A. Coldren

Nadir Dagli

John E. Bowers, Committee Chair

September 2004

© Copyright by Daniel Lasaosa

2004

ACKNOWLEDGEMENTS

This dissertation would not have been possible without the continuous guidance, support and encouragement (and some occasional pressure) from my advisor, Professor John E. Bowers, to whom I owe the opportunity of a most fulfilling and challenging period in my education. The contribution from Professors Daniel Blumenthal, Larry Coldren and Nadir Dagi is also invaluable, through most useful observations, comments and discussions.

Listing the names of all members of Professor Bowers' research group during my time in it would be too long, but I am very grateful to each and every one of them, because in one way or another they made it possible for me to make the best out of my years at UCSB. Especial thanks to Dr. Donato Pasquariello, for his expertise and effort, which made possible the first demonstration of InP-based TAP detectors; to our growers, Dr. Yi-Jen Chiu and Shaomin Wu for GaAs-based material, and Yae Okuno for InP-based growths; to Professor Joachim Piprek, for lending to this project his expertise in semiconductor device simulation; to Kian-Gap Gan, for help in the design and building of the measurement setup. To all of them I owe the pleasure of most interesting discussions, as well as to all other group members, among whom I'd like to especially recognize Drs. Thomas Liljeberg, Staffan Björilin and Adrian Keating. The words of experience and wisdom received in my first months at UCSB from Dr. Dubravko Babic and Professor Rajeev Ram proved incredibly useful during

all my graduate studies. Last, but not least, I am very grateful to Claudio Giuliano, for arranging my first meeting with Professor Bowers.

The device fabrication would not have been possible without the extremely competent and efficient cleanroom personnel; my most sincere thanks go therefore to Jack Whaley, Bob Hill, Neil Baker and Don Freeborn. Thanks also to all other cleanroom users who contributed to my device processing education with their advice.

My graduate education could not have been complete without courses taught by many excellent lecturers, who not only make continuously available in class their technical knowledge, but also their wisdom and expertise in the conduction of high-level research.

Thanks to all of Professor Bowers' assistants, from Kira Abrams to Hillary Greenlee, Val de Veyra at the ECE Student Office, Lynn Wilcoxon at the Graduate Division, and the Office of International Students and Scholars, for continuous help with paperwork and organization.

This list of acknowledgements would not be complete without all the people to whom I am indebted at a personal level. First and foremost, I can never be grateful enough to my parents, Santiago and Flor, for their unending love and support, and for teaching me with their example the most challenging lesson of all: how to truly and fully live life. Many friends and family members have been invaluable moral support through letters, e-mails, and many pleasant times spent together during my vacations. Most special thanks for their friendship and patience to Ambrosio, Antonio, Íñigo and

Javier, to all the rest of the yearly “teleco” dinner group, with whom I shared classes and fun during my undergraduate years, and to all my friends from Burlada: Jesús and Inés, Ana, Nuria, Begoña, María and many others who kept my electronic mailbox busy, my spirits high and my heart close to home despite the distance.

A home away from home is precious, and many people contributed to my having one: my roommates David and Paolo, my neighbors Antonio, Bernardo and Rodrigo, my friends Fernando, Jessica, Pablo, Alfredo, Marcelo, Marco, Vittorio, Ramesh, Ruben and so many others. I am very much indebted to all of them, for helping me celebrate success and overcome frustration, and for just plain good old-fashioned fun. But if somebody has truly been my family in this country, for the love that they have shown me, and for the way in which they always treated me as one of them, it is the Campos family in Fresno, who will always have a special place in my heart.

Finally, this project could have never been possible without the financial help of DARPA through the RFLICS program. I am also personally indebted to the Gobierno de Navarra, for partial personal support during a portion of this project.

To Santiago and Flor, for always being my parents.

In loving memory of Sebastiana and Ventura.

VITA

- July 1973 Born in Pamplona, Spain
- Sep. 1995 Bachelor of Science in Electrical Engineering, Institut National Polytechnique de Grenoble, France
- Master of Science in Electrical Engineering (Optics, Optoelectronics and Microwave), Institut National Polytechnique de Grenoble, France
- Oct. 1995 Bachelor of Science in Telecommunication Engineering, Universidad Pública de Navarra, Spain
- Jan. 1996-March 2002 and Graduate Student Researcher, Electrical and June-Dec. 2002 Computing Engineering, University of California, Santa Barbara
- March 1997 Master of Science in Electrical Engineering (Solid State), University of California, Santa Barbara
- April-June 2002 Teaching Assistant, Electrical and Computing and Jan.-March 2003 Engineering, University of California, Santa Barbara
- September 2004 Philosophy Doctor in Electrical Engineering, University of California, Santa Barbara (expected)

PUBLICATIONS

1. Y.J. Chiu, S.B. Fleisher, D. Lasaosa, J.E. Bowers, "Ultrafast (370GHz bandwidth) p-I-n traveling wave photodetector using low-temperature-grown GaAs," *Applied Physics Letters*, vol. 71, no. 17, pp. 2508-10, 1997.
- 2.- D. Lasaosa, Y.J. Chiu, J. Piprek, J.E. Bowers, "Traveling-wave amplification photodetector (TAP detector)," *Proceedings of the 13th Annual Meeting of the IEEE Lasers and Electro-Optics Society*, vol. 1, pp. 260-1, 2000.
- 3.- D. Lasaosa, Y.J. Chiu, J. Piprek, J.E. Bowers, "Modeling of traveling-wave amplification photodetectors (TAP detectors)," *Proceedings of the SPIE-Photonics West International Symposium*, vol. 4283, pp. 528-39, 2001.
- 4.- J. Piprek, D. Lasaosa, D. Pasquariello, J.E. Bowers, "Physics of waveguide photodetectors with integrated amplification," *Proceedings of the SPIE-Photonics West International Symposium*, vol. 4986, 2003.
- 5.- J. Piprek, D. Pasquariello, D. Lasaosa, J.E. Bowers, "1.55mm traveling-wave amplification photodetector," *Proceedings of the International Conference on Indium Phosphide and Related Materials (IPRM)*, pp. 499-501, 2003.

6.- J. Piprek, D. Pasquariello, D. Lasasosa, J.E. Bowers, "Novel waveguide photodetectors on InP with integrated light amplification," *Proceedings of the Electro-Chemical Society International Symposium*, pp. 1-8, 2003.

7.- J. Piprek, D. Lasasosa, D. Pasquariello, J.E. Bowers, "Optimization of GaAs amplification photodetectors for 700% quantum efficiency," *IEEE Journal of Selected Topics in Quantum Electronics (Optoelectronic Device Simulation Issue)*, vol. 9, no. 3, 2003.

8.- D. Lasasosa, D. Pasquariello, J. Piprek, J.E. Bowers, "Recent advances in photodetectors with distributed optical amplification," *Proceedings of the SPIE-ITCom International Symposium*, vol. 5246, 2003.

9.- D. Pasquariello, J. Piprek, D. Lasasosa, J.E. Bowers, "InP-based waveguide photodetector with integrated photon multiplication," *Proceedings of the SPIE-ITCom International Symposium*, vol. 5248, 2003.

*“Uno debe esforzarse siempre en hacer lo que no sabe hacer;
lo que se sabe hacer, ya está hecho.”*

*(One must always strive to do what one does not know how to do;
what one knows how to do has already been done.)*

(Eduardo Chillida, Spanish sculptor, 1924-2002)

ABSTRACT

Traveling-wave Amplifier-Photodetectors

by

Daniel Lasaosa

Optical preamplification at the receiving end of lightwave communication systems has traditionally been used to improve the signal-to-noise ratio (SNR) of the detected photocurrent. In recent years, integration of photodetectors with semiconductor optical amplifiers (SOAs) has become a topic of interest, as an electrically pumped, low-volume, low-cost alternative to erbium-doped fiber amplifiers (EDFAs). The research contained in this dissertation represents, to the best of my knowledge, the first attempt to demonstrate the possible advantages of a distributed combination of optical amplification and photodetection.

Traveling-wave amplifier photodetectors, or TAP detectors, combine optical gain and absorption in a distributed way, either alternating or acting simultaneously over an optical signal, in order to extract a large photocurrent without the need of handling high optical powers. Combined with a traveling-wave design, this approach could potentially achieve simultaneously high efficiency, high bandwidth and the

production of high unsaturated photocurrent. The penalty to pay for these advantages is the introduction of noise through the optical amplification process.

In this dissertation, three possible configurations of TAP detectors are proposed, and their performance is discussed. A detailed theoretical description of the properties of TAP detectors is presented, through simulation of their efficiency, bandwidth and noise figure. The effects on the device performance of spontaneous emission and amplified spontaneous emission (ASE), as well as gain saturation, are also discussed. Design rules are extracted from these theoretical analyses. The fabrication process and measured characteristics of GaAs-based TAP detectors with vertical coupling are also presented. The dependence of the external quantum efficiency on the amplification region bias current and incident optical power strongly supports the theory developed for these devices.

The theoretical analysis presented includes the, to the best of my knowledge, first noise model for optoelectronic devices featuring a distributed combination of amplification and photodetection. The experimental results presented include the, to the best of my knowledge, first proof of principle of the distributed combination of amplification and photodetection, as well as the demonstration of TAP detectors with external quantum efficiency in excess of 200%.

TABLE OF CONTENTS

Chapter 1: Introduction	1
Photodetectors in optical communications	1
Photodetector requirements	3
Trade-offs in photodetector performance	5
Motivation of this work	10
TAP detector configurations	13
TAP detectors with alternating amplification and absorption	14
TAP detectors with transverse coupling	20
Outline of the dissertation	25
Some notes on definitions	27
References	29
Chapter 2: DC characteristics of TAP detectors	31
Efficiency	32
Generic distributed amplifier-photodetectors	32
TAP detectors with alternating amplification and absorption	35
TAP detectors with transverse coupling	48
Background current	60
Dark current	61
Parasitic transistor in TAP detectors with vertical coupling	64
ASE current	74
ASE current in TAP detectors with alternating amplification and absorption	77
ASE current in TAP detectors with transverse coupling	89
Spontaneous emission current in TAP detectors with vertical coupling	97
Order of magnitude of ASE current and spontaneous emission current	101
Competition between signal and spontaneous emission for the available optical gain	106
Background current and measurable photocurrent	107
Competition between signal and spontaneous emission in TAP detectors with transverse coupling	110
Assumptions of the solving method	111
Solving the carrier density equilibrium equation	113
Simulated measurable photocurrent	118
Summary	129
References	131

Chapter 3: High-speed characteristics of TAP detectors	133
Microwave propagation in TAP detectors	134
Propagation of electrical waves in metal-insulator-semiconductor waveguides	134
Microwave propagation in TAP detectors with alternating amplification and absorption	145
Microwave propagation in TAP detectors with vertical coupling	154
Distributed photocurrent model	159
Propagation of optical and electrical signals	159
Frequency response of TAP detectors with alternating amplification and absorption	165
Frequency response of TAP detectors with vertical coupling	177
Summary	180
References	181
Chapter 4: Noise in the presence of distributed amplification and photodetection	183
Review of noise concepts	184
Noise in semiconductor optical amplifiers	189
Noise in photodiodes	197
Correlation between electron and photon fluctuations	201
Evolution of photon and electron number statistics in the presence of distributed amplification and photodetection	205
Photon and electron number fluctuations and their probabilities	206
Evolution of functions depending on photon and electron numbers	209
Evolution of the statistics of photon and electron numbers	214
Evolution of the average photon and electron numbers	220
Evolution of the photon number variance	222
Evolution of the covariance between photon and electron numbers	224
Evolution of the electron number variance	226
Consistency of the new noise model with previous models	228
Consistency with the photon statistics master equation	229
Consistency with Bernoulli's sampling formula	232
Fundamental noise limits for amplifier-photodetectors in a quasi-constant optical power regime	235
Summary	237
References	238

Chapter 5: Noise properties of TAP detectors	239
Forward- and backward-propagating optical signals	240
Effect of coupling loss and initial amplification section	245
Noise in TAP detectors with alternating amplification and absorption	250
Electron number variance	250
Contributions to the noise figure	256
Noise figure	263
Noise in TAP detectors with transverse coupling	272
Electron number variance	272
Contributions to the noise figure	276
Noise figure	282
Summary	290
Chapter 6: Fabrication of GaAs-based TAP detectors	291
Epitaxial structures for TAP detectors with vertical coupling	292
First generation	292
Second generation	299
Fabrication process	305
Outline of the fabrication process	306
Temperature budget	315
PMGI punch-through	316
On-chip test patterns	317
Gain and absorption diodes	318
Oxidation depth test	320
PMGI punch-through test pattern	321
Devices equipped with test pads	323
References	324
Chapter 7: Experimental results	327
Electrical characterization of TAP detectors	328
Optical characterization of TAP detectors	333
Measurement setup	334
Spontaneous emission, ASE and background current	336
Photocurrent	343
First generation	344
Second generation	350
Effect of temperature	356
Measured efficiency in InP-based TAP detectors	361
Summary	363
References	364

Chapter 8: Conclusions	365
Theoretical conclusions	366
General behavior of TAP detectors	366
Comparison of the proposed TAP detector configurations	368
Experimental conclusions	371
Future work	372
Appendix A: Gain and spontaneous emission in semiconductor optical amplifiers	377
Emission and absorption of photons in semiconductors	378
Density of optical modes and spontaneous emission coupling coefficient	379
Emission and absorption rates	381
Optical gain and amplified spontaneous emission power	384
Competition between signal and amplified spontaneous emission	389
Carrier density and local optical power	390
Calculation of the amplifier gain in the presence of saturation	394
Saturation power	396
References	398
Appendix B: Representations of the propagation characteristics of a microwave transmission line	399
Propagation in microwave transmission lines	400
Propagation coefficient and characteristic impedance	401
Voltage-current transmission matrix (ABCD matrix)	404
Voltage-current transmission matrix for periodic transmission lines	406
References	409
Appendix C: Noise properties of photodetectors	411
Bernoulli's sampling formula	412
Correlation between photon and electron numbers in photodetectors	418
Noise model for amplifier-photodetectors and its equivalence with Bernoulli's sampling formula	426
Properties of the polynomials $Q_N[x]=x(x-1)\dots(x-N+1)$	427
Photon number statistics in a photodetector	429
Electron number statistics in a photodetector	431
References	435

(This page is intentionally left blank)

CHAPTER 1

Introduction

In this introduction, the work done during this project will be motivated, providing intuitive explanation of the concept behind Traveling-wave Amplifier Photodetectors (TAP detectors). In order to do that, the main characteristics that photodetectors should present for optimum performance in optical communication systems will be first summarized. The research developed during this project will be then motivated through a brief intuitive explanation of the advantages and disadvantages that TAP detectors may have with respect to other conventional photodetection schemes. Finally, the TAP detector configurations studied during this project will be presented. The chapter concludes with an outline of the rest of the dissertation.

Photodetectors in optical communications

The demonstration of the first semiconductor laser diodes in the early 1960s opened the possibility for portable, cheap sources of coherent light. The

demonstration of low-loss light transmission in silica-based optical fibers showed that this coherent radiation could be transmitted over long distances. The high bandwidth of silica fiber, its small attenuation, and the possibility to dope it with rare-earth ions to achieve gain and extend the maximum propagation distance, have made possible the advent of long-haul, high-speed optical links, deployed worldwide since the 1980s. Today, multi-gigabit per second optical links are common in various communication systems. Although fiber to the home is not a reality for every user, optical links play an important role in long-distance data transmission for many different applications, from mobile telephony to cable television, and, of course, the internet, increasingly present in everyday life.

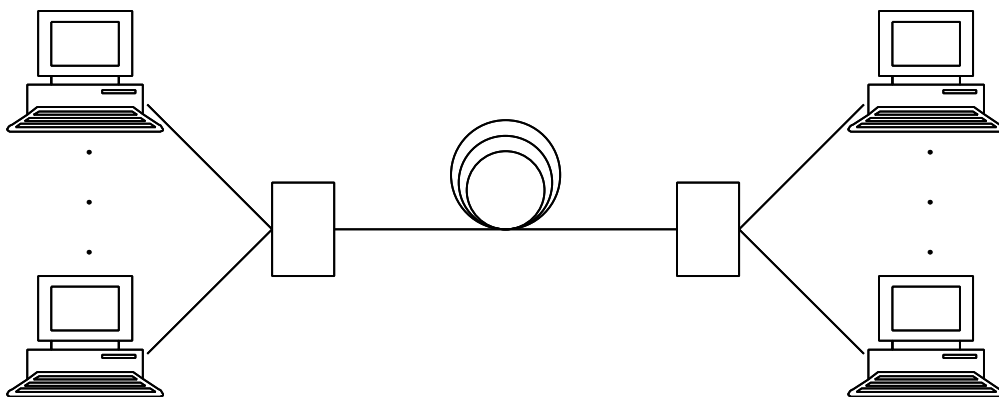


Figure 1.1: Optical links are more and more common in all kind of communications systems, even if fiber to the home is still not a reality for everybody. Represented is the internet, where users may connect themselves to a distribution node through an electrical connection, but long-distance information transfer is achieved through optical links.

In this section, the requirements for optimum detector performance in an optical communications link will be briefly presented. Next, some of the trade-offs between those requirements will be outlined. The purpose of this section is to give a flavor of

the challenges usually encountered in photodetector design, and to set the background for the motivation of research in traveling-wave amplifier-photodetectors.

Photodetector requirements

The particular configuration of an optical link may vary. However, since the overwhelming majority of applications are still electronic-based, from computers to phones, at some point the optically-coded information needs to be translated into an electronic signal. That role is traditionally played by photodiodes of a wide variety of types. The ideal characteristics of a detector for optical communications are high efficiency, high bandwidth, high saturation power and low noise. High saturation power and low noise ensure a wide range of input powers for which the optical signal will be accurately translated into an electrical signal. The high bandwidth is necessary for high data rate reception. High efficiency reduces the need of electrical amplifiers after the detector. Furthermore, since a background noise independent of the input optical signal will always exist, a higher efficiency results in a lower input optical power necessary to achieve the same output signal-to-noise ratio (SNR). This background noise may have different origins according to the type of photodetector, but thermal noise in the load resistor and dark current in the photodiode are always present. It is precisely the need of the received signal to rise above this background noise that motivated the introduction of optical preamplification before the photodetector. This is illustrated in Figure 1.2.

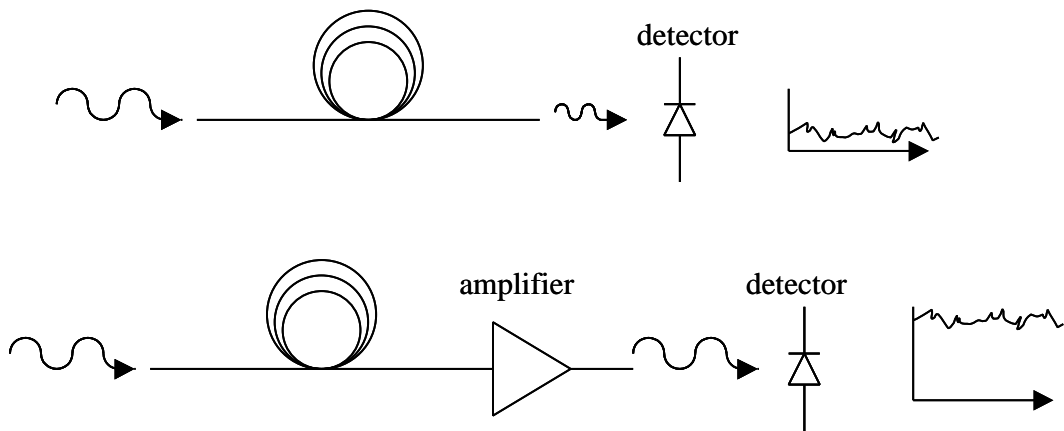


Figure 1.2: Detection of an optical signal after a long-distance propagation may result in photocurrent values close to the background noise level (top). The use of optical preamplification (bottom) helps improve the signal-to-noise ratio of the detected signal.

Optical preamplification is usually achieved through Erbium-doped fiber amplifiers (EDFAs), although semiconductor optical amplifiers (SOAs) may also be used. The latter option allows for the integration of photodetector and preamplifier, reducing space and cost. Bandwidth-efficiency products of over 2THz have been obtained using an SOA integrated with a waveguide detector [1]. Efforts to improve the performance of integrated SOAs and detector are still a current topic of research [2]. The use of preamplification results in larger optical power arriving to the photodetector. This is another reason for the importance of high saturation power.

The main characteristics for optimum photodetector behavior in an optical communications link have thus been presented. In the next paragraph, some trade-offs arising between these characteristics will be presented.

Trade-offs in photodetector performance

Several trade-offs present themselves in the performance of photodetectors. Probably the best known is the bandwidth-efficiency product limitation in vertically illuminated photodiodes. It arises from the dependence of both the bandwidth and the efficiency on the thickness of the active region. As the active region becomes thinner, the transit time of photogenerated carriers is shortened, resulting in an increase in the bandwidth, but less light is absorbed, resulting in a reduction of the efficiency, and *vice versa*. This gives rise to the definition of the bandwidth-efficiency product as a figure of merit for photodetectors. See figure 1.3 for a schematic representation of this effect.

In traveling-wave photodetectors, the propagation of the optical signal and the carrier extraction from the active region occur in orthogonal directions, allowing for a separate optimization of both dimensions [3]. Efficiency will increase with an increasing device length, whereas the transit time is determined by the active region thickness. However, longer devices will present higher microwave propagation loss. Traveling-wave photodetectors will thus run again into efficiency-bandwidth product limitations, although the limiting value will be higher than in the case of vertically-illuminated detectors.

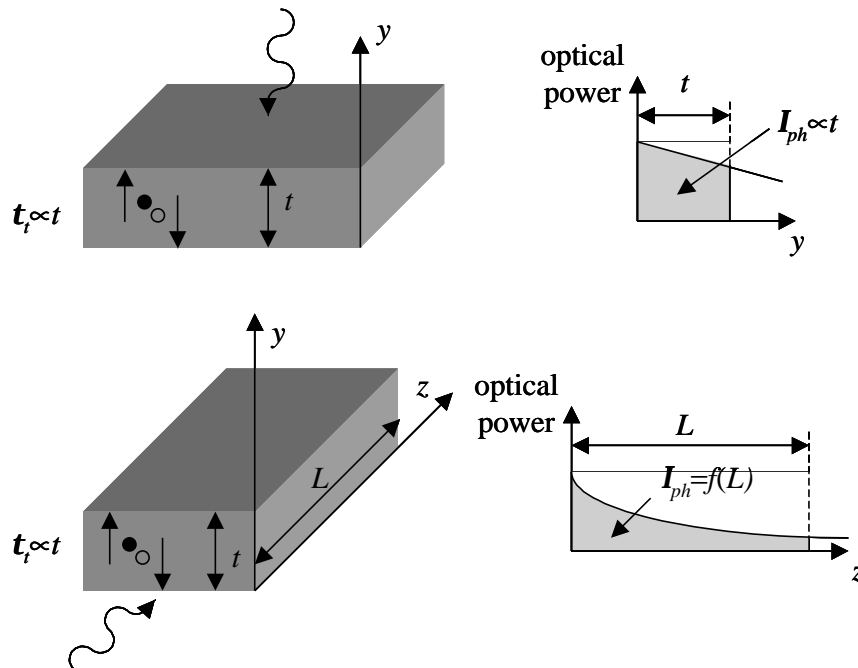


Figure 1.3: Comparison between vertically illuminated (top) and traveling-wave (bottom) detectors, showing the transit time t_r . The graphs on the right represent the evolution of optical power inside the device and the photocurrent generated (shaded region). The propagation of light and current in orthogonal directions allows traveling-wave detectors to bypass the bandwidth-efficiency product limit of vertically illuminated detectors through independent design of their thickness t and their length L .

A large concentration of electron-hole pairs being generated in the active region may result in a reduction of the device bandwidth. As electrons and holes separate due to the application of an external bias, spatial net charges are created. These electrical charges produce an electrical field in opposition to the applied voltage. For large concentrations of electrons and holes, the field is intense enough to result in an increase of the carrier transit time. Figure 1.4 schematically represents this effect, usually referred to as space-charge effect or field-screening effect.

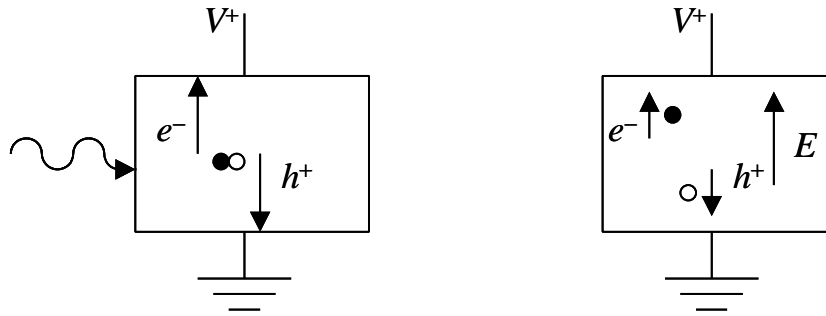


Figure 1.4: Space-charge effect or field-screening effect in detectors. Left: electrons (full dots) and holes (empty dots) are generated and start to separate due to the applied voltage V^+ . Right: as electrons and holes separate, an electrical field E appears due to the charge distribution in the active region, in opposition to the applied bias, slowing down the carrier transit.

This phenomenon, known as space-charge effect or field-screening effect, results in a trade-off between efficiency, bandwidth and saturation power. For strong input optical power, this may even result in a “bleaching” of the absorption due to a continued presence of previously generated free carriers in the active region. Intuitively, the saturation power may be increased by reducing the concentration of electron-hole pairs generated per unit volume. This may be achieved by reducing the confinement factor of the optical signal in the active region, i.e., the fraction of optical power that overlaps with the absorption region. As a result, in order to maintain the efficiency the dimensions of the active region need to be increased. If the active region thickness is increased, the transit time would become longer. If the area of a vertically-illuminated detector is made larger, the bandwidth would suffer a reduction, due to an increase in the RC time constant. In a traveling-wave structure, wider devices would exhibit higher microwave propagation loss per unit length. So, if either width or length are increased, the bandwidth would suffer too. Due to this

combination of events, a figure of merit has also been defined linking these three quantities [4], although its use is not as widespread as the efficiency-bandwidth product.

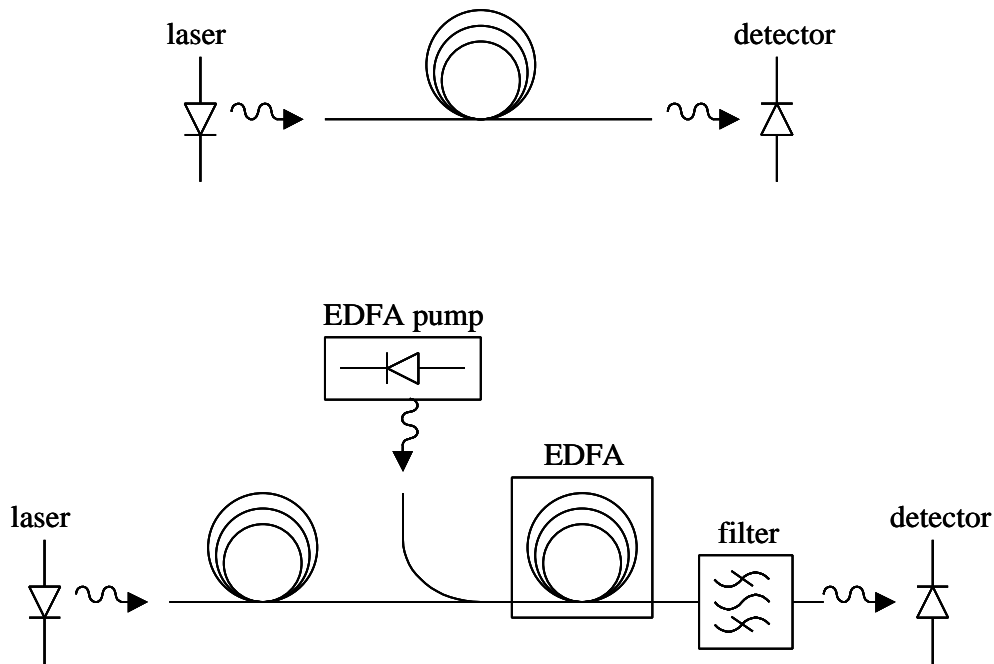


Figure 1.5: Comparison between detection with (bottom) and without optical preamplification (top). The introduction of optical preamplification typically entails the use of an EDFA with its corresponding pump source, and optical filtering, resulting in an increase in complexity, volume occupied and cost of the link.

The introduction of optical preamplification increases the output photocurrent, thus improving the SNR of the received signal. This happens at the expense of increased possibility of saturation, either in the amplifier or in the detector. Furthermore, optical amplification introduces optical noise. Optical filtering between amplifier and photodetector reduces the effect of this optical noise, resulting in a net

improvement of the signal-to-noise ratio. This improvement is obtained at the expense of complexity (and thus cost) and size. Figure 1.5 shows this increase in complexity, cost and space.

These are some of the most common trade-offs present in detector performance. They illustrate that improvement of some device characteristics may result in detriment of others. This is unfortunate, since it limits the overall performance that may be obtained from photodetectors. It provides, however, ample field of work and exciting opportunities for researchers.

Recent advances in photodetectors trying to break from these different trade-offs include the development of uni-traveling carrier photodiodes (UTC-PDs), where the absorption region is lightly p-doped, making hole transport much faster, resulting in large bandwidth and saturation power [5]. Other advances include avalanche photodiodes (APDs) with active regions engineered to better control the otherwise quite random multiplication process. This randomness typically results in reduced bandwidths and large noise figures. It has been recently demonstrated that the multiplication process may be partially controlled by creating device regions where carrier multiplication is inhibited or enhanced [6], and by the use of different materials for absorption and multiplication [7]. These strategies have been used to demonstrate lower noise and higher bandwidths than in traditional APDs. Despite these advances, the “perfect detector” does not exist yet.

In conclusion, the desirable characteristics of photodetectors in optical communication links have been presented and briefly motivated. Some of the trade-

offs arising among them have been presented, illustrating how improvements in some of the detector characteristics may be obtained in detriment of others.

Motivation of this work

In the previous section, the need to increase the efficiency, the bandwidth and the saturation power, and reduce the noise of photodetectors, was presented. Different trade-offs between these performance parameters were also briefly discussed. The main goal of the research contained in this thesis is the search for a new type of device that, combining optical amplification and absorption, would be able to produce a higher efficiency-bandwidth product without sacrificing saturation power. In this paragraph, traveling-wave devices combining optical amplification and absorption in a distributed way will be presented as a possible alternative to achieve this goal. We will call such devices Traveling-wave Amplifier Photo-detectors, or TAP detectors. This section will outline the advantages and disadvantages that such a distributed combination of optical gain and absorption would have, in terms of the desired characteristics of detectors for optical communications.

One of the main reasons why the trade-offs in detectors arise is due to the destructive nature of the photodetection process. As photocurrent is generated, the optical power is reduced. This immediately entails that, unless amplification of some kind is introduced, the maximum response that we may obtain out of a photodiode is one electron of photocurrent per photon of incident light. This constitutes a quantum efficiency of 100% in the conversion process.

Due to this destructive nature, photocurrent is not homogeneously generated in a photodetector. The optical power is larger at the device input, where the light is incident, resulting in a higher spatial density of photocurrent generation. As the optical power is absorbed, the current generation rate drops. Equal increments in the efficiency require thus larger and larger increments in device size, with negative repercussions on the bandwidth. Producing a photocurrent of a predetermined value becomes therefore easier if the incident power is larger. This, of course, increases the probability of saturation at the device input, where the photon concentration is highest.

The ideal solution to the situation described above would be a “non-destructive” photodetector, where current would be generated without light being absorbed. In such a device, an identical photocurrent could be generated with lower peak power, avoiding saturation up to higher output current values. At the same time, photocurrent generation would no longer be limited by an efficiency of 100%. Figure 1.6 schematically shows a comparison between a real detector and a “non-destructive” detector.

One possible solution is to compensate the photon absorption through optical amplification. If this amplification is introduced in a distributed way, a situation very similar to the one described in figure 1.6 for a “non-destructive” detector is possible. In order to secure a large bandwidth, a traveling-wave electrode configuration could be used. These characteristics constitute the rough draft of the devices that have been the object of the research described in this dissertation.

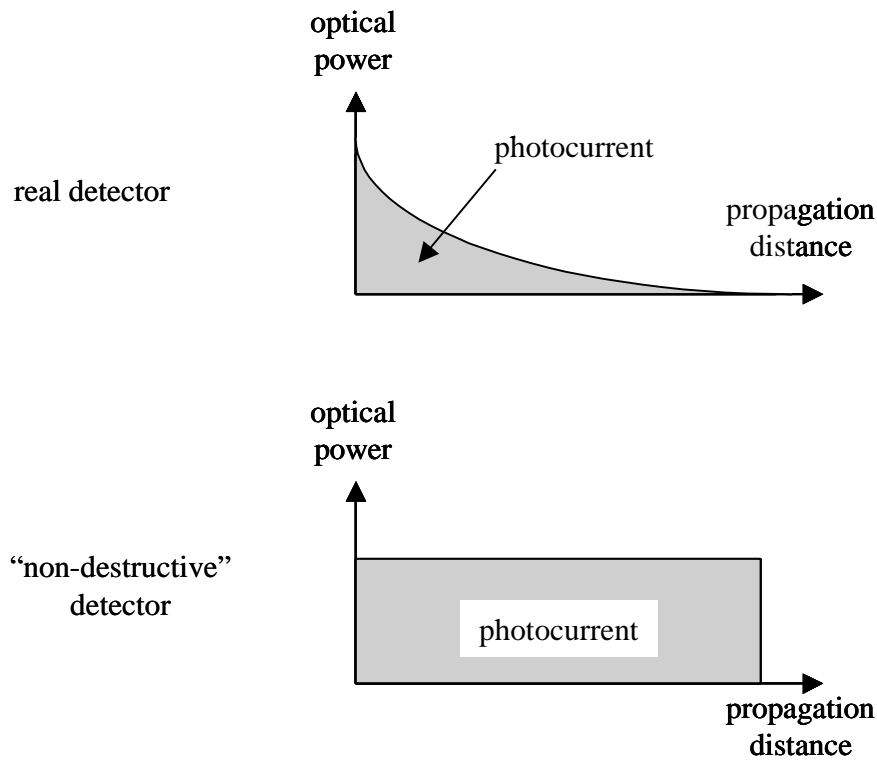


Figure 1.6: Comparison between a real photodetector (top) and a fictitious, “non-destructive” detector (bottom), showing the evolution of optical power as light propagates inside the device in both cases. The photocurrent generated after the optical power has traveled for a certain distance in the device (shaded area under the curve) is much larger in the second case. This would allow for higher efficiency with the same device length, for a larger bandwidth-efficiency product and the same saturation power.

The concept of the traveling-wave amplifier-photodetector, or TAP detector, is born. It is a device combining optical amplification and absorption in a distributed manner, presenting a traveling-wave electrode configuration. The distributed combination of amplification of detection allows it to generate high photocurrent with relatively low input optical power, while avoiding saturation, as described for the “non-destructive detector” shown schematically in figure 1.6. Its bandwidth may be

large because of its traveling-wave configuration, which has been successfully used in the past in record-holding devices [8].

As mentioned earlier, the “perfect detector” does not exist. In TAP detectors, noise and background current will be introduced during the optical amplification process. This will introduce new trade-offs, which will be analyzed in this dissertation. The inherent additional difficulty of combining gain and absorption on the same device will complicate the fabrication of such devices, adding probably to the production cost. Nonetheless, after the previous discussion in this paragraph, one idea stands clear: TAP detectors have the possibility of presenting simultaneously high responsivity and high bandwidth, without incurring in saturation. This is the main advantage sought in the work presented in this dissertation. In the next section, the specific configurations that have been the subject of this study will be presented.

TAP detector configurations

Before we can start the performance analysis or the design of the devices introduced in the previous section, a more detailed configuration needs to be established, since the idea of “distributed combination of absorption and gain in a traveling-wave configuration” is still quite vague. In this section, three different configurations producing this effect will be introduced. The next paragraphs will provide a brief description of these configurations, outlining their main characteristics.

TAP detectors with alternating amplification and absorption

One way of combining gain and absorption in a distributed fashion, which may also be achieved by combining discrete elements, is the alternation of amplifiers and photodetectors, as shown schematically in figure 1.7.

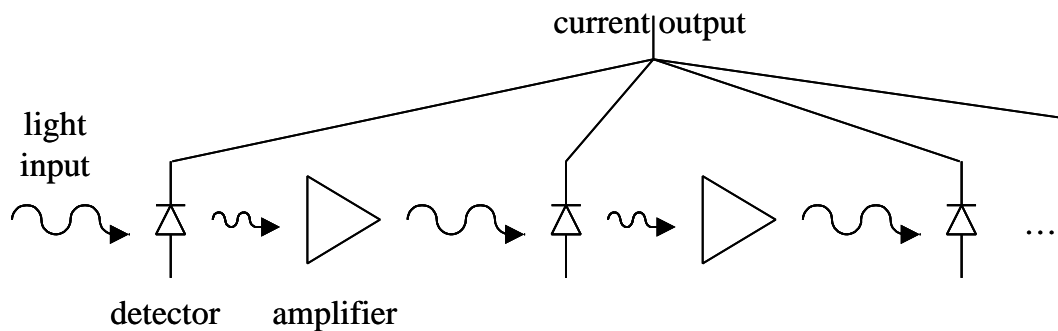


Figure 1.7: Alternating combination of amplification and detection. The light surviving absorption in one detector constitutes the input of the following amplifier in the chain. The current from all photodetectors is added.

This idea may be put into practice by using a waveguide with several contacts distributed along the direction of propagation of light, in such a way that forward-biased contacts for amplification alternate with reverse-biased contacts for absorption, as shown in figure 1.8. Because of the presence of nearby contacts with opposite polarities, the regions between them must provide electrical isolation.

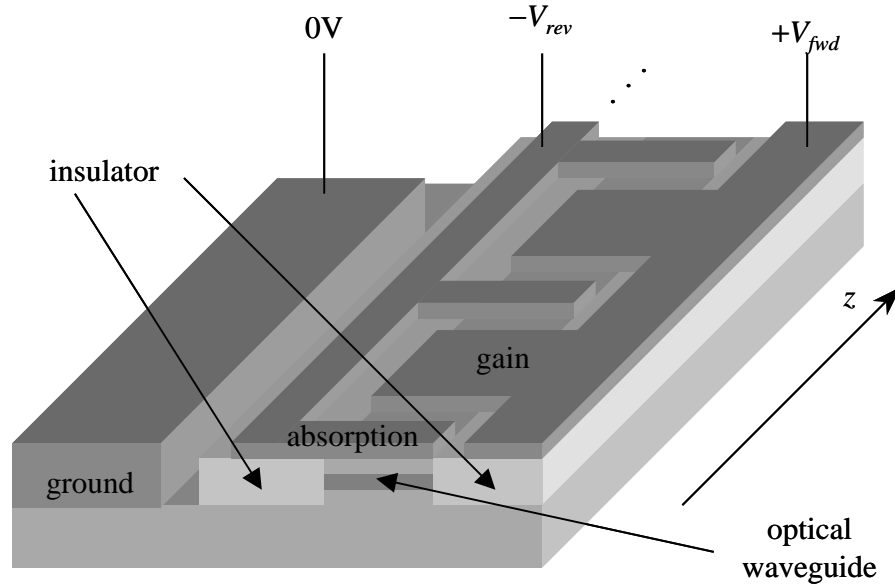


Figure 1.8: Three-dimensional representation of a TAP detector with alternating regions of amplification and absorption. Light propagates along the z direction.

This configuration was first proposed in [9], and an analysis of its main performance characteristics was first published in [10]. Intuitively, this configuration “recycles” the optical signal in a periodic configuration, where each period is constituted by an amplifier, a photodetector, and regions in between to provide electrical isolation between both devices. If each amplification region produces exactly enough gain to compensate for the absorption of the preceding detection region, each detection region, which may be viewed as an individual photodetector, will be excited by the same amount of optical power. Therefore, in the event of gain, absorption and loss canceling over each period formed by an amplification section and an absorption section, the total efficiency of the device will be equal to $N\mathbf{h}^{(1)}$, N being the number of absorption regions and $\mathbf{h}^{(1)}$ the efficiency of each one of them.

This configuration is clearly able to produce higher unsaturated current than classical photodetectors. This is expressed intuitively in Figure 1.9, where a conventional photodetector with pre-amplification is compared to a TAP detector with sequential gain and absorption.

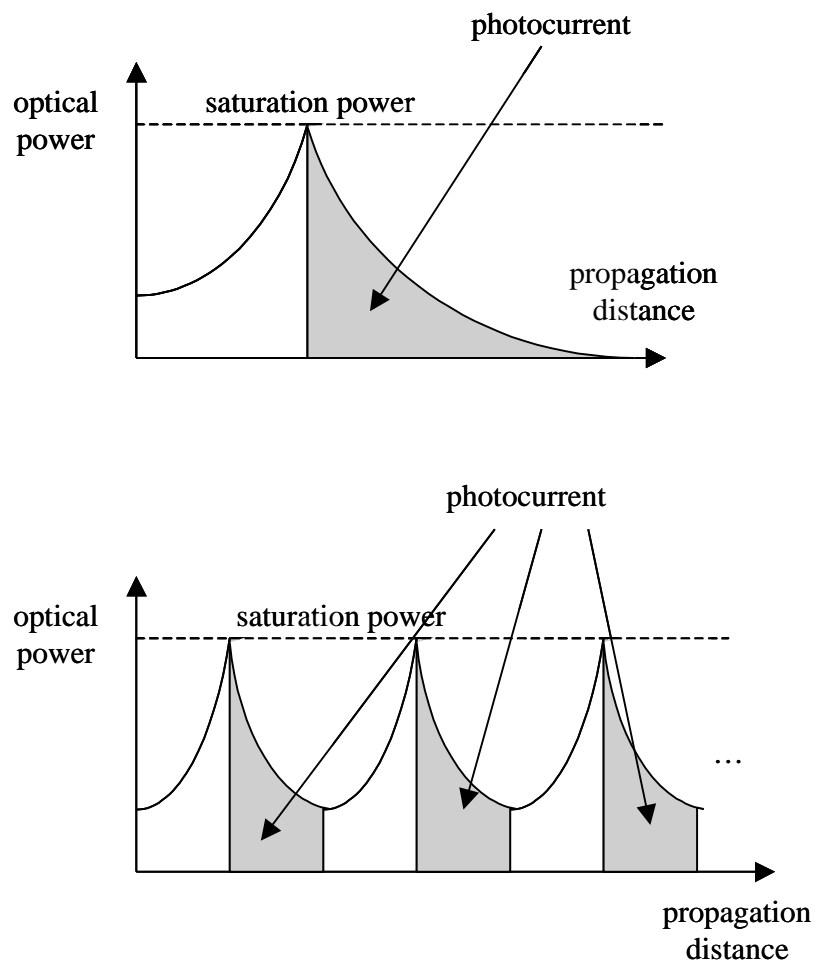


Figure 1.9: Comparison of the maximum unsaturated output photocurrent (shaded area) in a conventional photodetector with pre-amplification (top) and in a TAP detector with alternating gain and absorption (bottom). The horizontal dashed line represents the saturation power of each individual photodetector. Ideally, a large number of sections may be included, leading to an (a priori) arbitrarily large photocurrent.

Given the saturation power P_{sat} of a conventional photodetector, the maximum unsaturated photocurrent that may be extracted out of it is $RP_{sat}=(q/h\nu)h\nu P_{sat}$, h being its quantum efficiency, q the charge of an electron and $h\nu$ the energy of a photon. R is the detector responsivity, defined as the ratio between the generated photocurrent and the input optical power. Note that this value does not depend on the presence of an optical preamplifier, or on its gain, but only on the maximum power that the detector may handle and on its responsivity. Let us now assume that each individual photodetection region in a TAP detector with alternating gain and absorption has the same saturation power P_{sat} . Let us furthermore assume that each detection region has half the efficiency as a conventional photodetector. This assumption is made to allow for a significant fraction of the optical power to be “recycled” into the next amplification region. The total device efficiency is then given by $Nh^{(1)}=Nh/2$. The maximum unsaturated photocurrent is then $NR P_{sat}/2$, $N/2$ times higher than in the previous case. Note that we can, in principle, make this amount arbitrarily large by adding more periods of gain and absorption.

There are limitations to this approach, apart from the higher fabrication complexity, as outlined at the beginning of this section. First, the number of sections cannot be arbitrarily large. As we will later show, bandwidth decreases with the number of sections, while added noise increases [10]. Furthermore, larger number of periods also requires larger current to pump the amplification sections to produce the same gain. This also makes too many sections impractical, among other reasons because of the temperature increase due to Joule dissipation by the bias current

needed to pump all the amplification sections. Finally, detector designs specifically developed for large saturation power may not be compatible with integration as an alternating section of a larger device.

In terms of the high-frequency response, we need to remember that microwave loss, which increases with frequency and therefore sets an upper limit for the operation bandwidth of any optoelectronic device, is proportional to the device length. However, as shown in Figure 1.8, the metal that carries the generated photocurrent travels for a considerable fraction of the time over an insulator. This results in reduced losses over the case of an electrical waveguide traveling constantly directly over a doped semiconductor. Each absorption section introduces, however, a capacitive load and microwave losses. The bandwidth will be mostly determined by the number of periods and the length of each detection section, decreasing as each one of these two parameters increase. The efficiency, however, increases with the number of periods and the efficiency of each detection section, which in turn increases with the length of each absorption section. There exists therefore a trade-off between the efficiency and the bandwidth that may be simultaneously achieved using this configuration. This trade-off is investigated in this dissertation.

Optical processes introduce noise of various origins. Amplification produces fluctuations in the optical signal due to randomness in the gain process. Loss (through absorption, scattering or incomplete coupling) introduces partition noise due to the random selection of which photons survive and which ones do not. Incomplete detection produces a similar effect, due to the random selection of which photons

produce a collected electron-hole pair and which ones do not. The occurrence of these effects increases as the number of periods increases, resulting in growing noise. The trade-off between efficiency and noise addition will be investigated here.

Furthermore, each gain section will also generate amplified spontaneous emission (ASE) that may also be detected in the absorption sections. This will generate a background current. The relation between the background current and the photocurrent, and its dependence on the number of periods, needs also to be studied.

One important challenge presented by this configuration is the electrical isolation of the alternating contacts for the gain and absorption regions. This must be achieved while minimizing the negative effects on the optical properties of the device. Most electrical isolation techniques (e.g. ion implantation) tend to introduce heavy optical loss. Recent advances in intermixing techniques [11] make however this sequential combination of amplification and photodetection possible. In fact, lasers consisting of separate sections connected in series have been demonstrated, presenting record-high differential efficiency [12]. Similar schemes could be used to bring TAP detectors with alternating gain and absorption to reality in the near future.

In summary, TAP detectors with alternating gain and absorption have been introduced. They consist of a sequence of periods formed by an amplification section and a detection section, with sections providing electrical isolation in between. For an arbitrarily large number of periods, an arbitrarily large photocurrent could be achieved for a given input power. The number of periods may however not be arbitrarily large, because an increase in the number of periods results in an increase in

the microwave loss affecting the propagation of the generated photocurrent. Furthermore, the need to pump all amplification regions makes a large number of periods impractical. A higher number of periods results also in a larger background current being generated due to absorption of ASE, and an increase in the noise added through the amplification process. Whether these two undesired effects grow faster than the signal or not is studied in this dissertation.

TAP detectors with transverse coupling

Gain and absorption may act simultaneously on the optical signal. This situation may be understood by considering a single optical waveguide with two different active regions, one forward biased to provide gain, one reverse biased to collect absorbed light. It may also be understood by assuming two strongly coupled waveguides, one amplifying the light propagating through it, one absorbing it. Since most of the optical power traveling along the absorbing waveguide will quickly disappear, the coupling needs to be understood as mostly unidirectional. We will assume that both waveguides are parallel to one another, and to the propagation direction, either one on top of the other (in TAP detectors with vertical coupling [13]) or side by side (in TAP detectors with lateral coupling [9]-[10]).

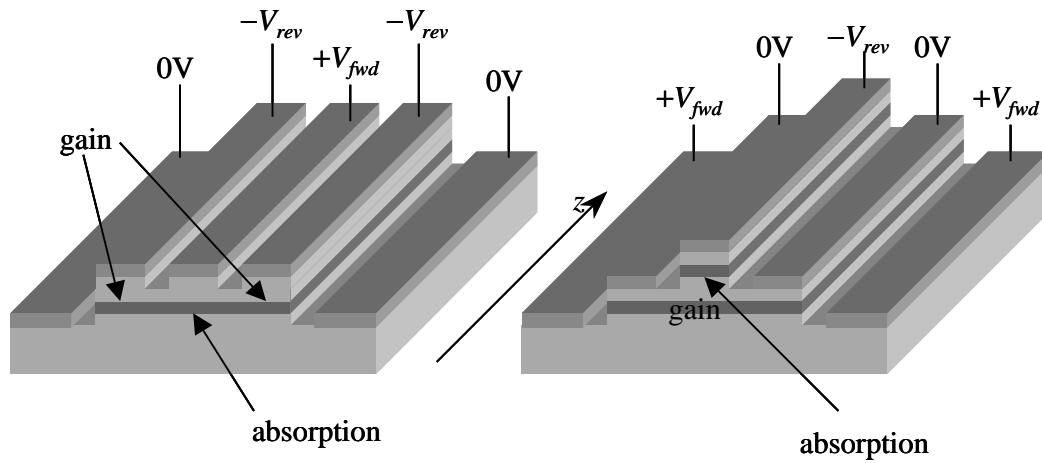


Figure 1.10: Combination of amplification and absorption via transverse coupling. TAP detectors are shown presenting lateral coupling (left) and vertical coupling (right). Light propagation occurs along the indicated z direction.

TAP detectors with vertical coupling have been fabricated both in GaAs and in InP. Comprehensive modeling and design improvements have allowed their performance to reach over 100% external quantum efficiency at $1.55\mu\text{m}$ wavelength [14], and over 200% at 850nm wavelength [13].

When gain, absorption and loss cancel out in this particular configuration, the optical power evolution and photocurrent generation are exactly as described in figure 1.6 for a “non-destructive” detector.

In these two configurations, the gain and absorption regions are strongly coupled. Thus, a weakly coupled waveguide model would not be accurate. Instead, one mode may be assumed to overlap with both amplification and absorption regions. The effect of each one will be determined by the modal confinement factor in that particular region. Figure 1.11 shows schematically the optical power spatial

distribution in a guided mode for the particular case of a TAP detector with vertical coupling. In the case where, as we mentioned earlier, gain, absorption and loss exactly cancel out, the optical power in the device would be constant, resulting in the generated photocurrent being proportional to the device length.

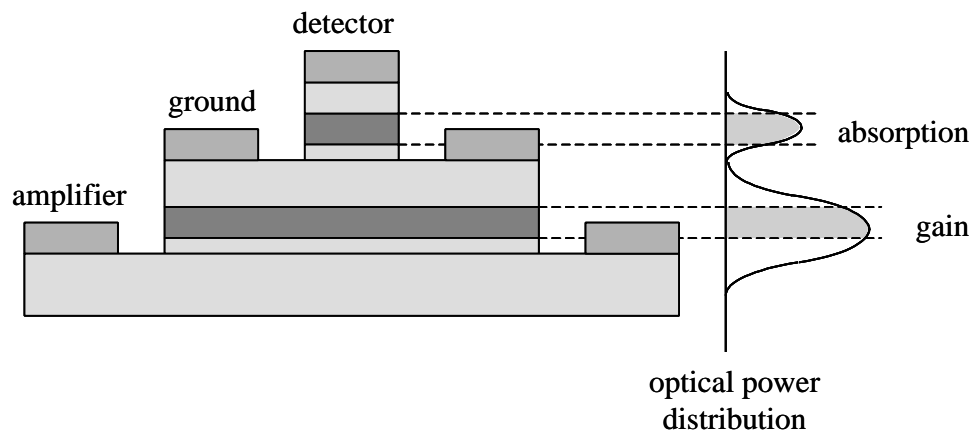


Figure 1.11: TAP detector with vertical coupling (left) and vertical optical power distribution (right). The ratio between each shaded area and the total area under the curve represents the confinement factor for that particular region. The contact labeled “ground” is common for the amplification and absorption regions. The other contacts are exclusive to each, and are labeled accordingly.

Just like in the case of TAP detectors with alternating gain and absorption, ASE will be produced in the amplification region. Part of it will again be absorbed, generating once more an undesired background current. Furthermore, and since spontaneous emission is generated in all directions of space, an additional background current will be generated by absorption of non-guided spontaneously emitted photons. Noise will also be added through the amplification process. The background current

and the noise need to be studied, and if necessary, trade-offs will need to be established between them and the device efficiency.

In terms of microwave propagation, the electrode carrying the signal (reverse-biased for absorption) will overlap with doped semiconductor regions over the entire device. This will result in higher loss per unit length than in the case of TAP detectors with alternating gain and absorption. At the same time, and because absorption and gain happen simultaneously in TAP detectors with transverse coupling, the length necessary to provide the same efficiency will be smaller.

Vertical coupling exhibits certain advantages over lateral coupling. One of them is the possibility to obtain in a single epitaxy different regions for gain and absorption. Thus, quantum wells may be grown for amplification and bulk for absorption in a single growth, resulting respectively in larger gain and easier carrier extraction. Another advantage stems from the need for electrical isolation between the gain and absorption diodes. The residual cladding and active region between gain and absorption contacts in TAP detectors with lateral coupling need to be made insulating to prevent a large conduction between these electrodes, which would result in a large background current, and at the same time a less efficient current injection into the amplifier active region, with the ensuing reduction in the available optical gain. TAP detectors presenting vertical coupling do not have that problem. Carriers may leak through the gain region and the claddings, but this effect may be inhibited with suitable bandgap engineering.

TAP detectors with vertical coupling exhibit these two same advantages over TAP detectors presenting alternating gain and absorption. The latter, however, admit the possibility of integrating other functions, such as filtering through wavelength-selective absorption between amplification and detection sections. This may be very convenient to reduce the effect of the ASE produced in the device.

In summary, two TAP detector configurations presenting transverse coupling have been introduced in this paragraph. In these configurations, a guided mode overlaps with two different regions, one reverse-biased to provide absorption, one forward-biased for amplification. Both regions may be placed one on top of another, or side by side, giving raise to configurations with vertical and lateral coupling, respectively. TAP detectors with transverse coupling will intuitively produce a photocurrent proportional to their length when gain and absorption are made to cancel out. Similarly as in the case of TAP detectors with alternating gain and absorption, noise and background current will be produced, stemming from randomness in the amplification process and ASE generation in the gain region. The bandwidth will decrease with device length. Trade-offs between the background current, the added noise, the bandwidth and the efficiency need to be studied. The paragraph concluded with a brief comparison between the three configurations presented. A more detailed comparison is established later on in this dissertation, after a more complete study of the three configurations is presented.

Outline of the dissertation

This dissertation constitutes, to the best of my knowledge, the first study of photo-detectors combining amplification and absorption in a distributed way.

As summarized in an intuitive way in the previous section, Traveling-wave Amplifier Photo-detectors have the potential of providing simultaneously high efficiency and high bandwidth without compromising the saturation power, at the expense of an increase in noise. In principle, amplification and absorption may be combined in many different ways. This work has concentrated in studying mostly three configurations, two out of which may be analyzed theoretically in equivalent fashion (presenting vertical and lateral coupling).

TAP detectors with vertical coupling were successfully fabricated and measured. The experimental results obtained from these devices provided proof of principle for the concept of distributed amplification and absorption, both in the GaAs and InP systems. In fact, external quantum efficiencies larger than 100% were demonstrated in both material systems. This was not, however, the only important contribution made by this work. Extensive simulation was performed, leading to the design that allowed these experimental results to happen. Moreover, some of these simulations were performed using new models specifically developed for this purpose, due to the lack of appropriate prior theoretical study applicable to these particular devices. These models may be very useful to any further research on TAP detectors, or on the effects and characteristics of the distributed combination of gain and absorption. This

dissertation will present the theoretical study performed on TAP detectors, including their efficiency, bandwidth, saturation, noise, and dependence on device geometry and design parameters. The fabrication of TAP detectors with vertical coupling and the experimental results obtained with these devices are also presented. The organization of the rest of the dissertation, which includes the aforementioned information, is now detailed.

Chapter 2 presents the theoretical study of the DC behavior of TAP detectors, namely the study of their efficiency, the background current generated, and the saturation processes that are generated by the competition of signal and ASE. Design rules are extracted from those analyses. Chapter 3 discusses the high-frequency response and the bandwidth of TAP detectors. The noise properties of these devices could not be studied with prior models, so chapter 4 presents a new noise model developed to take into account the effect of a distributed combination of amplification and absorption on the statistics of the optical power as it travels along the device and of the generated photocurrent. This model is applied in chapter 5 to TAP detectors. All along these four chapters, special emphasis will be placed on providing a good intuitive understanding of the processes occurring in TAP detectors and the relations between their different performance parameters, including trade-offs between them whenever they arise. Obtaining design rules for TAP detectors is another important goal of these chapters. Chapter 6 discusses the fabrication of TAP detectors, presenting the process developed for this purpose, some of the difficulties encountered and how they were solved. Chapter 7 shows the experimental results

obtained from fabricated TAP detectors. Finally, chapter 8 summarizes and discusses all the previous information, and points toward possible future routes for TAP detector research.

Some notes on definitions

In TAP detectors, and due to the distributed combination of amplification and absorption, the conversion factor between the electrical output and the optical input cannot be separated in the product of an amplifier gain multiplied by a detection efficiency. Efficiency is usually understood as the output-to-input ratio used to describe processes where a numerical value describing the output cannot be larger than the value describing the input. In this dissertation, however, and because of the effect of the distributed combination of gain and absorption, the efficiency of a TAP detector will be defined as the ratio between the output photocurrent, expressed in units of electrons per unit time, and the input optical power, expressed in units of photons per unit time. Because of the presence of optical gain, this definition may obviously violate the upper limit of one, typically assumed inherent in the definition of the efficiency of a process. In the interest of clarity, I will throw caution to the wind and adopt this generalized definition of efficiency. For fair comparison, the generalized efficiency of a detector with optical preamplification needs to be defined as the ratio between the electrical output of the detector, expressed in electrons per second, and the optical input of the amplifier, expressed in photons per second.

Another concept that will be loosely used throughout this dissertation is that of normalization. Usually, normalization refers to the situation when several values are divided by a constant, or by a reference value, in order to establish a comparison either among the former, or between the former and the latter. In TAP detectors, several processes occur at the same time, such as amplification and absorption of the input signal, and generation and absorption of amplified spontaneous emission (ASE). In order to establish a comparison between these processes, it may be very useful to find the ratio between two different variable amounts, such as the total photocurrent and the peak optical power inside the device, or between the photocurrent generated by absorption of ASE in the entire device and the ASE power generated in a certain section of it. The calculation of those ratios will be, in many cases, referred to as “normalization”. This will happen only when it is understood that the ratio helps shine light on the nature of a particular process, or brings forth intuitive understanding of how the effect of two different processes combines in the behavior of the entire device. Even though this is not consistent with the traditional use of the word “normalization”, this generalized use will be present throughout the dissertation to help bring clarity and understanding to the performance analysis of TAP detectors. One particularly clear example is what is defined in chapter 2 as the “efficiency normalized to peak power”. This concept is defined as the ratio between the total output photocurrent and the highest optical power present along the device. It is extremely useful, since it compares how the combination of amplification and absorption may lead to high photocurrent outputs with small optical power input, but

incurring into saturation if this is achieved by a large net gain, product of an imbalance between amplification and absorption. Other such ratios will be referred to as “normalizations” in this dissertation.

References

- [1] D.Wake, “A 1550-nm millimeter wave photodetector with a bandwidth-efficiency product of 2.4THz,” *Journal of Lightwave Technology*, vol. 10, n. 7, pp. 908-12, 1992.
- [2] X. Fengnian, J. Wei, V. Menon, S.R. Forrest, “Monolithic integration of a semiconductor optical amplifier and a high bandwidth p-i-n photodiode using asymmetric twin-waveguide technology,” *IEEE Photonics Technology Letters*, vol. 15, no. 3, pp. 452-4, 2003.
- [3] J.E. Bowers, C.A. Burrus, Jr., “Ultrawide-band long-wavelength p-i-n photodetectors,” *IEEE Journal of Lightwave Technology*, vol. 5, n. 10, pp. 1339-50, 1987.
- [4] L.Y. Lin, M.C. Wu, T. Itoh, “Figure of merit for high-power, high-speed photodetectors,” *Technical Digest of the Conference on Optical Fiber Communications*, vol. 6, pp. 40-1, 1997.
- [5] N. Shimizu, N. Watanabe, T. Furuta, T. Ishibashi, “InP-InGaAs uni-traveling-carrier photodiode with improved 3-dB bandwidth of over 150 GHz,” *IEEE Photonics Technology Letters*, vol. 10, no. 3, pp. 412-4, 1998.
- [6] S. Wang, J.B. Hurst, F. Ma, R. Sidhu, X. Sun, X.G. Zheng, A.L. Holmes Jr., A. Huntington, L.A. Coldren, J.C. Campbell, “Low-noise impact-ionization-engineered avalanche photodiodes grown on InP substrates,” *IEEE Photonics Technology Letters*, vol. 14, no. 12, pp. 1722-4, 2002.
- [7] A.R. Hawkins, W. Wu, P. Abraham, K. Streubel, J.E. Bowers, “High gain-bandwidth-product silicon heterointerface photodetector,” *Applied Physics Letters*, vol. 70, no. 3, pp. 303-5, 1997.
- [8] Y.J. Chiu, S.B. Fleischer, J.E. Bowers, “High-speed low-temperature-grown GaAs p-i-n traveling-wave photodetector,” *IEEE Photonics Technology Letters*, vol. 10, no.7, pp.1012-4, 1998.
- [9] D. Lasaosa, Y.J. Chiu, J. Piprek, J.E. Bowers, “Traveling-wave amplification photodetector (TAP detector),” *Proceedings of the 13th IEEE/Lasers and Electro-Optics Society Annual Meeting*, vol. 1, pp. 260-1, 2000.
- [10] D. Lasaosa, Y.J. Chiu, J. Piprek, J.E. Bowers, “Modeling of traveling-wave amplification photodetectors (TAP detectors),” *Proceedings of the SPIE Photonics West International Symposium*, vol. 4283, pp. 528-39, 2001.
- [11] E.J. Skogen, J.S. Barton, S.P. Denbaars, L.A. Coldren, “A quantum-well-intermixing process for wavelength-agile photonic integrated circuits,” *IEEE Journal of Selected Topics in Quantum Electronics*, vol. 8, no. 4, pp. 863-9, 2002.
- [12] J.T. Getty, E.J. Skogen, L.A. Coldren, “Multistage segmented 1.55 μ m lasers with record differential efficiency, low thresholds, and 50 Ω matching,” *Proceedings of the 15th IEEE/Lasers and Electro-Optics Society Annual Meeting*, 2002.

[13] D. Lasoasa, D. Pasquariello, J. Piprek, J.E. Bowers, "Recent advances in photodetectors with distributed optical amplification," *Proceedings of the SPIE-ITCom International Symposium*, vol. 5246, 2003.

[14] D. Pasquariello, J. Piprek, D. Lasoasa, J.E. Bowers, "InP-based waveguide photodetector with integrated photon multiplication," *Proceedings of the SPIE-ITCom International Symposium*, vol. 5248, 2003.

CHAPTER 2

DC characteristics of TAP detectors

In this chapter, the DC characteristics of TAP detectors will be analyzed. This will include their DC efficiency to an optical input, the background current that exists independently of that input, and the effects of the competition between the amplified spontaneous emission (ASE) and the signal for the available optical gain. In the case of TAP detectors with vertical coupling, the effects of a parasitic transistor that appears in the structure will also be discussed. First, we will show how the efficiency of TAP detectors may be calculated for the different configurations presented in the previous chapter, assuming that no spontaneous emission is present. Next, we will describe the physical origin of the background current that will exist independently of the optical input, and quantify the main contributions, generated by the absorption in the detection region of spontaneous emission (amplified or not) generated in the gain region. Then, the effect of the parasitic transistor appearing in TAP detectors with vertical coupling will be discussed. Finally, the effect of competition between the

ASE and the signal for the available gain will be studied. Design rules will be established out of these analyses.

Efficiency

As it has been claimed in the introduction, the distributed combination of amplification and photodetection is capable of producing high efficiency and high bandwidth without compromising the saturation power. In this paragraph, it will be shown how the efficiency of TAP detectors may be calculated. In a first section, the general equations, valid in the presence of distributed amplification and photodetection for all possible configurations of TAP detectors, will be deduced. In the next two sections, these equations are applied to the two particular configurations introduced in the previous chapter.

Generic distributed amplifier-photodetectors

As an optical mode travels inside a distributed amplifier-photodetector, both gain and absorption affect the optical power contained in it. We can define position-dependent modal confinement factors for the gain and the absorption, noted respectively by $\Gamma_g(z)$ and $\Gamma_a(z)$, together with the position-dependent material gain and absorption per unit length, noted respectively by $g(z)$ and $\mathbf{a}(z)$. z is the direction of propagation of light inside the device. We will assume that the device input is at $z=0$, and the output at $z=L$. Together with the amplification and absorption, the third process that will affect light as it travels is optical loss, through various mechanisms,

such as scattering or free-carrier absorption. Let us denote $l(z)$ the loss per unit length. Neglecting the effect of spontaneous emission, the mode experiences then a position-dependent net variation rate per unit length $\Delta g(z)$ given by

$$\Delta g(z) = \Gamma_g(z)g(z) - \Gamma_a(z)\mathbf{a}(z) - l(z) \quad (2.1).$$

As the mode travels in the device, the optical power changes. We will define $P_{opt}(z)$ as the optical power that arrives to position z in the device, traveling from lower to higher values of z . We will also define $I_{ph}(z)$, the cumulative photocurrent that has been generated as the light has traveled from 0 to z , i.e., the current that is generated in the detector region comprised between 0 and z . See figure 2.1 for a schematic representation.

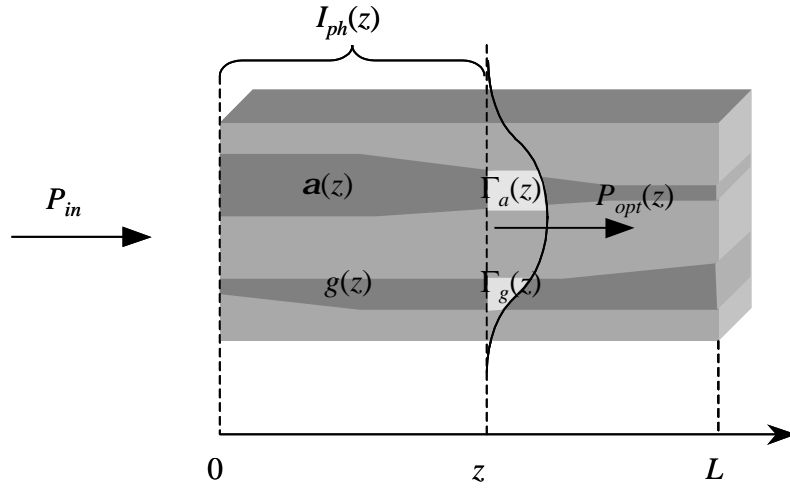


Figure 2.1: Schematic representation of an amplifier-photodetector for the purposes of calculating its efficiency. Position-dependent gain $g(z)$ and absorption $a(z)$ in the amplification and detection regions, respectively, are indicated, as well as modal confinement factors in these respective regions, $\Gamma_g(z)$ and $\Gamma_a(z)$. The device input is at $z=0$, its output at $z=L$. The local optical power at position z , $P_{opt}(z)$, is also indicated. $I_{ph}(z)$ represents the photocurrent collected as the optical signal has traveled from 0 to z .

Ignoring by now the effect of spontaneous emission, and assuming that only one guided mode exists in the device, the evolution of the optical power $P_{opt}(z)$ is described by the following equation:

$$\frac{dP_{opt}(z)}{dz} = \Delta g(z) P_{opt}(z) \quad (2.2),$$

with the initial condition $P_{opt}(0) = \mathbf{h}_c P_{in}$, P_{in} being the input optical power and \mathbf{h}_c the coupling factor into the considered mode. The photocurrent $I_{ph}(z)$ generated as the input optical signal has traveled from 0 to z is described by

$$\frac{dI_{ph}(z)}{dz} = \frac{q}{\mathbf{h}\mathbf{m}} \Gamma_a(z) \mathbf{a}(z) P_{opt}(z) \quad (2.3),$$

with the obvious initial condition $I_{ph}(0) = 0$. The solutions to these equations are written as

$$P_{opt}(z) = \mathbf{h}_c P_{in} e^{\int_0^z \Delta g(x) dx} = \mathbf{h}_c P_{in} G(z) \quad (2.4),$$

$$I_{ph}(z) = \frac{q}{\mathbf{h}\mathbf{m}} \mathbf{h}_c P_{in} \int_0^z \Gamma_a(x) \mathbf{a}(x) G(x) dx = \frac{q}{\mathbf{h}\mathbf{m}} \mathbf{h}_c P_{in} \mathbf{h}(z) \quad (2.5).$$

The total photocurrent generated by the TAP detector is given by $I_{ph}(L)$. $G(z)$ is the cumulative optical signal gain that the signal experiences traveling from 0 to z . $\mathbf{h}(z)$ is the cumulative internal quantum efficiency from 0 to z , i.e., the ratio between the total amount of photocurrent generated as the optical signal has traveled from 0 to z , and the coupled input optical power, expressed respectively in units of electrons per unit time and photons per unit time. The external quantum efficiency of the device is

obviously given by $\mathbf{h}_c \mathbf{h}(L)$. $G(z)$ and $\mathbf{h}(z)$ are introduced in order to simplify the notation, and will become most useful in later sections and chapters.

Note that, when the device waveguide supports multiple modes, the effect of all of them needs to be taken into account. In the general case where the device optical waveguide is multimode, the total optical power and the cumulative photocurrent are described by the following relations:

$$P_{opt}(z) = P_{in} \sum \mathbf{h}_c e^{\int_0^z \Delta g(x) dx} \quad (2.6),$$

$$I_{ph}(z) = \frac{q}{h\nu} P_{in} \sum \mathbf{h}_c \int_0^z \Gamma_a(x) \mathbf{a}(x) e^{\int_0^x \Delta g(y) dy} dx \quad (2.7),$$

where the sum is carried out over all modes. The confinement factors, and therefore the net gain per unit length Δg , will in general be different for each mode. The coupling coefficient \mathbf{h}_c will also be different from mode to mode.

In the next two sections, we will use these equations to calculate the efficiency of TAP detectors in the two different configurations presented in chapter 1.

TAP detectors with alternating amplification and absorption

In order to calculate the efficiency of a TAP detector with alternating amplification and absorption, let us assume that all amplification sections are identical, with gain g per unit length, amplification section length L_g , and modal confinement factor in the active region Γ_g . We will furthermore assume that all

absorption sections are also identical, with material absorption \mathbf{a} , absorption section length L_a and modal confinement factor in the absorption region Γ_a . Let us call $\mathbf{h}^{(1)}$ the efficiency of each detection section, and l the loss per unit length, which we will assume to be constant all along the device. This situation is shown schematically in figure 2.2.

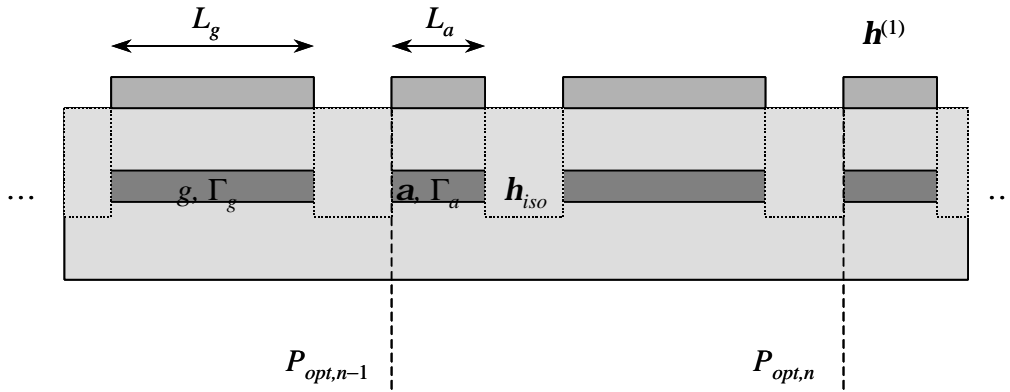


Figure 2.2: Cross-section of a TAP detector with alternating gain and absorption, showing the parameters used for the calculation of the efficiency in a TAP detector with alternating amplification and absorption. $h^{(1)}$ is the efficiency of each detection section (all assumed identical). The length, material gain or absorption, and confinement factors of the amplification and detection sections are indicated. The areas where the active (darker) region is interrupted represent the isolation sections. Light propagation occurs from left to right. $P_{opt,n}$ represents the optical power that arrives to the n -th detection region.

If we call $P_{opt,n}$ the amount of optical power that arrives to the n -th detection section, we can find, integrating (2.2) over one period, the following recursive relation:

$$P_{opt,n} = e^{(\Gamma_g g - l)L_g - (\Gamma_a a + l)L_a} (\mathbf{h}_{iso})^2 P_{opt,n-1} = \Delta G P_{opt,n-1} \quad (2.8),$$

where ΔG is defined as the net gain per period, and the initial condition is given by $P_{opt,1} = \mathbf{h}_c P_{in}$, leading to

$$P_{opt,n} = \mathbf{h}_c P_{in} \Delta G^{n-1} \quad (2.9).$$

The term \mathbf{h}_{iso} represents the fraction of power that remains after passing through each of the isolation regions existing between amplification and detection regions, i.e., $1 - \mathbf{h}_{iso}$ is the loss introduced by each isolation region.

Integrating now (2.3) over one absorption section, its efficiency $\mathbf{h}^{(1)}$ may be calculated:

$$\mathbf{h}^{(1)} = \frac{\Gamma_a \mathbf{a}}{\Gamma_a \mathbf{a} + l} \left[1 - e^{-(\Gamma_a \mathbf{a} + l)L_a} \right] \quad (2.10).$$

For a total of N absorption sections, the total photocurrent produced by the device I_{ph} and the total external quantum efficiency \mathbf{h}_{ext} are written as

$$I_{ph} = \sum_{n=1}^N \frac{q}{\mathbf{h}\mathbf{m}} \mathbf{h}^{(1)} P_{opt,n} = \frac{q}{\mathbf{h}\mathbf{m}} P_{in} \mathbf{h}_c \mathbf{h}^{(1)} \frac{\Delta G^N - 1}{\Delta G - 1} \quad (2.11),$$

$$\mathbf{h}_{ext} = \frac{\mathbf{h}\mathbf{m}}{q} \frac{I_{ph}}{P_{in}} = \mathbf{h}_c \mathbf{h}^{(1)} \frac{\Delta G^N - 1}{\Delta G - 1} \quad (2.12).$$

For values of ΔG close to 1, i.e., when the optical power that arrives to each detector is approximately the same, ΔG^N may be expanded as $((\Delta G - 1) + 1)^N$ using Newton's binomial formula, leading to the following approximation:

$$\mathbf{h}_{ext} \Big|_{|\Delta G - 1| \ll 1} \approx \mathbf{h}_c \mathbf{h}^{(1)} N + \mathbf{h}_c \mathbf{h}^{(1)} \binom{N}{2} (\Delta G - 1) \quad (2.13).$$

The value for the efficiency given in equation (2.13) is very close to the exact value when $|\Delta G - 1|N \ll 1$, and a good approximation whenever $|\Delta G - 1|N < 1$.

For a coupling efficiency of 50%, a realistic efficiency of each of the individual detection sections of 50% (in order to allow for the gain in the amplification section to compensate for the optical power lost through absorption and loss), we find a total external quantum efficiency of approximately 0.25 per section.

Finally, note that, without additional processing complexity, the first section of the TAP detector may be made an amplification region instead of a detector region, as shown in figure 2.3. In such case, this first section may be longer than the rest of the amplification regions, and independently biased, to provide a different optical gain G_1 . This, of course, results in saturation for lower input optical power, but without reduction in the maximum unsaturated photocurrent. The efficiency is then increased by a factor of $G_1 h_{iso}$, where the loss in the isolation region between the first amplification section and the first detection section has been assumed to be the same as for any other isolation section. This leads to the following final result:

$$\mathbf{h}_{ext} = \mathbf{h}_c G_1 \mathbf{h}_{iso} \mathbf{h}^{(1)} \frac{\Delta G^N - 1}{\Delta G - 1} \simeq \mathbf{h}_c G_1 \mathbf{h}_{iso} \mathbf{h}^{(1)} N + \mathbf{h}_c G_1 \mathbf{h}_{iso} \mathbf{h}^{(1)} \binom{N}{2} (\Delta G - 1) \quad (2.14).$$

Using this approach, external quantum efficiencies higher than 10 may be easily achieved for devices with 5 sections.

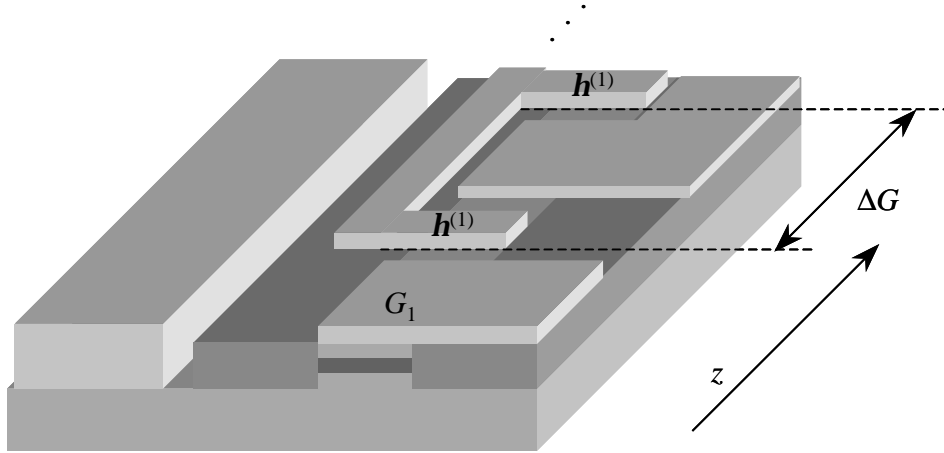


Figure 2.3: TAP detector with alternating amplification and absorption with an added gain section at the beginning of the device. The net gain per period ΔG , the gain of the first amplification section G_1 and the efficiency of each individual detection section $h^{(1)}$ are indicated. Light propagation occurs in the z direction.

One interesting parameter is the ratio between the total photocurrent in electrons per second and the maximum optical power in photons per second arriving to any detector region. This ratio offers us an insight on how high an efficiency we may obtain without saturating the device, since the overall device saturation will begin to show as soon as any of the different absorption or amplification sections starts to saturate. We will call this parameter the efficiency normalized to peak power, and denote it by h_{nor} . Note that dividing the total efficiency by the peak optical power inside the device does not constitute a normalization in the strict sense, since the peak power is a changing parameter.

One of the features of the efficiency normalized to the peak power is that, given a certain internal saturation power P_{sat} , such that if that power is present at any point inside the device, this one would begin to saturate, then the maximum unsaturated photocurrent that a detector may produce is given by $h_{nor}P_{sat}$. In that sense, what we

call the efficiency normalized to peak power would actually be the maximum unsaturated photocurrent in electrons per second normalized to the internal saturation power in photons per second.

If $\Delta G < 1$, more power will arrive to the first detection section than to any other. In that case, the efficiency normalized to peak power is always lower than for the case where $\Delta G = 1$, since each detector section will produce less photocurrent than the first, for a lower total efficiency with the same peak power:

$$\mathbf{h}_{nor}|_{\Delta G < 1} = \frac{h\mathbf{m}}{q} \frac{I_{ph}}{P_{opt,1}} = \mathbf{h}^{(1)} \sum_{n=0}^{N-1} \Delta G^{n-1} < N\mathbf{h}^{(1)} \quad (2.15).$$

For $\Delta G > 1$, the maximum power will arrive to the last detection section, resulting in

$$\mathbf{h}_{nor}|_{\Delta G > 1} = \frac{h\mathbf{m}}{q} \frac{I_{ph}}{P_{opt,N}} = \mathbf{h}^{(1)} \frac{\Delta G^N - 1}{\Delta G^{N-1} (\Delta G - 1)} = \mathbf{h}^{(1)} \sum_{n=0}^{N-1} \frac{1}{\Delta G^{n-1}} < N\mathbf{h}^{(1)} \quad (2.16).$$

In both cases, \mathbf{h}_{nor} will decrease as $\Delta G - 1$ grows in absolute value, since each one of the terms in the sum decreases, both in (2.15) and in (2.16). The optimum value for \mathbf{h}_{nor} is therefore $N\mathbf{h}^{(1)}$, and happens when gain, absorption and loss exactly cancel out in each period. In other words, increasing the gain per period in order to increase the overall device efficiency results in the peak optical power growing faster than the photocurrent. Figure 2.4 shows this behavior.

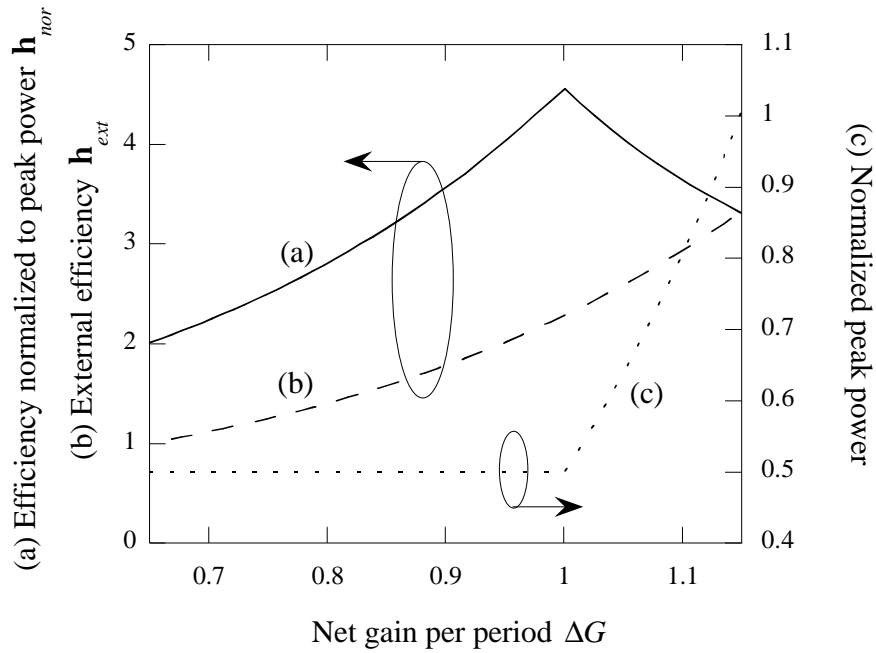


Figure 2.4: Simulated efficiency normalized to the peak optical power inside the device (a) as the net gain per period changes. Also shown are the device external quantum efficiency (b), and the peak optical power (c) normalized to the input power. The coupling coefficient is assumed to be $h_c=50\%$. The results shown were simulated for a device consisting of 6 periods, each one of them 50mm long, the isolation and detection sections being 2mm and 4mm long, respectively.

Note that, with the inclusion of a gain section first, both the peak power and the efficiency increase by a factor G_1 , resulting in the same value for the normalized efficiency. Note finally that, for traditional passive detectors with optical preamplification, h_{nor} can never be higher than 1.

We will now use the previously established equations to simulate the behavior of TAP detectors with realistic values of gain, absorption and loss. In all calculations, we will consider that the length of a period formed by a gain section, an absorption section and the isolation sections in between is fixed at $50\mu\text{m}$. This is necessary to keep the effect of microwave reflections affecting the generated photocurrent to a

minimum, up to frequencies in the order of 100GHz, as will be discussed in chapter 3. We will also assume that the length of each isolation region is kept to $2\mu\text{m}$, providing an added loss of $\sim 0.5\text{dB}$ per isolation section, resulting in an estimated value of $h_{iso}=0.9$. This is realistic for state-of-the-art intermixing techniques [1]. The gain sections will be assumed to have a quantum well (QW) based active region, with a confinement factor of 15%, whereas the absorption sections will have a bulk active region, with a larger confinement factor of 40%. The material absorption will be taken to be 9000cm^{-1} (typical value for GaAs at 850nm wavelength [2]), and the material gain between 2000 and 3000cm^{-2} (ibid.) (see, for example, [3] p. 172). Finally, the background loss will be slightly overestimated, and assumed to be 20cm^{-1} (see, for example, [3] p. 198). The input coupling efficiency will be set at 50%.

Given the constraint of fixed length per period, the effect of varying lengths for the amplification and absorption regions will now be shown. Let us first consider how the net gain per period is affected by the detection section length, as the material gain varies in the range given above. This behavior is shown in figure 2.5.

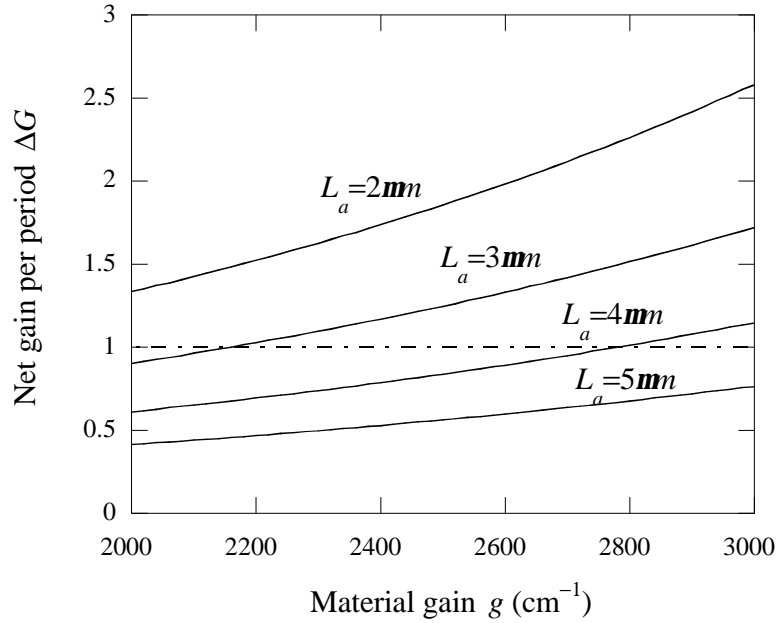


Figure 2.5: Simulated net optical gain per period as a function of material gain, for different absorption section lengths L_a . The total period length is 50mm, and the isolation section length is 2mm. The confinement factors are set to 15% and 40% in the gain and absorption sections, respectively. The material absorption in the detection section is 9000cm^{-1} , and the background loss is 20cm^{-1} . 90% of the optical power survives after passing through each isolation section. The horizontal dashed-dotted line marks the exact compensation between gain, absorption and loss in each period.

For typical values of material gain and confinement factors, we can deduce from the previous graph that gain, absorption and loss will cancel out when the detector length is kept around $4\mu\text{m}$, i.e., about 1/10 of the amplification section length. It will be shown in chapter 3 that this ratio also results in characteristic impedance close to 50Ω , and low microwave loss.

The efficiency of each individual detection section is also calculated, and shown in figure 2.6.

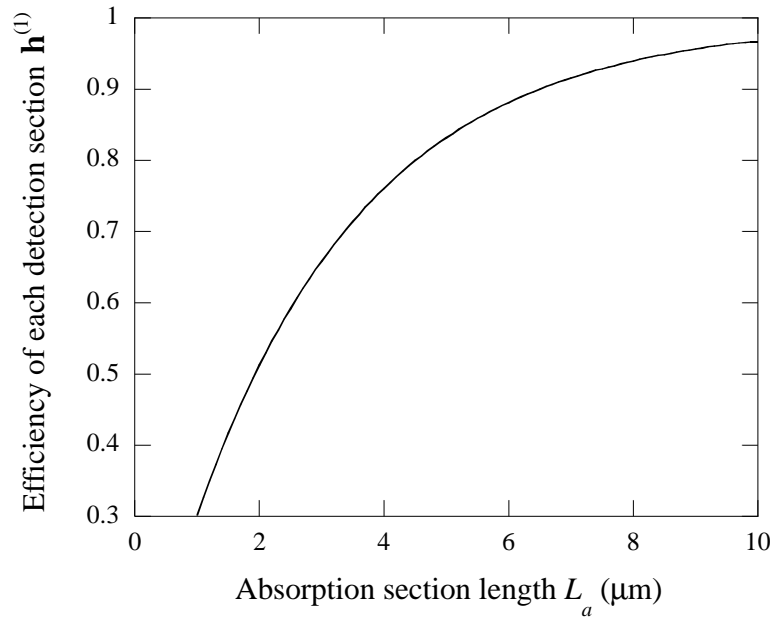


Figure 2.6: Simulated efficiency of each absorption section as a function of its length L_a . The confinement factor is 40%, and the material absorption is 9000cm^{-1} . The background loss is 20cm^{-1} .

The values obtained in the 2-4 μm range are close to the 50% assumed above, which are realistic for absorption, amplification and loss to cancel out.

The total device efficiency is shown in figure 2.7, as a function of material gain and for different number of periods. It may be observed that for absorption regions longer than 4 μm , the maximum efficiency quickly decreases for the same value of the material gain, and does not grow significantly with the period number. This is due to the fact that the material gain is no longer high enough to compensate for the absorption. Note also that, as the detection section length increases, the efficiency for $N=2$ periods is much lower than for higher period number, even when the material

gain is small. This seems to indicate that the effect of the distributed amplification and detection only shows itself after a minimum number of periods.

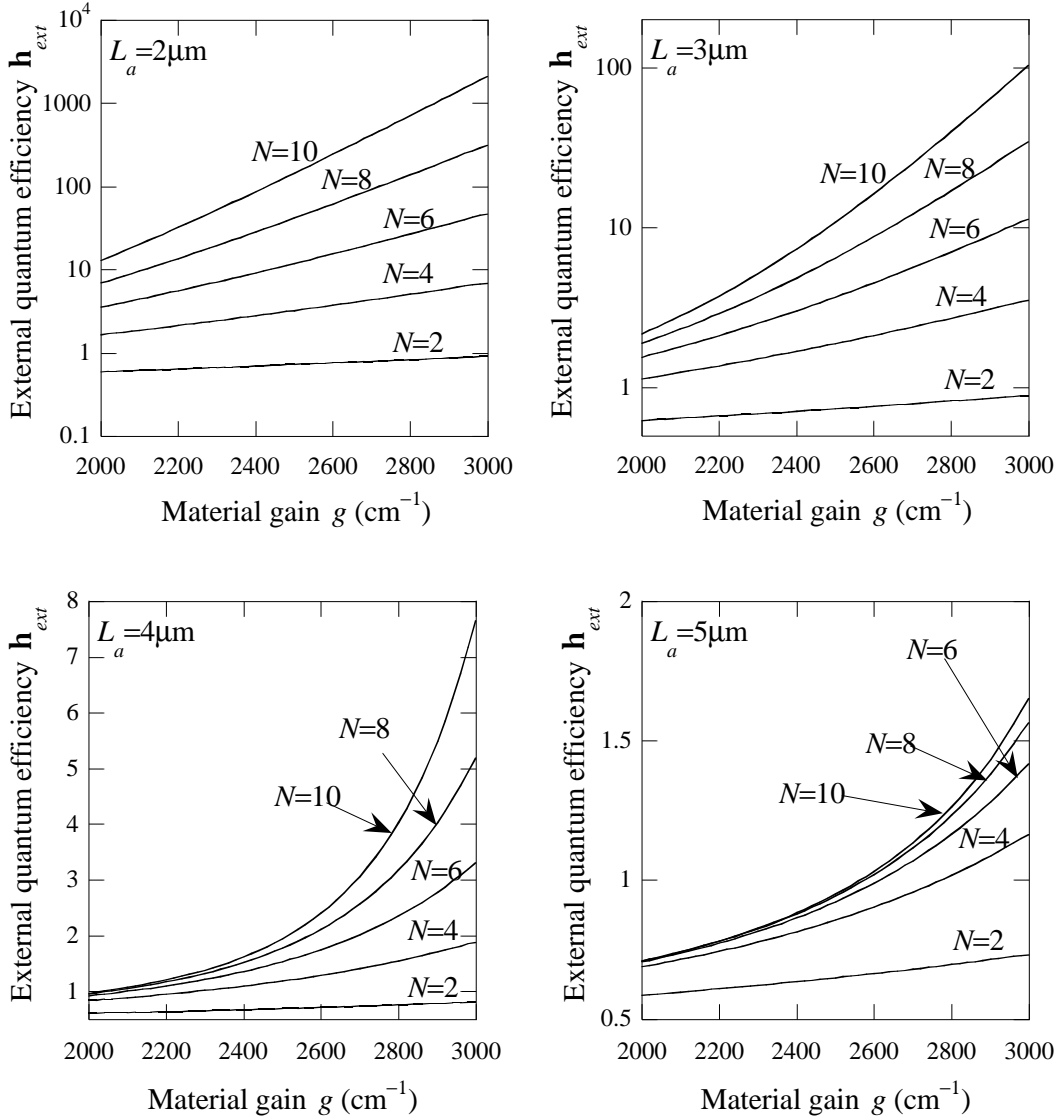


Figure 2.7: Simulated external quantum efficiency for a TAP detector with sequential gain and absorption with detection section lengths of 2mm (top left), 3mm (top right), 4mm (bottom left) and 5mm (bottom right), as a function of material gain, and for different number of periods N . The total period length is 50mm, and each isolation section is 2mm long. The confinement factors are set to 15% and 40% in the gain and absorption sections, respectively. The material absorption is assumed to be 9000cm^{-1} , and the coupling coefficient into the device 50%. 90% of the optical power survives after passing through each isolation section.

Some of the previous plots show efficiencies in the order of 100 or higher. However, this would be realistic only for very low input powers, since the peak optical power necessary for that high efficiency is also very large. This is illustrated in figure 2.8, where the peak optical power inside the device, normalized to the input power, is shown as a function of material gain, and for different numbers of periods, in the case where the detection sections are $3\mu\text{m}$ long.

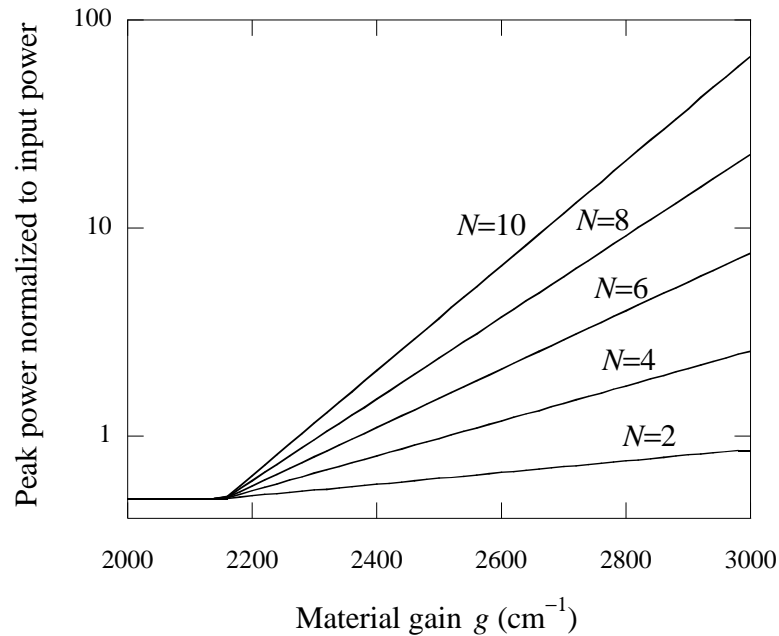


Figure 2.8: Simulated peak optical power normalized to input power as a function of material gain, and for different number of periods N . The total period length is 50mm, and the absorption and isolation sections are 3 and 2mm long, respectively. The confinement factors are set to 15% and 40% in the gain and absorption sections, respectively. 90% of the optical power survives after passing through each isolation section.

We can see how efficiencies in the order of 50 require a peak optical power about 100 times larger than the input optical power, which as mentioned above, is realistic

only for very low input powers. This shows the importance of the normalized efficiency, which was also simulated. The results are shown in figure 2.9.

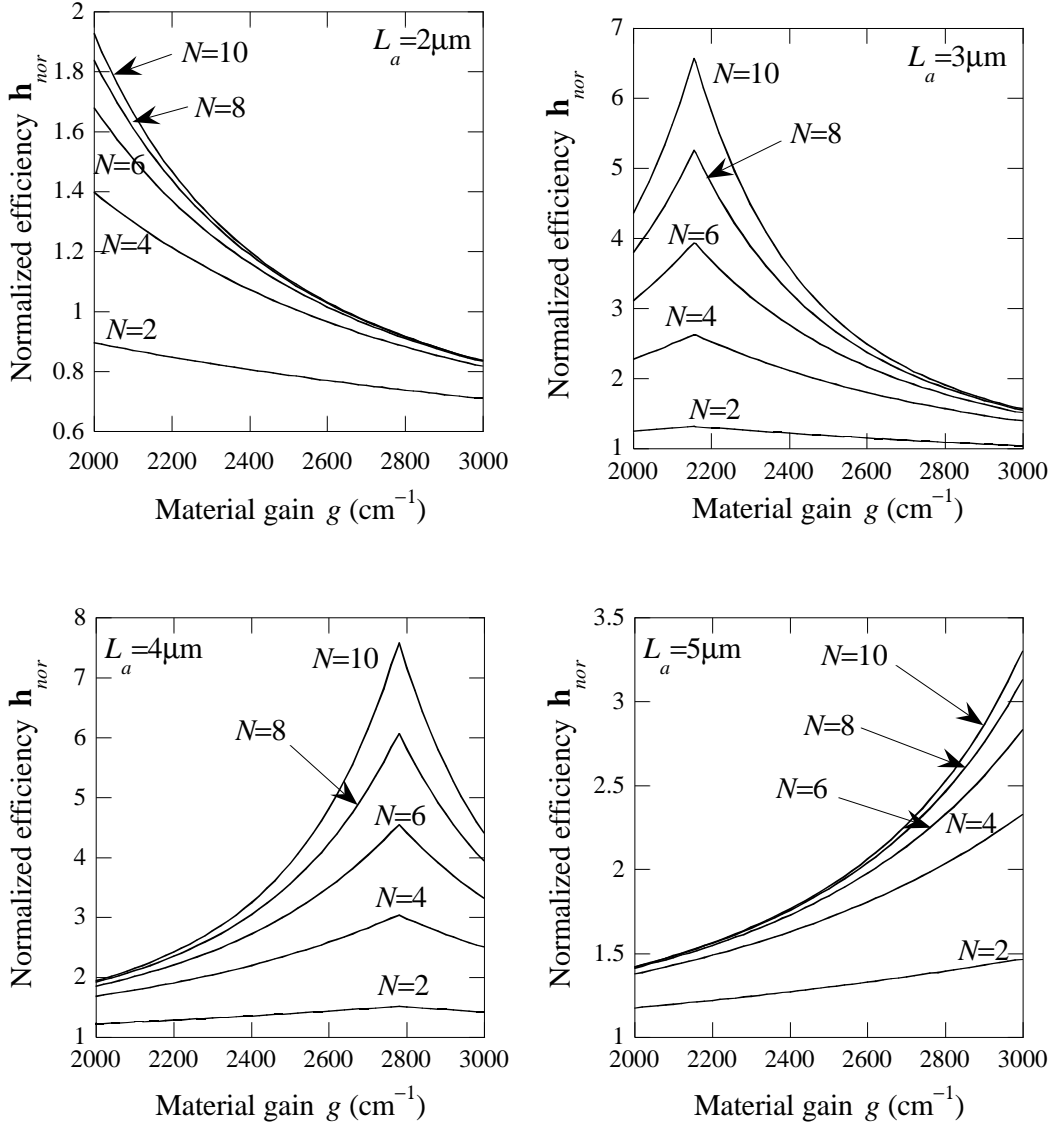


Figure 2.9: Simulated quantum efficiency normalized to peak power for a TAP detector with sequential gain and absorption with detection section lengths of 2mm (top left), 3mm (top right), 4mm (bottom left) and 5mm (bottom right), as a function of material gain, and for different number of periods N . The total period length is 50mm, and the isolation sections are 2mm long. The confinement factors are set to 15% and 40% in the gain and absorption sections, respectively. The material absorption is assumed to be 9000cm^{-1} , and the coupling coefficient into the device 50%. 90% of the optical power survives after passing through each isolation section.

These graphs show how the highest possible normalized efficiency happens when gain, absorption and loss cancel out (compare figures 2.9 and 2.5). It also shows, as mentioned above, how devices with detection sections 3-4 μm long produce best results in terms of high efficiency without saturation for realistic values of material gain.

In conclusion, in this paragraph the responsivity of TAP detectors with alternating gain and absorption has been analyzed. External quantum efficiencies in the order of 10 are shown to be possible with these devices. A parameter has been presented, the quantum efficiency normalized to peak power, which describes how efficient the detector may be without incurring saturation, showing how values larger than one are possible, as opposed to conventional passive detectors. Typical values of material gain and absorption yield optimum performance with detection sections \sim 3-4 μm long for devices with 50 μm period length.

The efficiency of TAP detectors with transverse coupling will be studied next.

TAP detectors with transverse coupling

In the case of either lateral or vertical coupling, we may assume that the device cross-section does not change along the direction of propagation of light. Therefore, Γ_a , Γ_g , \mathbf{a} and g may be assumed to be constant over the entire length of the device. See figure 2.10 for a schematic representation of this situation. In consequence, Δg is constant, and the solutions to equations (2.6) and (2.7) may be written, for a device of length L , in the following form:

$$P_{opt}(z) = P_{in} \mathbf{h}_c e^{\Delta g z} \quad (2.17);$$

$$I_{ph} = \frac{q}{h\mathbf{m}} P_{in} \mathbf{h}_c \Gamma_a \mathbf{a} \frac{e^{\Delta g L} - 1}{\Delta g} \quad (2.18).$$

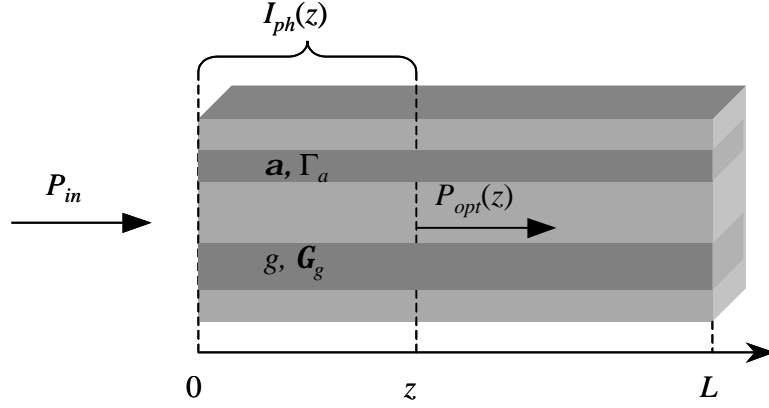


Figure 2.10: Parameters for the calculation of the efficiency in a TAP detector with transverse coupling. The material gain g and absorption a of the amplification and detection regions, respectively, are shown, as well as the confinement factors in each of them. Local optical power $P_{opt}(z)$ and cumulative photocurrent $I_{ph}(z)$ are also indicated.

We are mostly interested in the case where $|\Delta g L| \ll 1$, so that the optical power does not change significantly along the device. In this particular case, the following approximation holds:

$$I_{ph} \Big|_{|\Delta g L| \ll 1} \simeq \frac{q}{h\mathbf{m}} P_{in} \mathbf{h}_c \Gamma_a \mathbf{a} L \left(1 + \frac{\Delta g L}{2} \right) \quad (2.19).$$

The external quantum efficiency of the device may then be written in the following form:

$$\mathbf{h}_{ext} \Big|_{|\Delta g L| \ll 1} \simeq \mathbf{h}_c \Gamma_a \mathbf{a} L \left(1 + \frac{\Delta g L}{2} \right) \quad (2.20).$$

This number may be clearly more than 1 for long devices. The material absorption \mathbf{a} is usually in the order of $1\mu\text{m}^{-1}$. For a realistic confinement factor in the absorption region, in the order of 5% (to allow for easy compensation of the absorption by the gain) and a realistic coupling efficiency of 50%, the external quantum efficiency per unit of device length is approximately $0.025\mu\text{m}^{-1}$. Thus, for a device of $400\mu\text{m}$, efficiencies in the order of 10 are possible.

When several modes are supported by the optical waveguide, not only the coupling coefficient, but also the confinement factors in the absorption and gain region will be different. This makes nearly impossible to balance gain and absorption in all modes simultaneously. Therefore, for multimode devices, we cannot perform simultaneously the previous approximations for all modes, and the equation that we need to use for the total efficiency is

$$\mathbf{h}_{ext} = \sum_i \mathbf{h}_{c,i} \Gamma_{a,i} \mathbf{a} \frac{e^{\Delta g_i L} - 1}{\Delta g_i} \quad (2.21),$$

where i belongs to a set of indices used to number the device-supported modes, and $\mathbf{h}_{c,i}$, $\Gamma_{a,i}$ and Δg_i are respectively the coupling efficiency, confinement factor in the absorption region and net gain per unit length for the i -th mode.

Under these conditions, and after propagation over a long enough distance, one mode will dominate over the rest, the one with highest value of Δg . In order to avoid saturation of the amplifier, gain and absorption must be close to cancellation for that mode. This will result in most of the other modes suffering important net attenuation

as they propagate along the device. Therefore, even in highly multimode devices, we can expect important contribution to the photocurrent from just a few modes. For the rest of the modes, we can assume that ΔgL is negative and large in absolute value. The valid approximation for the photocurrent extracted from one of those modes is

$$I_{ph} \approx \frac{q}{\hbar\mathbf{m}} P_{in} \mathbf{h}_c \frac{\Gamma_a \mathbf{a}}{|\Delta g|} = \frac{q}{\hbar\mathbf{m}} P_{in} \mathbf{h}_c \frac{\Gamma_a \mathbf{a}}{\Gamma_a \mathbf{a} + l - \Gamma_g g} \approx \frac{q}{\hbar\mathbf{m}} P_{in} \mathbf{h}_c \quad (2.22).$$

The behavior of these modes can be compared to that of modes in a traditional detector. Intuitively, this makes perfect sense, since we can neglect the effect of the amplification region if the absorption is too large compared to the gain. If their confinement factor in the detector is large, these modes will survive only for a very short distance (a few microns). The total device efficiency may be approximated by the following formula:

$$\mathbf{h}_{ext} \approx \sum_i \mathbf{h}_{c,i} \Gamma_{a,i} \mathbf{a} L \left(1 + \frac{\Delta g_i L}{2} \right) + \sum_j \mathbf{h}_{c,j} \quad (2.23),$$

where the index i is used to number all the device modes for which gain and absorption are close to cancellation, while the index j denotes all modes heavily dominated by absorption. For long devices ($L > 100\mu\text{m}$), we can predict that the first term of the sum will nearly always dominate.

In the case of TAP detectors with vertical coupling, we can also include, with no additional fabrication complexity, an amplification section at the beginning of the device, as shown in figure 2.11.

Denoting the gain of this initial amplification region by G_1 , both the optical power and the efficiency will be multiplied by G_1 . The price to pay for this higher efficiency is, once more, saturation for lower input optical power. The maximum unsaturated photocurrent, however, does not change *a priori*.

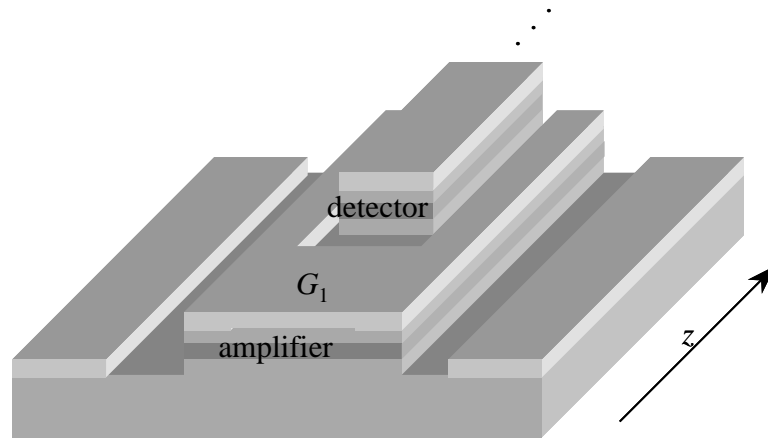


Figure 2.11: Schematic representation of a TAP detector with vertical coupling, with an added gain section at the beginning of the device. The gain G_1 of the first amplification region is indicated. Light propagation occurs along the z direction.

Similarly as in the case of TAP detector with alternating gain and absorption, we may define an efficiency normalized to peak power, taking this time the highest possible power along the device. The calculation is not, however, as straight-forward as in the previous configuration, since modes may be present that will experience net gain, reaching their maximum in the end of the device, and others may exist that present heavy net attenuation, peaking at the input. The sum of their contributions may therefore reach its maximum at some position that depends on the confinement factors of each mode, the coupling efficiency into each one of them, and the material gain and absorption of the amplification and detection region, respectively. The

location and value of the maximum optical power is not easily calculated, but some approximations may be made to estimate the normalized efficiency. We may ignore the effect of heavily attenuated modes, since the trade-off between amplification and efficiency is the main concern at this point in the discussion. Furthermore, we will ignore all modes except the one with highest value of Δg , assuming that it is this one that dominates overwhelmingly at $z=L$. Consequently, we will also ignore the contribution to the total photocurrent by other modes, resulting in a normalized efficiency of

$$\mathbf{h}_{nor}|_{\Delta g > 0} = \frac{h\nu}{q} \frac{I_{ph}}{P_{in} h_c e^{\Delta g L}} = \Gamma_a \mathbf{a} \frac{1 - e^{-\Delta g L}}{\Delta g} \simeq \Gamma_a \mathbf{a} L \left(1 - \frac{\Delta g L}{2} \right) \quad (2.24).$$

This expression, as mentioned above, takes into account only the mode presenting highest positive value of Δg . The approximation yielding the last expression is valid, as always, when $|\Delta g L| \ll 1$. The normalized efficiency will never be higher than the device internal efficiency, (compare (2.24) with (2.20)), and as we increase the gain to produce larger photocurrent, the peak optical power once more grows faster than the efficiency, resulting again in optimum performance for zero or very small net optical gain per unit length.

In the case where no mode experiences net gain, the peak power will happen for $z=0$, resulting in a normalized efficiency identically equal to the internal quantum efficiency, which will be always lower than in the case where constant optical power

is achieved along the device. The optimum normalized efficiency happens again when amplification, absorption and loss exactly compensate.

In the case where a gain section is included in the device first, as shown in figure 2.11, and since both the peak power and the efficiency are multiplied by the gain G_1 introduced by that section, the efficiency normalized to peak power will not change.

We will now use the previous expressions to calculate the efficiency for TAP detectors with transverse coupling given realistic geometric and material parameters. First of all, we will assume that only one mode exists, that exhibits larger overlap with the amplification region than with the absorption region. This overlap will be assumed constant along the device. Since the mode needs to extend over a relatively large ($\sim 1\mu\text{m}$ at least) vertical or lateral distance to have significant overlap with both regions, we may assume that the sum of the confinement factors in both is limited to 25%. Other modes will be assumed to suffer net attenuation large enough for the power contained in them to be considered negligible after a short ($\sim 10\mu\text{m}$) distance of propagation. Their contribution to the photocurrent will be thus neglected at this point. The material absorption that will be used is 9000cm^{-1} , and the material gain will be allowed to vary between 2000 and 3000cm^{-1} , both values being typical for GaAs at 850nm wavelength. The input coupling coefficient into this mode will be assumed to be 50%, and the background optical loss 20cm^{-1} .

Using the previous values, figure 2.12 shows the net modal gain per unit length for different ratios r between gain and absorption modal confinement factors:

$$r = \frac{\Gamma_g}{\Gamma_a} \quad (2.25).$$

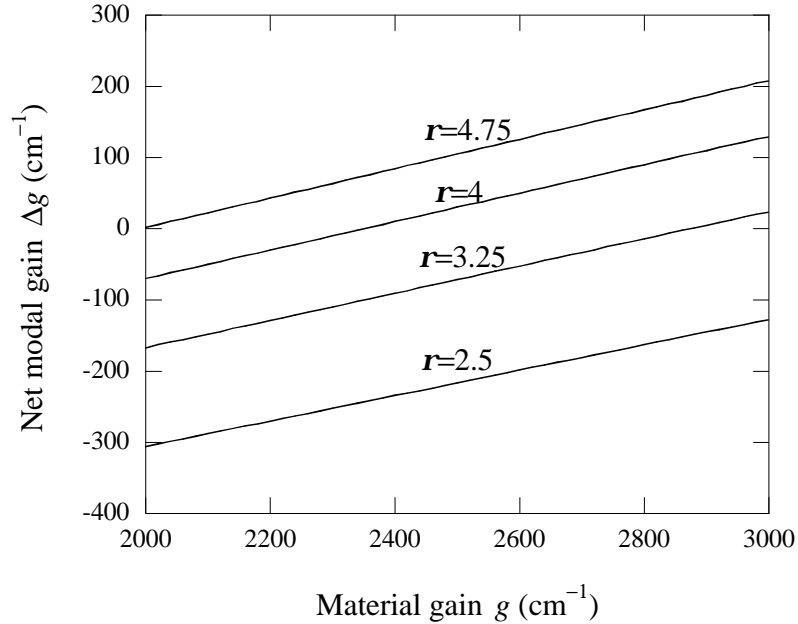


Figure 2.12: Simulated net modal gain for TAP detectors with transverse coupling as a function of material gain. $r=G_g/G_a$ is the ratio between the modal confinement factors in the gain and absorption regions. The sum G_g+G_a is kept equal to 25%. The material absorption in the detection region is 9000cm^{-1} , and the background loss 20cm^{-1} .

For realistic values of material gain, cancellation between gain, absorption and loss is possible for gain modal confinement factors about 4 times larger than absorption modal confinement factors. Figure 2.13 show the calculated efficiency as a function of material gain in the amplification region, for different device lengths and ratios between gain and absorption confinement factors.

Note that the efficiency seems to be always quite smaller for the case $L=100\mu\text{m}$ than for the rest. Similarly as in the case of TAP detectors with alternating gain and

absorption, there seems to be the need for a certain device length so that the effect of the distributed amplification and absorption may show itself.

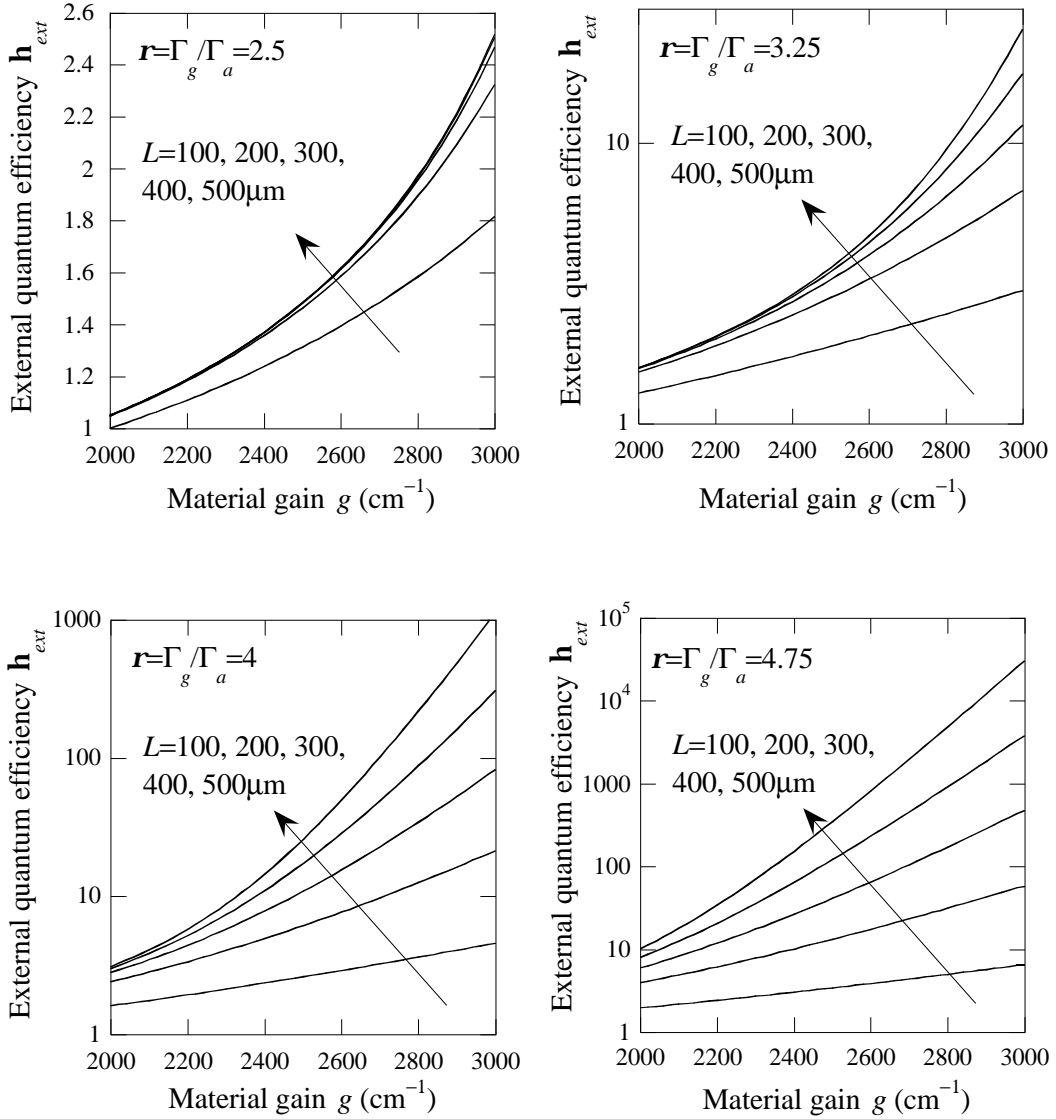


Figure 2.13: Simulated external quantum efficiency of TAP detectors with transverse coupling as a function of material gain, for different device lengths L . The values of the ratio between the confinement factors in the gain and absorption regions $r = \Gamma_g / \Gamma_a$ are 2.5 (top left), 3.25 (top right), 4 (bottom left) and 4.75 (bottom right), while $\Gamma_g + \Gamma_a = 25\%$ for all the plots. The material absorption in the detection region is 9000cm^{-1} , the background loss 20cm^{-1} and the coupling efficiency 50%. All vertical scales are logarithmic except for the top left plot ($r=2.5$).

As shown in figure 2.13, very high efficiencies (in the order of 1000 or more) may be achieved by TAP detectors with transverse coupling. However, for those to be possible, the peak optical power inside the device needs to be several orders of magnitude higher than the input optical power, as shown in figure 2.14, for the case where $\Gamma_g=20\%$, $\Gamma_a=5\%$ ($r=4$).

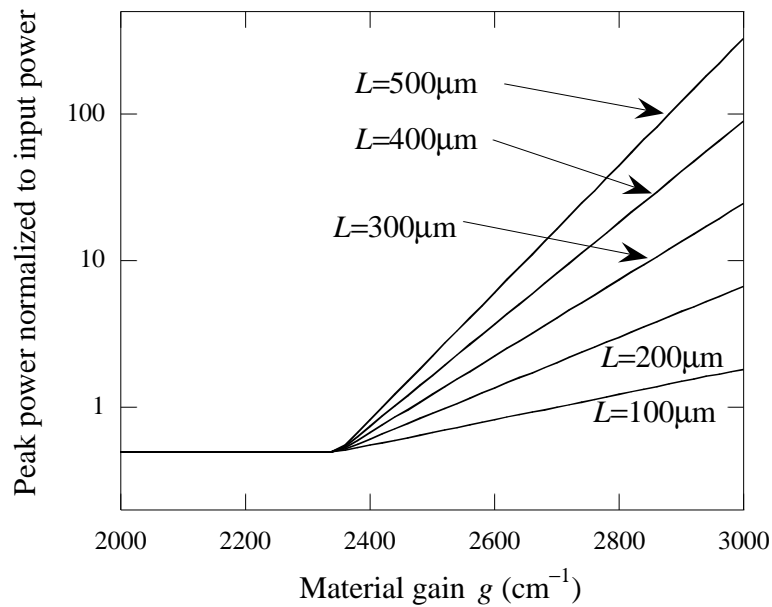


Figure 2.14: Simulated peak optical power inside a TAP detector with transverse coupling, normalized to input power, as a function of material gain, and for different device lengths L . The confinement factors in the gain and absorption region are, respectively, $\Gamma_g=20\%$ and $\Gamma_a=5\%$. The material absorption is 9000cm^{-1} and the background loss 20cm^{-1} . The coupling efficiency is $h_c=50\%$.

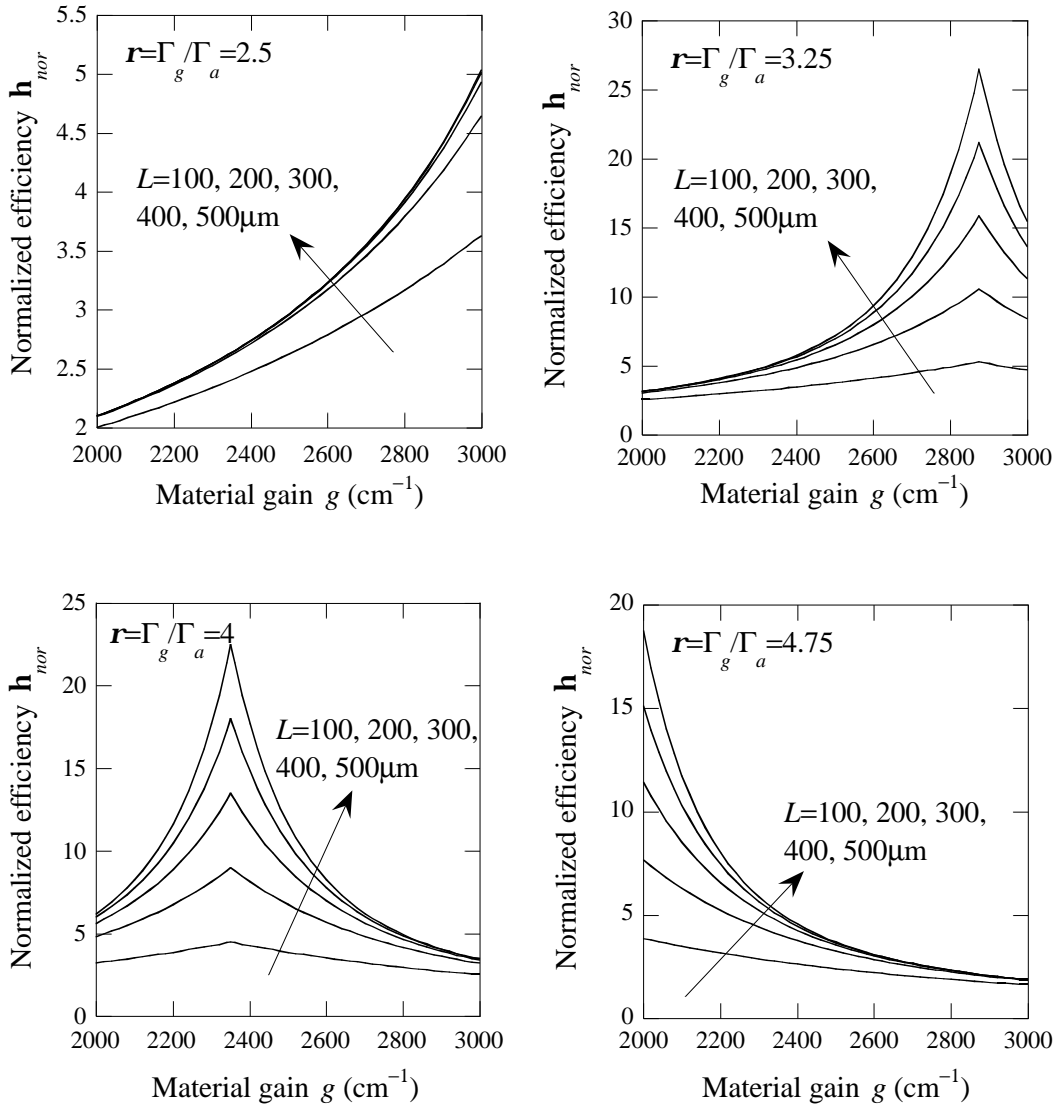


Figure 2.15: Simulated efficiency normalized to peak power for TAP detectors with transverse coupling as a function of material gain, for different device lengths L . The values of the ratio between the confinement factors in the gain and absorption regions $r = \Gamma_g / \Gamma_a$ are 2.5 (top left), 3.25 (top right), 4 (bottom left) and 4.75 (bottom right), while $G_g + G_a = 25\%$ for all the plots. The material absorption in the detection region is 9000cm^{-1} , the background loss 20cm^{-1} and the coupling efficiency 50%.

It is therefore very useful to calculate also the efficiency normalized to peak power, shown in figure 2.15. As described above, the normalized efficiency is largest for values of gain that produce constant optical power along the device, reaching

values well over 10. It also shows how a ratio between 3 and 4 between modal gain and absorption confinement factors is advisable for optimum results. Finally, it also shows how a relatively large difference exists between devices that are 100 μm long and longer devices. It will be shown later in this dissertation how bandwidth and noise requirements, as well as competition between ASE and signal for the available gain, limit the useful device lengths to a maximum of 300-400 μm , resulting in optimum device lengths between 200 and 400 μm .

In conclusion, the efficiency for TAP detectors with transverse coupling has been analyzed in this section, obtaining equations that allow its calculation. It has been shown how, for realistic values of material gain and absorption, external quantum efficiencies well over 10 are possible. From those simulations, it may be concluded that, for optimum trade-off between efficiency and saturation, a ratio of 3-4 is necessary between gain and absorption modal confinement factors, which we may use as a design rule for TAP detectors with transverse coupling.

This chapter has dealt up to now with the efficiency of TAP detectors, assuming that signal amplification and absorption are the only phenomena happening in the device. In the next paragraphs, non-idealities arising in TAP detectors will be described. Specifically, background current, and competition between amplified spontaneous emission (ASE) and signal for the available gain, will be analyzed.

Background current

Even in the absence of an optical input, and independently of it, there are three main mechanisms that generate current flow in the detector. One of them is the current of the reversed-biased absorption regions. This current is typically much smaller than $1\mu\text{A}$. Another source of current is the imperfect electrical isolation between gain and absorption diodes. Because of the amplification sections being forward-biased, and the absorption sections reverse-biased, we can expect a large (5-10V) voltage difference between their contacts. Even for good electrical isolation ($10\text{M}\Omega$), this translates into a current flow of $\sim 1\mu\text{A}$. This allows us to neglect the effect of the reverse current of the absorption diode. A final source of current is the absorption in the detection sections of amplified spontaneous emission (ASE) and spontaneous emission generated in the gain sections. We will denote them respectively by I_{ASE} and I_{sp} . These two contributions will be referred to as ASE current and spontaneous emission current, and will be shown to produce the chief contribution of the background current. We will refer to the contribution of all other effects, which do not involve the generation or absorption of light, as dark current, and denote it by I_{dark} . The sum of the ASE current, spontaneous emission current and dark current will add up to the total background current I_{bck} .

In the next sections, the different contributions to the background current will be studied.

Dark current

In this section, the dark current associated to the reverse bias detection diode will be neglected, since it may be assumed to be much smaller than the contribution due to the imperfect electrical isolation between gain and absorption regions, as argued above.

The mechanism of generation of dark current due to imperfect electrical isolation between gain and absorption regions varies between the TAP detector configurations. In the case of a TAP detector with alternating gain and absorption, its origin will be conduction between the gain and absorption regions through the remaining of the top cladding, and the intrinsic active region or separate confinement heterostructure (SCH) in the isolation sections. In TAP detectors with lateral coupling, the dark current is generated in a very similar manner, through conduction in the intrinsic region of the optical waveguide. This is schematically represented in figure 2.16.

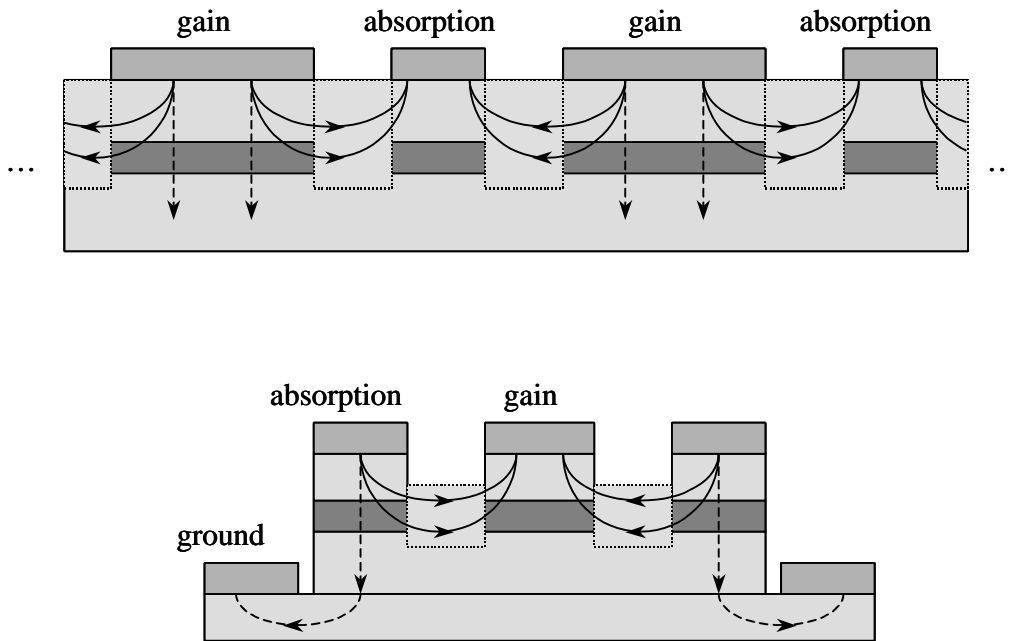


Figure 2.16: The origin of the main contribution to the dark current in TAP detectors with alternating gain and absorption (top) and with lateral coupling (bottom) is related to conduction through the isolation region. The dashed lines represent the desired bias current flow. The full lines represent the stray current through the isolation regions that adds to the dark current. Light propagation in the device is left to right or right to left in the TAP detector with alternating gain and absorption represented, and perpendicular to the plane of the figure for the TAP detector with lateral coupling. The contacts are labeled with the function that they perform, i.e., gain for the amplification diode contact, absorption for the detection diode contact and ground for the common contact.

The actual magnitude of the dark current will vary with the exact epilayer structure and the bias applied to the device. In TAP detectors with alternating amplification and absorption, the total resistance between gain and detection electrodes will be roughly the parallel of $2N$ resistances of very close value, each one of them representing the resistance between an amplifier and each one of its closest neighboring detector. In the case of TAP detectors with lateral coupling, the total resistance will be inversely proportional to the device length, or the dark current will be proportional to the device length. Therefore, when gain and absorption are close

to cancellation, the ratio between efficiency and dark current will be mostly independent on device length or number of periods, for TAP detectors with lateral coupling or alternating amplification and absorption, respectively.

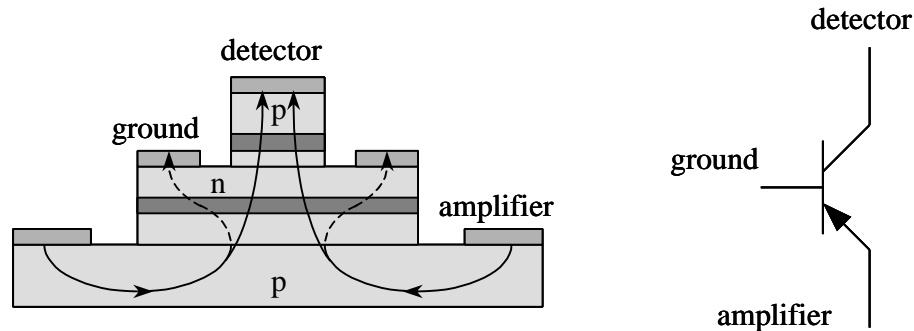


Figure 2.17: The origin of the dark current in TAP detectors with vertical coupling is the leakage of carriers through the middle cladding. Left: Cross-section of a TAP detector by a plane perpendicular to the direction of propagation of light. The dashed arrow represents the desired current flow. The full line represents the current flow that will contributed to the dark current. Right: equivalent circuit of the parasitic transistor, assuming that top and bottom claddings are p-type doped, and the middle cladding is n-type doped, as indicated in the device cross-section. The transistor terminals and the TAP detector contacts are labeled with the same name for clarity.

In TAP detectors with vertical coupling, there is not a direct path for current to travel from the amplifier to the detector contact without passing through both the amplification and absorption diode. The presence of alternate claddings, p- and n-doped, gives rise however to a parasitic transistor, where carriers injected into the amplifier region from its bottom cladding that are not captured in the quantum wells may leak through the middle cladding. The reverse bias applied to the absorption region will then capture those carriers, generating current in the detector. In fact, the result is equivalent to that of a parasitic transistor, where the emitter, the collector and

the base are the bottom, top and middle cladding layers, as schematically represented in figure 2.17.

For devices of equal width but different length, the injected current per unit area necessary to achieve the same net gain per unit length will be roughly the same, leading to a very similar leak current per unit area, or a dark current that will be also proportional to the device length. The effect of the parasitic transistor, and more specifically how to avoid or decrease its effect is important enough, however, to perform a more detailed analysis. This study is carried out in the next paragraph.

Parasitic transistor in TAP detectors with vertical coupling

The effect of the parasitic transistor appearing in TAP detectors with vertical coupling, shown in figure 2.17, will be analyzed in this section.

The usual operating point for this transistor is described by the emitter-base diode (amplifier diode) being forward-biased, while the collector-base diode (detection diode) is reverse-biased. Under these conditions, majority carriers in the emitter (lower cladding) are injected into the intrinsic material (active region) of the emitter-base diode (amplifier). We may assume that those who do not recombine in this intrinsic region will reach the base (middle cladding), and either recombine there through dielectric relaxation, or reach the base-collector diode (detection), as shown in figure 2.18. The emitter-base diode current may therefore be found as the sum of three contributions. One is the recombination current in the amplifier diode intrinsic region. This includes the recombination in the quantum wells (radiative or not) and

in the separate confinement heterostructure (SCH). Another one is the current due to carriers injected from the bottom cladding into the middle cladding, and diffusing there as minority carriers. Similarly, there is a diffusion current of carriers injected from the base into the emitter. The leakage current, contributing to the base-collector current, will be generated by the diffusion of some of the minority carriers injected from the bottom cladding into the detection diode.

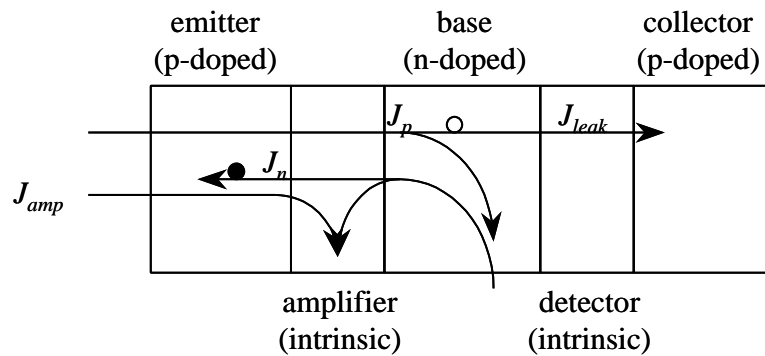


Figure 2.18: Currents in the parasitic transistor for TAP detectors with vertical coupling. Four contributions are identified in the figure, which shows the particular case where emitter (top cladding) and collector (bottom cladding) are p-type doped, while the base (middle cladding) is n-type doped. Minority carriers (electrons, represented by a full dot, and holes, represented by an empty dot) are injected into the base and emitter from the emitter and base, producing respectively vertically-traveling current densities J_n and J_p . These minority carriers either recombine in or diffuse through the emitter and base, respectively. Electron-hole pairs recombine in the intrinsic region in the amplification (emitter-base) diode, giving raise to a recombination current density J_{amp} . A fraction of the carriers injected from the bottom cladding diffuse through the middle cladding and reach the detection diode, giving raise to the parasitic leakage current density J_{leak} . The latter is the contribution from the parasitic transistor to the background detector current. The space-charge region of amplification and detection diodes is assumed to approximately coincide with the intrinsic regions.

In order to perform an analysis of this transistor, several assumptions may be made. First, we will consider that no minority carriers are injected into the top or middle cladding from the middle or top cladding, respectively, since the detection

diode is reverse-biased. For the same reason, we will assume that all minority carriers diffusing through the base and reaching the detection diode will contribute to the detector background current through the leakage current density J_{leak} . We will furthermore assume that this leakage current is the only contribution from the parasitic transistor to the detector background current, the rest of the dark current being accounted by the typical reverse current of the diode in the case where the amplifier diode would not be present. The minority carriers traveling through the base may be assumed to diffuse, rather than drift through it. Finally, the space-charge region of the amplification and detection diodes will be assumed to coincide with the intrinsic layers in the device.

As it is customary, currents entering the transistor through the emitter, base and collector contacts will be denoted by I_E , I_B and I_C , respectively. If A is the cross-sectional area of the active region through which current flows vertically, we find

$$I_E = A(J_{amp} + J_n + J_p) \quad (2.26),$$

$$I_B = -A(J_{amp} + J_n - J_{leak} + J_p) \quad (2.27),$$

$$I_C = -AJ_{leak} \quad (2.28).$$

The bias current for the amplifier is obviously $I_{bias}=I_E$. The contribution from the parasitic transistor to the background current of the detector is given by I_C . The most interesting result from a study of this transistor would be the ratio $|I_C/I_E|$, which would describe the fraction of the bias current that contributes to the detector background

current. Let us now therefore write relations between the different current contributions.

The recombination current from the active region has, as aforementioned, two components. One is given by the recombination in the quantum wells (denoted by J_{QW}) and the other by recombination in the SCH (which we will call J_{SCH}). The injection efficiency \mathbf{h}_i of an amplifier diode or a laser diode is typically defined as the fraction of carriers in the bias current that are captured and recombine in the active region, meaning by that the quantum wells. We can therefore write

$$J_{QW} = \frac{\mathbf{h}_i I_E}{A} = \frac{\mathbf{h}_i}{1 - \mathbf{h}_i} (J_{SCH} + J_n + J_p) \quad (2.29),$$

where $J_{QW} + J_{SCH} = J_{amp}$.

The recombination current in the SCH may be written as:

$$J_{SCH} = q w'_{SCH} \frac{p_{SCH}}{\mathbf{t}_{SCH}} \quad (2.30),$$

where p_{SCH} is the hole concentration in the SCH at the operating point (assumed similar to the electron concentration), and \mathbf{t}_{SCH} is the carrier lifetime in the SCH, which includes the effect of all types of recombination processes. w'_{SCH} is an effective thickness of the SCH, defined to compensate for possible position-dependent variations of electron and hole concentrations inside it.

The minority diffusion currents are usually found under one of two approximations, the so-called long-base and short-base approximations (see for

example [4], pp. 235-9). The choice of the approximation requires knowledge of the carrier diffusion length. The distance they need to travel needs also to be known, i.e., the distance between the active regions of amplifier and detector diodes for the minority carriers injected into the base, and the distance between the amplifier diode active region and the bottom contact for the minority carriers injected into the emitter. The latter will be in the order of a few microns, whereas the former may be assumed to be in the 0.5-1 μm range. At relatively high dopant concentrations (10^{18}cm^{-3}), the diffusion lengths may be estimated to be in the order of 0.5 μm for holes, 1 μm for electrons (see for example [5], p. 298). The minority carrier diffusion current in the emitter may then be approximated in the long-base picture, leading to

$$J_n \approx qD_n \frac{n_{i,E}^2}{N_A L_n} \left(e^{\frac{qV_{EB}}{kT}} - 1 \right) \quad (2.31),$$

where D_n is the diffusivity of electrons, $n_{i,E}$ the intrinsic carrier concentration, N_A the acceptor concentration and L_n the diffusion length of electrons, all of them defined in the emitter. The diffusion length L_n is given by the relation $L_n^2 = D_n t_n$, where t_n is the minority carrier lifetime in the emitter. V_{EB} is again the emitter-base forward bias applied to the amplifier diode.

This long-base approximation will not, in general, be valid in the base, because the base length is not necessarily much longer than the minority carrier diffusion length in it. The short-base approximation assumes, in its simplest form, that the excess hole density is linear in the base, decreasing from its maximum value at the

edge of the emitter-base diode space-charge region to 0. We will call $x=0$ and $x=w_B$ respectively the edges of the emitter-base and collector-base diode space-charge regions and the base. In a short base approximation, we find that J_{leak} and J_p are approximately equal, and given by the following relation:

$$J_{leak} \approx J_p = -qD_p \frac{dp}{dx} = qD_p \frac{n_{i,B}^2}{N_D w_B} \left(e^{\frac{qV_{EB}}{kT}} - 1 \right) \quad (2.32).$$

In a long-base approximation, the hole concentration decays exponentially from its value at $x=0$, due to recombination and diffusion, resulting in the following approximation:

$$J_{leak} \approx J_p e^{-\frac{w_B}{L_p}} = qD_p \frac{n_{i,E}^2}{N_A L_p} e^{-\frac{w_B}{L_p}} \left(e^{\frac{qV_{EB}}{kT}} - 1 \right) \quad (2.33).$$

The hole diffusion length L_p satisfies the relation $L_p^2 = D_p t_p$, where t_p is the minority carrier lifetime in the base.

In a short base approximation, inserting (2.29), (2.30), (2.31) and (2.32) into (2.26) and (2.28), we may find

$$\left| \frac{I_C}{I_E} \right| \approx \frac{(1-h_i)}{1 + \frac{t_p L_n w_B N_D n_{i,E}^2}{t_n L_p L_p N_A n_{i,B}^2} + \frac{t_p w_B w'_{SCH} N_D p_{SCH}}{t_{SCH} L_p^2 n_{i,B}^2 e^{\frac{qV_{EB}}{kT}}}} \quad (2.34).$$

In a long-base approximation, we may use (2.33) instead of (2.32), leading to

$$\left| \frac{I_C}{I_E} \right| \approx \frac{(1-h_i) e^{-\frac{w_B}{L_p}}}{1 + \frac{t_p}{t_n} \frac{L_n}{L_p} \frac{N_D}{N_A} \frac{n_{i,E}^2}{n_{i,B}^2} + \frac{t_p}{t_{SCH}} \frac{w'_{SCH}}{L_p} \frac{N_D P_{SCH}}{n_{i,B}^2 e^{\frac{qV_{EB}}{kT}}}} \quad (2.35).$$

In TAP detectors with vertical coupling, the middle cladding may be assumed heavily doped for good lateral electrical conduction of the amplifier diode bias current. As mentioned earlier, its thickness is in the 0.5-1 μ m range, for optimum optical coupling between amplifier and detector, and once again for good lateral conduction of the amplifier bias current. Therefore, we may assume that the base thickness and the hole diffusion length will be, in principle, in the same order of magnitude. It is easy to see that, except for the exponential factor in the numerator, (2.34) and (2.35) are identical when $w_B=L_p$. We may thus assume that (2.35) is, at least from an intuitive point of view describing how the different device parameters affect the leakage current, a good approximation of the ratio between the transistor contribution to the total detector background current and the amplifier bias.

Let us now analyze the different factors that appear in equation (2.35) and how they affect the leakage current, specifically in terms of comparing a TAP detector with a traditional transistor.

In traditional transistors, the base is usually kept very thin. The intuitive reason for such a design is to allow most of the minority carriers injected from the emitter into the base to diffuse through it and reach the collector. As expressed in the short-base approximation, this leads to the exponential in the numerator being very close to

1. In TAP detectors, the exponential factor is thus smaller than one, and may be typically found in the 0.1-0.5 range.

The term in the denominator comparing the minority carrier currents from base to emitter and from emitter to base is

$$\frac{\mathbf{t}_p}{\mathbf{t}_n} \frac{L_n}{L_p} \frac{N_D}{N_A} \frac{n_{i,E}^2}{n_{i,B}^2} \quad (2.36).$$

In a short-base transistor, this term is multiplied by the ratio w_B/L_p , which is much smaller than 1. Adjusting the material and the doping concentrations in base and emitter allows further reduction of this term. In TAP detectors, the amplifier bias current travels laterally through both top and middle cladding, usually resulting in these layers designed to present high doping concentrations, which may be furthermore assumed to be comparable. The material used will also be similar in both claddings (e.g., 20% AlGaAs in GaAs-based TAP detectors and InP in InP-based devices), allowing us to assume that $n_{i,E}$ and $n_{i,B}$ will be very close to one another, and similarly so will \mathbf{t}_p and \mathbf{t}_n . Finally, the electron and hole diffusion lengths are found, under these assumptions, to be in a ratio in the range between 2 to 1 and 5 to 1. Therefore, even if careful bandgap engineering leads to the value expressed in (2.36) being very small compared to 1 in traditional n-p-n transistors, this value will be in the 1-10 range for p-n-p TAP detectors, and in the 0.1-1 range for n-p-n TAP detectors.

In traditional transistors, quantum wells do not exist between emitter and base, leading to the $1-h_i$ term in the numerator to be identically 1. In TAP detectors, for optimum performance, this injection efficiency needs to be high. This results, as a bonus, on a lower leakage current. Simulations presented later in this chapter will show that the injection efficiency for TAP detectors fabricated in GaAs may be estimated to be, in theory, about 50%. We can then approximate $1-h_i$ as 0.5.

The final term in equation (2.35) results from comparing the SCH recombination current and the minority hole diffusion current in the base, and is written as

$$\frac{\mathbf{t}_p}{\mathbf{t}_{SCH}} \frac{w'_{SCH}}{L_p} \frac{N_D p_{SCH}}{n_{i,B}^2 e^{\frac{qV_{EB}}{KT}}} = \frac{\mathbf{t}_p}{\mathbf{t}_{SCH}} \frac{w'_{SCH}}{L_p} \frac{p_{SCH}}{p(0)} \quad (2.37),$$

where $p(0)$ is the minority hole injected into the base at its interface with the space-charge region. This number will be always lower than the hole concentration in the SCH, and their ratio will be larger as the confinement improves. In fact, good confinement may even result in p_{SCH} being orders of magnitude larger than $p(0)$. Furthermore, w'_{SCH}/L_p may be assumed in the order of 1, since both lengths may be assumed to be in the order of $0.5\mu\text{m}$. Finally, the hole lifetime in the SCH may be assumed smaller than in the base. In fact, for high injection and good confinement, spontaneous emission from recombination of electrons and holes in the SCH may result in $\mathbf{t}_{SCH} \ll \mathbf{t}_p$, i.e., a very small ratio between the leakage current and the injected current. Therefore, good confinement of carriers in the SCH, desirable for optimum TAP detector performance, results also in a much larger recombination current in the

SCH than minority carrier diffusion current in the middle cladding, significantly reducing the leakage current. The term expressed in (2.37) may therefore be made more than an order of magnitude larger than 1 through appropriate confinement. In traditional transistors, the SCH itself does not exist. However, a current contribution is in fact generated by recombination in the space-charge region between emitter and base. But the thickness of this region is in general much smaller than $1\mu\text{m}$. Furthermore, a lack of confinement results in the carrier concentration in this space-charge region and the minority carrier concentration injected into the base being approximately equal. More importantly, this term is multiplied by the ratio w_B/L_p in a short-base approximation.

As a summary of the previous discussion, it has been shown that in traditional transistors with a short base, especially those with an n-p-n configuration, the ratio between collector and emitter currents may be made smaller than, but approximately equal to 1. However, in TAP detectors, this ratio may be made very small, especially through an improvement in the injection efficiency and in the confinement of carriers in the amplification region SCH. When the middle cladding doping is high, the base thickness is in the order of the hole diffusion length, resulting in further degradation of the TAP detector performance as a transistor, i.e., a reduction in the detector background current. In general, p-n-p TAP detectors will also present lower leakage currents than n-p-n devices. The conclusions of the previous discussion will be supported by the experimental evidence in later chapters of this dissertation.

As a summary for this entire section, we can conclude that, for TAP detectors with alternating gain and absorption or with lateral coupling, good electrical isolation between gain and absorption contacts is necessary. Otherwise, the ratio between efficiency and dark current will severely reduce the range of input optical powers for which these devices may be useful. However, etching through the active region may result in optical reflections between sections in TAP detectors with alternating gain and absorption, and in important scattering loss in both cases. Furthermore, ion implantation, which may be used to turn conducting or intrinsic semiconductor into semi-insulating material, will create heavy optical loss due to increased absorption. Therefore, elaborate isolation schemes will be necessary, possibly including regrowth, selective quantum well intermixing, or both [1]. In the case of TAP detectors with vertical coupling, leakage of carriers through the middle cladding needs to be inhibited. This may be achieved through a combination of good electrical confinement in the amplification diode, together with the use of p-doped top and bottom claddings, and n-doped middle cladding.

ASE current

In this section, the background current generated by detection of amplified spontaneous emission generated in the gain region will be studied. This contribution to the total background current will be called “ASE current”. It will be first shown how that current may be calculated in the case of a generic amplifier-photodetector. This calculation procedure will be then applied to the different TAP detector configurations studied in this dissertation.

As discussed in appendix A, the accurate description of ASE generation inside an SOA requires the use of the following equation:

$$\frac{dp_{opt}(z, \mathbf{n})}{dz} = [\Gamma_g g(\mathbf{n}) - l] p_{opt}(z, \mathbf{n}) + h\mathbf{n}\Gamma_g r_{st,em}(\mathbf{n}) \quad (2.38),$$

where $p_{opt}(\mathbf{n})$ is the optical power spectral density at frequency \mathbf{n} , and $r_{st,em}$ is the stimulated emission rate normalized to the optical intensity, defined by

$$r_{st,em}(\mathbf{n}) = \frac{R_{st,em}(h\mathbf{n})}{N_p v_g} \quad (2.39),$$

where $R_{st,em}(h\mathbf{n})$ is the stimulated emission rate per unit volume and time at energy $h\mathbf{n}$, N_p is the photon concentration per unit volume and v_g the group velocity. Defining in a similar way the stimulated absorption rate normalized to the optical intensity, $r_{st,ab}$, the material gain is given by their difference:

$$g(\mathbf{n}) = r_{st,em}(\mathbf{n}) - r_{st,ab}(\mathbf{n}) \quad (2.40).$$

The gain and the stimulated emission rate normalized to optical intensity may or may not be position dependent.

In TAP detectors, not only the ASE that propagates together with the signal needs to be considered, but also the backward-traveling ASE, since it also contributes to the background current. At first approximation, we can consider that the ASE current in a TAP detector will be the sum of two currents. These are the background currents of two TAP detectors where light propagates only forward, one with input at $z=0$ and output at $z=L$, and another with input at $z=L$ and output at $z=0$. The problem is thus

simplified to finding the current generated by the ASE propagating in one direction in a TAP detector, calculating it for the two “virtual” devices described above, and then adding both contributions.

In a TAP detector, and for the purposes of light amplification, absorption of light in the detector region may be considered as optical loss. Therefore, equation (2.38) may be rewritten as

$$\begin{aligned}\frac{dp_{opt}(z,\mathbf{n})}{dz} &= [\Gamma_g g(\mathbf{n}) - \Gamma_a \mathbf{a}(\mathbf{n}) - l] p_{opt}(z,\mathbf{n}) + \hbar \mathbf{n} \Gamma_g r_{st,em}(\mathbf{n}) \\ &= \Delta g(\mathbf{n}) p_{opt}(z,\mathbf{n}) + \hbar \mathbf{n} \Gamma_g r_{st,em}(\mathbf{n})\end{aligned}\quad (2.41),$$

where l is now the pure optical loss due to events such as light scattering or free carrier absorption. The total ASE power $P_{ASE}(z)$ may be calculated at any position by solving with the initial condition $p_{opt}(0,\mathbf{n})=0$, and then integrating $p_{opt}(z,\mathbf{n})$ over the amplifier bandwidth:

$$P_{ASE}(z) = \int p_{opt}(z,\mathbf{n}) d\mathbf{n} \quad (2.42).$$

The ASE current generation equation is a modification of (2.3):

$$\frac{dI_{ASE}(z)}{dz} = q \int \Gamma_a \mathbf{a}(\mathbf{n}) \frac{p_{opt}(z,\mathbf{n})}{\hbar \mathbf{n}} d\mathbf{n} \quad (2.43).$$

The integral is performed over the bandwidth of the amplifier, in order to take into account the contribution from ASE generated at all wavelengths. The confinement factor and the material absorption may or may not be position dependent. Note that (2.42) and (2.43) describe the contribution of the forward

traveling ASE only. The contribution from the backward propagating ASE will be calculated in a similar fashion.

The formalism presented up to now will next be used to find the ASE current in the TAP detector configurations studied in this chapter.

ASE current in TAP detectors with alternating amplification and absorption

The ASE photocurrent in TAP detectors with alternating amplification and absorption will be calculated using the assumptions under which the efficiency was derived. Thus, the material gain and absorption will be assumed to be constant in the amplification and detection regions, respectively, and all sections performing the same function will be assumed to be identical to one another. Under these assumptions, the ASE power density may be calculated easily by turning the differential equation (2.41) into a recursive relation. This is achieved by integrating the differential equation over one device period:

$$P_{ASE,n+1}(\mathbf{n}) = \Delta G(\mathbf{n}) P_{ASE,n}(\mathbf{n}) + h_{iso} P_{ASE}^{(1)}(\mathbf{n}) \quad (2.44),$$

where $P_{ASE,n}(\mathbf{n})$ is the ASE spectral power density arriving to the n -th detector and $P_{ASE}^{(1)}(\mathbf{n})$ is the ASE spectral density generated by each individual amplification section. The latter may be calculated by integrating (2.41) and (2.42) over one gain section:

$$P_{ASE}^{(1)}(\mathbf{n}) = h\mathbf{m} \frac{\Gamma_g r_{st,em}(\mathbf{n})}{\Gamma_g g(\mathbf{n}) - l} \left[e^{(\Gamma_g g(\mathbf{n}) - l)L_g} - 1 \right] \quad (2.45).$$

The initial condition for (2.44) depends on whether the first section provides amplification or detection. In the latter case, we obviously encounter $p_{ASE,1}(\mathbf{n})=0$. Otherwise, the value of $p_{ASE,1}(\mathbf{n})$ may be calculated by using an equation totally analogous to (2.45), but using the parameters describing the first amplification section, which may be different than the rest. The frequency-dependent net gain per period $\Delta G(\mathbf{n})$ in (2.44) is just the straightforward generalization of the net gain per period defined in (2.8), for any frequency in the amplifier bandwidth, taking into account the frequency dependence of material gain and absorption. Thus we find, for $n>1$:

$$p_{ASE,n}(\mathbf{n}) = \Delta G(\mathbf{n})^{n-1} p_{ASE,1}(\mathbf{n}) + \mathbf{h}_{iso} p_{ASE}^{(1)}(\mathbf{n}) \frac{\Delta G(\mathbf{n})^{n-1} - 1}{\Delta G(\mathbf{n}) - 1} \quad (2.46).$$

The total ASE power is calculated by integrating the previous result over the amplifier bandwidth.

It is interesting at this point to study the evolution of the ASE along the device, comparing it to the evolution of the signal. For simplicity, we will use for this comparison a flat-band approximation. In such an approximation, the amplifier gain and spontaneous emission are supposed to have a constant value over its optical bandwidth $\Delta \mathbf{n}_o$, leading to

$$P_{ASE,n} = \Delta G^{n-1} P_{ASE,1} \Delta \mathbf{n}_o + \mathbf{h}_{iso} P_{ASE}^{(1)} \frac{\Delta G^{n-1} - 1}{\Delta G - 1} \Delta \mathbf{n}_o \quad (2.47),$$

where $P_{ASE,n}$ is the ASE power arriving to the n -th detection section.

The first term in the RHS of (2.47) represents the contribution to the ASE made by the first amplification region. The second term represents the effect of the ASE generated by all other gain sections. Figure 2.19 shows the evolution of the ASE generated by all sections except the first one, i.e., the evolution of ASE in a device where the first active section provides absorption. The ASE power may be normalized to the ASE power produced by each single amplification section, independently of the ASE arriving to it from other gain sections. This way, the effect of the net gain per period and the number of sections may be better appreciated. The normalized ASE power plotted in Figure 2.19 is thus defined as:

$$\frac{P_{ASE,n}}{\mathbf{h}_{iso} P_{ASE}^{(1)} \Delta \mathbf{n}_o} = \frac{\Delta G^{n-1} - 1}{\Delta G - 1} \quad (2.48).$$

When the net gain is very small ($\Delta G \ll 1$), the normalized ASE power arriving to each detection section may be approximated by $1 + \Delta G$. Intuitively, if the absorption and loss overwhelm the gain, each detector is going to receive the contribution from the previous two amplification sections; the effect of any other gain section is severely diminished by the net loss present in the device. When ΔG is close to 1, the normalized ASE arriving to each detector section may be approximated as:

$$\left. \frac{P_{ASE,n}}{\mathbf{h}_{iso} P_{ASE}^{(1)} \Delta \mathbf{n}_o} \right|_{\Delta G=1} \simeq n - 1 + \binom{n-1}{2} (\Delta G - 1) \quad (2.49).$$

To the first order, the ASE arriving to each detection section is linear with the position of that section, increasing along the device. Finally, if $\Delta G \gg 1$, the change is exponential, i.e, the ASE, just like the signal, grows very rapidly along the device.

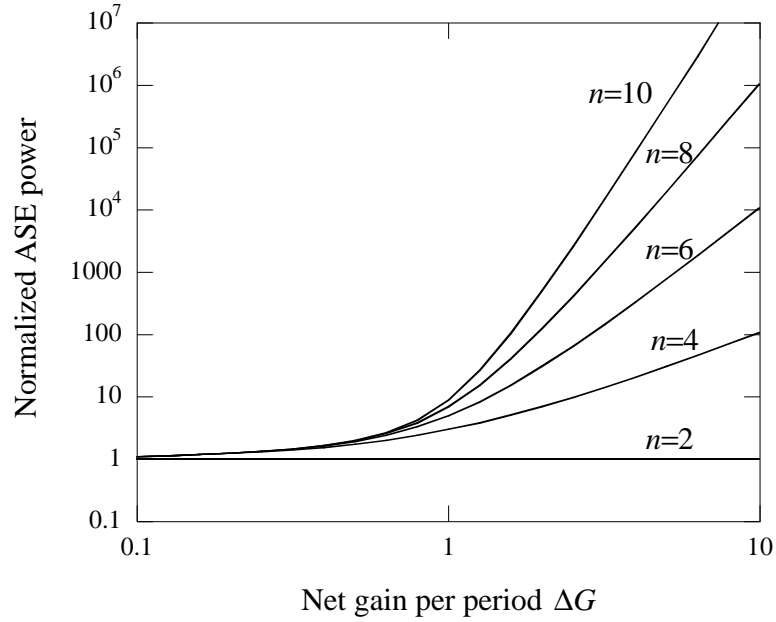


Figure 2.19: Simulated ASE power arriving to the n -th detection section, normalized to the ASE power generated by each individual amplification section, as a function of the net gain per period ΔG . The first section of the device is assumed to provide absorption, i.e., no contribution to the ASE from an initial gain section is taken into account.

It is very interesting therefore to define the ratio between ASE power and amplified signal power arriving to each detection section. Calling $P_{opt,n}$ the contribution from the signal arriving to each detector section, defined by equation (2.9), and taking into account the effect of the first amplification section through its gain G_1 , we can easily find:

$$\frac{P_{ASE,n}}{P_{opt,n}} = \frac{\Delta n_o}{h_c G_1 P_{in}} \left[p_{ASE,1} + h_{iso} p_{ASE}^{(1)} k_{opt}(\Delta G, n) \right] \quad (2.50),$$

where the parameter $k_{opt}(\Delta G, n)$ is defined as

$$k_{opt}(\Delta G, n) = \frac{\Delta G^{n-1} - 1}{\Delta G^{n-1}(\Delta G - 1)} \quad (2.51).$$

Note that nowhere else in (2.50) do ΔG or n appear. It contains thus all the information about how the number of sections and the net gain per period affect the ratio between ASE and signal power arriving to each detection section. This parameter will be referred to as the ASE optical power generation coefficient. Intuitively, it is the ratio between the ASE power and the signal power arriving to each detection section, normalized, the former to the ASE power generated in each individual amplification section, and the latter to the input power coupled into the device and amplified by the first gain section. Its evolution is shown in figure 2.20.

It can be observed that, when the net gain per period becomes less than 1, the ASE very quickly becomes much larger than the signal, especially for sections far away from the input. This is due to the fact that the signal decays very rapidly, but the ASE arriving to each detection section is kept nearly constant by the immediately preceding amplification section. When ΔG is much larger than one, both the signal and the ASE increase exponentially, leading to a much lower ratio between them, which is also nearly constant for all sections. When the signal barely changes from period to period, the ASE increases linearly along the device, thus leading to a ratio that increases also linearly with the number of sections. Obviously, the best signal to noise ratio will be obtained for very high values of the net gain per period. This,

however, defeats the purpose of TAP detectors, leading to a behavior similar to that of a traditional photodetector with preamplification. This becomes obvious when we consider that, in this particular case, most of the photocurrent is generated only in the last absorption sections of the device, where the optical power is largest.

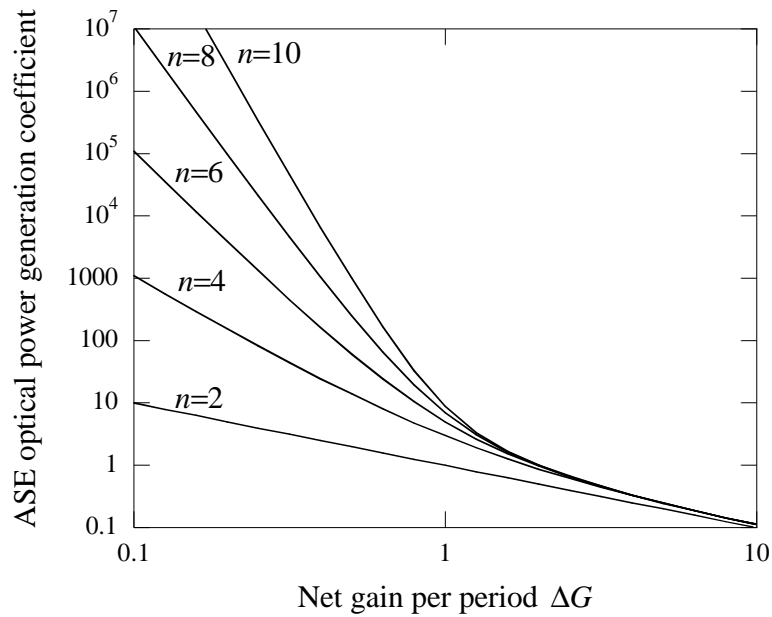


Figure 2.20: Simulated ASE optical power generation coefficient as a function of the net gain per period, for different detection sections. Intuitively, this parameter represents the ratio between the ASE power and the signal power arriving to each detection section, the former normalized to the ASE power generated in each gain section, the latter to the input optical power coupled into the device. The first section of the device is assumed to provide absorption, i.e., no contribution to the ASE from an initial amplification section is taken into account.

Note finally that the value of the net gain per period and the ASE generated in each amplification section are not fully independent on one another, since both depend on the stimulated emission rate in the gain section. However, small relative changes in the material gain in the amplification region, and thus small changes in the ASE produced by one section, may result in large relative changes of the net gain per

period. In that sense, the ASE optical power generation coefficient, if not exact, is still a very good approximation of the evolution of the ratio between ASE power and signal power along a TAP detector.

We can now calculate the ASE current produced in a TAP detector with alternating gain and absorption. At this point, we will restore the generality by returning once more to the frequency-dependent ASE power spectral density, as expressed in equation (2.46). The frequency-dependent efficiency of each section, $\mathbf{h}^{(1)}(\mathbf{n})$, may also be defined through (2.10), using frequency-dependent material gain and absorption. The total ASE current for a device featuring N periods is then calculated by summing the contribution from each detection section:

$$\begin{aligned}
I_{ASE, fwd} &= \int \sum_{n=1}^N \left[\frac{q}{h\mathbf{m}} \mathbf{h}^{(1)}(\mathbf{n}) p_{ASE, n}(\mathbf{n}) \right] d\mathbf{n} \\
&= q \int \mathbf{h}^{(1)}(\mathbf{n}) \frac{p_{ASE, 1}(\mathbf{n})}{h\mathbf{m}} \frac{\Delta G(\mathbf{n})^N - 1}{\Delta G(\mathbf{n}) - 1} d\mathbf{n} \\
&\quad + q \int \mathbf{h}_{iso} \mathbf{h}^{(1)}(\mathbf{n}) \frac{p_{ASE}^{(1)}(\mathbf{n})}{h\mathbf{m}} \frac{\Delta G(\mathbf{n})^N - 1 - N[\Delta G(\mathbf{n}) - 1]}{[\Delta G(\mathbf{n}) - 1]^2} d\mathbf{n}
\end{aligned} \tag{2.52}$$

The sub-index *fwd* is added to the ASE current to signify that this is the contribution made only by the forward-propagating ASE. Assuming that the last section of the device provides absorption, the description of the backward-traveling ASE is identical to the forward-propagating ASE, removing the contribution from the first amplification section. The total ASE current is given by

$$\begin{aligned}
I_{ASE} = & q \int \mathbf{h}^{(1)}(\mathbf{n}) \frac{p_{ASE,1}(\mathbf{n})}{h\mathbf{m}} \frac{\Delta G(\mathbf{n})^N - 1}{\Delta G(\mathbf{n}) - 1} d\mathbf{n} \\
& + 2q \int \mathbf{h}_{iso} \mathbf{h}^{(1)}(\mathbf{n}) \frac{p_{ASE}^{(1)}(\mathbf{n})}{h\mathbf{m}} \frac{\Delta G(\mathbf{n})^N - 1 - N[\Delta G(\mathbf{n}) - 1]}{[\Delta G(\mathbf{n}) - 1]^2} d\mathbf{n}
\end{aligned} \tag{2.53}$$

By comparison of the first term in the last member of (2.53), and (2.12), we can see that the effect of a first amplification section is equivalent to that of having an extra input of ASE with spectral density $p_{ASE,1}(\mathbf{n})$, coupled with 100% efficiency. This result is intuitively obvious given the device configuration. When the net gain per period is 1, we find

$$\begin{aligned}
I_{ASE}|_{\Delta G(\mathbf{n})=1} = & Nq \int \mathbf{h}^{(1)}(\mathbf{n}) \frac{p_{ASE,1}(\mathbf{n})}{h\mathbf{m}} d\mathbf{n} \\
& + N(N-1)q \mathbf{h}_{iso} \int \mathbf{h}^{(1)}(\mathbf{n}) \frac{p_{ASE}^{(1)}(\mathbf{n})}{h\mathbf{m}} d\mathbf{n}
\end{aligned} \tag{2.54}$$

This is an intuitively very clear result: when the net gain per period is exactly 1, the ASE current is given by the absorption in each one of the detectors of the ASE produced in the first amplification region, and the ASE produced in each one of the other $N-1$ amplification sections. This is schematically represented in figure 2.21.

The interesting conclusion to be drawn is that, when gain and absorption are close to mutual cancellation, the ASE current increases more rapidly with the number of sections (with a quadratic dependence) than the efficiency (linear with the number of sections). This sets a limit to the number of sections that may be effectively used before the background current limits the device performance. It also constitutes the first penalty that we encounter to the use of distributed amplification and absorption.

A trade-off needs therefore to be established between the tolerable amount of background current and the desired efficiency. Equation (2.54) is also a first intuitive symptom that the noise figure will vary roughly proportionally to the efficiency, establishing also a trade-off between these two device parameters. This trade-off will be discussed later on.

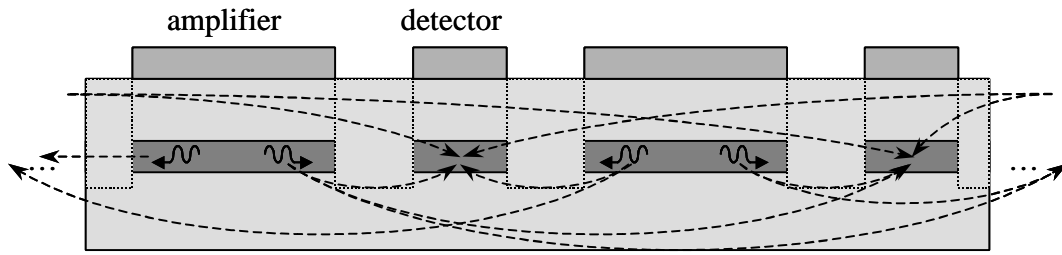


Figure 2.21: Each amplification section generates forward- and backward-traveling ASE, represented by wiggly arrows. When the net gain per period is equal to one, the amount of ASE that arrives to each detector is $N-1$ times the ASE generated by each amplification region in each direction. The detector will receive contributions from forward-traveling ASE generated in the gain sections before itself, and from backward-traveling ASE generated in gain sections after itself, as represented by the dashed arrows.

A parameter of interest which can be defined to evaluate, not only the trade-off between the ASE current and the efficiency, but the effect that the gain and the number of periods has in it, is the ratio between ASE photocurrent and the photocurrent due to the input signal. Given the complexity of equation (2.53), we will now perform again a flat-band approximation before going any further. This simplifies the equation describing the ASE current:

$$I_{ASE} \simeq \frac{q\mathbf{h}^{(1)}\Delta\mathbf{n}_o}{h\mathbf{m}_0} \left[p_{ASE,1} \frac{\Delta G^N - 1}{\Delta G - 1} + 2\mathbf{h}_{iso} p_{ASE}^{(1)} \frac{\Delta G^N - 1 - N(\Delta G - 1)}{(\Delta G - 1)^2} \right] \quad (2.55).$$

With this approximation, the ratio between ASE photocurrent and signal photocurrent may be written as

$$\frac{I_{ASE}}{I_{ph}} \simeq \frac{\Delta n_o}{h_c G_1 P_{in}} \left[P_{ASE,1} + h_{iso} P_{ASE} {}^{(1)}\mathbf{k}_{elec}(\Delta G, N) \right] \quad (2.56),$$

where we have defined the ASE current generation coefficient, $\mathbf{k}_{elec}(\Delta G, N)$, as

$$\mathbf{k}_{elec}(\Delta G, N) = 2 \frac{\Delta G^N - 1 - N(\Delta G - 1)}{(\Delta G^N - 1)(\Delta G - 1)} \quad (2.57).$$

Note that the gain per period and the total number of sections do not appear in (2.56) except through the parameter \mathbf{k}_{elec} . The first term in the square brackets in (2.56) represents the effect of the ASE generated in the first amplification section. The effect of that first amplification section is equivalent to that of a preamplifier before a traditional photodetector, adding ASE power that will be detected later with the same efficiency as the input signal itself. The second term describes the effect of the distributed amplification and photodetection in the background current. The ASE current generation coefficient represents therefore the ratio between the ASE current generated in the device and the signal photocurrent, the former normalized to the ASE optical power generated in each amplification region, the latter to the input optical power coupled into the device. \mathbf{k}_{elec} is thus a good measure of how the distributed combination of gain and absorption contributes to generate background current through detection or ASE, scaling this effect to the increase in the total device efficiency obtained by this combination.

It is interesting to note that the ASE power spectral density produced in each one of the intermediate amplification sections, $p_{ASE}^{(1)}$, is divided not by the gain of each one of those sections, but by the gain of the initial section, G_1 . This means, of course, that the more gain the first amplification section produces, the less important the effect of the ASE produced in any other amplification section becomes. We can then think about making the initial gain G_1 large in order to minimize the effect of the ASE photocurrent. This, however, defeats once more the purpose of TAP detectors, which is providing a large efficiency without a large increase in the peak optical power inside the device.

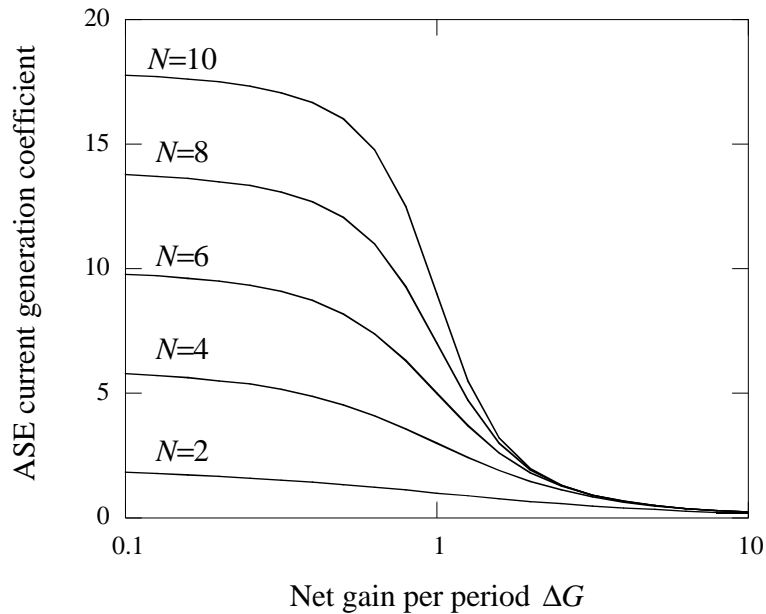


Figure 2.22: Simulated ASE current generation coefficient as a function of the net gain per period, for different numbers of periods. Intuitively, this parameter represents the ratio between the total ASE current and the signal photocurrent, the former normalized to the ASE power generated in one absorption section, the latter to the input power coupled into the device. The first section of the device is assumed to provide absorption, i.e., no contribution to the ASE current from an initial amplification section is taken into account.

Let us now study the evolution of the parameter $k_{elec}(\Delta G, N)$. Its value, as a function of the net gain per period, and for different values of the total number of periods, is shown in Figure 2.22.

For very small values of ΔG , the TAP detector works as a regular detector, almost all the signal photocurrent being generated in the first absorption section. ASE, however, gets generated in all amplification sections, being also almost all of it absorbed in the immediately neighboring detection sections. Evaluating (2.57) for $\Delta G=0$ we find a value of $2N-2$ for the ASE current generation coefficient, which is a good approximation when $\Delta G < 0.2$, as shown in the graph. For very large values of the net gain per period, the value of k_{elec} tends to $2/\Delta G$, independently of the number of sections. Under this condition, the TAP detector works as a traditional photodetector with preamplification, most of the current being generated in the last absorption section, be it due either to the input signal or to ASE. The factor of 2 stems from the fact that the backward-propagating ASE also adds to the background current. Finally, when gain, absorption and loss are close to cancellation, i.e., around $\Delta G=1$, we can approximate the value of k_{elec} as

$$k_{elec}(\Delta G, N) \approx (N-1) \left[1 - \frac{N+1}{6} (\Delta G - 1) \right] \quad (2.58).$$

At $\Delta G=1$, i.e., for perfect cancellation between gain, absorption and loss, the value of k_{elec} is exactly equal to $N-1$. This intuitively corresponds to the fact that

each detector receives ASE contributions from each one of the $N-1$ intermediate amplification sections.

In summary, it has been shown in this paragraph that the ASE power and the ASE current grow faster than the amplified signal power and the signal photocurrent, except in the case where the net gain per section is very large. However, this case does not present any clear advantage over traditional photodetectors preceded by an optical amplifier. Cancellation between gain and absorption results in a trade-off arising between the device efficiency and the ratio between background current and signal photocurrent. In fact, this ratio is roughly proportional to the number of periods, and therefore proportional to the efficiency.

ASE current in TAP detectors with transverse coupling

In this paragraph, the ASE current generated in a TAP detector with transverse coupling will be discussed. In order to be able to easily take into account the effect of an initial section providing gain only, as shown in figure 2.11, we will consider that position $z=0$ is chosen where the simultaneous combination of gain and absorption starts, and $z=L$ at the end of the device, as shown in figure 2.23. Other than that, the same assumptions will be made as for the calculation of the device efficiency, i.e., the material gain and absorption, the confinement factors and the loss will be assumed constant along the device.

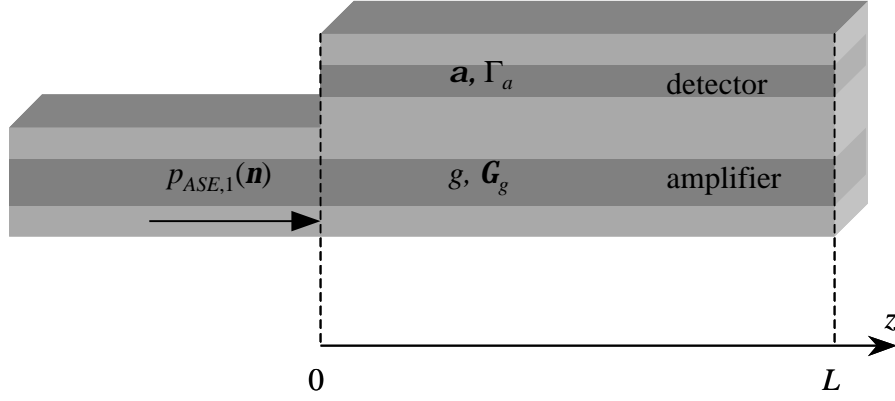


Figure 2.23: Parameters used for the calculation of the ASE current in TAP detectors with transverse coupling. The beginning of the simultaneous action of gain and absorption is chosen at $z=0$, whereas the device ends at $z=L$. The initial amplification section produces ASE with a power spectral density $p_{ASE,1}(n)$, as indicated. Also indicated are the material gain and absorption, and the confinement factors in the amplification and detection regions, which are assumed to be position-independent, same as the optical loss.

Let us therefore assume that the initial amplification section produces ASE with a spectral density $p_{ASE,1}(\mathbf{n})$. Then, equations (2.41) and (2.43) may be easily integrated in closed form, with the initial condition $p_{opt}(z, \mathbf{n})=p_{ASE,1}(\mathbf{n})$:

$$p_{opt}(z, \mathbf{n}) = e^{\Delta g(\mathbf{n})z} p_{ASE,1}(\mathbf{n}) + \hbar \mathbf{n} \Gamma_g r_{st,em}(\mathbf{n}) \frac{e^{\Delta g(\mathbf{n})z} - 1}{\Delta g(\mathbf{n})} \quad (2.59);$$

$$I_{ASE,fwd}(z) = q \int \Gamma_a \mathbf{a}(\mathbf{n}) \frac{p_{ASE,1}(\mathbf{n}) e^{\Delta g(\mathbf{n})z} - 1}{\hbar \Delta g(\mathbf{n})} d\mathbf{n} \quad (2.60).$$

$$+ q \int \Gamma_a \mathbf{a}(\mathbf{n}) \Gamma_g r_{st,em}(\mathbf{n}) \frac{e^{\Delta g(\mathbf{n})z} - 1 - \Delta g(\mathbf{n})z}{\Delta g^2(\mathbf{n})} d\mathbf{n}$$

The subscript *fwd* in the ASE current denotes that this is the contribution from forward-traveling ASE only. Backward-traveling ASE will add the exact same contribution, except for the term describing the absorption of ASE generated in the

first amplification section, i.e., the first term in the RHS of (2.60), resulting in a total ASE current that may be expressed as

$$\begin{aligned}
I_{ASE} = & q \int \Gamma_a \mathbf{a}(\mathbf{n}) \frac{P_{ASE,1}(\mathbf{n})}{h\nu} \frac{e^{\Delta g(\mathbf{n})z} - 1}{\Delta g(\mathbf{n})} d\mathbf{n} \\
& + 2q \int \Gamma_a \mathbf{a}(\mathbf{n}) \Gamma_g r_{st,em}(\mathbf{n}) \frac{e^{\Delta g(\mathbf{n})z} - 1 - \Delta g(\mathbf{n})z}{\Delta g^2(\mathbf{n})} d\mathbf{n}
\end{aligned} \tag{2.61}.$$

It is interesting to define the ratio between the ASE optical power and the signal that arrive at a certain position. Calling again G_1 the gain in the first amplification region, and $P_{opt}(z)$ the signal optical power that arrives to position z , and is given by equation (2.17), in a flat-band approximation we can find the following relation:

$$\frac{P_{ASE}(z)}{P_{opt}(z)} = \frac{P_{opt}(z) \Delta \mathbf{n}_o}{P_{in} \mathbf{h}_c G_1 e^{\Delta g z}} = \frac{\Delta \mathbf{n}_o}{P_{in} \mathbf{h}_c G_1} \left[P_{ASE,1} + h\nu \Gamma_g r_{st,em} \mathbf{k}_{opt}(\Delta g, z) \right] \tag{2.62},$$

where we have defined the ASE optical power generation coefficient as:

$$\mathbf{k}_{opt}(\Delta g, z) = \frac{1 - e^{-\Delta g z}}{\Delta g} \tag{2.63}.$$

The intuitive meaning of this parameter is the following: $\mathbf{k}_{opt}(\Delta g, z)$ is the ratio between the ASE optical power and the signal optical power at a given position z in the device, the former being normalized to the spontaneous emission power coupled into guided modes in each direction and per unit length, and the latter being normalized to the input optical power coupled into the device and amplified by the first gain section. In other words, the evolution of $\mathbf{k}_{opt}(\Delta g, z)$ with increasing z expresses how much faster does the ASE grow with respect to the input signal. This

parameter is plotted, as a function of the net gain per unit length, and for different positions, in figure 2.24.

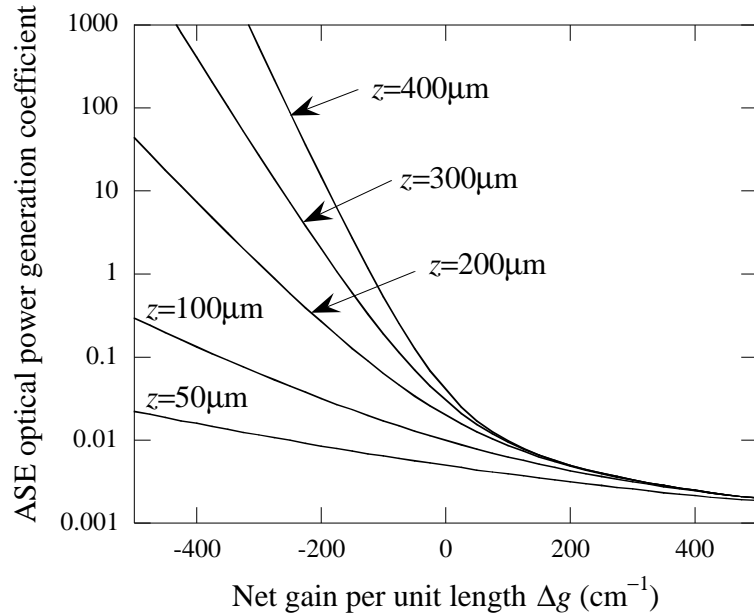


Figure 2.24: Simulated ASE optical power generation coefficient as a function of the net gain per unit length, for different positions along the device. Intuitively, this parameter represents the ratio between the ASE power and the signal power arriving to each position, the former normalized to the spontaneous emission power coupled into the guided mode per unit length, and the latter to the input optical power coupled into the device. No contribution to the ASE from an initial amplification section is taken into account, i.e., it is assumed not to exist.

Note that there is a very large increase (nearly exponential) of this coefficient when the net gain per unit length is large in absolute value and negative. This is caused by the input signal being quickly attenuated, whereas spontaneous emission is generated all along the device. When the net gain per unit length is large and positive, the ASE optical power generation coefficient may be approximated by $1/\Delta g$. Note that this approximation does not lead to an accurate interpretation, since for the net gain per unit length to be large, the stimulated emission must dominate over all

other events. Thus, eventually $\Gamma_g r_{st,em}$ and Δg become comparable, and the ratio between ASE and signal power may be approximated by:

$$\left. \frac{P_{ASE}(z)}{P_{opt}(z)} \right|_{\Delta g z \gg 1} \simeq \frac{\Delta n_o}{P_{in} \mathbf{h}_c G_1} [P_{ASE,1} + h\nu] \quad (2.64).$$

This result may be interpreted as the signal and ASE growing at approximately the same rate. Obviously, the ASE power to signal power is thus minimized, but at the expense of incurring in saturation for much lower input optical power. Finally, when the net gain per unit length is very small, i.e., $|\Delta g L| \ll 1$, we can perform the following approximation:

$$\mathbf{k}_{opt}(\Delta g, z) \Big|_{|\Delta g L| \ll 1} \simeq z \left(1 - \frac{\Delta g z}{2} \right) \quad (2.65).$$

In other words, the ratio between ASE power and signal power increases linearly as the optical signal propagates along the device.

Let us now finally study the ratio between the photocurrent generated by the signal and the ASE current, given by

$$\frac{I_{ASE}(L)}{I_{ph}(L)} = \frac{\Delta n_o}{\mathbf{h}_c G_1 P_{in}} [P_{ASE,1} + h\nu \Gamma_g r_{st,em} \mathbf{k}_{elec}(\Delta g, L)] \quad (2.66),$$

where we have defined the ASE current generation coefficient $\mathbf{k}_{elec}(\Delta g, L)$ as

$$\mathbf{k}_{elec}(\Delta g, L) = 2 \frac{e^{\Delta g L} - 1 - \Delta g L}{\Delta g (e^{\Delta g L} - 1)} \quad (2.67).$$

This parameter expresses thus the ratio between ASE current and signal photocurrent, the former being normalized to the spontaneous emission generated and coupled into guided modes per unit length, and the latter to the input optical power coupled and amplified in the first gain section. The ASE current generation coefficient is shown, as a function of net gain per unit length, and for different device lengths, in figure 2.25.

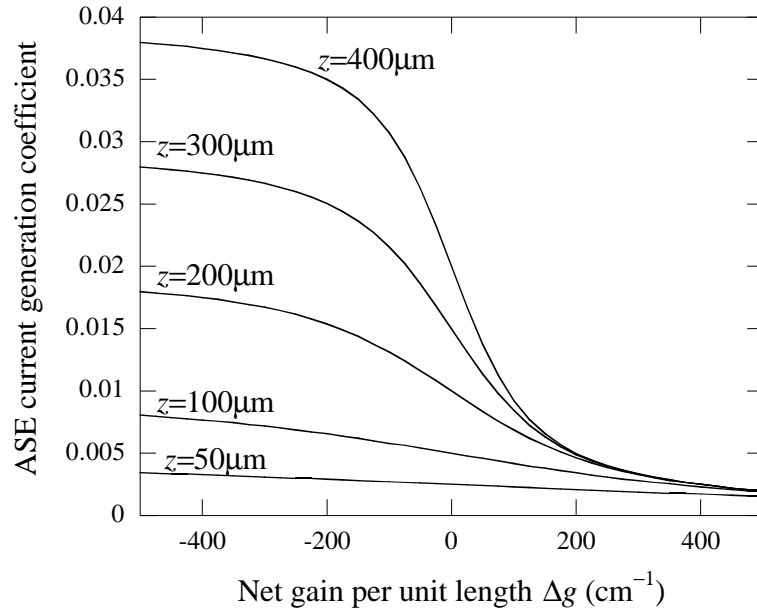


Figure 2.25: Simulated ASE current generation coefficient as a function of the net gain per unit length, for different device lengths. Intuitively, this parameter represents the ratio between the ASE current and the signal photocurrent generated in the entire device, the former normalized to the spontaneous emission power generated and coupled into the guide mode per unit length, and the latter to the input optical power coupled into the device. No contribution to the ASE from an initial amplification section is taken into account, i.e., it is assumed not to exist.

When the net gain per unit length is negative and large in absolute value, the limit of the previous expression is $2L$. This is intuitively explained by the fact that the signal is quickly absorbed, the amplification making its presence barely felt, i.e., the

internal efficiency of the device being close to one, while the spontaneous emission coupled into guided modes is quickly absorbed, and thus the ASE is constant along the device. Note that the term “ASE” is used here loosely, because the absorption dominating overwhelmingly, there is no real net amplification of the spontaneous emission. The factor of 2 appears because both forward- and backward-propagating ASE is generated.

When the net gain per unit length is large and positive, both ASE and signal increase at a very similar rate. At this point, we need to remember once more that this situation is only possible when $\Gamma_g r_{st,em}$ and Δg are comparable, leading to the following, more meaningful expression:

$$\left. \frac{I_{ASE}(L)}{I_{ph}(L)} \right|_{\Delta g L \gg 1} \simeq \frac{\Delta n_o}{h_c G_1 P_{in}} [p_{ASE,1} + 2h\nu] \quad (2.68).$$

In other words, most of the entire device works as an amplifier, the majority of the photocurrent being detected in its end. The result is thus similar to the ratio of ASE current to photocurrent for a photodetector preceded by an amplifier that provides a gain G_1 , while generating an ASE spectral power density $p_{ASE,1}$.

Note also that, although a large net gain per unit length leads to a small ratio between ASE current and signal photocurrent, this is only possible when the optical power grows very rapidly inside the device. This would, of course, defeat the purpose of TAP detectors by incurring into saturation for lower input optical power.

Finally, when gain and absorption are close to mutual cancellation, we may approximate

$$k_{elec}(\Delta g, L)|_{|\Delta g L| \ll 1} \approx z \left(1 - \frac{\Delta g L}{6} \right) \quad (2.69).$$

In other words, the ratio between ASE current and signal photocurrent is roughly proportional to the device length. This happens when the signal photocurrent is approximately proportional to the device length, whereas the ASE current follows a roughly quadratic dependence, the ASE optical power itself being approximately linear with the position along the device.

In summary, it has been shown in this paragraph that the ASE power and the ASE current, in a TAP detector with transverse coupling, grow faster than the amplified signal power and the signal photocurrent, except in the case where the net gain per unit length is very large. This case does not present though any clear advantage over traditional photodetectors preceded by an optical amplifier. When the net gain per unit length is very small in absolute value, the ratio between background current and signal photocurrent is roughly proportional to the device length, and thus to the device efficiency, resulting in a trade-off between these two performance parameters.

Once the ASE current generation has been discussed, the generation of background current due to detection in the absorption region of spontaneous emission generated in the gain region will be studied in the next paragraph.

Spontaneous emission current in TAP detectors with vertical coupling

Light is spontaneously emitted in all directions of space in the amplifier region. Part of it will be absorbed in the detection region, leading to an added component in the background current. This contribution may be expected to be very small in TAP detectors with alternating gain and absorption, given that spontaneous emission would need to travel very close in a very small angle around the direction of propagation in order to reach a detector from even the nearest neighbor amplifier. A large fraction of this spontaneous emission will actually be coupled into propagating modes, and its effect on the background current is taken into account through the ASE current. In TAP detectors with transverse coupling, however, this is not true anymore, since most of the ASE will be seeded by photons spontaneously emitted in a small angle around the longitudinal direction of propagation, but a non-negligible fraction of the spontaneous emission, emitted either around the vertical direction or the lateral direction, will reach the detection region. In this paragraph, the contribution from this spontaneous emission to the total background current will be estimated for the particular case of TAP detectors with vertical coupling. In the case of TAP detectors with lateral coupling, the calculation is performed in an analogous way, leading in general to a much smaller value, due to the thickness of the active region being in general much smaller than its width, and to the separation between gain and absorption regions being in general smaller in devices with vertical coupling.

Figure 2.26 shows only the gain and absorption regions of a TAP detector with vertical coupling, indicating their length L , their width (assumed identical) w , and the vertical separation between their midpoints d .

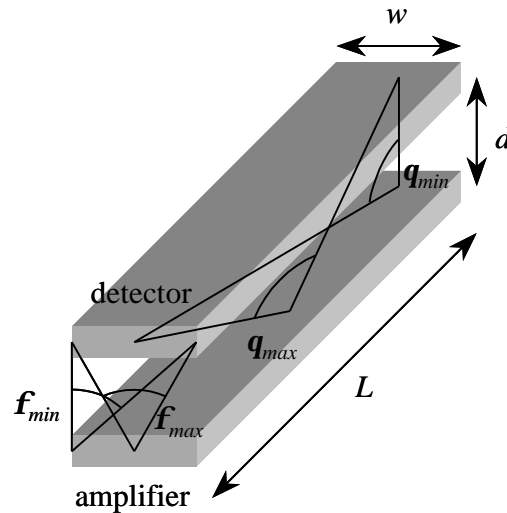


Figure 2.26: Gain and absorption regions in a TAP detector with vertical coupling. Indicated are their length L , their width w (assumed identical) and the separation between their midpoints d . q_{min} and q_{max} indicate respectively the minimum and maximum angles subtended, in a vertical plane parallel to the direction of propagation, by the detector region from any point in the gain region in the same plane. f_{min} and f_{max} indicate respectively the minimum and maximum angles subtended, in a vertical plane perpendicular to the direction of propagation, by the detector region from any point in the gain region in the same plane.

Let us define, as represented in the figure, q_{min} and q_{max} as the minimum and maximum angles subtended, in a longitudinal plane, by the detection region from any point in the absorption region. Since $L \gg d$, we may approximate them, respectively, by $p/2$ and p . Let us furthermore define f_{min} and f_{max} as the minimum and maximum angles subtended, in a longitudinal plane, by the detection region from any point in the absorption region. These two angles are defined by

$$\frac{w}{d} = \tan(\mathbf{f}_{min}) = 2 \tan\left(\frac{\mathbf{f}_{max}}{2}\right) \quad (2.70).$$

Since the device length L is much larger than the separation between active regions d , we may assume that the contribution from positions along the amplifier where the angle subtended by the detection region is close to \mathbf{q}_{min} is negligible, and thus the fraction of photons spontaneously emitted in the active region that reach the detection region may be estimated by the average of \mathbf{f}_{min} and \mathbf{f}_{max} , divided by the total angle around an axis parallel to the direction of propagation, i.e., by $(\mathbf{f}_{min} + \mathbf{f}_{max})/4\mathbf{p}$. Figure 2.27 expresses this value as a function of the ratio w/d .

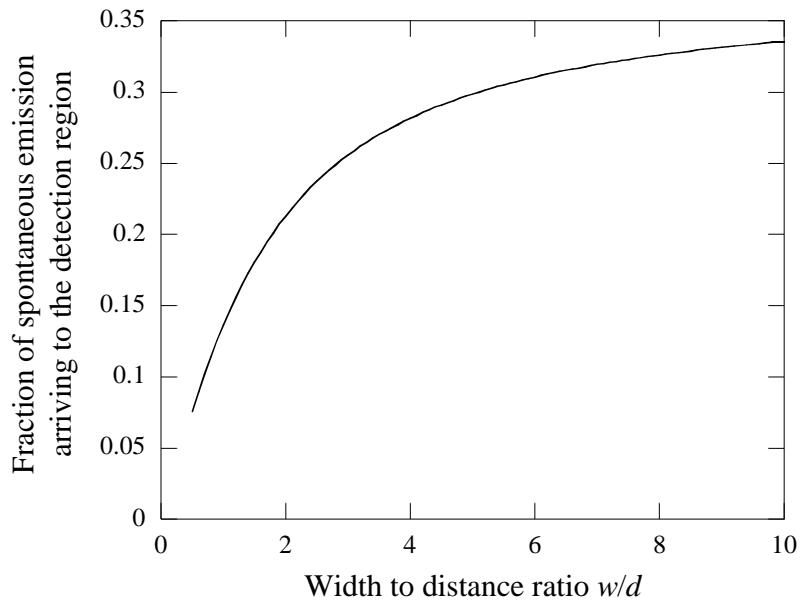


Figure 2.27: Simulated estimate of the fraction of spontaneous emission from the gain region that will arrive to the detection region in a TAP detector with vertical coupling, as a function of the ratio between their width w (assumed identical for both regions) and their separation d .

So, for example, for a typical device active width of $3\mu\text{m}$, and a separation between 0.5 and $1\mu\text{m}$ between active regions, about 25-30% of the spontaneously emitted photons in the gain region will actually arrive to the absorption region. Not all these photons will be absorbed, but a fraction $1-\exp(-\mathbf{a}L_{int})$, \mathbf{a} being the material absorption and L_{int} an effective interaction length. The lower bound of this interaction length may be assumed to be twice the thickness of the detection region, for photons spontaneously emitted in the vertical direction, which due to the reflection at the top contact of the detector have a double pass through the absorption region (other reflections are neglected). Of the total number of photons emitted vertically in the gain region, half (those emitted upward) will indeed reach the detector. The interaction length will be much larger than the absorption length $1/\mathbf{a}$ for photons emitted with a small angle with respect to the direction of propagation in the device. However, a smaller fraction of the photons emitted in this range of angles will reach the detection region. We can thus estimate the effective fraction of photons that are absorbed in the detection region as $1-\exp(-2\mathbf{a}t)/2$, t being in this case the thickness of the detection region. For a typical material absorption of 9000cm^{-1} and an active region thickness between 200 and 300nm , this leads to about $2/3$ of the photons that arrive to the detection region actually being absorbed in it. In other words, for an active region thickness in the range used for this calculation, the result expressed in figure 2.40, multiplied by $2/3$, expresses an estimate of the total fraction of spontaneously emitted photons that are absorbed and contribute to the background current in the detector. For the rest of this section, we will assume that

this fraction is known, and we will denote it by r_{sp} . For realistic devices, and per the previous discussion, this value may be estimated as 15-20%. Obviously, if the spontaneous emission rate per unit volume and time in the active region R_{sp} is known, the contribution to the background current introduced by this spontaneous emission may be expressed as

$$I_{sp} = q r_{sp} R_{sp} S L \quad (2.71),$$

where S is the cross-sectional area of the gain region. Note that the dependence of the spontaneous emission current with the device length is linear, resulting in no additional trade-off between its contribution to the background current and the device efficiency. Furthermore, large relative variations of the net gain per unit length may be achieved with small changes in the carrier density, and consequently small variations in the spontaneous emission rate. An increase in the net gain per unit length will thus result in a much larger increase of the signal photocurrent than the corresponding increase in the spontaneous emission current.

We will proceed, in the next subparagraph, to compare this value to the ASE current previously calculated, and to provide numerical estimates for both.

Order of magnitude of ASE current and spontaneous emission current

It was claimed, at the beginning of this chapter, that the main source of background current is the absorption in the detection region of ASE generated in the gain region. We estimated that other sources (such as the imperfect electrical isolation between the detector and amplifier contacts) would produce dark currents in

the order of a few μA , while their dependence on the number of periods or device length would be roughly linear, in the respective cases of TAP detectors with alternating gain and absorption and with transverse coupling. The order of magnitude of the ASE current and the spontaneous emission current will now be estimated, in order to compare them to other possible sources of background current and between themselves.

Performing a flat-band approximation, and neglecting the effect of the initial amplification region, the total ASE current in a TAP detector with transverse coupling, expressed in (2.61), may be simplified into

$$I_{ASE} = 2q\Delta n_o (\Gamma_a \mathbf{a}) (\Gamma_g r_{st,em}) \frac{e^{\Delta g L} - 1 - \Delta g L}{\Delta g^2} \quad (2.72).$$

When gain and absorption are close to cancellation, we may perform the following approximation:

$$I_{ASE} = q\Delta n_o (\Gamma_a \mathbf{a} L) (\Gamma_g r_{st,em} L) \quad (2.73).$$

We will now substitute into this equation some of the values used in the previous section for the calculation of the device efficiency, i.e., material absorption of 9000cm^{-1} , device length of $200\mu\text{m}$, and confinement factors is gain and absorption region of 20% and 5%. We will furthermore assume that $r_{st,em}$ may be approximated by 5000cm^{-1} . Typical bandwidths for SOAs are in the order of 10-20THz. This yields values of ASE current in the order of $300\mu\text{A}$ - $600\mu\text{A}$. The only other source of

background current that may compete is therefore the current generated by absorption of spontaneous emission, I_{sp} .

Let us now find the ratio between these two contributions in a flat band approximation. As shown in appendix A, we may write

$$R_{sp} = \frac{\mathbf{r}_0}{N_p} R_{st,em} \Delta \mathbf{n}_o = \mathbf{r}_0 v_g r_{st,em} \Delta \mathbf{n}_o \quad (2.74),$$

where N_p is the photon density per unit volume in the amplifier medium, \mathbf{r}_0 the blackbody radiation density and v_g the guided velocity of light in the amplifier waveguide. Using the expression for the blackbody radiation found in this chapter, we may then write the total spontaneous emission current as

$$I_{sp} = 8\mathbf{p} q \mathbf{r}_{sp} \frac{n^2 SL}{\mathbf{l}_0^2} r_{st,em} \Delta \mathbf{n}_o \quad (2.75),$$

where n is the index of refraction of the amplifier medium, and \mathbf{l}_0 the central wavelength of the amplifier. Let us assume that 20% of the spontaneously emitted photons produce an electron of photocurrent. Let us again assume, as when the ASE current was calculated, that the stimulated emission rate normalized to the optical intensity is 5000cm^{-1} , and the bandwidth is 10THz. For a refractive index of 3.5, a 200 μm long device emitting at 0.85 μm , with a 3 μm wide active region consisting of seven QWs, 8nm thick each, would produce around 2mA of spontaneous emission current. This value corresponds to between 3 and 6 times the ASE current produced

by the same device operating close to zero net gain. In fact, the ratio between spontaneous emission current and ASE current may be written as:

$$\frac{I_{ASE}}{I_{sp}} = \frac{\Gamma_g \Gamma_a \alpha I_0^2 L e^{\Delta g L} - 1 - \Delta g L}{4 \rho r_{sp} n^2 S (\Delta g L)^2} \quad (2.76).$$

When gain and absorption are close to cancellation, absorption of spontaneous emission will be the major contribution to the background current of the device. As the device length increases, the ratio between the ASE current and the spontaneous emission current increases linearly, leading to similar values of these two contributions for device lengths between 0.5 and 1mm. An increase in the net gain per unit length produces likewise a relative increase of the ASE current with respect to the spontaneous emission current.

In summary, the previous two paragraphs have discussed the generation of background current in TAP detectors due to absorption in the detection regions of ASE and spontaneous emission generated in the gain region. The order of magnitude of both ASE current and spontaneous emission current were estimated, resulting in values much larger than those expected from other background current contributions. It has been shown that, for large net gain per period in TAP detectors with alternating gain and absorption, and for large net gain per unit length in TAP detectors with transverse coupling, the signal photocurrent and ASE current grow at the same rate with the number of periods and the device length, respectively. However, this situation would not introduce any significant improvement over a traditional detector preceded by an optical amplifier. In the case where gain and absorption are close to

cancellation, it has been shown in previous sections that the device efficiency was roughly linear with the number of periods or the device length, in the cases of TAP detectors with alternating gain and absorption and with transverse coupling, respectively. In this section, it was shown that the dependence of the ASE photocurrent is roughly quadratic. This introduces a trade-off between the device efficiency and the ratio between the signal photocurrent and the ASE photocurrent, since the former is roughly proportional to the number of periods or the device length, and the latter roughly inversely proportional, their product thus being close to constant. In the particular case of TAP detectors with vertical coupling, it was shown that, for realistic device lengths, the main contribution to the background current when the net gain per unit length is negative or very small may be expected from absorption of spontaneous emission, rather than of ASE. This dominance of the spontaneous emission current becomes less important with device length and with increasing net gain per unit length.

Competition between signal and spontaneous emission for the available optical gain

The electron and hole concentrations in the active region of an electrically-pumped SOA are affected by several different processes: current injection, carrier escape (e.g. via thermionic emission), non-radiative recombination, spontaneous emission and stimulated emission and absorption (see for example [3], pp. 29-31). Under DC operation, the combination of all these processes results in an equilibrium carrier concentration. Changing the amount of optical power present inside the SOA will result in a change in the stimulated emission rate, and thus in a different equilibrium carrier concentration. In the absence of an optical input, all stimulated transitions are triggered by the ASE. In the presence of an optical input, the optical power in the SOA will increase, leading to a lower equilibrium carrier concentration. The spontaneous and stimulated emission rates will thus decrease, resulting in a lower ASE and spontaneous emission production. Reciprocally, the production of ASE in the SOA reduces the carrier concentration, thus resulting in a lower material gain available for the signal. This establishes a competition between signal and ASE for the available optical gain. The equations allowing us to describe the effects of this competition are introduced in appendix A. In this section, these equations will be used to give a qualitative understanding of the effects of such competition in the behavior of TAP detectors. First, the concept of measurable photocurrent in TAP will be introduced. This concept is necessary to take into account the change in ASE

photocurrent due to the presence of the input optical signal. Next, and using the formalism introduced in appendix A, the effect of the competition between signal, spontaneous emission and ASE in the TAP detector response will be described.

Background current and measurable photocurrent

As described in the previous section, most of the background current existing in TAP detectors is originated by the absorption in the detector region of the ASE or spontaneous emission generated in the gain region. With the addition of an input signal, both the ASE and the spontaneous emission generated in the device will decrease, as briefly introduced above, and described in more detail in appendix A. This will obviously result in lower ASE and spontaneous emission currents in the presence of an input signal. However, in the absence of any filtering mechanism, the ASE current, spontaneous emission current and the signal photocurrent cannot be distinguished. Only their sum may be measured. Therefore, we cannot directly access the true photocurrent generated by the distributed amplification and absorption of the input optical signal, only the difference between the total current in the presence and in the absence of said optical signal. This difference between the total current and the background current in the absence of an optical input will be referred to as measurable photocurrent from here henceforth. Calling $I_{ASE}(P_{in})$, $I_{sp}(P_{in})$ respectively the ASE and spontaneous emission currents generated in the device when an optical input of power P_{in} is present, and $I_{ph}(P_{in})$ the true photocurrent generated by said input the measurable photocurrent, I_{meas} , may be defined as follows:

$$I_{meas}(P_{in}) = I_{ph}(P_{in}) + I_{ASE}(P_{in}) + I_{sp}(P_{in}) - I_{ASE}(0) - I_{sp}(0) \quad (2.77).$$

We can similarly define a measurable efficiency, $\mathbf{h}_{meas}(P_{in})$, as:

$$\mathbf{h}_{meas}(P_{in}) = \frac{h\nu}{q} \frac{I_{meas}(P_{in})}{P_{in}} \quad (2.78).$$

The concept of measurable photocurrent is schematically expressed through figure 2.28.

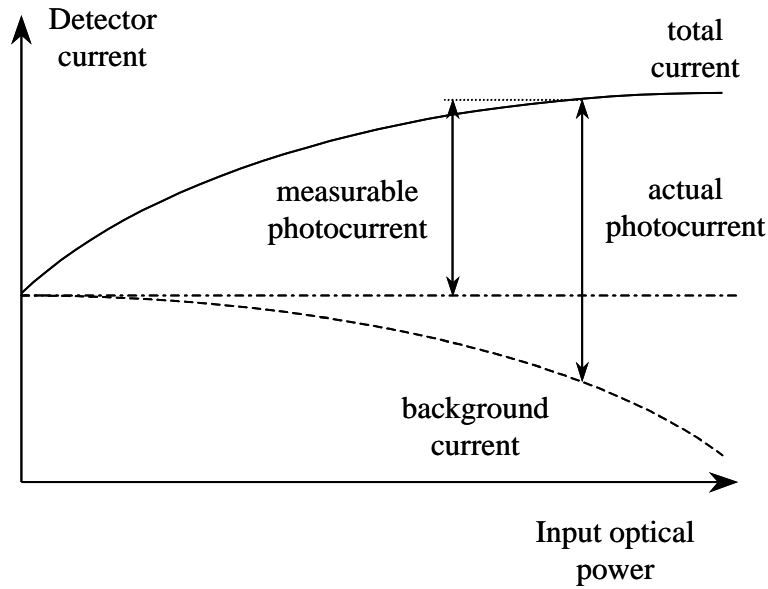


Figure 2.28: The total current generated in a TAP detector in the presence of an optical input (full line) is the sum of the background current produced in the presence of that input (dashed line) and the actual photocurrent generated by said input. As the input power increases, the ASE and spontaneous emission decrease, resulting in a lower value of the measurable photocurrent, i.e., the difference between the total current and the background current in the absence of an input. The value of the background current in the absence of an optical input (dash-dotted line) is also shown for clarity.

This effect exists also in traditional SOAs, in the sense that the output optical power in an SOA is the sum of the amplified input signal and the ASE power.

However, it will be clear soon that in TAP detectors the competition between signal, spontaneous emission and ASE has more dramatic consequences.

In a traditional SOA, only the forward-traveling ASE exits the device at its output, together with the amplified signal. The backward-traveling ASE will leave the SOA through its input, thus being separated from the signal. Furthermore, post-amplification filtering is usually implemented, resulting in much of the ASE power being eliminated. Therefore, the total ASE power indistinguishably added to the amplified total optical output may be considered to be very small compared to the amplified signal power, as expressed in figure 2.29. A reduction in this ASE power will result in a barely noticeable change in the total optical power. As a conclusion, the only noticeable effect of the competition between signal and ASE is the reduction of the material gain.

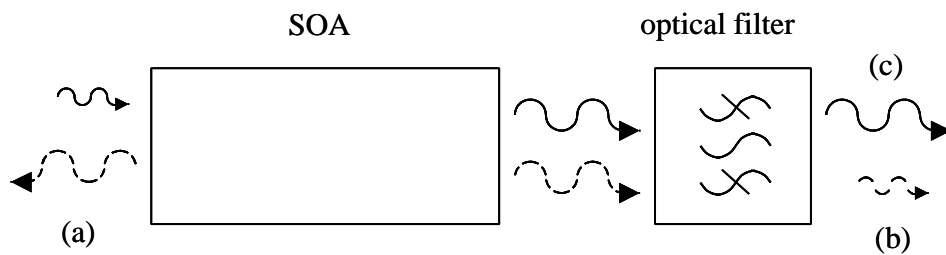


Figure 2.29: Schematic representation of the signal (full wiggly arrows) and ASE (dashed wiggly arrows) produced in a typical SOA. Backward-propagating ASE (a) leaves the device at its input, and is thus separated from the signal. Optical filtering at the output leaves a small contribution of ASE (b) added to the amplified signal (c). A reduction in this ASE value due to competition between signal and ASE results in a barely noticeable change in the total optical power.

In TAP detectors, however, both forward- and backward-traveling ASE generate background current, in addition to spontaneous emission in the case of TAP detectors with transverse coupling. Furthermore, even though optical filtering may possibly be added in TAP detectors, the current configurations studied in this dissertation do not include it. Any reduction in the production of spontaneous emission or in ASE, whether forward- or backward-propagating, and for any frequency in the optical bandwidth of the gain region, will thus be reflected directly in a reduction of the background current. The effect of this competition needs therefore to be studied in more detail, and will have more severe repercussions than in the case of SOAs.

In summary, this paragraph has introduced the concept of measurable photocurrent and measurable efficiency in TAP detectors, which take into account the effect of competition between signal, spontaneous emission and ASE for the available gain. The need to study the effect of this competition has also been justified. In the next section, this effect will be quantified by solving the carrier equilibrium equation together with the optical power propagation equation, as outlined in appendix A, and for the case of TAP detectors with transverse coupling.

Competition between signal and spontaneous emission in TAP detectors with transverse coupling

In order to accurately take into account the effect of competition between signal and ASE for the available optical gain, and as discussed in appendix A, a system of two equations needs to be solved self-consistently. The first equation is the carrier density equilibrium equation in the amplifier region. It expresses that, in DC

operation, the different processes that generate and annihilate electron-hole pairs in the gain region need to cancel their effects. This equation needs to be satisfied simultaneously for all positions along the device. The second equation is the optical power evolution equation, where signal and forward- and backward-traveling ASE are taken into account.

In this section, a way to solve these equations will be presented, in the particular case of TAP detectors with vertical coupling and without an initial gain section. First, the assumptions for the solving method will be stated. Next, the way to solve the equations in an indirect way under the simplifications considered will be presented. Finally, the results from the calculation will be shown and discussed.

Assumptions of the solving method

The two equations that need to be self-consistently solved are the following:

$$\frac{\mathbf{h}_i I}{qV} = R_{nr} + R_{sp} + (R_{st,em} - R_{st,ab}) \quad (2.79);$$

$$\frac{dp_{opt}(z, \mathbf{n})}{dz} = \Delta g(\mathbf{n}) p_{opt}(z, \mathbf{n}) + \mathbf{h} \mathbf{n} \Gamma_g r_{st,em}(\mathbf{n}) \quad (2.80).$$

As expressed in more detail in appendix A, these two equations are linked. On one hand, the net optical gain and stimulated emission rate normalized to optical intensity, appearing in (2.80), depend on the carrier density. On the other hand, the stimulated emission and absorption rates in (2.79) depend on the local optical power. In a strict model, the carrier density N is position dependent, and therefore so are

position-dependent the non-radiative recombination rate R_{nr} , the spontaneous recombination rate R_{sp} , the net gain per unit length Δg , and the stimulated emission normalized to optical intensity $r_{st,em}$. These quantities depend only on the carrier concentration, so once the latter is known, the former may be calculated too. In appendix A, a model is outlined that solves the system formed by (2.79) and (2.80) by dividing an SOA longitudinally into a series of sections where the carrier concentration is assumed to be constant. In the case of TAP detectors with transverse coupling, the carrier density will be assumed to be constant in the entire device. This approximation is possible because the only position-dependent term in (2.79) is the difference between the stimulated emission rate and the stimulated absorption rate. Now, since TAP detector operation becomes most interesting when the net gain per unit length is very small, approximating in this case the amplified optical signal along the device by its average value does not produce a large error. Furthermore, it has been shown that, when the net gain per unit length is small, the ASE power grows linearly along the device. This is true, of course, both for the forward- and the backward-traveling ASE. Thus, their sum will also be close to constant along the device, and approximating it by its average value results also in a small error. This assumption allows us to consider (2.79) as a position-independent equation, i.e., an equation that needs to be solved once, its solution being valid for the entire device. Furthermore, and as a consequence, it also allows us to consider the net gain per unit length and the stimulated emission rate normalized to optical intensity, appearing in (2.80), as position independent. In this case, this equation may be solved in closed

form, as shown in (2.17) and (2.59). These two results may be spatially averaged, resulting in

$$P_{opt} \approx \frac{1}{L} \int_0^L P_{opt}(z) dz = h_c P_{in} \frac{e^{\Delta g(\mathbf{n}_0)L} - 1}{\Delta g(\mathbf{n}_0)L} \quad (2.81),$$

$$p_{ASE}(\mathbf{n}) \approx \frac{1}{L} \int_0^L p_{ASE}(z, \mathbf{n}) dz = h\mathbf{m} \frac{\Gamma_g r_{st,em}(\mathbf{n})}{\Delta g(\mathbf{n})} \frac{e^{\Delta g(\mathbf{n})L} - 1 - \Delta g(\mathbf{n})L}{\Delta g(\mathbf{n})L} \quad (2.82),$$

where $P_{opt}(z)$ denotes the position-dependent optical power contained in the signal, and P_{opt} will denote hereafter its spatially-averaged value. Similarly, $p_{ASE}(z, \mathbf{n})$ denotes the position-dependent ASE spectral power density, and $p_{ASE}(\mathbf{n})$ will denote henceforth its spatially-averaged value.

Thus, under the assumption that the net gain per unit length is small, and that the optical power does not change radically inside the device, the system may be simplified into one single position-independent equation:

$$\frac{h_i I}{qV} = AN + CN^3 + R_{sp}(N) + [R_{st,em}(N, P_{in}) - R_{st,ab}(N, P_{in})] \quad (2.83).$$

Note that both the spontaneous emission rate and the stimulated emission and absorption rates include contributions at all frequencies. In the next subparagraph, an indirect way of solving this equation will be presented.

Solving the carrier density equilibrium equation

In the previous subparagraph, it has been shown that assuming the optical power close to constant along a TAP detector with vertical coupling results in important

simplifications when trying to calculate the effect of the competition between signal and ASE for the available optical gain. The initial system of two coupled equations has been shown to simplify into (2.83). Although this equation is considerably simpler than the initial system, it is still not obvious to solve it. In this subparagraph, an indirect method to perform this task will be presented.

Let us assume for a moment that the carrier density N in the amplification region is known when a certain monochromatic signal at frequency \mathbf{n}_0 , containing a known optical power P_{in} , is incident on a TAP detector with vertical coupling. Now, since the carrier density determines all parameters describing the interaction between the gain region and the light inside the device, knowing N would enable us to calculate the frequency-dependent gain $g(\mathbf{n})$, net gain per unit length $\Delta g(\mathbf{n})$, and stimulated emission rate normalized to input power $r_{st,em}(\mathbf{n})$. All parameters and values present in equations (2.81) and (2.82) would then be known to us, and we could easily calculate the spatially-averaged signal power P_{opt} and ASE spectral power density $p_{ASE}(\mathbf{n})$. As shown in appendix A, the difference between stimulated emission and absorption rates may be calculated as

$$R_{st,em} - R_{st,ab} = \frac{1}{S} \int \frac{\Gamma g(\mathbf{n}) p_{ASE}(\mathbf{n})}{h\mathbf{n}} d\mathbf{n} + \frac{1}{S} \frac{\Gamma g(\mathbf{n}_0) P_{opt}}{h\mathbf{n}_0} \quad (2.84),$$

where S is the amplification region cross-sectional surface. The integral needs to be performed over the amplifier bandwidth, so that the first term in the RHS of (2.84)

represents the contribution to the stimulated emission and absorption rates from ASE at all frequencies. The second term represents the contribution from the signal.

Thus, assuming that the carrier concentration N and the input optical power P_{in} are known, all terms in the RHS of (2.83) may be calculated. Assuming the injection efficiency known, the bias current that needs to be injected into the amplifier region to produce this situation may be found. Performing this calculation for different values of the carrier concentration, and for a given input optical power, would allow us, through interpolation, to obtain the carrier concentration present in the amplification active region as a function of bias current, and for a given optical power.

Note that, since the spatially-averaged signal optical power and ASE spectral power density are intermediate steps in this calculation, they can be associated to the calculated amplifier bias current. In other words, for a given input power, the spatially-averaged signal optical power and ASE power spectral density, as a function of amplifier bias current, may be found. This includes the case of zero input optical power. Since the carrier concentration determines also the spontaneous emission rate, the background current due to detection of both spontaneous emission and ASE, and either in presence or in absence of an input signal, $I_{sp}(P_{in})$ and $I_{ASE}(P_{in})$, and $I_{sp}(0)$ and $I_{ASE}(0)$, may be found, as well as the photocurrent due to said signal, $I_{ph}(P_{in})$. The measurable photocurrent may then be found via (2.77), thus quantifying the effect of the competition between spontaneous emission and signal for the available optical gain. This computation process is schematically represented in figure 2.30.

The calculation of the ASE current, spontaneous emission current and signal photocurrent from the spatially-averaged ASE power spectral density and signal power is extremely simple when the absorption in the detection region is position-independent:

$$I_{ph}(P_{in}) = \frac{q}{h\mathbf{m}_0} \int_0^L \Gamma_a \mathbf{a}(\mathbf{n}_0) P_{opt}(z) dz = \frac{q}{h\mathbf{m}_0} [\Gamma_a \mathbf{a}(\mathbf{n}_0) L] P_{opt} \quad (2.85);$$

$$\begin{aligned} I_{ASE}(P_{in}) &= \int \left[\frac{q}{h\mathbf{m}_0} \int_0^L \Gamma_a \mathbf{a}(\mathbf{n}) p_{ASE}(z, \mathbf{n}) dz \right] d\mathbf{n} \\ &= \int \frac{q}{h\mathbf{m}} [\Gamma_a \mathbf{a}(\mathbf{n}) L] p_{ASE}(\mathbf{n}) d\mathbf{n} \end{aligned} \quad (2.86).$$

The calculation of the spontaneous emission current may be performed assuming an appropriate value for the fraction r_{sp} of spontaneously emitted photons that contribute to the background current:

$$I_{ASE}(P_{in}) = q r_{sp} S L \int R_{sp}(\mathbf{n}) d\mathbf{n} \quad (2.87).$$

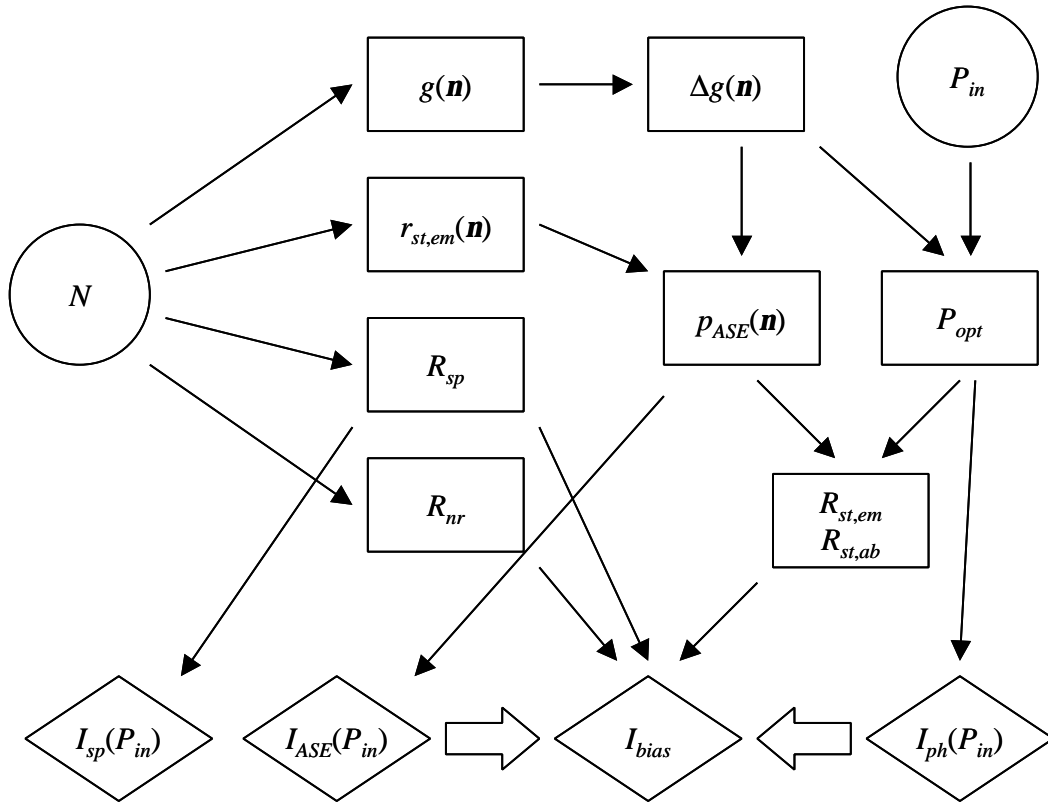


Figure 2.30: Knowing the input power P_{in} , and assuming known the carrier concentration N , the different recombination rates (non-radiative R_{nr} , spontaneous R_{sp} and stimulated $R_{st,em}$ and $R_{st,ab}$) may be found, from where the amplifier bias current I_{bias} can be calculated. Intermediate results include the material gain $g(n)$, net gain per unit length $\Delta g(n)$, stimulated emission rate normalized to optical input $r_{st,em}(n)$, and spatially-averaged ASE power spectral density $p_{ASE}(n)$ and signal power P_{opt} . From the last two, input power-dependent ASE current $I_{ASE}(P_{in})$ and signal photocurrent $I_{ph}(P_{in})$ are found, and may be expressed as a function of the input power P_{in} and the amplifier bias I_{bias} . The input-power dependent spontaneous emission current $I_{sp}(P_{in})$ may also be calculated from the spontaneous emission rate.

It has then been shown that the amplifier bias current necessary to sustain a certain carrier concentration, in the presence of a known input signal, may be easily calculated when the net optical power per unit length is assumed to be small. Intermediate results in the calculation process allow us to easily find the ASE and spontaneous emission currents, and signal photocurrent, associated to that bias current

and input power. The measurable photocurrent for a given input power may then be found by subtracting the sum of the three of them in the presence and in the absence of said input power, i.e., their sum when the input power has a certain value and when there is no input power (and consequently no photocurrent).

In the next subparagraph, the results obtained from this calculation will be shown and discussed.

Simulated measurable photocurrent

In this subparagraph, the results of the previous calculation, using realistic parameters for a TAP detector with vertical coupling, will be discussed. First, the parameters describing the material, and used in the simulation, will be presented. Next, the results of the simulation will be shown, and finally discussed.

Let us consider an active region formed by seven 8nm GaAs quantum wells with 8nm Al_{0.15}Ga_{0.85}As barriers. Using commercially available software packages, the values for material gain and spontaneous emission rate, as a function of wavelength, and for different carrier concentrations, may be found. In this case, the calculation was performed using APSYS 4.3.3, by Crosslight Software [6]. The results from this calculation are shown in figure 2.31.

The signal wavelength is assumed to be at the peak of the gain, i.e., 853nm. Non-radiative recombination is defined by coefficients $A=10^7\text{s}^{-1}$ and $C=4 \cdot 10^{30}\text{cm}^6\text{s}^{-1}$ (see, for example, [3], p. 160). The background loss is 20cm^{-1} . Both the detector and the

amplifier are assumed to be $3\mu\text{m}$ wide, the former being defined by etch, the latter by oxidation of high Al-content layers on top and bottom of the amplifier waveguide.

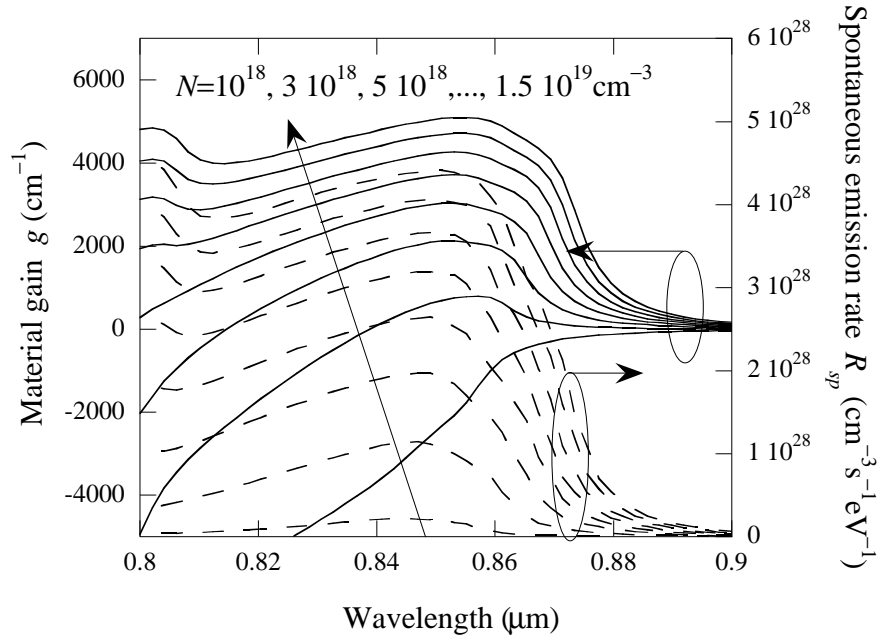


Figure 2.31: Simulated material gain (full lines) and spontaneous emission rate (dashed lines) as a function of wavelength and for different carrier densities, for an amplifier active region consisting on seven 8nm GaAs quantum wells with 8nm $\text{Al}_{0.15}\text{Ga}_{0.85}\text{As}$ barriers. The carrier concentration grows from 10^{18} to $1.5 \cdot 10^{19} \text{cm}^{-3}$ at $2 \cdot 10^{18} \text{cm}^{-3}$ intervals.

The gain and spontaneous emission shown in figure 2.31 do not take into account many-body effects (not available in the program at the time of calculation). The temperature for which the calculation was performed was room temperature (300°K). Performing the simulation with the values shown in figure 2.31 will however allow for an intuitive description of the effects of the competition between ASE and signal. Comparing these simulations to experimental results will also help establish the influence of temperature in the device performance.

For a suitable epitaxial layer design to be described in detail later, incorporating the amplifier active region modeled in figure 2.31, and for this detector and amplifier active region widths, the only mode to experience positive net gain per unit length presents modal confinement factors in the amplification and detection active regions of approximately 16% and 4%, respectively. The maximum optical coupling coefficient from a diffraction-limited gaussian beam into this mode is around 50%. The last three values were found using BeamPROP 5.0, by RSoft Design Group [7]. The injection efficiency was assumed to be independent of amplifier bias current and carrier density. All results will be plotted as a function of the injected bias current $h_i I_{bias}$. The material absorption in the absorption region, made of bulk GaAs, is shown in figure 2.32 [2].

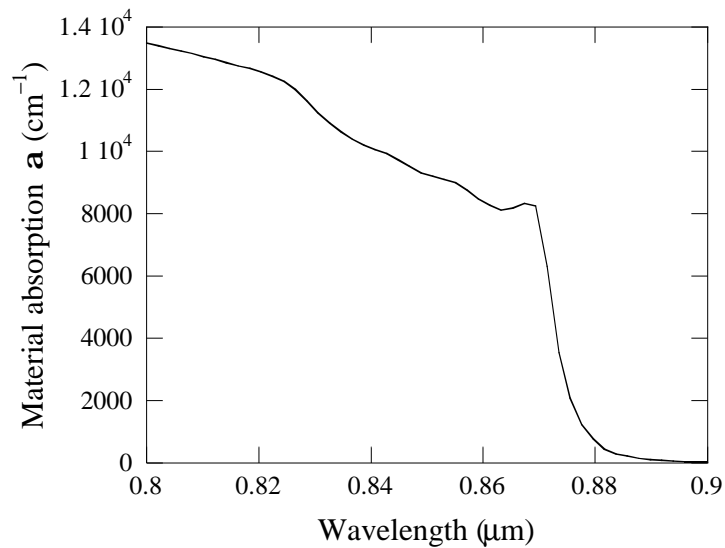


Figure 2.32: Material absorption as a function of wavelength for bulk GaAs. The carrier concentration is assumed to present its intrinsic value.

Let us define the actual external quantum efficiency as the ratio between the photocurrent generated by the input signal, expressed in units of electrons per second, divided by the input optical power, expressed in units of photons per second. The effect of the reduction in the background current with increasing input optical power is described in figures 2.33, by comparing the actual external efficiency and the measurable external efficiency, for device lengths of 100, 200, 300 and 400 μm , each of them excited with input powers of 1 μW , 10 μW , 100 μW and 1mW.

One easily identifiable trend is very important in figure 2.33. The efficiency, both actual and measured, decreases due to the increase in optical power. This is due in both cases to the competition of the photons present in the device for the available electron-hole pairs that recombine to produce amplification. In the case of the actual efficiency, the signal itself depletes the carriers injected into the amplifier active region. This effect is mostly due to the signal itself, and not to the ASE, but its nature is the same. It could be intuitively understood as competition between the input signal photons among themselves for the available optical gain. As the input signal increases, the carrier concentration gets progressively depleted, resulting in a lower net modal gain, which leads to a lower efficiency. This is analogous to gain saturation in traditional SOAs and lasers.

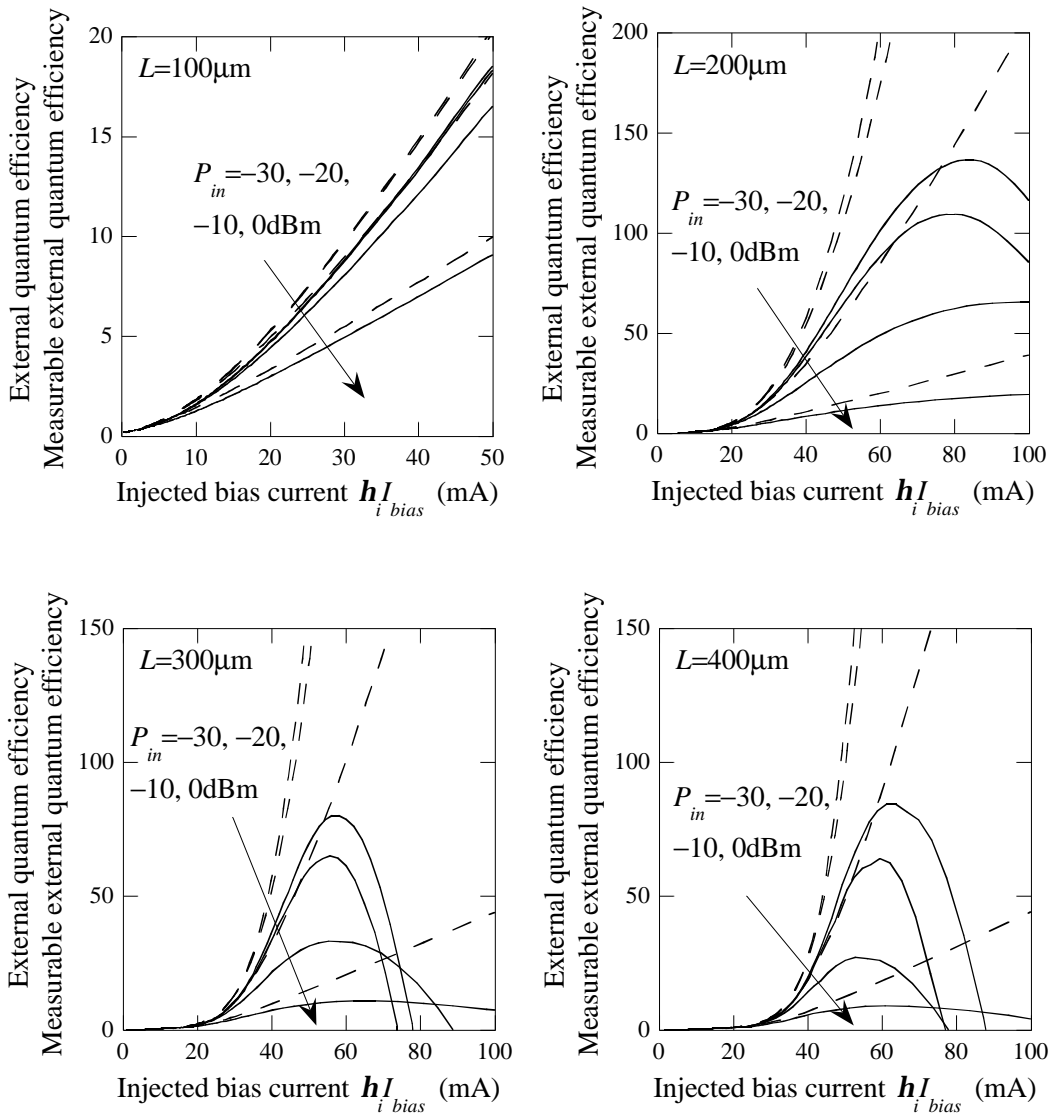


Figure 2.33: Simulated measurable (full line) and actual (dashed line) external quantum efficiency in a TAP detector with vertical coupling, for different input optical powers, and as a function of the injected amplifier bias current. The device length takes different values: 100mm (top left), 200mm (top right), 300mm (bottom left) and 400mm (bottom right). The confinement factors in the gain and absorption regions are 16% and 4%, respectively. The material gain and absorption and the spontaneous emission rate in the QWs are as shown in figures 2.31 and 2.32.

In the case of the measurable efficiency, the competition between spontaneous emission and signal clearly shows itself. As the input power increases, the depletion of the carrier concentration does not only result in a reduction in the amplification of

the input signal, but also in a decreased production of spontaneous emission and ASE, leading immediately to a reduction in the background current. As shown especially for device lengths of 200 μm and higher, this effect is quite dramatic, and of increasing importance as the device length grows. According to the discussion earlier on this chapter, most of the background current is generated by absorption of spontaneous emission, rather than ASE. It is therefore important to distinguish which one of these two components of the background current affects most the measurable photocurrent.

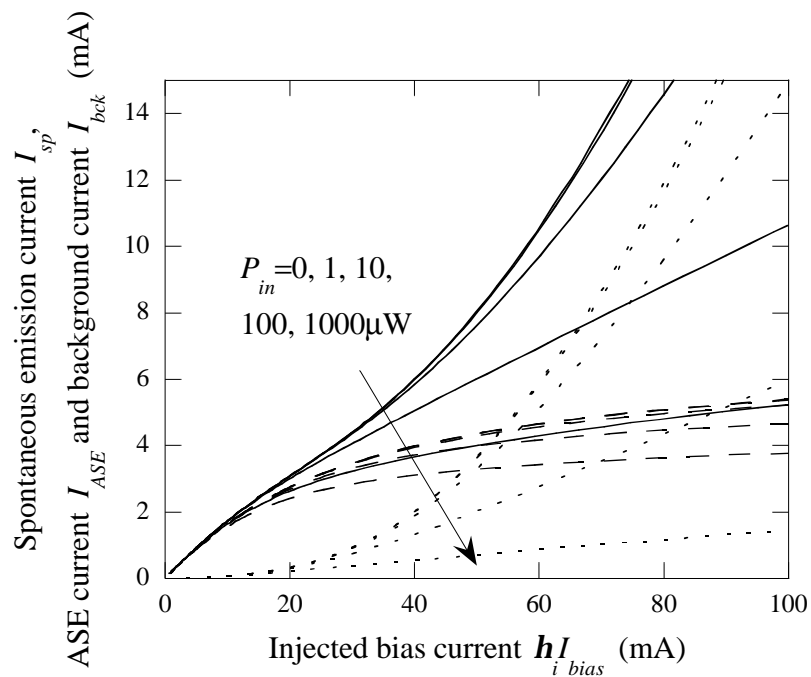


Figure 2.34: Simulated background current (full line) for a TAP detector with vertical coupling of length 200 μm as a function of the amplifier bias current, as the input power changes from 0 to 1mW. Also shown are the contributions to this background current from absorption of spontaneous emission (dashed line) and ASE (dotted line). The device efficiency is shown in the top right plot of figure 2.33.

Figure 2.34 shows, for the particular case of a 200 μm long device, the reduction in the background current as a consequence of an increase in the input optical power. The spontaneous emission current, the ASE current and the total background current are plotted. The latter is assumed equal to the sum of the former two contributions, any other source producing a negligible effect.

It is clear that most of the change in the measurable efficiency is related directly to the reduction in the ASE current, whose variations with the input power are much more pronounced than those of the spontaneous emission current. It is also interesting to note that, as the bias current increases and the net optical gain in the device starts to grow, absorption of ASE becomes eventually the major source of background current. The consequent increase in the stimulated emission rate (in the presence or absence of signal) leads to the carrier population varying very slowly with increasing amplifier bias. This must not be mistaken with carrier clamping in semiconductor lasers (see for example [3], p. 40), but it is a relatively similar effect, as an increase in the amplified optical power inside the device (lasing or not) leads to a slowly-varying carrier density with injection. This is expressed in figure 2.35, where the carrier concentration in the active region is plotted as a function of the amplifier bias current for increasing optical power, always for a 200 μm long device.

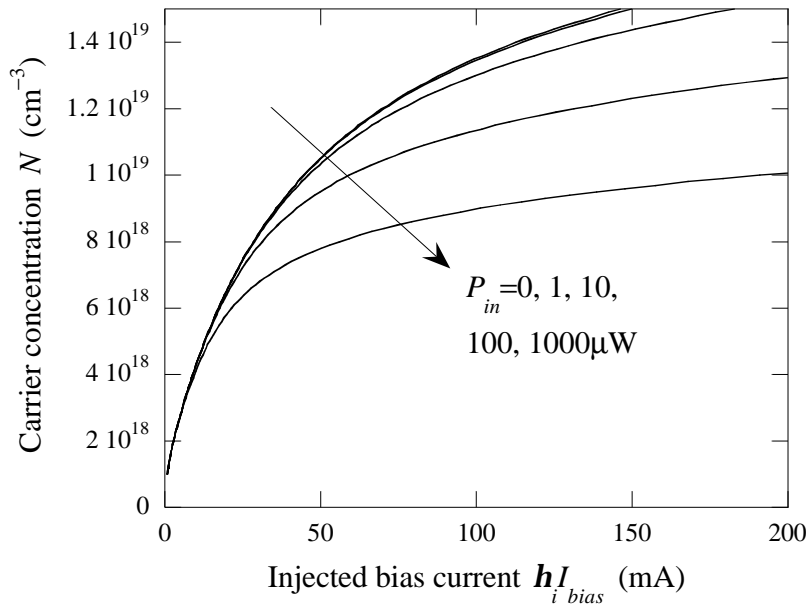


Figure 2.35: Simulated carrier concentration in the amplifier active region of a TAP detector with vertical coupling, as a function of amplifier bias current, for different input optical powers. The device length is 200mm, and its external efficiency is shown in the top right plot of figure 2.33.

Figure 2.35 shows how the carrier concentration tends indeed to a saturation value as the injected bias current increases, this value decreasing with the input optical power. This is intuitively consistent with the competition for the available electron-hole pairs between the different recombination mechanisms. The competition between signal and spontaneous emission shows itself also, but for much smaller values of bias current and quantum efficiency, as shown in figure 2.36, where the actual and measurable external quantum efficiencies are shown for the particular case of a 100 μ m long device.

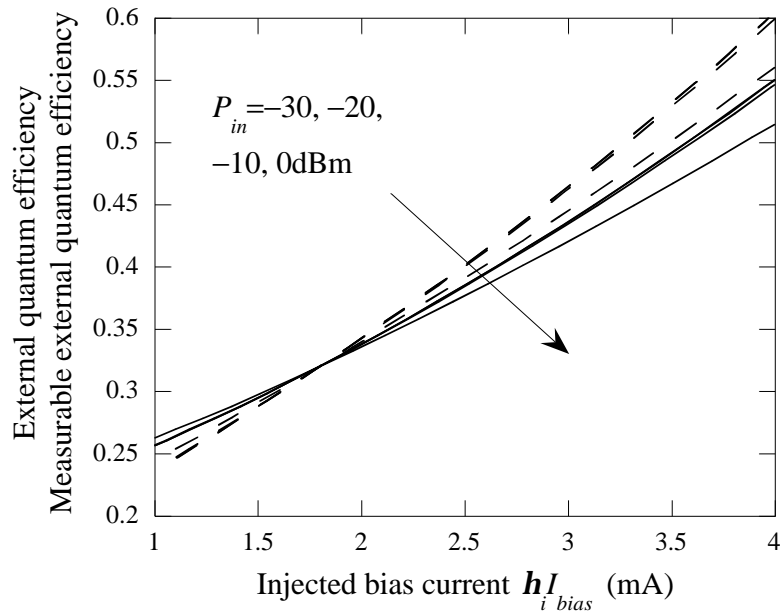


Figure 2.36: Simulated measurable (full line) and actual (dashed line) external quantum efficiency in a TAP detector with vertical coupling, for different input optical powers. The device length is 100mm. The confinement factors in the gain and absorption regions are 16% and 4%, respectively. The material gain and absorption and the spontaneous emission rate in the QWs are as shown in figures 2.31 and 2.32.

It is noteworthy to observe that a cross-over point exists for which all efficiencies are equal or their differences are negligible. This corresponds to the amplifier bias for which the amplification region becomes transparent. There is therefore no net change in the carrier distribution due to the presence of the signal, and simultaneously the amplifier has no effect in the optical power. Below this bias current, the amplifier active region produces net absorption. The introduction of an optical signal results thus in an increase in the carrier density, which in turn results in the production of more spontaneous emission (the ASE power level and is still negligible for this bias, and varies very little with the carrier density), producing the apparent increase of the efficiency for higher optical input powers. It is also important to note that, even

though a reduction in the measurable efficiency due to a decrease in the spontaneous emission current exists, and accounts for the different efficiencies shown in figure 2.52, this effect is much smaller than the reduction due to the competition between ASE and signal for larger amplifier bias currents. The reason for that is that the ASE current increases both with device length and with bias current much faster than the spontaneous emission current, and faster than the signal itself. A decrease in the carrier density due to an increase in the average optical power will lead thus to a larger change in the ASE current than in any other contribution to the total detector current for positive values of the net gain per unit length.

Before concluding this discussion, it is necessary however to make one clear observation. As shown in the carrier density plotted in figure 2.35, compared to the background current shown in figure 2.34, the most dramatic effects of the competition between signal and ASE will appear for values of the carrier concentration larger than in the order of $8 \cdot 10^{18} \text{cm}^{-3}$. This corresponds to values of the material gain close to 3000cm^{-1} . Therefore, based on the previous discussions in this chapter, this would entail that the net gain per unit length is positive, and actually large ($\Delta g L > 1$). The approximations made in this section are thus not entirely accurate for the corresponding input bias currents. TAP detectors will begin to show signs of saturation due to the competition between signal and spontaneous emission for lower input powers, and when the amplifier bias current and consequently the external efficiency are lower. In fact, averaging the optical power results in effectively “slowing down” the onset of saturation, i.e., letting the competition of signal and

spontaneous emission show its effect only for higher values of the input optical power or the amplifier bias current than those which would produce saturation in a real device. The results shown here, although not quantitatively exact, are however qualitatively correct. When interpreting experimental results from real devices, it will be necessary therefore to take into account the effect of averaging in the previous simulation, as well as the effect of temperature on the gain for a given carrier density, and also the gain reduction due to many-body effects. This will be further developed in later chapters.

In conclusion, this section has discussed the effects of competition between signal and spontaneous emission for the available optical gain. This effect is argued to be much more important in TAP detectors than in traditional SOAs, because of the close relationship between ASE, both forward- and backward-traveling, and background current, and also due to the absence of spontaneous emission and ASE filtering in the TAP detector configurations as presented in this dissertation so far. Simulations show how the increase of the optical input of a TAP detector results, via a decrease in the background current, in an important saturation of the external quantum efficiency of TAP detectors. This effect is shown to increase with the input optical power, the bias current and the device length. Although these simulated results cannot be claimed to be quantitatively exact, because of the approximations made in obtaining them, they can still be claimed to provide a qualitatively correct picture. We can thus expect a decrease in the external quantum efficiency with increase optical power, which will happen due to a reduction of the spontaneous emission current when the

net gain per unit length is negative or very small, and due to a reduction of the ASE current when the net gain per unit length is large. The simulations show the latter effect to be more important than the former, especially for large values of the external quantum efficiency. We can also conclude from the previous discussion and results that deviating from a negative or very small net gain per unit may quickly result in device saturation due to competition between signal and ASE.

Summary

This chapter has presented and discussed the DC operation characteristics of TAP detectors. The behavior of TAP detectors with alternating gain and absorption and TAP detectors with transverse coupling is found to depend very similarly on the number of periods and the device length, respectively.

When gain and absorption are close to mutual cancellation, the device efficiency is found to be approximately linear with the number of periods or device length. The main contribution to the background current produced independently on the input optical signal is argued to stem from the absorption in the detection regions of the ASE produced in the amplification regions. In the case where gain and absorption are close to cancellation, this background current depends on the number of periods or device length through a roughly quadratic law. This results in a trade-off between the device efficiency and the ratio between the detected photocurrent produced by the signal and the background current produced by the absorption of ASE. The background current generated in TAP detectors with transverse coupling due to

absorption of spontaneous emission varies linearly with the device length, and does not introduce therefore any trade-off.

The background current becomes more dominant when the optical power suffers large net loss as it propagates. Under this condition, the input optical power will be quickly attenuated, resulting in regions of the device producing barely any photocurrent related to the input optical signal. Spontaneous emission is produced and detected all along the device, from where the performance degradation in this case stems.

When the signal experiences large net gain as it propagates, the situation is not very dissimilar from traditional photodetectors preceded by an optical amplifier. The total device efficiency grows, and the production of current by absorption of the amplified input signal and absorption of ASE increase following roughly the same law as a function of the number of periods or device length. TAP detectors operated under these conditions do not present, however, significant intuitive advantages over the combination of a photodetector and a preamplifier.

The competition of ASE and signal for the available gain results in carrier depletion as the input optical power grows, with the ensuing reduction in the optical gain. The lack of optical filtering of the ASE and spontaneous emission in the configurations proposed in the previous chapter results in a reduction in the device efficiency, partly due to the input optical signal experiencing less gain, but also due to a reduction in the background current in the presence of a higher optical input. Due to the impossibility to distinguish between the photocurrent generated by either the

signal or the ASE, the reduction in the ASE current translates directly in a reduction of the measurable photocurrent. When the net gain per unit length is large and positive, this effect is shown to be quite important. The results simulated point thus to the need of introducing in the future optical filtering to reduce the amount of photocurrent reduced by absorption of ASE and spontaneous emission, and to the conclusion that the optimum operating condition for these devices is when gain and absorption are close to mutual cancellation.

This chapter has therefore presented a full theoretical characterization of the DC operation characteristics of TAP detectors, discussing their efficiency and the effect of spontaneous emission and ASE generation and absorption in their performance.

References

- [1] E.J. Skogen, J.S. Barton, S.P. Denbaars, L.A. Coldren, "A quantum-well-intermixing process for wavelength-agile photonic integrated circuits," *IEEE Journal of Selected Topics in Quantum Electronics*, vol. 8, no. 4, pp. 863-9, 2002.
- [2] E.D. Palik, ed., "Handbook of optical constants of solids," *Academic Press*, 1998.
- [3] L.A. Coldren, S.W. Corzine, "Diode lasers and photonic integrated circuits," *John Wiley & Sons*, 1995.
- [4] R.S. Muller, T.I. Kamins, "Device electronics for integrated circuits," 2nd edition, *John Wiley & Sons*, 1986.
- [5] V. Swaminathan, A.T. Macrander, "Material aspects of GaAs and InP based structures", *Prentice-Hall Inc.*, 1991.
- [6] APSYS 4.3.3, *Crosslight Software*, 2001 (<http://www.crosslight.com>).
- [7] BeamPROP 5.0, *RSoft Design Group*, 2001 (<http://www.rsoftdesign.com>).

(This page is intentionally left blank)

CHAPTER 3

High-speed characteristics of TAP detectors

Traveling-wave detectors are optoelectronic devices that feature in general two waveguides: an optical waveguide where light propagates and is absorbed, and an electrical waveguide where the generated photocurrent travels towards the device output. A lumped model is insufficient to simulate the characteristics of the electrical waveguide. A distributed model is necessary in order to take into account all phenomena related to the propagation of the photocurrent. Such phenomena include the microwave attenuation as the generated photocurrent propagates, the velocity mismatch between the optical and electrical signals, and the reflections associated to the impedance mismatch between the electrical waveguide and the load. In this chapter, the bandwidth of TAP detectors will be modeled, and the results of the simulations discussed, through the study first of the microwave propagation characteristics, followed by the application of a distributed photocurrent model.

Microwave propagation in TAP detectors

The frequency response of traveling-wave detectors is determined mostly by the propagation of the generated photocurrent towards the device electrical output. This propagation needs therefore to be modeled in TAP detectors, in order to simulate their frequency response. In this section, the model used to describe the propagation of electrical waves in TAP detectors will be presented. First, some brief remarks about the propagation of electrical waves in metal-insulator-semiconductor structures will be made. Based on these remarks, an equivalent circuit model will be presented. Using this equivalent circuit model, the microwave propagation characteristics will be described through the microwave propagation coefficient g_{el} and characteristic impedance Z_c . Results of calculations of these two parameters will be presented for TAP detectors with alternating gain and absorption and for TAP detectors with vertical coupling.

Propagation of electrical waves in metal-insulator-semiconductor structures

Electrical fields propagating in a metal-insulator-semiconductor structure are affected by different phenomena. Any material presenting a finite, non-zero resistivity will introduce dissipation loss. The interaction between the field and the waveguide will result also in a propagation velocity different than the speed of light in vacuum. The propagation velocity and the loss will depend on the characteristics of the different waveguide layers, but also on the distribution of the field in each one

of them. Finally, changes in the waveguide geometry, e.g. at the input or output of the device, may result in reflections due to mismatch between the propagation characteristics of different sections of the waveguide. An accurate description of these effects requires the solution of Maxwell's equations, finding the different modes supported by the structure and the propagation characteristics of each one of them. This "full-wave" description, although accurate, is not very practical in realistic devices, given the difficulty involved in the solution of Maxwell's equations for arbitrary geometries and material characteristics. An entirely equivalent way to describe the propagation characteristics is found by considering the propagation of voltage and current waves (see for example [1], chapter 3). Assuming that z is the direction of propagation, and that the wave travels from lower to higher values of the coordinate z , the voltage and current waves, $V^+(z)$ and $I^+(z)$, may be described by the following equations:

$$\frac{V^+(z)}{V^+(0)} = \frac{I^+(z)}{I^+(0)} = e^{-\mathbf{g}_{el}z} \quad (3.1),$$

$$\frac{V^+(z)}{I^+(z)} = Z_c \quad (3.2),$$

where Z_c the characteristic impedance and \mathbf{g}_{el} is the microwave propagation coefficient, expressed typically as

$$\mathbf{g}_{el} = \mathbf{a}_{el} + j\mathbf{b}_{el} \quad (3.3).$$

\mathbf{a}_{el} is the attenuation coefficient per unit length, and \mathbf{b}_{el} is related to the phase velocity v_p through

$$v_p = \frac{\mathbf{w}}{\mathbf{b}_{el}} \quad (3.4).$$

This description assumes that the waveguide is homogeneous, i.e., equations (3.1) and (3.2) are only valid for a range of positions where the characteristics of the waveguide itself do not change.

For an arbitrary waveguide, the relation between the geometry and material properties of the waveguide, and the microwave propagation coefficient and characteristic impedance are not easily found, and require, as mentioned earlier, a “full-wave” solution of Maxwell’s equation. However, there are three main propagation regimes in metal-insulator-semiconductor waveguides. Each regime accepts approximations that help simplify the problem considerably. The propagation regime depends mostly on the semiconductor properties and the frequency considered, since the main differentiating factor is the penetration distance of the field into the different materials, also known as skin depth. For a material with resistivity \mathbf{r} , and magnetic permeability \mathbf{m} the skin depth \mathbf{d}_s at a given angular frequency \mathbf{w} is given by (see for example [1], p. 54)

$$\mathbf{d}_s(\mathbf{w}) = \sqrt{\frac{2\mathbf{r}}{\mathbf{w}\mathbf{m}}} \quad (3.5).$$

For very small frequencies, i.e., when the wavelength is much larger than the waveguide dimensions, the solution of Maxwell’s equations is very close to a

transverse-electric-magnetic (TEM) mode, and semiconductor materials present behaviors similar to those of lossy dielectrics (quasi-TEM regime). The effect of the semiconductor layers may therefore be accurately described through their dielectric loss tangent. For very large frequencies, the penetration of the field into the semiconductor layers is very small, and these may be assumed to behave like lossy conductors (skin-depth regime). For intermediate values, such simplifications are not possible. The full-wave solutions to Maxwell's equations present lower phase velocity than would be expected from the combination of the permeability and permittivity of the semiconductor material (slow-wave regime). Probably the first full description of these three propagating regimes was performed for metal-silicon oxide-silicon microstrip waveguides [2], but the principle holds for other material systems and waveguide geometries. In fact, traveling-wave detectors may indeed be assumed to be metal-insulator-semiconductor waveguides. The insulator would be represented by the reverse-biased absorption region, whereas the semiconductor regions would correspond to the claddings. The substrate will belong to the former or the latter depending on whether it is semi-insulating or not. For the typical range of cladding resistivity useful for such devices ($r \sim 10^{-3} \Omega \text{cm}$, corresponding to a mobility of $\sim 10^4 \text{m}^2 \text{V}^{-1} \text{s}^{-1}$ and a carrier concentration of $\sim 10^{17} \text{cm}^{-3}$), and assuming that the permeability is not too different from that of vacuum, we find, for frequencies $f \sim 10 \text{GHz}$, a skin depth $d_s \sim 10^{-3} \text{cm} = 10 \mu\text{m}$, well in the order of magnitude of typical device dimensions. Consequently, the electrical propagation properties in high-speed traveling-wave optoelectronic devices will be mostly either in the slow-wave regime

(for undoped or semi-insulating substrate) or the skin-depth regime (for doped substrate). However, the presence of a doped substrate results in important added loss, and must therefore be avoided. Slow-wave effects may be assumed to dominate in this case.

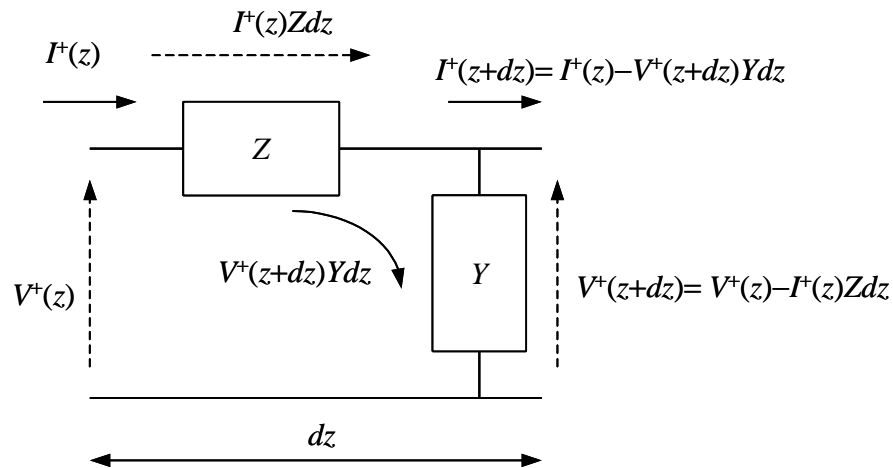


Figure 3.1: Equivalent circuit model for an electrical waveguide. Each section of differential length dz may be modeled as a series impedance Zdz and a parallel admittance Ydz . The voltage and current waves arriving to and leaving this section are represented by full-line (voltage) and dashed (current) arrows, and their difference as a function of the equivalent circuit elements are indicated. The impedance per unit length Z and admittance per unit length Y are, in general, frequency dependent.

The need for full-wave solutions of Maxwell's equations may however be circumvented. Good agreement between experimental results, full-wave solutions and equivalent circuit models has been demonstrated, as long as the slow-wave effects are represented through added loss in the semiconductor and metal (see for example [3]). Apart from this difference, the same equivalent circuit used to model quasi-TEM modes may be used. In order to find the equivalent circuit of an electrical waveguide, we consider it divided into sections of differential length dz , as shown in

figure 3.1. To each section, frequency-dependent impedance $Z(\mathbf{w})dz$ and admittance $Y(\mathbf{w})dz$ are associated.

The evolution of the voltage and current waves of angular frequency \mathbf{w} is described by the following equations:

$$\frac{dV^+}{dz} = -Z(\mathbf{w})I^+ \quad (3.6).$$

$$\frac{dI^+}{dz} = -Y(\mathbf{w})V^+ \quad (3.7).$$

Both equations may be combined into:

$$\frac{1}{V^+} \frac{d^2V^+}{dz^2} = \frac{1}{I^+} \frac{d^2I^+}{dz^2} = Z(\mathbf{w})Y(\mathbf{w}) \quad (3.8).$$

The solutions of this equation are obviously of the form (3.1), where

$$\mathbf{g}_{el}(\mathbf{w}) = \sqrt{Z(\mathbf{w})Y(\mathbf{w})} \quad (3.9).$$

The root with positive real part needs to be chosen. Otherwise, the electrical signal would grow with propagation, which is not true for passive waveguides.

Inserting (3.9) into (3.1), and substituting into (3.6) and (3.7) yields

$$Z_c(\mathbf{w}) = \frac{V^+}{I^+} = \frac{Z(\mathbf{w})}{\mathbf{g}_{el}(\mathbf{w})} = \frac{\mathbf{g}_{el}(\mathbf{w})}{Y(\mathbf{w})} = \sqrt{\frac{Z(\mathbf{w})}{Y(\mathbf{w})}} \quad (3.10).$$

For lines supporting TEM or quasi-TEM modes, the impedance Zdz is the result of the series combination of an inductance Ldz and a resistance Rdz , whereas the admittance Ydz is expressed as the combination in parallel of a capacitance Cdz and a

conductance Gdz . This is schematically represented in figure 3.2. This figure also shows the modifications necessary to take into account slow-wave effects in waveguides that allow modes traveling under this regime, which will be discussed next.

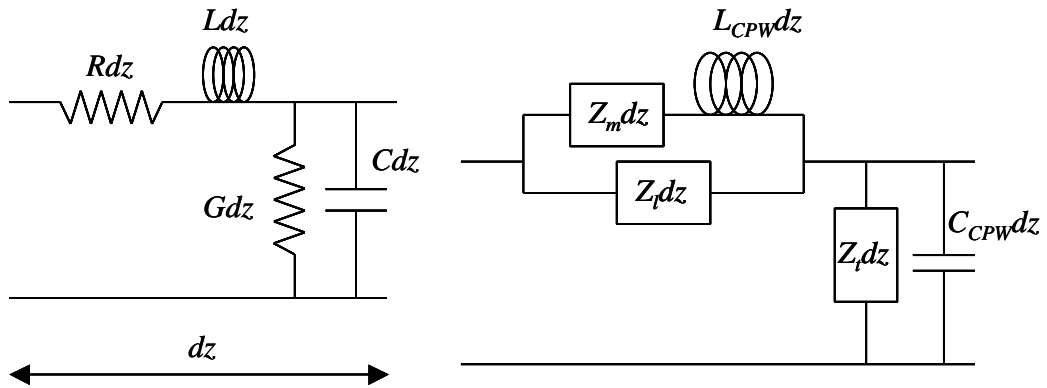


Figure 3.2: Equivalent circuit model for each section of differential length dz in an electrical waveguide supporting TEM or quasi-TEM modes (left). The equivalent circuit features a series resistance Rdz and inductance Ldz , together with a parallel capacitance Cdz and conductance Gdz . The equivalent circuit on the left allows the description of slow-wave effects in high-speed optoelectronic devices featuring a coplanar waveguide (CPW). The inductance L_{CPW} and capacitance C_{CPW} are identical to the quasi-TEM regime model. The substitution of R and G by the metal impedance Z_m and the transverse impedance Z_t , respectively, and the addition of the longitudinal impedance Z_l take into account added loss in the metal and semiconductor. These new impedances are, in general, frequency dependent.

For a waveguide supporting quasi-TEM modes, the microwave propagation coefficient and the characteristic impedance are given by

$$Z_c = \sqrt{\frac{R + j\omega L}{G + j\omega C}} \quad (3.11),$$

$$\mathbf{g}_{el} = \sqrt{(R + j\omega L)(G + j\omega C)} \quad (3.12).$$

Note that if $R=G=0$, the characteristic impedance is purely real, while the microwave propagation coefficient is purely imaginary, i.e., the waveguide is lossless. Moreover,

$$v_p = \frac{1}{\sqrt{LC}} \quad (3.13),$$

i.e., the waveguide is non dispersive, since the phase velocity is independent on the frequency. This corresponds to the ideal case where the metal is a perfect conductor, while all other materials are perfect insulators.

Let us now consider the case of a traveling-wave optoelectronic device where the slow-wave effects dominate. For the purposes of this dissertation, the study will be limited to that of devices featuring a coplanar waveguide (CPW). This transmission line is ideally formed by a central strip that carries the signal, and two ground half-planes at either side. This waveguide allows for device fabrication on semi-insulating substrates, with the consequent reduction of microwave loss. Furthermore, it is suitable for easy interconnection for integration, or for packaging with unbalanced high-speed connectors such as V- or K- [4]. This transmission line has been used to produce traveling-wave photodetectors with bandwidths up to 172GHz in GaAs [5] and sub-picosecond impulse response in traveling-wave detectors with low-temperature-grown GaAs absorption regions [6].

Given the width w_m and thickness t_m of the central metal strip of a CPW, as well as its magnetic permeability \mathbf{m}_m and resistivity \mathbf{r}_m , the impedance per unit length $Z_m(\mathbf{w})$ associated to this metal line in a slow-wave regime is given by [7]

$$Z_m(\mathbf{w}) = \frac{1}{w_m} \sqrt{\frac{j\omega\mathbf{m}_m}{\mathbf{s}_m}} \coth \left[(1+j) \frac{t_m}{\mathbf{d}_s(\mathbf{w})} \right] \quad (3.14).$$

The inductance and capacitance per unit length, however, do not change. For the particular case of a CPW, they can be found through conformal mapping techniques (see for example [1], pp. 175-180 and 886-910), resulting in

$$C_{CPW} = 4\epsilon_0\epsilon_{eff} \frac{K(k)}{K(k')} \quad (3.15),$$

$$L_{CPW} = \frac{\mathbf{m}_0}{4} \frac{K(k')}{K(k)} \quad (3.16),$$

where the parameters k and k' are defined as functions of the metal width w_m and the width of the gap between the signal strip and the ground planes w_g by

$$k = \frac{w_m}{w_m + 2w_g} \quad (3.17),$$

$$k' = \sqrt{1-k^2} \quad (3.18),$$

and $K(k)$ is the complete elliptic integral of the first kind,

$$K(k) = \int_0^{\pi/2} \frac{d\mathbf{q}}{\sqrt{1-k^2 \sin^2 \mathbf{q}}} \quad (3.19).$$

The effective dielectric permittivity ϵ_{eff} may be assumed to be

$$\epsilon_{eff} = \frac{\epsilon_r + 1}{2} \quad (3.20),$$

where ϵ_r is the relative dielectric permittivity of the substrate. An exact solution would require the averaging of the permittivity of the different semiconductor layers. However, given the relatively small variation of this parameter with the aluminum composition (13.2 for GaAs, 12.5 for $\text{Al}_{0.2}\text{Ga}_{0.8}\text{As}$, as seen for example in [8], p. 12), and the predominance of GaAs in the substrate, we may assume $\epsilon_r=13$, and therefore $\epsilon_{eff}=7$.

Finally, and as mentioned earlier, the loss in the semiconductor needs to be taken into account. Assuming a semiconductor cladding of width w_c , thickness t_c , dielectric permittivity ϵ_c and resistivity r_c , its contributions to the longitudinal and transverse impedance per unit length, Z_l and Z_t respectively, are given by [9]

$$Z_l(\mathbf{w}) = \frac{r_c}{w_c t_c} \quad (3.21),$$

$$Z_t(\mathbf{w}) = \frac{t_c}{w_c} \frac{r_c}{1 + j\omega \epsilon_c r_c} \quad (3.22).$$

These equations assume homogeneous current distribution, and do not consider possible device symmetries. These will be taken into account for the particular cases presented later on in this chapter. Note that the contribution from Z_l will appear in parallel with the inductance L_{CPW} and the metal impedance Z_m , whereas the transverse impedance Z_t will substitute the parallel admittance G , being therefore in parallel also with the capacitance C_{CPW} . In series with Z_t , however, the capacitance C_i introduced by the intrinsic active region (assumed to act as an insulator) will be also present.

Given the width w_i , thickness t_i and dielectric permittivity ϵ_i of the active region, this capacitance per unit length is given by

$$C_i = \epsilon_i \frac{w_i}{t_i} \quad (3.23).$$

The final equivalent circuit described is shown in figure 3.2. It is noteworthy that the transverse impedance associated to the semiconductor cladding layers may be written as the parallel of a resistance R_c and a capacitance C_c , written in the following form:

$$R_c = r_c \frac{t_c}{w_c} \quad (3.24);$$

$$C_c = \epsilon_c \frac{w_c}{t_c} \quad (3.25).$$

R_c/dz is the DC resistance that would be calculated for vertical conduction of current through the cladding, whereas $C_c dz$ would be the capacity of a parallel-plate capacitor with horizontal plates, filled with the cladding material, and with its same dimensions. In other words, the slow-wave effect may be fully described by taking into account the skin effect and dissipation loss in the metal, as well as an added capacitive loading due to the presence of the semiconductor layers. The result of this additional capacitive loading will be a slower propagation velocity and higher microwave loss. The intuitive explanation of this double behavior may be that, since the resistivity of semiconductor materials is in the range between conductors and insulators, their behavior will share part of both. Obviously, the higher the cladding

resistivity, the closer its behavior will be to that of a capacitor, as evidenced in equation (3.22).

In summary, the microwave propagation characteristics in generic traveling-wave optoelectronic devices have been presented in this paragraph. More specifically, the slow-wave regime has been argued to dominate in these devices. The need to find full-wave solutions of Maxwell's equations in order to describe their high-speed behavior is circumvented through the use of an equivalent circuit model. This model takes into account the slow-wave effects through loss in the metal and semiconductor. The semiconductor introduces also capacitive loading, which will furthermore slow down the electrical propagation.

In the next paragraphs, the microwave propagation characteristics for TAP detectors will be calculated using the generic method shown above, for the particular device configurations studied in this dissertation.

Microwave propagation in TAP detectors with alternating amplification and absorption

In this paragraph, the microwave propagation characteristics of TAP detectors with alternating gain and absorption will be simulated and discussed.

TAP detectors with alternating gain and absorption present an inhomogeneous waveguide, i.e., the geometry and characteristics of the waveguide vary along the device. This is shown in figure 3.3, through a schematic representation of a top view and two cross-sections taken at the gain and absorption sections.

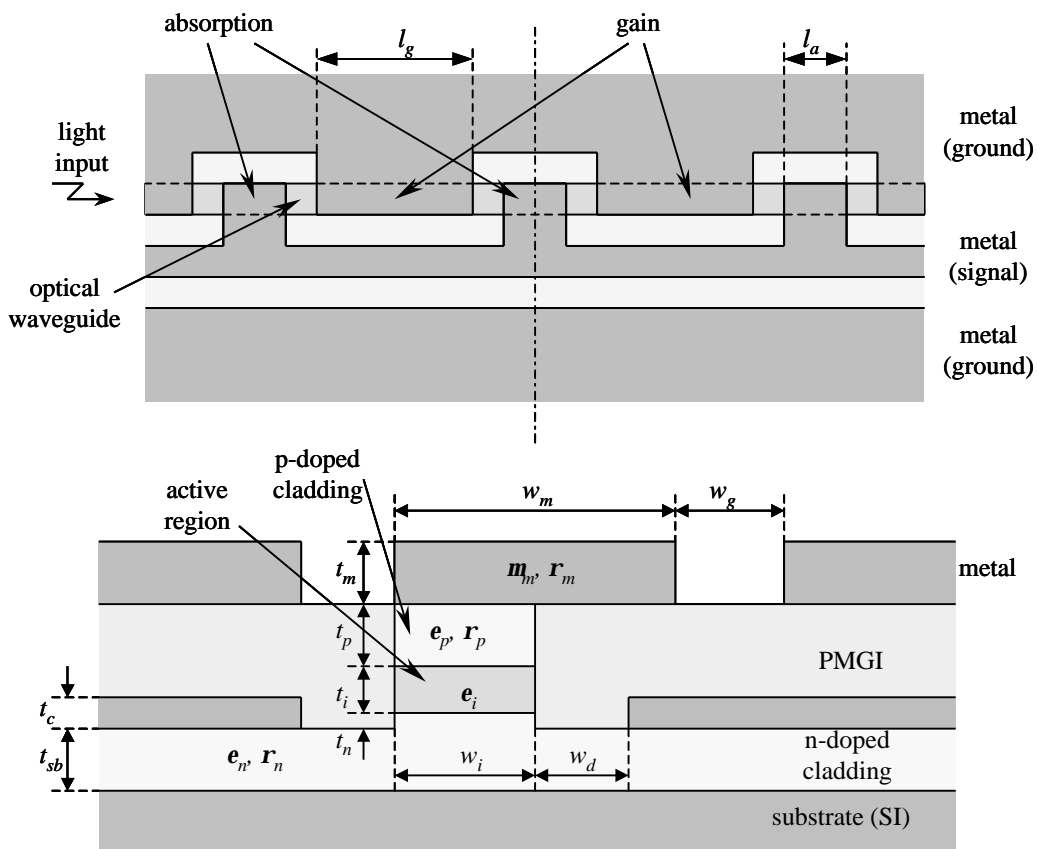


Figure 3.3: TAP detector with alternating gain and absorption: schematic top view (top) and cross-section at the absorption section (bottom, position indicated by the dash-dotted line on the top view). In the gain section, the waveguide behavior corresponds to a quasi-TEM regime (the CPW signal electrode does not touch the doped semiconductor), whereas slow-wave effects dominate in the absorption section. Dimensions and material characteristics are indicated.

Reflections may occur at each one of the discontinuities in the waveguide configuration. The combination of these reflections may result in undesired resonant behavior if the period length is in the order of, or much larger, than the electrical field wavelength. For a signal at 100GHz, the associated free-space wavelength is approximately 3mm, results in a guided half-wavelength around $500\mu\text{m}$. The period length must therefore be much smaller than this length. In order to avoid this

resonant behavior, we may choose to limit the period length to $50\mu\text{m}$. This explains the use of said value in the simulations of TAP detectors with alternating gain and absorption presented in chapter 2.

The periodicity of the transmission line may be used to simplify the calculation of the microwave propagation characteristics associated to it, as described in appendix B. This requires first the modeling of each one of the sections involved. We will assume that the differences between the behavior of the gain and isolation sections are negligible and that the entire period is made of an absorption section of length l_a , and a gain section of length $50\mu\text{m}-l_a$.

Let us now express, as a function of the parameters indicated in figure 3.3, the different equivalent circuit elements shown in figure 3.2, for the particular case of the absorption section. The metal impedance $Z_m(\mathbf{w})$, the capacitance C_{CPW} and inductance L_{CPW} associated to the CPW and the capacitance of the intrinsic absorption region C_i are given by equations (3.14), (3.15), (3.16) and (3.23), respectively. The longitudinal impedance Z_l , which is real and frequency-independent, is written in the following form

$$\frac{1}{Z_l} = \frac{w_i t_p}{3\mathbf{r}_p} + \frac{w_i t_n}{3\mathbf{r}_n} + \frac{(w_i + 2w_d + 2w_m) t_s}{3\mathbf{r}_s} \quad (3.26),$$

where w_m is the transfer length of the n-contact, given by

$$w_m = \sqrt{\frac{r_{nc} t_n}{\mathbf{r}_n}} \quad (3.27),$$

where r_{nc} is the characteristic resistance of the n-contact. Factors of 3 have been introduced in (3.26) to account for the spatial current distribution. Note that the bottom cladding has been divided into two parts for modeling purposes, the top one having the same width as the intrinsic active region, the bottom one being in principle infinite in width. The subscript s is used for the latter, in order to differentiate it from the former. We may refer to the bottom part of the n-doped cladding as doped sublayer or conductive sublayer.

The transverse impedance Z_t is written in the following way:

$$Z_t(\mathbf{w}) = \frac{1}{w_i} \left[\frac{t_{pc} \mathbf{r}_{pc}}{1 + j\omega \mathbf{e}_{pc} \mathbf{r}_{pc}} + \frac{t_p \mathbf{r}_p}{1 + j\omega \mathbf{e}_p \mathbf{r}_p} + \frac{t_n \mathbf{r}_n}{1 + j\omega \mathbf{e}_n \mathbf{r}_n} \right] + \frac{1}{2t_{sb}} \left(w_d + w_t + \frac{w_i}{6} \right) \frac{\mathbf{r}_n}{1 + j\omega \mathbf{e}_n \mathbf{r}_n} \quad (3.28),$$

where t_{pc} and \mathbf{r}_{pc} represent the thickness and resistivity of the p-contact. We may assume $t_{pc}=10\text{nm}$, and calculate \mathbf{r}_{pc} from the thickness t_{pc} and the characteristic resistance for the p-contact, r_{pc} , estimated at $5 \cdot 10^{-6} \Omega \text{cm}^2$. A factor of 3 has again been introduced to describe the spatial current distribution, while factors of 2 take into account the device symmetry.

The equivalent circuit model for the gain region is a simplification of the one shown in figure 3.2, since the capacitance C_i , and the longitudinal and transverse impedances Z_t and Z_l are not present, because the signal-carrying electrode of the CPW does not come in touch with anything other than the insulating PMGI. The impedance Z_m , the inductance L_{CPW} and the capacitance C_{CPW} are thus all that

remains, the loss introduced by the insulator being neglected in comparison with the loss introduced by the metal. The loss introduced by the semiconductor in the absorption region, averaged over the entire period, will also be much higher than the loss introduced by the insulator in the gain region. Note however that the signal electrode width w_m is different than in the absorption region. The appropriate, smaller value needs thus to be used in the calculation of the propagation characteristics of the gain region.

Let us now introduce the default values chosen for the different parameters shown in figure 3.3. The signal electrode will present a thickness of $t_m=1.5\mu\text{m}$ and the resistivity of gold ($r_m=2.3\cdot 10^{-6}\Omega\text{cm}$). Its width in the gain region will be assumed to be $2\mu\text{m}$. A gap $w_g=2\mu\text{m}$ wide will exist between signal and ground electrodes. We will allow the intrinsic region width w_i to vary between 2 and $4\mu\text{m}$, resulting in a metal width in the absorption region of 6-8 μm . The thickness of the p-cladding, intrinsic, n-cladding and n-doped sublayer will be $t_p=600$, $t_i=200$, $t_n=200$ and $t_s=600\text{nm}$ respectively. The resistivity of the doped claddings will be assumed to be $r_p=0.02\Omega\text{cm}$, $r_n=0.005\Omega\text{cm}$, $r_s=0.002\Omega\text{cm}$. The sublayer is assumed to present a higher donor concentration than the fraction of the n-cladding immediately below and having the same width as the active region. This is a good compromise between high doping to achieve low resistance, and low doping close to the active region to avoid free-carrier absorption. Finally, the characteristic resistance for the n-contact will be

taken as $r_{nc}=10^{-6}\Omega\text{cm}^2$. The length of the absorption region l_a will be assumed to change from 3 to $5\mu\text{m}$.

Using the previous values, the propagation characteristics of the gain and absorption region may be calculated. As described in detail in appendix B, the voltage-current transmission matrix or ABCD matrix may be used to express the overall microwave propagation characteristics as a function of those of the gain and absorption sections, since the ABCD matrix describing the sequence of two different waveguides is equal to the product of their respective ABCD matrices. The matrix elements are related to the propagation characteristics by the following equation:

$$\begin{pmatrix} A & B \\ C & D \end{pmatrix} = \begin{pmatrix} \cosh(\mathbf{g}_{el}L) & Z_c \sinh(\mathbf{g}_{el}L) \\ \frac{1}{Z_c} \sinh(\mathbf{g}_{el}L) & \cosh(\mathbf{g}_{el}L) \end{pmatrix} \quad (3.29).$$

The so obtained overall microwave propagation characteristics are shown in figures 3.4-3.5.

The microwave loss is described by the field attenuation coefficient, defined as the attenuation in decibels (dB) suffered by the field for a given device length, typically $100\mu\text{m}$.

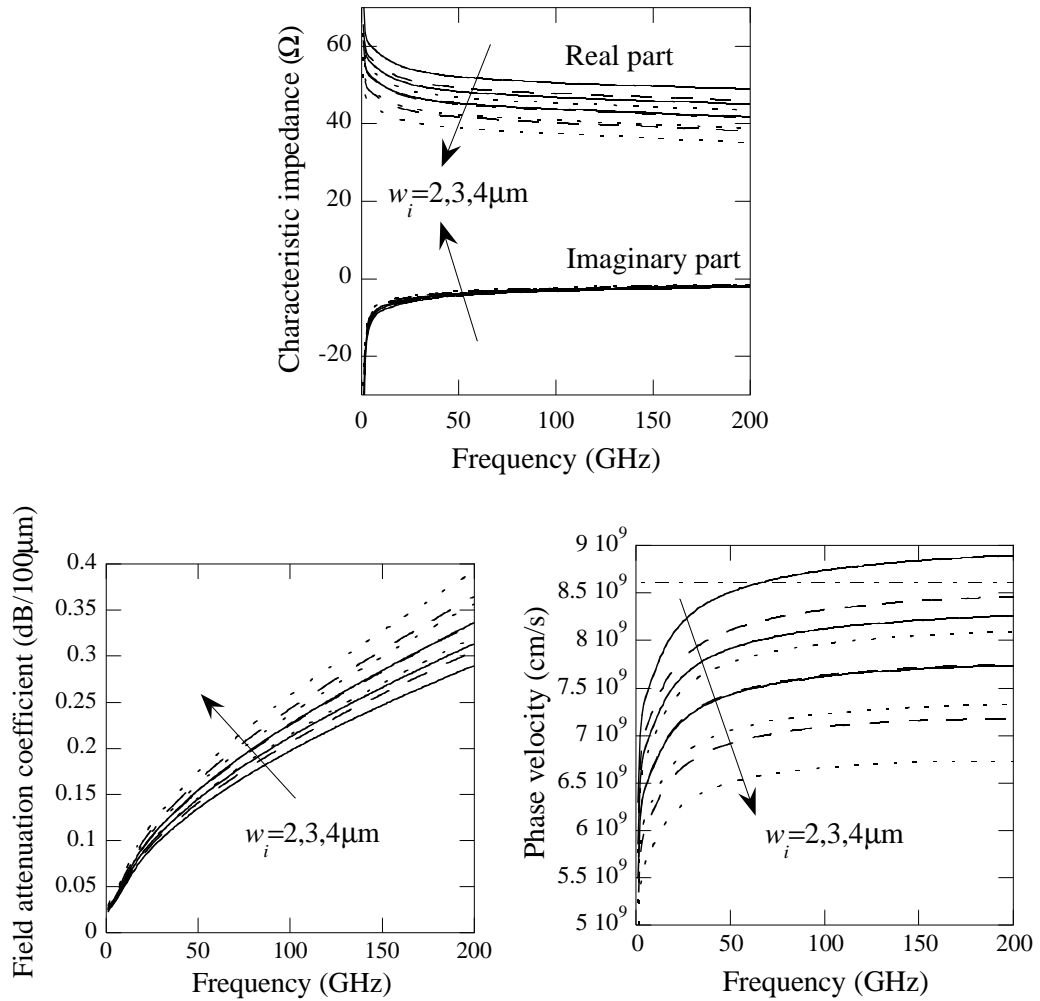


Figure 3.4: Simulated microwave propagation characteristics in TAP detectors with alternating gain and absorption, for different absorption section lengths and intrinsic region widths: real and imaginary parts of the characteristic impedance (top), field attenuation coefficient (bottom left) and phase microwave phase velocity (bottom right). The period length is 50mm. The absorption section length is 3mm (full lines), 4mm (dashed lines) and 5mm (dotted lines). The intrinsic region width is 2, 3 and 4mm. All other dimensions and all material parameters are default as described earlier in this section. The arrows indicate the direction of increasing intrinsic region width.

Figure 3.4 shows that the overall microwave propagation characteristics of TAP detectors with alternating gain and absorption may be compared to those of a capacitively-loaded transmission line. This capacitive load is introduced by the presence of the semiconductor material under the signal-carrying electrode in the

absorption region. The effect of this capacitive load increases, as seen in figure 3.4, with both the length and the width of the absorption region. It manifests itself in a reduction of the characteristic impedance and propagation velocity, and an increase in the propagation loss, as the surface of the “load capacitor” (intrinsic absorption region) grows.

It is noteworthy that both velocity matching to the optical propagation and impedance matching to 50Ω are simultaneously possible. This occurs for an intrinsic region width of $\sim 2\mu\text{m}$, and an absorption section length of $3\text{-}4\mu\text{m}$. In chapter 2, this range of absorption section lengths was argued to provide also cancellation between gain and absorption for realistic values of the amplification section gain. These three conditions may therefore be met at the same time, providing optimum device performance, both DC and high-speed. This advantage of TAP detectors with alternating gain and absorption was first presented in [10], while the simulation method for the microwave propagation characteristics of these devices was first discussed in detail in [11].

One additional degree of freedom in the design that helps meet the three conditions simultaneously is the thickness of the intrinsic region. Figure 3.5 shows how changes in this parameter affect the microwave propagation characteristics.

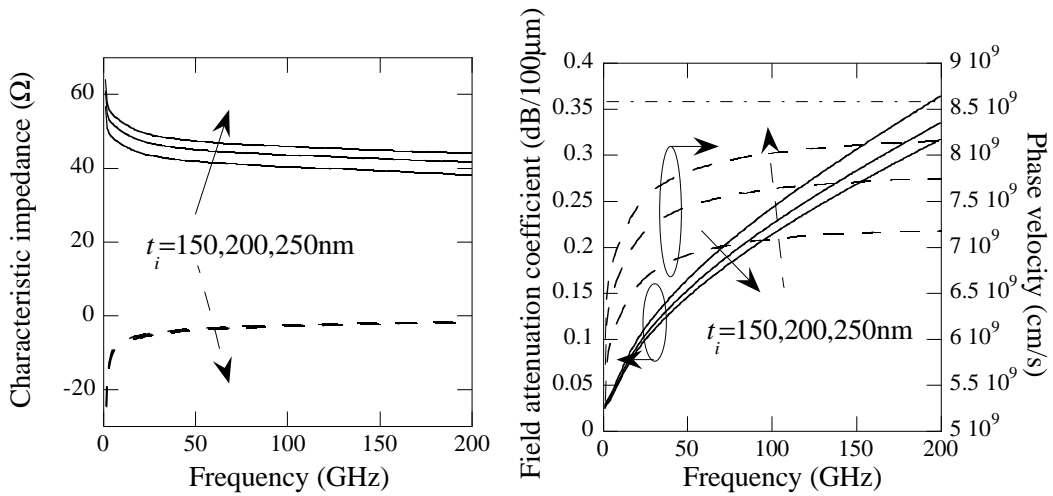


Figure 3.5: Simulated microwave propagation characteristics in TAP detectors with alternating gain and absorption, for different values of the intrinsic region thickness: left: real part (full lines) and imaginary part (dashed lines) of the characteristic impedance; right: field attenuation coefficient (full lines) and phase velocity (dashed lines). The period length is 50mm, the absorption section is 4mm long and the intrinsic active region 3mm wide. All other values are default, producing for an intrinsic region thickness of 200nm the results shown in figure 3.4. The optical phase velocity (horizontal dash-dotted line) is shown in the microwave phase velocity graph for comparison. The full and dashed line arrows indicate the direction of increasing intrinsic thickness for the full and dashed line plots, respectively.

Comparing figures 3.4-3.5 shows that increasing the active region thickness in the absorption region (increasing the “load capacitor” thickness) has a similar effect in the microwave propagation characteristics as decreasing the absorption section length in each period. However, the former results in an increase in the confinement factor in the absorption region, thus reducing the net gain per period, while the latter decreases the absorption suffered by the signal in each period, increasing the net gain per period. Therefore, the net gain per period may be tailored while leaving the microwave propagation characteristics unchanged, or *vice versa*.

The microwave propagation characteristics of TAP detectors with alternating gain and absorption have been modeled and discussed. It has been shown that

simultaneous velocity matching and impedance matching to 50Ω is possible in these devices, occurring for values of the absorption section length that result in cancellation between gain and absorption in each period for realistic values of the material gain in the amplification section. Furthermore, the active region thickness in the absorption region allows us to independently vary the microwave propagation characteristics and the net gain per period. This is a very important advantage of TAP detectors with alternating gain and absorption, since their DC and high-speed behavior may be optimized simultaneously.

In the next paragraph, the microwave propagation characteristics of TAP detectors with vertical coupling will be explored.

Microwave propagation in TAP detectors with vertical coupling

In this paragraph, the microwave propagation characteristics of TAP detectors with vertical coupling will be simulated and discussed. Figure 3.6 shows a schematic cross-section of a TAP detector with vertical coupling, together with the equivalent circuit describing the microwave propagation in this device.

The transverse impedance associated to the claddings is divided into two parts, in parallel with one another, to describe the two possible paths of the current from the detector to ground. Z_n accounts for the lateral conduction path through the n-type cladding, whereas Z_p describes the effect of vertical conduction through the n-type

cladding and the amplifier active region, followed by lateral conduction through the p-type doped sublayer.

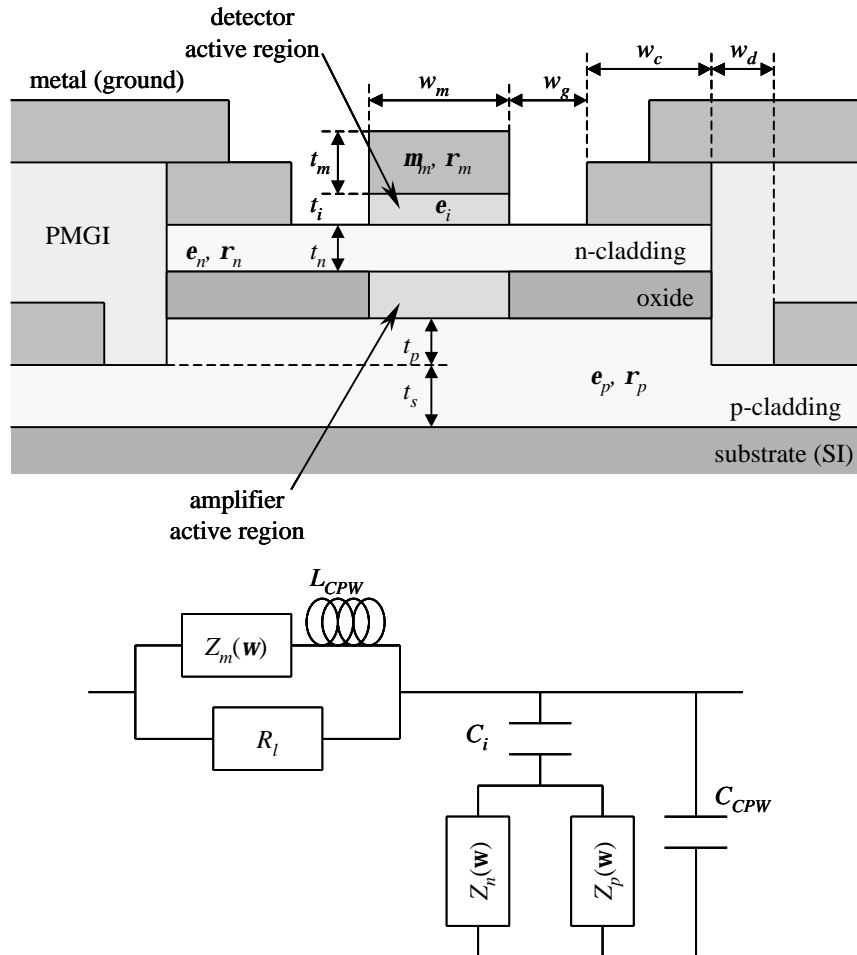


Figure 3.6: Schematic cross-section of a TAP detector with vertical coupling (top) and equivalent circuit model for microwave propagation (bottom). The cross-section is taken on a plane perpendicular to the direction of propagation of light. The dimensions of the different regions are indicated, as well as their relevant material properties (resistivity and permittivity). The equivalent circuit features the different parameters describing the behavior of high-speed optoelectronic devices under a slow-wave regime.

Note that, in the case of Z_p , the width for vertical conduction has been identified with the detector width w_m , defined by its top metal contact, but no impedance has

been associated to the amplifier intrinsic region, since the differential resistance of a forward-biased diode is very small, while the oxide behaves as a perfect insulator.

The metal impedance $Z_m(\mathbf{w})$, the capacitance C_{CPW} and inductance L_{CPW} associated to the CPW and the capacitance of the intrinsic absorption region C_i are given by equations (3.14), (3.15), (3.16) and (3.23), respectively. The rest of the elements need to be described as follows:

$$\frac{1}{R_l} = \frac{w_r t_n}{3r_n} + \frac{w_r t_p}{3r_p} + \frac{(w_r + 2w_d + 2w_{tp})t_s}{3r_s} \quad (3.30),$$

$$Z_n(\mathbf{w}) = \frac{1}{2t_n} \frac{r_n}{1 + j\mathbf{w}r_n \mathbf{e}_n} \left(\frac{w_m}{6} + w_g + w_m \right) \quad (3.31),$$

$$Z_p(\mathbf{w}) = \frac{r_n t_n}{w_m (1 + j\mathbf{w}r_n \mathbf{e}_n)} + \frac{r_p t_p}{w_m (1 + j\mathbf{w}r_p \mathbf{e}_p)} + \frac{1}{2t_s} \frac{r_s}{1 + j\mathbf{w}r_s \mathbf{e}_s} \left(\frac{w_m}{6} + w_g + w_c + w_d + w_{tp} \right) \quad (3.32),$$

where $w_r = w_m + 2w_g + 2w_c$ is the ridge width, and w_m and w_{tp} are the n- and p-contact transfer lengths, defined as in (3.27). In (3.30)-(3.32), note that thickness and width are exchanged for the layers where the conduction is lateral rather than vertical. Factors of 2 have been introduced to take into account the device symmetry, whereas factors of 3 are used to describe the effect of non-uniform spatial current distribution.

The default values for width, thickness, resistivity and permittivity used in the simulation of the microwave propagation characteristics in TAP detectors with vertical coupling correspond to device geometry and material properties of fabricated

TAP detectors with vertical coupling that produced experimentally and external quantum efficiency in excess of 200% [12]. The epitaxial structure used in these devices will be described in more detail in chapter 6. The signal electrode width and thickness are respectively $w_m=3\mu\text{m}$, $t_m=1.5\mu\text{m}$, while its resistivity is assumed to be $r_m=2.3\cdot 10^{-6}\Omega\text{cm}$ (corresponding to gold). Note that the width of the signal electrode is also the width of the detection region. The intrinsic absorption region is $t_i=300\text{nm}$ thick, while its relative permittivity is $\epsilon_i=13.2$ (corresponding to GaAs). All other permittivities are taken as for $\text{Al}_{0.2}\text{Ga}_{0.8}\text{As}$, i.e., $\epsilon_n=\epsilon_p=\epsilon_s=12.5$. The gap between signal and ground electrodes, the width of the contact to the n-type cladding and the distance between the ridge and the contact to the p-type cladding are $w_g=w_c=w_d=2\mu\text{m}$. The thickness of the n-type cladding, p-type cladding and p-doped conductive sublayer is $t_n=700\text{nm}$, $t_p=300\text{nm}$, $t_s=400\text{nm}$, while their resistivity is $r_n=0.005\Omega\text{cm}$, $r_p=0.05\Omega\text{cm}$, $r_s=0.01\Omega\text{cm}$, respectively. The lower resistivity of the p-doped sublayer with respect to the p-type cladding is a consequence of a design incorporating lower doping close to the gain active region, in order to avoid free-carrier absorption. Finally, the characteristic resistances of the contacts to the n- and p-doped claddings are respectively $r_{cn}=10^{-6}\Omega\text{cm}^2$ and $r_{cp}=5\cdot 10^{-6}\Omega\text{cm}^2$. Results obtained for these parameter values, while letting the absorption region width vary from 2 to $4\mu\text{m}$, are shown in figure 3.7.

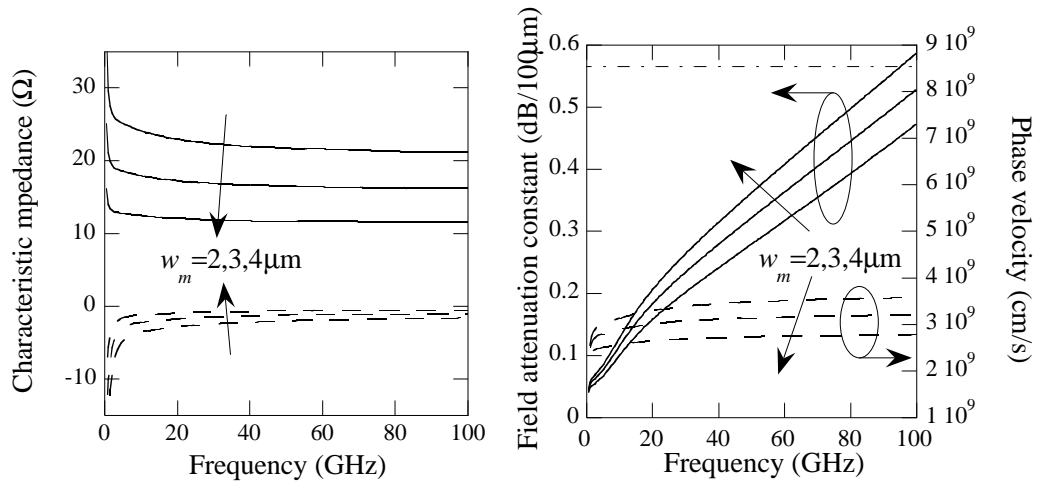


Figure 3.7: Microwave propagation characteristics in TAP detectors with vertical coupling, for different values of the intrinsic region width (equal to the signal electrode width w_m): left: real part (full lines) and imaginary part (dashed lines) of the characteristic impedance; right: field attenuation coefficient (full lines) and phase velocity (dashed lines). All other parameters take their default values as detailed earlier in this section. The optical phase velocity (horizontal dash-dotted line) is shown in the microwave phase velocity graph for comparison. The arrows indicate the direction of increasing intrinsic.

Unlike in the case of TAP detectors with vertical coupling, it is clear from figure 3.7 that, for realistic dimensions and material properties, velocity and impedance matching are not easily achieved in TAP detectors with vertical coupling. Furthermore, comparing 3.4 and 3.7 allows us to conclude that the attenuation per unit length will be much larger in the case of TAP detectors with vertical coupling. This is a direct consequence of the uninterrupted interaction of the electrical waveguide with the doped semiconductor layers in TAP detectors with vertical coupling.

The microwave propagation characteristics of TAP detectors with alternating gain and absorption and with vertical coupling have thus been modeled in this section. TAP detectors with alternating gain and absorption present lower propagation loss

than TAP detectors with vertical coupling. The former allow also for simultaneous velocity and impedance matching. This is not easily achieved in the latter.

In the next section, a distributed photocurrent model will be used to model the frequency response of TAP detectors, based on the microwave propagation characteristics presented in this section.

Distributed photocurrent model

In this section, the distributed photocurrent model used in the analysis of the bandwidth of TAP detectors will be introduced. The frequency response of traveling-wave detectors in general needs to be calculated by using a distributed photocurrent model, where the device is divided into small segments of length dz along the direction of propagation of light. Each segment will produce a certain amount of current, which then will propagate along the device traveling-wave electrodes with a certain velocity, while suffering microwave attenuation. Upon reaching the input or output end of the device, microwave reflections due to impedance mismatch will occur. The effect of these phenomena in the generated photocurrent needs to be taken into account. This effect will be different for the current generated in each segment, depending on its position along the device, and on the total device length.

Propagation of optical and electrical signals

Let us assume that a traveling-wave detector (with or without optical amplification) is fed with a short pulse of light. As the pulse travels along the device,

photocurrent gets generated. Both the optical signal and the generated current change as they travel, due to the presence of gain, absorption and loss, as well as due to a non-zero travel time. The most common way to express that change is using the propagation coefficient $\mathbf{g}=\mathbf{a}+j\mathbf{b}$, through the following relations:

$$P_{opt}(z) = P_{opt}(0) e^{-\mathbf{g}_{opt}z} = \frac{\mathbf{h}_c P_{in}}{h\mathbf{n}_o} e^{-\mathbf{a}_{opt}z} e^{j\mathbf{b}_{opt}z} \quad (3.33),$$

$$dI_{ph,fwd,out}(z) = dI_{ph,fwd}(z) e^{-\mathbf{g}_{el}(L-z)} \quad (3.34),$$

where both optical and electrical signal are assumed to travel from lower to higher values of z , P_{in} is the power contained in the input optical signal, \mathbf{n}_o its central frequency, \mathbf{h}_c the input optical coupling efficiency, $dI_{ph,fwd}(z)$ denotes the forward-traveling photocurrent generated in a differential element of length dz around position z , $dI_{ph,fwd,out}(z)$ its contribution to the total photocurrent collected at the output, and the device is assumed to extend from $z=0$ to $z=L$. The optical attenuation \mathbf{a}_{opt} is not to be confused with the material absorption in the detection region \mathbf{a} . In TAP detectors, the optical attenuation has the same magnitude as the net modal gain Δg and opposite sign:

$$\mathbf{a}_{opt}(z) = -\Delta g(z) = \Gamma_a(z)\mathbf{a}(z) + l - \Gamma_g(z)g(z) \quad (3.35),$$

where as always Γ_a and Γ_g are the mode confinement factors in the absorption and gain regions, respectively, \mathbf{a} and g are the material absorption and material gain in the detection and amplification regions, respectively, and l is the optical loss. Since the

electrical bandwidth of most optoelectronic devices is very small compared to their optical bandwidth, we may assume that for all frequencies of interest the optical attenuation is constant, and so is the phase velocity $v_{p,opt}$, resulting in

$$\mathbf{b}_{opt}(\mathbf{w}) = \frac{2\mathbf{p}\mathbf{n}_o + \mathbf{w}}{v_{p,opt}} \quad (3.36).$$

The forward-traveling photocurrent that is generated in an element of length dz around position z generates thus a contribution at the device output that may be written as follows:

$$dI_{ph,fwd,out}(z) = \frac{1}{2} \frac{q}{\hbar\mathbf{m}} P_{opt}(0) e^{-\mathbf{g}_{el}L} \Gamma_a(z) \mathbf{a}(z) e^{(\mathbf{g}_{el} - \mathbf{g}_{opt})z} dz \quad (3.37),$$

where the photocurrent generated at a certain position is assumed to be divided equally between forward- and backward-propagating contributions.

The backward-propagating photocurrent generated in the same interval, assuming a perfect electrical reflection created by a perfect open circuit at the device input (i.e., at $z=0$), will generate a contribution $dI_{ph,bck,out}(z)$ at the device output that may be written as:

$$dI_{ph,bck,out}(z) = \frac{1}{2} \frac{q}{\hbar\mathbf{m}} P_{opt}(0) e^{-\mathbf{g}_{el}L} \Gamma_a(z) \mathbf{a}(z) e^{-(\mathbf{g}_{el} + \mathbf{g}_{opt})z} dz \quad (3.38).$$

Integrating (3.37) and (3.38) over the device length, and adding both contributions, we find the output photocurrent in the case where no reflections exist at the device output. Note that the previous equations take into account both electrical propagation loss (through \mathbf{g}_{el}) and velocity mismatch between forward- and

backward-propagating electrical and optical waves (through the exponent $g_{el}-g_{opt}$ in (3.37)). The total frequency-dependent photocurrent for a device of length L may then be written in the following form:

$$I_{ph}(\omega) = \frac{q}{hm_o} \frac{\hbar_c P_{in}}{2} \mathbf{r}(\omega) e^{-g_{el}(\omega)L} \int_0^L \Gamma_a(z) \mathbf{a}(z) e^{(g_{el}(\omega)-g_{opt}(\omega))z} dz + \frac{q}{hm_o} \frac{\hbar_c P_{in}}{2} \mathbf{r}(\omega) e^{-g_{el}(\omega)L} \int_0^L \Gamma_a(z) \mathbf{a}(z) e^{-(g_{el}(\omega)+g_{opt}(\omega))z} dz \quad (3.39).$$

The factor $\mathbf{r}(\omega)$ is introduced to model the effect of a possible impedance mismatch between the load and the device, resulting in multiple reflections as shown schematically in figure 3.8.

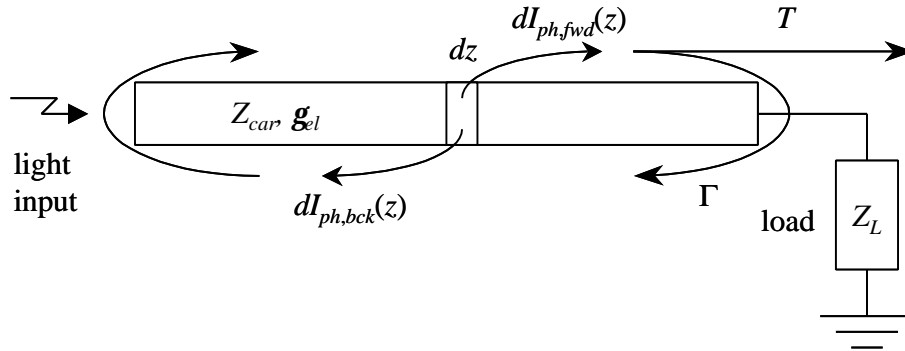


Figure 3.8: Propagation of the generated photocurrent in a generic traveling-wave detector. The microwave propagation velocity and loss are taken into account through the propagation coefficient g_{el} . A perfect open circuit is assumed at the device input. The mismatch between the load impedance Z_L and the characteristic impedance of the line Z_{car} causes a fraction T of the electrical current to be transmitted, and a fraction Γ to be reflected at the device output. The effect of all these phenomena is calculated for the photocurrent generated in an element of differential length dz . Both forward- and backward-propagating contributions (denoted respectively by $dI_{ph,fwd}(z)$ and $dI_{ph,bck}(z)$) from all such elements are added to find the frequency response of the detector.

Forward-traveling photocurrent will arrive at the device output without suffering any reflection. Backward-propagating photocurrent will arrive at the same position

after suffering a total reflection at the device input. These two contributions will then be partially collected, with a frequency-dependent transmission coefficient T . The reflected photocurrent will then travel an entire roundtrip around the device, reflecting at the input, until arriving again at the output, where partial transmission and reflection will occur again, and so and so forth. The result of these successive transmissions and reflections may be expressed indeed by a factor $\mathbf{r}(\mathbf{w})$, which is equal to the sum of an infinite geometric progression:

$$\begin{aligned} \mathbf{r}(\mathbf{w}) &= T + Te^{-2\mathbf{g}_{el}L}\Gamma + Te^{-4\mathbf{g}_{el}L}\Gamma^2 + \dots = \lim_{n \rightarrow \infty} \frac{1 - (\Gamma e^{-2\mathbf{g}_{el}L})^{n+1}}{1 - \Gamma e^{-2\mathbf{g}_{el}L}} \\ &= \frac{T(\mathbf{w})}{1 - \Gamma(\mathbf{w})e^{-2\mathbf{g}_{el}(\mathbf{w})L}} \end{aligned} \quad (3.40).$$

The n -th term in this geometric progression (T being the 0-th) accounts for the photocurrent that exits the device after n complete roundtrips in the electrical waveguide, i.e., after n reflections at the output before finally being collected. It has been assumed that the real part of \mathbf{g}_{el} is positive, i.e., the electrical waveguide is lossy. This is true in most conventional traveling-wave devices. As shown in appendix B, the frequency-dependent current transmission and reflection coefficients at the device output, denoted by T and Γ respectively, are defined as

$$T = \frac{2Z_{car}}{Z_L + Z_{car}} \quad (3.41),$$

$$\Gamma = \frac{Z_L - Z_{car}}{Z_L + Z_{car}} \quad (3.42).$$

Z_L is typically, although not necessarily, equal to 50Ω , but the characteristic impedance of the electrical waveguide is, in general frequency-dependent.

The combination of equation (3.39) with the multiplication factor (3.40) provides a good description of the effect of the propagation of the optical and electrical signals in a traveling-wave detector, taking into account, as mentioned during this paragraph, the microwave propagation loss, the velocity mismatch between the optical and electrical signals, the impedance mismatch between the device and the load, and the presence of forward- and backward-propagating electrical signals. Once the frequency-dependent photocurrent has been thus calculated, dividing it by the input optical power would produce the transfer function $H(\mathbf{w})$ of the device. The 3dB-bandwidth is found as the frequency for which the magnitude squared of the transfer function (expressed as electrons of photocurrent generated by each photon in the input signal) falls below half the value of the external quantum efficiency squared. We may therefore define a normalized transfer function $H_n(\mathbf{w})$, as

$$\begin{aligned}
H_n(\mathbf{w}) &= \frac{h\mathbf{m}}{q\mathbf{h}_{ext}} \frac{I_{ph}(\mathbf{w})}{P_{in}} \\
&= \frac{\mathbf{h}_c}{2\mathbf{h}_{ext}} \frac{T}{1-\Gamma e^{-2\mathbf{g}_{el}L}} e^{-\mathbf{g}_{el}L} \int_0^L \Gamma_a(z) \mathbf{a}(z) e^{(\mathbf{g}_{el}-\mathbf{g}_{opt})z} dz \\
&\quad + \frac{\mathbf{h}_c}{2\mathbf{h}_{ext}} \frac{T}{1-\Gamma e^{-2\mathbf{g}_{el}L}} e^{-\mathbf{g}_{el}L} \int_0^L \Gamma_a(z) \mathbf{a}(z) e^{-(\mathbf{g}_{el}+\mathbf{g}_{opt})z} dz
\end{aligned} \tag{3.43}$$

The frequency-dependence of \mathbf{g}_{el} , \mathbf{g}_{opt} , T and Γ is not explicitly shown for simplicity in the notation. The device 3dB-bandwidth (or simply bandwidth) f_{3dB} is

thus given by the frequency value for which the magnitude squared of the normalized transfer function falls to one half:

$$\left|H_n(2p f_{3dB})\right|^2 = \frac{1}{2} \quad (3.44).$$

In the next paragraphs, the microwave propagation characteristics described in the previous section will be used to model the frequency response of TAP detectors and calculate their bandwidth.

Frequency response of TAP detectors with alternating amplification and absorption

In this paragraph, the frequency response of TAP detectors with alternating gain and absorption will be modeled and discussed, by applying the distributed photocurrent model to this particular case.

Integrating (3.37) and (3.38) over the n -th absorption section (out of a total of N), and denoting the net gain per period by ΔG and the efficiency of each absorption region by $\mathbf{h}^{(1)}$, we find the contribution from this section to the total forward- and backward-traveling photocurrent collected at the output:

$$\Delta I_{ph, fwd, out}(n) = \frac{1}{2} \mathbf{h}_c \mathbf{h}^{(1)} \frac{q}{h\nu} P_{in} e^{-\mathbf{g}_{el}(N-1)l_{per}} \Delta G^{n-1} e^{(\mathbf{g}_{el} - j\mathbf{b}_{opt})(n-1)l_{per}} \quad (3.45),$$

$$\Delta I_{ph, bck, out}(n) = \frac{1}{2} \mathbf{h}_c \mathbf{h}^{(1)} \frac{q}{h\nu} P_{in} e^{-\mathbf{g}_{el}(N-1)l_{per}} \Delta G^{n-1} e^{-(\mathbf{g}_{el} + j\mathbf{b}_{opt})(n-1)l_{per}} \quad (3.46).$$

The normalized transfer function may therefore be found by adding respectively (3.45) and (3.46), for $n=1, \dots, N$, subsequently multiplying their sum by the coefficient

describing the effect of multiple roundtrips, $\mathbf{r}(\mathbf{w})$, and dividing the result by the input optical power and the external quantum efficiency:

$$H_n(\mathbf{w}) = \frac{\mathbf{h}_c \mathbf{h}^{(1)}}{2\mathbf{h}_{ext}} \mathbf{r}(\mathbf{w}) e^{-\mathbf{g}_{el}(N-1)l_{per}} \left[\frac{\Delta G^N e^{(\mathbf{g}_{el} - j\mathbf{b}_{opt})Nl_{per}} - 1}{\Delta G e^{(\mathbf{g}_{el} - j\mathbf{b}_{opt})l_{per}} - 1} + \frac{\Delta G^N e^{-(\mathbf{g}_{el} + j\mathbf{b}_{opt})Nl_{per}} - 1}{\Delta G e^{-(\mathbf{g}_{el} + j\mathbf{b}_{opt})l_{per}} - 1} \right] \quad (3.47).$$

Using the microwave propagation characteristics found in the previous section, the frequency response of TAP detectors with alternating gain and absorption was calculated. The effect of the number of periods and net gain per unit length in this bandwidth was explored. In all simulated results presented in the rest of this section, the absorption section length is $4\mu\text{m}$ long, and the absorption active region is $3\mu\text{m}$ wide. Consistently with the values used in chapter 2 for the calculation of the DC characteristics of these devices, the coupling efficiency is assumed to be 50%, the confinement factor in the absorption region 40% and the material absorption 9000cm^{-1} . Figure 3.9 shows the magnitude squared of the normalized transfer function for different values of the number of periods and the net gain per unit length.

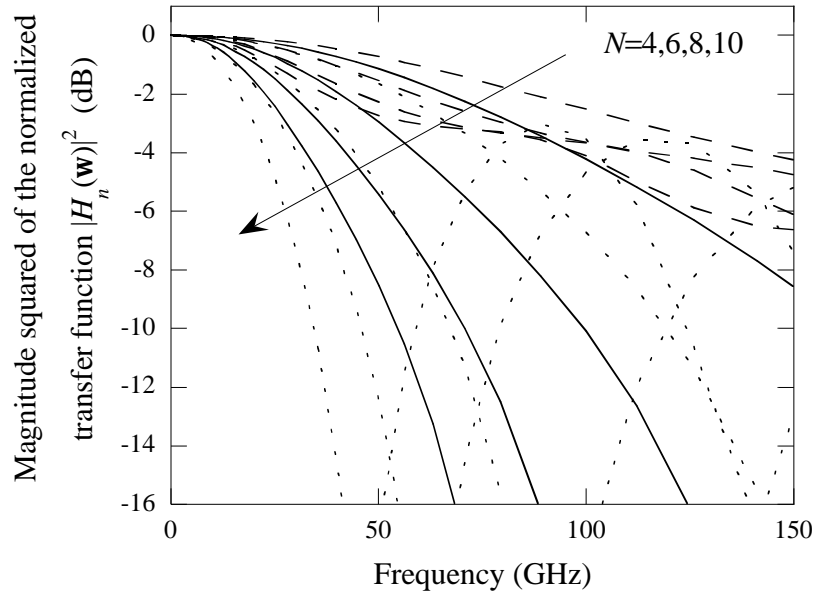


Figure 3.9: Simulated magnitude squared of the normalized transfer function of TAP detectors with alternating gain and absorption, for different values of the number of periods N . The net gain per period DG is 1 (full lines), 0.5 (dashed lines) and 2 (dotted lines). The absorption section length is 4mm long, and the width of the active region is 3mm. The microwave propagation characteristics for this device are found in figures 3.4. The termination at the output is 50W. The arrow indicates the direction of increasing number of periods.

Two main mechanisms contribute to limit the bandwidth. One of them is the microwave attenuation. The other one is the phase difference between the forward- and backward-traveling photocurrent contributions, added at the device output. As the frequency increases, both components add in phase (for very low frequencies), then in opposition (creating a dip in the frequency response), again in phase, and so and so forth. The evolution of this phase difference as a function of the frequency is accelerated by an increase in the device length, i.e., in the number of periods. Furthermore, an increase in the net gain per unit length causes most of the photocurrent to be generated close to the output of the device. The relative path

length difference between both components is thus increased for larger values of the net gain per unit length, contributing to a faster decay in the frequency response. These effects clearly show in figure 3.9, through the different dips and secondary peaks in the frequency response. The envelope of all the secondary peaks corresponds to the loss-limited response when the phase delay between the different photocurrent contributions is ignored.

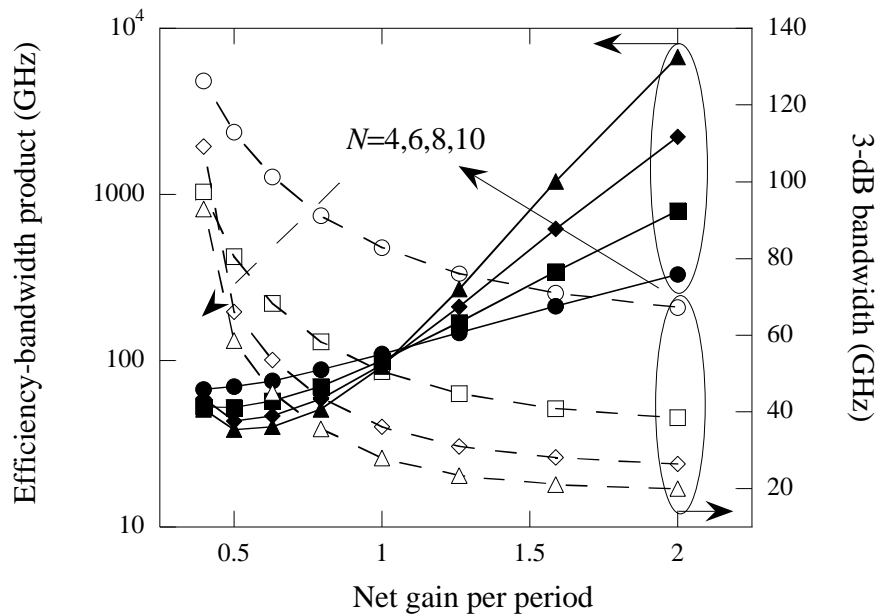


Figure 3.10: Simulated efficiency-bandwidth product (full lines, solid symbols) and bandwidth (dashed lines, empty symbols) of TAP detectors with alternating gain and absorption as a function of the net gain per period DG for different values of the number of periods N . The absorption section is 4mm long, and the width of the active region is 3mm. The input coupling efficiency is assumed to be 50%, the confinement factor in the absorption region 40% and the material absorption 9000cm^{-1} . The microwave propagation characteristics for this device are found in figure 3.4. The full and dashed line arrows indicate the direction of increasing number of periods for the full and dashed plots, respectively.

As mentioned in chapter 1, the efficiency-bandwidth product is an important figure of merit for photodetectors in general. This figure of merit is shown in figure

3.10, together with the device bandwidth, as a function of the net gain per period and for different number of periods.

Even in the absence of an initial amplification region, efficiency bandwidth products in the order of 1THz are possible in TAP detectors with alternating gain and absorption. As expected from figure 3.9, the bandwidth decreases with the number of periods and the net gain per period. However, the efficiency bandwidth product increases with these two parameters except for small values of the net gain per period, i.e., an increase in the net gain per period results in the efficiency growing by a factor larger than the factor by which the bandwidth decreases. For very small values of the net gain per unit length, most of the photocurrent is generated close to the device input, reducing the effect of the addition out of phase of the forward- and backward-propagating photocurrent components. As the net gain per period increases, this effect becomes more important, since photocurrent is generated now along the entire device.

Note also that the 3-dB bandwidth remains over 40GHz for 6 periods or less. Finally, it is also interesting to realize that the bandwidth efficiency product is very similar for all different values of the number of periods when the net gain per unit length is close to 1. This is due to the fact that, in that particular case, the efficiency grows approximately linearly with the number of periods, while the bandwidth is inversely proportional to the device length.

The bandwidth limit may be increased by terminating the device at input and output by 50Ω loads, and subsequently adding the currents collected at both ends. The device bandwidth may thus be increased without any detriment in the efficiency. The backward-propagating current would in this case suffer a reflection Γ at the input (assumed identical at input and output), while a fraction T is collected. The forward-traveling photocurrent reflected at the output, and the backward-traveling photocurrent reflected at the input would now propagate towards the input and the output, respectively, suffering partial reflection and partial collection, and so and so forth. The coefficient $\mathbf{r}(\mathbf{w})$ that describes the effect of multiple reflections needs therefore to be modified into

$$\mathbf{r}(\mathbf{w}) = T + Te^{-\mathbf{g}_{el}L}\Gamma + T\Gamma^2e^{-2\mathbf{g}_{el}L} + \dots = \frac{T(\mathbf{w})}{1 - \Gamma(\mathbf{w})e^{-\mathbf{g}_{el}(\mathbf{w})L}} \quad (3.48).$$

The total collected photocurrent generated by the n -th section is then found by multiplying this modified roundtrip coefficient by the sum of the forward-traveling photocurrent that arrives to the output $\Delta I_{ph, fwd, out}$ and the backward-traveling photocurrent that arrives to the input, both taken prior to any reflection. The former is expressed in (3.45). The latter, denoted by $\Delta I_{ph, bck, in}$, is written as follows:

$$\Delta I_{ph, bck, out}(n) = \frac{1}{2} \mathbf{h}_c \mathbf{h}^{(1)} \frac{q}{h\nu} P_{in} \Delta G^{n-1} e^{-(\mathbf{g}_{el} + j\mathbf{b}_{opt})(n-1)l_{per}} \quad (3.49).$$

This equation takes into account the propagation of the optical signal from the device input to the n -th detection section, and the propagation of the generated photocurrent back to the device input. Equation (3.49) may be again added for

$n=1,2,\dots,N$ to take into account contributions from all detection sections. Together with the contribution from the forward-traveling photocurrent, we can write the normalized transfer function in the case where both input and output are terminated by the loads of the same value in the following form:

$$\begin{aligned}
H_n(\mathbf{w}) = & \frac{\mathbf{h}_c \mathbf{h}^{(1)}}{2\mathbf{h}_{ext}} \frac{T e^{-\mathbf{g}_{el}(N-1)l_{per}}}{1 - \Gamma e^{-\mathbf{g}_{el}(N-1)l_{per}}} \frac{\Delta G^N e^{(\mathbf{g}_{el} - j\mathbf{b}_{opt})Nl_{per}} - 1}{\Delta G e^{(\mathbf{g}_{el} - j\mathbf{b}_{opt})l_{per}} - 1} \\
& + \frac{\mathbf{h}_c \mathbf{h}^{(1)}}{2\mathbf{h}_{ext}} \frac{T}{1 - \Gamma e^{-\mathbf{g}_{el}(N-1)l_{per}}} \frac{\Delta G^N e^{-(\mathbf{g}_{el} + j\mathbf{b}_{opt})Nl_{per}} - 1}{\Delta G e^{-(\mathbf{g}_{el} + j\mathbf{b}_{opt})l_{per}} - 1}
\end{aligned} \tag{3.50}.$$

The first and second terms in the right hand side of (3.50) describe the contribution from all initially forward-traveling photocurrent and all initially backward-traveling photocurrent, respectively, collected at either input or output, and after any number of reflections. The magnitude squared of this new normalized transfer function is plotted in figure 3.11, for different values of the number of periods and of the net gain per period.

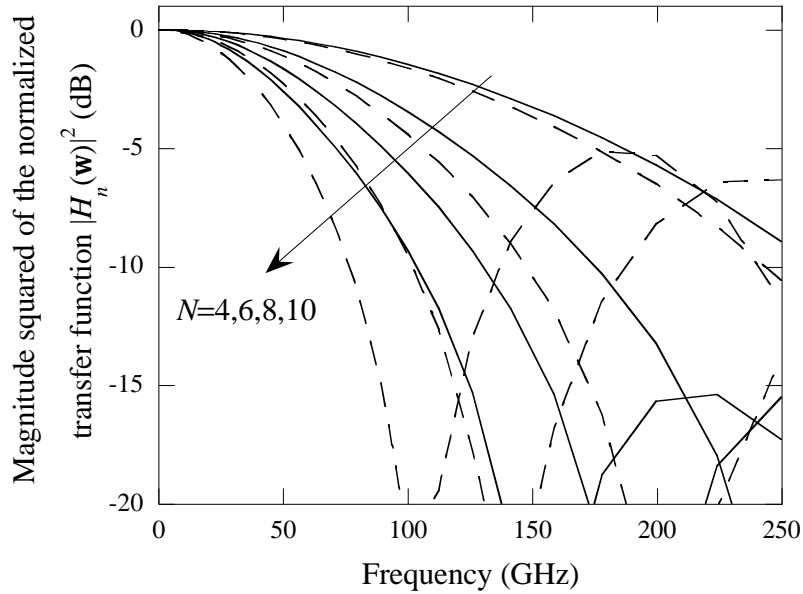


Figure 3.11: Simulated magnitude squared of the normalized transfer function of TAP detectors with alternating gain and absorption terminated at input and output, for different values of the number of periods N and of the net gain per period. Both terminations are 50W. The net gain per period DG is 1 (full lines), 0.5 (dashed lines) and 2 (dotted lines). The absorption section length is 4mm long, and the width of the active region is 3mm. The microwave propagation characteristics for this device are found in figure 3.4, and the response with open circuit at the input in figure 3.9.

Note that in this case the plots for values of the net gain per period whose product is one overlap nearly perfectly. This makes perfect sense intuitively if the effect of velocity matching is neglected, since the device being now fully symmetric because of the equal loads at input and output, the same response normalized to the external quantum efficiency is obtained by coupling into the device an optical signal with power P_{in} when the net gain per period is ΔG , and an optical signal with power $\Delta G^{n-1}P_{in}$ when the net gain per period is $1/\Delta G$. The fact that these curves overlap so closely allows us to defend once more that the effect of velocity mismatch in TAP detectors with alternating gain and absorption is negligible.

The dips in the frequency response shown in figure 3.9 have not disappeared indeed, but their effect has been substantially mitigated, the first dip in each curve appearing now at a higher frequency. The fact that they still exist, however, clearly indicates that the phase difference between forward- and backward-propagating photocurrent contributions, whether collected at the input or at the output of the device, is still the major factor limiting the bandwidth, followed by microwave attenuation. It is also interesting to note that even though the peaks shown in figure 3.11 for devices terminated at both ends reach lower values than those shown in figure 3.9 for devices with an open circuit at the input, these peaks actually happen for higher frequencies. The envelope of these peaks, i.e., the loss-limited frequency response without taking into account the relative phase delay of the different photocurrent contributions, would actually be higher than in the previous case. This is due to the fact that the generated photocurrent needs now to propagate for a lower distance inside the device before having the possibility of being collected.

The improvement in the bandwidth without detriment in the efficiency produces higher values of the efficiency-bandwidth product, as evidenced in figure 3.12.

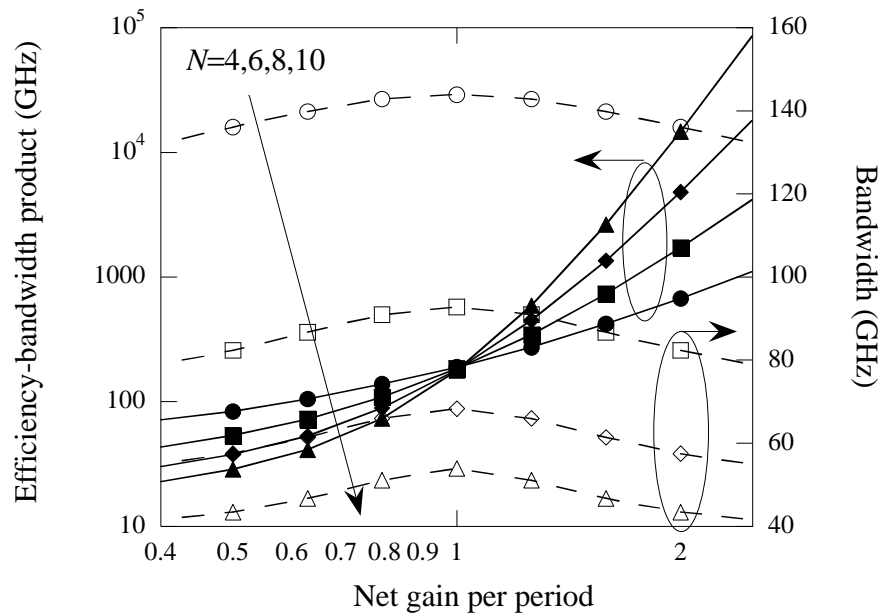


Figure 3.12: Simulated efficiency-bandwidth product (full lines, solid symbols) and bandwidth (dashed lines, empty symbols) of TAP detectors with alternating gain and absorption as a function of the net gain per period DG for different values of the number of periods N . The absorption section is 4mm long, and the width of the active region is 3mm. The input coupling efficiency is assumed to be 50%, the confinement factor in the absorption region 40% and the material absorption 9000cm^{-1} . The microwave propagation characteristics for this device are found in figures 3.4. The efficiency-bandwidth product for these devices with an open circuit termination at the input are shown in figure 3.10.

In figure 3.12, the net gain per period has been plotted in a logarithmic scale. This shows that the spatial symmetry of the device, now that both input and output are terminated, produces the same bandwidth for any two values of the net gain per period whose product is one. As argued earlier, this is compelling evidence that velocity mismatch is not an important factor in the device bandwidth. The optimum bandwidth is obtained when gain and absorption exactly cancel out in each period. Again, this is clear evidence that the main limiting effect is once more the phase difference between the different contributions to the total photocurrent. This phase

difference is indeed larger for the contributions generated at either end of the device, and shows its effect more importantly when either optical absorption or gain dominate. These situations are equivalent to a device featuring one single photocurrent source, located respectively at the input or at the output of the device. Neglecting the effect of reflections at input and output because of impedance mismatch, the total photocurrent would then be the sum of two contributions, one collected close to the source, one collected after having traveled half a roundtrip along the device.

Another aspect of great interest shown in figure 3.12 is that efficiency-bandwidth products as high as 1THz are possible with devices featuring 6 periods, and a net gain per period under 2. Since the first section in the device provides absorption, and due to the 50% input coupling efficiency, this situation is thus obtained for a peak power in the device in the order of 10 times higher than the input optical power. With an initial amplification section, 10THz efficiency-bandwidth products may be reached with input optical powers about 100 times larger than the input optical power. This is not unreasonable for input signals in the order of $1\mu\text{W}$. The penalty to pay for these advantages is a higher device complexity.

Finally, and before making the concluding remarks for this paragraph, note that the device characteristics chosen for the simulation of the efficiency-bandwidth product (intrinsic region width of $3\mu\text{m}$, absorption section length of $4\mu\text{m}$) are not those that provide either optimum impedance and velocity matching, or lowest propagation loss, but rather an average of the ensemble considered in figures 3.4.

They are, however, those most realistically promising to achieve the compensation between gain and absorption in each period for a significant efficiency of each detection section.

In summary, the bandwidth of TAP detectors with alternating gain and absorption has been modeled and discussed. It has been shown that the main two factors limiting the bandwidth in these devices are the relative phase difference between the photocurrent contributions collected at different points of the device, either forward or backward traveling, and the microwave propagation loss. Terminating the device at both ends with 50Ω loads is shown to be an important technique that may be used to increase substantially (double) the bandwidth. Collecting the photocurrent at both ends achieves this goal with no penalty to the external quantum efficiency of the device. The microwave propagation characteristics of these devices (velocity and impedance matching, low attenuation) result in bandwidths in excess of 40GHz for up to 6 periods when the input is open, and close to 100GHz when both ends are terminated. When the net gain per period is close to one, the efficiency bandwidth product is very similar for devices with different numbers of periods, and may be expected to be in the 80-100GHz range for devices with open input, 150-200GHz range for devices terminated at input and output. Efficiency-bandwidth products in excess of 1THz are realistically possible, even in the absence of an initial amplification region.

In the next paragraph, the frequency response of TAP detectors with vertical coupling will be modeled and discussed.

Frequency response of TAP detectors with vertical coupling

The frequency-dependent photocurrent generated in TAP detectors with vertical coupling may be found, under the assumption that the net gain per unit length is position-independent, by simple direct integration of (3.39):

$$I_{ph}(\mathbf{w}) = \frac{q}{hm_o} \frac{\mathbf{h}_c \Gamma_a \mathbf{a} P_{in}}{2} \frac{T e^{-\mathbf{g}_{el} L}}{1 - \Gamma e^{-2\mathbf{g}_{el} L}} \left[\frac{e^{(\mathbf{g}_{el} - \mathbf{g}_{opt})L} - 1}{\mathbf{g}_{el} - \mathbf{g}_{opt}} + \frac{1 - e^{-(\mathbf{g}_{el} + \mathbf{g}_{opt})L}}{\mathbf{g}_{el} + \mathbf{g}_{opt}} \right] \quad (3.51).$$

The normalized transfer function may then be found as outlined earlier in this section:

$$H_n(\mathbf{w}) = \frac{1}{2} \frac{T e^{-\mathbf{g}_{el} L}}{1 - \Gamma e^{-2\mathbf{g}_{el} L}} \frac{\Delta g}{e^{\Delta g L} - 1} \left[\frac{e^{\Delta g L} e^{(\mathbf{g}_{el} - j\mathbf{b}_{opt})L} - 1}{\Delta g + (\mathbf{g}_{el} - j\mathbf{b}_{opt})} + \frac{e^{\Delta g L} e^{-(\mathbf{g}_{el} + j\mathbf{b}_{opt})L} - 1}{\Delta g - (\mathbf{g}_{el} + j\mathbf{b}_{opt})} \right] \quad (3.52),$$

where Δg is, as always in these devices, the net gain per unit length. For the microwave propagation characteristics plotted in figure 3.7, and specifically for an absorption region width of $3\mu\text{m}$, this results in the simulated normalized transfer function plotted in figure 3.13.

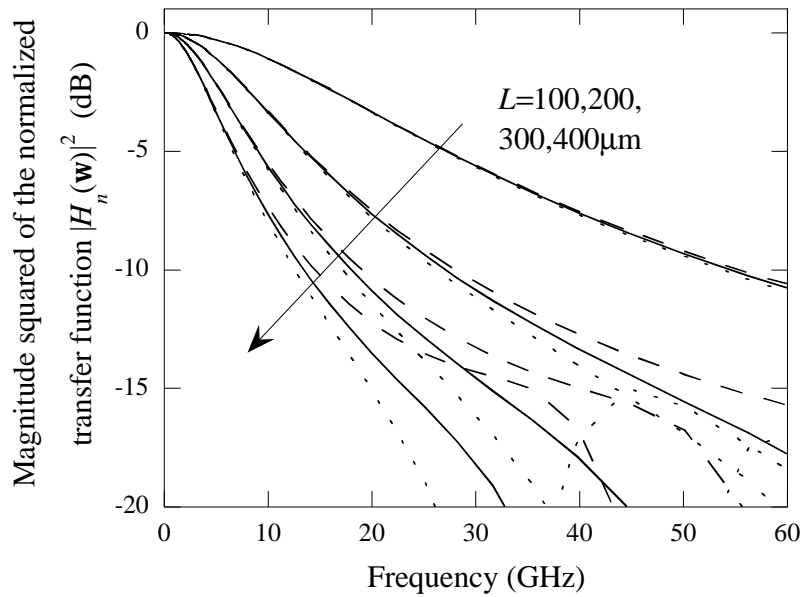


Figure 3.13: Simulated magnitude squared of the normalized transfer function of TAP detectors with vertical coupling, for different values of the device length L and of the net gain per unit length Dg . The simulated microwave propagation characteristics for this device are found in figure 3.8, the absorption region width being 3mm. The net gain per unit length is 0 (full lines) - 20cm^{-1} (dashed lines) and 20cm^{-1} (dotted lines).

We may see in figure 3.13 the same type of dips and peaks in the frequency response that appeared in figure 3.11 for TAP detectors with alternating gain and absorption. We may assume therefore that they are one again created by the phase difference between photocurrent contributions generated at different positions along the device, and that travel in opposite directions. However, these dips and valleys happen beyond the 3dB-bandwidth of the device, i.e., this effect has little importance for TAP detectors with vertical coupling. This is further evidenced by the 3dB-bandwidth being the same for devices with the same length, despite the different spatial distribution of the photocurrent generation, which is caused by the change in the net gain per period. In other words, the device bandwidth depends almost solely

on its length, and not on where the photocurrent is generated. Together with the simulated microwave propagation characteristics plotted in figure 3.7, this allows us to conclude that the chief factors limiting the frequency performance of TAP detectors with vertical coupling are the microwave attenuation and the impedance mismatch. In other words, the combination of a strong reflection at the output and heavy attenuation during subsequent roundtrip propagations dominate over any other effect.

The simulated efficiency-bandwidth product for these devices is shown in figure 3.14.

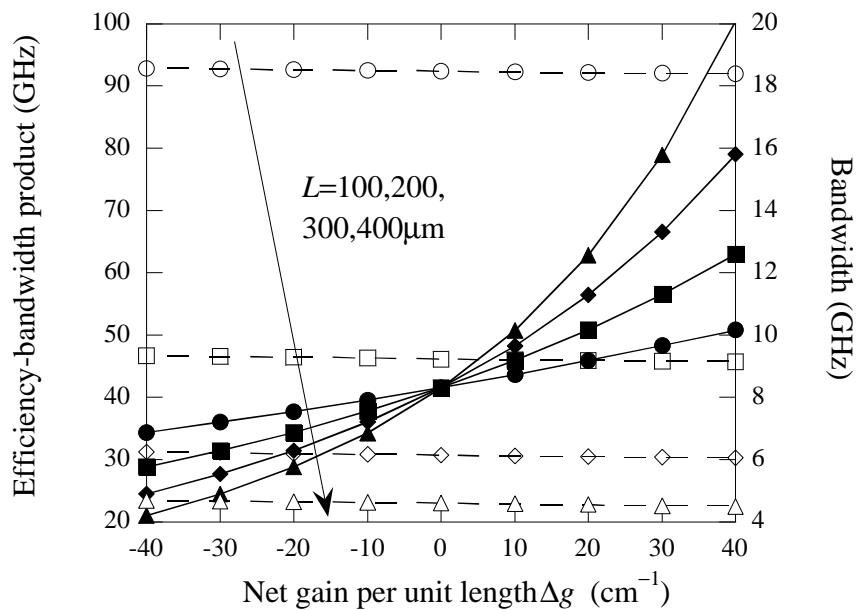


Figure 3.14: Simulated efficiency-bandwidth product (full lines, solid symbols) and bandwidth (dashed lines, empty symbols) of TAP detectors with vertical coupling as a function of the net gain per unit length Δg for different values of the device length L . The absorption region is 3mm wide. The input coupling efficiency is assumed to be 50%, the confinement factor in the absorption region 5% and the material absorption 9000cm^{-1} . The simulated microwave propagation characteristics for this device are found in figure 3.7.

As predicted in figure 3.13, the bandwidth of TAP detectors with vertical coupling barely depends on the net gain per unit length, being inversely proportional to the device length. This causes once more the efficiency bandwidth product to be very similar for different device lengths when gain and absorption are close to cancellation. Due to the larger attenuation than in their counterparts with alternating gain and absorption, bandwidths higher than 20GHz are possible only for short TAP detectors with vertical coupling ($<100\mu\text{m}$). Bandwidth-efficiency products in excess of 50GHz without an initial amplification section are however possible, since the bandwidth is barely affected by an increase in the net gain per unit length, whereas the efficiency rapidly grows.

In summary, the frequency response of TAP detectors with vertical coupling has been studied. Due to the uninterrupted interaction between the electrical field and the doped semiconductor layers, these devices feature higher propagation loss and more severe reflections at the device output, resulting in lower bandwidth and efficiency bandwidth product than in the case of TAP detectors with alternating gain and absorption. Nevertheless, efficiency-bandwidth product values above 50GHz are possible in these devices.

Summary

In conclusion, this chapter has discussed the high-speed performance of TAP detectors, through simulation and discussion. It has been argued that the performance

of TAP detectors with alternating gain and absorption will be superior to that of TAP detectors with vertical coupling, since the former may be designed to present velocity and impedance matching, as well as lower propagation loss, while still achieving compensation between gain and absorption. The performance of TAP detectors with alternating gain and absorption is limited mainly by the phase difference between the different photocurrent contributions generated at different absorption sections, microwave loss being a secondary factor. Terminating input and output with 50W loads and adding the current collected at both ends should allow for efficiency-bandwidth products in the range of 1-10THz, with bandwidths in the order of 150-200GHz. High speed performance of TAP detectors with vertical coupling is limited mostly by impedance mismatch and propagation loss in the ensuing roundtrips traveled by the generated photocurrent. Despite the fact that only short (<100mm) devices would present bandwidth in the order of 20GHz, efficiency-bandwidth products in the order of 50GHz should be possible with this configuration.

References

- [1] R.E. Collin, "Foundations for microwave engineering," 2nd edition, *McGraw-Hill*, 1992.
- [2] H. Hasegawa, M. Furukawa, H. Yanai, "Properties of microstrip line on Si-SiO₂ system," *IEEE Transactions on Microwave Theory and Technology*, vol. MTT-19, no. 11, pp. 869-81, 1971.
- [3] Tuncer E., Neikirk D.P., "Highly accurate quasi-static modeling of microstrip lines over lossy substrates," *IEEE Microwave and Guided Wave Letters*, vol. 2, no. 10, pp. 409-11, 1992.
- [4] C.P. Wen, "Coplanar waveguide, a surface strip transmission line suitable for nonreciprocal gyromagnetic device applications," *Proceedings of the IEEE 1969 G-MTT International Microwave Symposium*, pp. 110-5, 1969.
- [5] K.S. Giboney, R.L. Nagarajan, T.E. Reynolds, S.T. Allen, R.P. Mirin, M.J.W. Rodwell, J.E. Bowers, "Travelling-wave photodetectors with 172-GHz bandwidth and 76-GHz bandwidth-efficiency product," *IEEE Photonics Technology Letters*, vol. 7, no. 4, pp. 412-4, 1995.

- [6] Y.J. Chiu, S.B. Fleischer, J.E. Bowers, "Subpicosecond (570 fs) response of p-i-n traveling wave photodetector using low-temperature-grown GaAs," *Technical digest of the International Topical Meeting of Microwave Photonics MWP '97*, pp. 295-7, 1998.
- [7] D. Jager, "Slow-wave propagation along variable Schottky-contact microstrip line (SCML)," *IEEE Transactions on Microwave Theory and Technology*, vol. MTT-25, no. 9, pp. 566-73, 1976.
- [8] L.A. Coldren, S.W. Corzine, "Diode lasers and photonic integrated circuits," *John Wiley & Sons*, 1995.
- [9] K.S. Giboney, "Travelling-wave photodetectors," *University of California, Santa Barbara*, Ph.D. Dissertation, 1995.
- [10] D. Lasaosa, Y.J. Chiu, J. Piprek, J.E. Bowers, "Traveling-wave amplification photodetector (TAP detector)," *Proceedings of the IEEE LEOS Annual Meeting*, vol. 1, pp. 260-1, 2000.
- [11] D. Lasaosa, Y.J. Chiu, J. Piprek, J.E. Bowers, "Modeling of traveling-wave amplification photodetectors (TAP detectors)," *Proceedings of the SPIE Photonics West Conference*, vol. 4283, pp. 528-39, 2001.
- [12] D. Lasaosa, D. Pasquariello, J. Piprek, J.E. Bowers, "Recent advances in photodetectors with distributed optical amplification," *Proceedings of the SPIE-ITCom Symposium*, vol. 5246, 2003.

CHAPTER 4

Noise in the presence of distributed amplification and photodetection

Noise models exist both for semiconductor optical amplifiers (SOAs) and photodiodes. However, to the best of my knowledge, there is no model prior to this work that describes the noise in the presence of distributed amplification and photodetection. In this chapter, the new noise model developed to describe the noise characteristics of TAP detectors will be presented. First, some basic concepts will be reviewed. Next, the characteristics of two well-established noise models, one describing noise in SOAs, another one in photodiodes, will be briefly summarized. The former is based on the photon statistics master equation, the latter on Bernoulli's sampling formula. Then, the new noise model will be introduced. Since a requirement for any new model is that it is consistent with previously well-established models under known circumstances, it will be shown that the new noise model produces the same result as the photon statistics master equation when describing the evolution of the optical noise in an SOA, and the same result than Bernoulli's

sampling formula when applied to photodiodes without optical amplification. This comparison will be discussed in this chapter, though some mathematical proofs are included in appendix C. Finally, the new model will be used to predict a trade-off between efficiency and noise figure that will be studied in more detail in the next chapter.

Review of noise concepts

In this section, some of the basic concepts allowing us to describe the noise for an arbitrary signal will be reviewed. In particular, we will give mathematical descriptions for the average value, the variance and the signal-to-noise ratio (SNR) of a signal, as well as the noise figure (NF) of a device, which quantifies its performance in terms of noise.

Let $x(t)$ be a time-dependent signal. Its average value or expectation value $\langle x \rangle$ is defined by

$$\langle x \rangle = \lim_{T \rightarrow \infty} \frac{1}{T} \int x(t) dt \quad (4.1),$$

where the integral is performed over a time interval of duration T . Let us now assume that $x(t)$ is the superposition of the actual desired signal that carries some information and some random fluctuations. We can assume that the portion of $x(t)$ which carries the information is actually equal to its average value, and write

$$x(t) = \langle x \rangle + \Delta x(t) \quad (4.2),$$

where the expectation value of the fluctuations $\Delta x(t)$ is zero. The average total power P_x can then be written as the expectation value of the signal squared, or

$$P_x = \langle x^2 \rangle = \langle x \rangle^2 + \langle \Delta x^2 \rangle \quad (4.3).$$

We find therefore that the power contained in the noise is given, in average, by

$$\langle \Delta x^2 \rangle = \langle x^2 \rangle - \langle x \rangle^2 = \mathbf{s}_x^2 \quad (4.4).$$

The quantity \mathbf{s}_x^2 is called the variance of the signal $x(t)$, and describes therefore the power contained in the noise associated to it. Its square root, \mathbf{s}_x , is called the standard deviation or root-mean-square (RMS) deviation.

When two or more interdependent signals (let us say, for the sake of the argument, that they are $x(t)$ and $y(t)$) need to be considered, it may be very useful to define their covariance, $\mathbf{s}_{x,y}$, as

$$\mathbf{s}_{x,y} = \langle xy \rangle - \langle x \rangle \langle y \rangle \quad (4.5).$$

If the two signals are statistically independent on one another, their covariance is zero.

The signal quality in terms of noise can be described by the ratio of signal power to noise power, or signal-to-noise ratio (SNR), defined mathematically as

$$\text{SNR} = \frac{\langle x(t) \rangle^2}{\langle \Delta x^2(t) \rangle} = \frac{\langle x \rangle^2}{\mathbf{s}_x^2} \quad (4.6).$$

Let us now consider a given device, which takes an input signal $x_{in}(t)$ and produces, after transmission or processing of some kind, an output signal $x_{out}(t)$. The effect of such a device in the signal quality in terms of noise can be described by the change in the SNR between the input and the output. We define thus the noise figure (NF) of a device as the ratio between input and output SNR:

$$\text{NF} = \frac{\text{SNR}_{in}}{\text{SNR}_{out}} = \frac{\langle x_{in} \rangle^2 \mathbf{S}_{x_{out}}}{\langle x_{out} \rangle^2 \mathbf{S}_{x_{in}}} \quad (4.7).$$

Obviously, the larger SNR, the better signal quality (the fraction of power contained in the noise is small compared to the signal power), and the lower the NF, the less signal degradation the device produces in terms of noise.

Let us consider finally the case of a quantized signal, where the information is carried by a succession of discrete, individual events, such as the arrival of a photon or an electron to the input or the output of a device. In that case, we can define a probability distribution P_n of the event happening n times (such as the arrival of n photons to a certain point in an optical link or the generation of n electrons of photocurrent in a detector) in a given time interval. Given that probability distribution, and assuming that the information is carried by how many times the event happens, the following definitions of average value and variance apply:

$$\langle n \rangle = \sum_{n=0}^{\infty} n P_n \quad (4.8).$$

$$\mathbf{s}_n^2 = \langle n^2 \rangle - \langle n \rangle^2 = \sum_{n=0}^{\infty} n^2 P_n - \left[\sum_{n=0}^{\infty} n P_n \right]^2 \quad (4.9).$$

In general, we may define the expectation value or average value of any function $f(n)$ that depends on the number of event counts:

$$\langle f(n) \rangle = \sum_{n=0}^{\infty} f(n) P_n \quad (4.10).$$

The noise properties of a quantized signal are therefore fully described by the probability distribution P_n . One important set of functions is the set of natural powers of the event count n . Their expectation values constitute the moments of the probability distribution. The N -th moment of the probability distribution is defined as

$$\langle n^N \rangle = \sum_{n=0}^{\infty} n^N P_n \quad (4.11).$$

One of the important properties of the moments of a probability distribution is that the set of all moments, where N takes all positive integer values, unequivocally determines the probability distribution that generates them. In other words, a probability distribution is completely described by the expectation values of n^N , when N takes all positive integer values, as an alternative to P_n , where n takes all non-negative integer values. Note that by the definition of a probability distribution, the 0-th order moment is obviously 1.

A particularly important probability distribution when dealing with discrete events is the Poisson distribution:

$$P_n = \frac{\langle n \rangle^n}{n!} e^{-\langle n \rangle} \quad (4.12).$$

It describes the probability of n counts of a given event during a fixed time interval, with an average count number $\langle n \rangle$, and given that individual events happen independently of one another. The statistical properties of highly attenuated light, and light emitted by light-emitting diodes (LEDs) or lasers below threshold, may be described to a very good approximation by this distribution. A state of light described by this probability distribution is called a coherent state. The noise associated to it is referred to as shot noise, and is also called the standard quantum limit (SQL), since it is the minimum amount of noise possible in a classical photon beam. In a random signal described by Poisson's probability distribution, the variance is equal to the average value, or

$$s_n^2 = \langle n \rangle \quad (4.13).$$

For an arbitrary signal, the difference between its variance and its average value is usually referred to as excess noise.

In summary, we have introduced the main concepts allowing the description of noise, and their mathematical definitions. The next sections will show how these concepts apply to the cases of SOAs and photodiodes.

Noise in semiconductor optical amplifiers

In this section, the origin and description of noise in SOAs will be briefly discussed. First, the physical origin of noise will be introduced. Next, its mathematical description via the photon statistics master equation will be shown.

An SOA is a device that relies on the basic property of light amplification via stimulated emission of photons, which semiconductors possess, and is especially useful in direct band-gap semiconductors. An electron in the conduction band can recombine with a hole in the valence band, emitting a photon. Emission may be stimulated, generating a photon identical to an already existing one, or spontaneous, resulting in the creation of a photon with random phase. Stimulated absorption of a photon, resulting in its annihilation, and the creation of an electron-hole pair, may also occur. The description of these phenomena and the relation between them is discussed in appendix A. Each one of these events has a certain probability of occurring, but whether it will occur or not, and the exact moment when it will occur are not predetermined. Thus, if a certain number of photons enter an SOA, the expected output photon number is just the product of the average input photon number times the amplifier average gain. However, deviations from this average gain value will occur, due to the aforementioned randomness in the amplification process. This results in a steady, well-determined input photon flux producing an uncertain output photon number, or an amplified signal plus noise. Figure 4.1 shows schematically this behavior, by considering an SOA with an input consisting of

photon groups of the same value, and showing the corresponding photon number output.

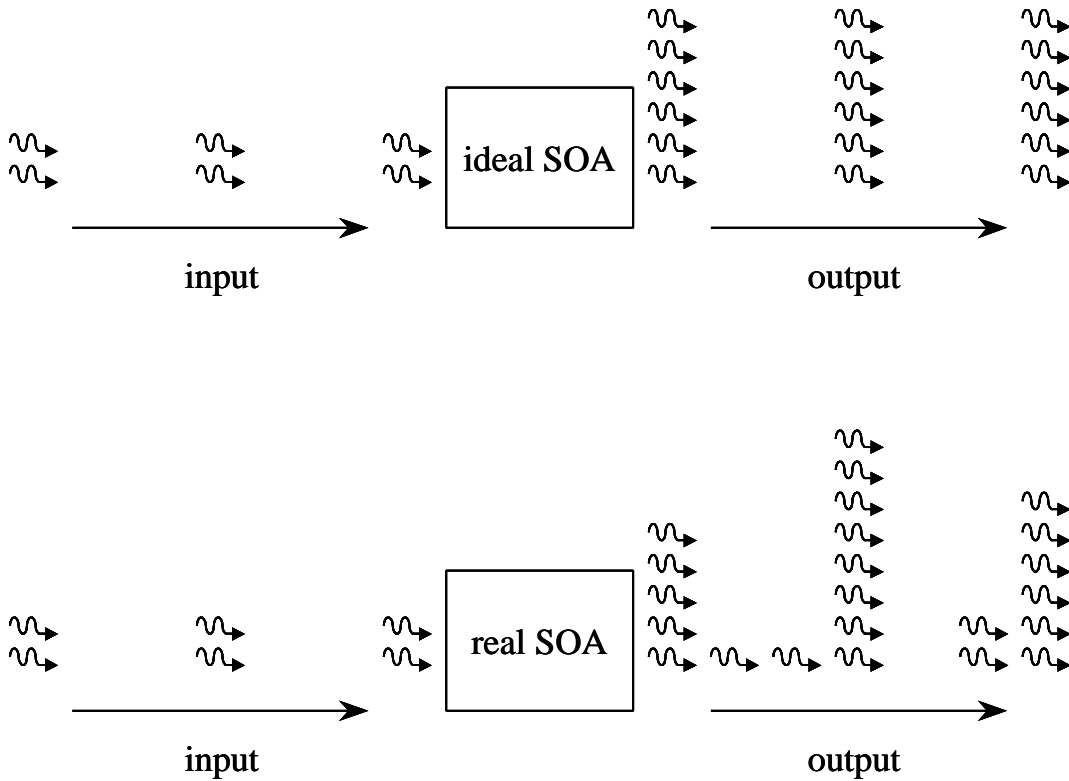


Figure 4.1: Sources of noise in an SOA. Discrete stimulated emission events occur randomly, though with a known average value. This results in different amplification for several identical light pulses. The addition of randomly occurring spontaneous emission results in random addition of photons to these pulses, and addition of photons even in the absence of input light. An ideal amplifier (top) would produce identical output pulses as a response to a stream of identical input pulses. A real amplifier (bottom) produces uneven pulses, and additional light even in the absence of an input.

One final source of noise is related to the quantized nature of light itself, and is related to the fact that the photon number may take only non-negative integer values, changing always by an integer number. In the rest of this section, the photons statistics master equation or forward Kolmogorov equation [1] will be introduced. Intuitive explanations will be given to its origin and to the results of applying it to

SOAs. The best way to quantify the effect of both gain randomness and spontaneous emission of photons, as well as the effect of signal quantization, is through a birth-death-immigration (BDI) method. Stimulated emission of a photon may be understood as a “birth” event, and its probability of occurring is proportional to the already existing population, as is also proportional to the probability of the annihilation of a photon via optical loss or stimulated absorption in the amplifier active region, which may be viewed as a “death” event. Finally, spontaneous emission increases the photon population independently of its value, and may be understood as “immigration”.

Birth-death models have been used since the 1940s to describe the statistics of populations of living organisms or physical particles in different fields of science (see for example [2]). The addition of immigration-like events is necessary to take into account spontaneous emission in SOAs. The first BDI model of noise in SOAs is probably the work of Shimoda, Takahasi and Townes [1]. They proposed the following equation to describe the evolution of the photon statistics in an SOA:

$$\frac{dP_n}{dz} = a[(n-1)P_{n-1} - nP_n] + b[(n+1)P_{n+1} - nP_n] + c(P_{n-1} - P_n) \quad (4.14).$$

All the noise sources described above are taken into account in this equation, called the photon statistics master equation, or forward Kolmogorov equation for optical amplifiers, which describes the evolution, in an gain medium, of the probability of counting a certain number of photons in a given time interval at a certain position. $P_n(z)$ is the probability of the photon count being n in that time

interval at position z along the direction of propagation. The parameters a , b and c are average gain, loss, and spontaneous emission values, respectively, expressed in units of inverse of length. In other words, if n photons are counted arriving to position z during a time interval, the probability of a stimulated emission event happening between z and $z+dz$ during that time interval is given by the product of n , a and dz . Similarly, the combination of stimulated absorption and loss are described by a probability per unit length and per photon count equal to b . Finally, c is the probability that a spontaneous emission event will happen, per unit length, in the considered time interval. Intuitively, (4.14) expresses that the probability of having n photons at position $z+dz$ is equal to the probability of having $n-1$ photons at z , multiplied by the probability that an emission event (spontaneous or stimulated) happens between z and $z+dz$, plus the probability of having $n+1$ photons at z , multiplied by the probability that one of them is absorbed or lost between z and $z+dz$, plus the probability of having n photon counts at z , and no event happening between z and $z+dz$. The probability of any two or more events happening is proportional to a second or higher power of dz , and does not therefore contribute to the derivative of P_n . Note that b describes the probability of any photon being annihilated. It thus encompasses stimulated absorption, either in the amplifier active region or anywhere else in the device, and optical loss, due to a wide range of phenomena, such as scattering or free carrier absorption.

Starting from the photon statistics master equation, we may find the description of the evolution of the average photon number, which we will denote by $\langle n_p \rangle$, along the amplifier:

$$\begin{aligned} \frac{d\langle n_p \rangle}{dz} &= \frac{d}{dz} \sum_{n=0}^{\infty} n P_n = \sum_{n=0}^{\infty} n \frac{dP_n}{dz} = (a-b) \sum_{n=0}^{\infty} n P_n + c \sum_{n=0}^{\infty} P_n \\ &= (a-b)\langle n_p \rangle + c \end{aligned} \quad (4.15).$$

In a similar way, we can also find that

$$\frac{d\langle n_p^2 \rangle}{dz} = \sum_{n=0}^{\infty} n^2 \frac{dP_n}{dz} = 2(a-b)\langle n_p^2 \rangle + (a+b+2c)\langle n_p \rangle + c \quad (4.16);$$

$$\frac{d\mathbf{s}_{n_p}^2}{dz} = \frac{d\langle n_p^2 \rangle}{dz} - \frac{d\langle n_p \rangle^2}{dz} = 2(a-b)\mathbf{s}_{n_p}^2 + (a+b)\langle n_p \rangle + c \quad (4.17).$$

The combination of (4.15) and (4.17) yields an interesting intuitive consideration. The average photon number experiences a gain per unit length equal to $a-b$. The constant term c describes the addition of photons via spontaneous emission, independently of the input photon number. Since the units of the variance are photon number squared, the rate at which the variance will be amplified, per unit length, will be double that, i.e., $2(a-b)$. This is expressed in the first term in the right-hand side (RHS) of (4.17). The other terms may be understood as the noise sources. In fact, in a Langevin noise description, the noise sources present a contribution to the signal variance equal to the sum of the rates at which they happen. In other words, the autocorrelation of the noise sources affecting a particle number is equal to the sum of

particle change rates (see for example [3], pp. 540-6). In this case, the extra terms in the RHS of (4.17) are indeed the stimulated emission rate, spontaneous emission rate and the rate of stimulated absorption or loss, per unit length. This strongly supports the interpretation that the source of noise in SOAs is the randomness associated to these processes. Further interpretation may be obtained by defining a cumulative position-dependent gain $G(z)$, as the net amplification that the input signal would experience from the device input (assumed to be at $z=0$) to position z . This allows us to rewrite (4.15) and (4.17) in a more simplified way, referring the photon count and its variance to the input, dividing them by the cumulative gain and its square, respectively:

$$\frac{d}{dz} \left[\frac{\langle n_p \rangle}{G} \right] = \frac{c}{G} \quad (4.18);$$

$$\frac{d}{dz} \left[\frac{\mathbf{s}_{n_p}^2 - \langle n_p \rangle}{G^2} \right] = \frac{2a \langle n_p \rangle}{G^2} \quad (4.19).$$

The interpretation started above may then be carried a little bit further, saying that the excess noise over the standard quantum limit is generated by randomness in the gain and in the spontaneous emission. The shot noise term may be therefore understood as a consequence of the photon number quantization. The RHS in (4.19) may indeed be related to randomness in the photon emission events stimulated by either the input signal or the spontaneous emission. This may be understood by the presence of the product of the stimulated emission coefficient, a , and the total average

photon number, which includes contributions from both amplified input signal and amplified spontaneous emission (ASE). If a , b and c are constant, and $c=a\Delta\mathbf{n}_o$, $\Delta\mathbf{n}_o$ being the amplifier bandwidth (as described in appendix A for a flat-band approximation), integration of (4.18) and (4.19), with the double initial condition that both the average input photon number and the photon number variance are equal to $n_{p,in}$, yields the following approximated values:

$$\langle n_p \rangle \simeq Gn_{p,in} + n_{sp} (G-1)\Delta\mathbf{n}_o = Gn_{p,in} + n_{p,ASE} \quad (4.20),$$

$$\begin{aligned} \mathbf{s}_{n_p}^2 &\simeq Gn_{p,in} + n_{sp} (G-1)\Delta\mathbf{n}_o + 2n_{p,in}n_{sp}G(G-1) + n_{sp}^2 (G-1)^2 \Delta\mathbf{n}_o \\ &= Gn_{p,in} + n_{p,ASE} + 2Gn_{p,in} \frac{n_{p,ASE}}{\Delta\mathbf{n}_o} + \frac{n_{p,ASE}^2}{\Delta\mathbf{n}_o} \end{aligned} \quad (4.21),$$

where $n_{p,ASE}$ is the average photon number generated by amplification of the spontaneous emission, and n_{sp} is the population inversion factor, defined as

$$n_{sp} = \frac{R_{st,em}}{R_{st,em} - R_{st,ab}} \quad (4.22).$$

For the approximation (4.21) to be valid, the flat band approximation needs to apply, because the stimulated emission and absorption rates are, in general, frequency dependent. In the most general case, it is therefore impossible to define the population inversion factor as a plain numerical value. Furthermore, the total loss needs to be much smaller than the modal gain. Otherwise, n_{sp} needs to be substituted by the following value:

$$n_{sp} \rightarrow \frac{\Gamma_g R_{st,em}}{\Gamma_g (R_{st,em} - R_{st,ab}) - l} = \frac{\Gamma_g R_{st,em}}{\Gamma_g g - l} \quad (4.23).$$

The need for the previous conditions to be satisfied has led to different proposed formulations describing the noise generated in SOAs, specifically for the cases where the net gain is zero or negative [4]. In the particular case of TAP detectors, where the net gain is, in general, much smaller than the stimulated emission rate normalized to the optical intensity, the population inversion factor n_{sp} does not provide a good measure of the optical noise generated as the signal travels along the device.

In a classical wave-like description, the third and fourth terms in the RHS of (4.21) do appear in the noise contribution, but not the first and the second, unless a vacuum field is introduced in the picture (see for example [5]). The third and fourth terms are usually referred to as beat noise terms, since their origin, in a wave-like picture, is associated to the beating in a photodetector of the field generated by amplification of the input signal and the field generated by amplification of the spontaneous emission. The third term is usually called spontaneous-signal beat noise term, and the fourth term is called spontaneous-spontaneous beat noise term. In this model, however, the shot noise (first two terms) appears as an immediate consequence of signal quantization, without the addition of a vacuum field, and the third and fourth terms may be tracked back to random fluctuations in the gain acting on the input signal and the ASE, respectively.

The photon statistics master equation is thus a very powerful model for noise in SOAs, since it describes the evolution of the noise by taking into account the physical

processes that alter the photon number as the optical signal propagates along the amplifier. This equation may also be used to connect each noise term to its physical origin, i.e., signal quantization for shot noise and randomness in the amplification process for the so-called beat noise terms.

Noise in Photodiodes

A semiconductor photodiode relies on stimulated absorption to generate electron-hole pairs from photons. There are in this case two different quantities, the photon count n_p and the electron count n_e , which need to be considered. Holes may be assumed to leave the device active region in opposite direction to the electrons, and both their counts may be assumed identical. Apart from the noise associated to the photodetection process, other noise sources may be considered to affect the photocurrent variance, such as thermal noise in the load resistor, or the shot noise associated to the background current of the photodiode itself, in the absence of any optical input (dark current). The effect of these noise sources has been thoroughly studied, and may be considered, *a priori*, independent of whether the photodetection process includes distributed optical amplification or not. At this point, the discussion will focus on the noise contributions from the photodetection process itself. These additional noise sources will thus be not included at this point. Since they are statistically independent from the photodetection process, the photocurrent variance associated to these processes may be added later to the variance originated by the photon absorption events. In this section, we will thus concentrate only on the noise

characteristics of photodiodes stemming from the detection process itself, i.e., from the conversion of photon counts into electron counts. Appendix C shows in detail how Bernoulli's sampling formula describes the randomness associated to this process. The results of that description and its physical interpretation will be now summarized.

The description of the noise characteristics of the photodetection process requires two different probability distributions, one for the photon count, P_n , and one for the electron count, P'_m . For a lumped detector of quantum efficiency \mathbf{h} , these two probability distributions may be related to one another through Bernoulli's sampling formula (see, for example [6], p. 156):

$$P'_m = \sum_{n=m}^{\infty} \binom{n}{m} \mathbf{h}^m (1-\mathbf{h})^{n-m} P_n \quad (4.24).$$

This result was obtained in 1969 by Scully and Lamb [7]. Intuitively, equation (4.24) tells us that the probability of having m output electrons given an n -photon input is given by the probability of m of those photons being detected (since \mathbf{h} being the average detector efficiency, it is also the probability that one photon would generate one electron) and $n-m$ of them not being detected, summed over all possible ways in which this may happen, i.e., multiplied by the number of possible non-ordered subsets of m elements that may be taken, without repetition, from an n -element set.

We can consider equation (4.24) as describing a random selection process, where the left hand side (LHS) shows the probability of m elements being chosen (electrons of photocurrent generated per unit time), given the probability distribution of n elements in the set from where the selection is made (input photons per unit time).

If the input signal is in a coherent state with an average photon number $\langle n_p \rangle$, then the output electron statistics are described by

$$P'_m = \sum_{n=m}^{\infty} \binom{n}{m} \mathbf{h}^m (1-\mathbf{h})^{n-m} \frac{\langle n_p \rangle^n}{n!} e^{-\langle n_p \rangle} = \frac{[\mathbf{h}\langle n_p \rangle]^m}{m!} e^{-\mathbf{h}\langle n_p \rangle} \quad (4.25).$$

Thus, the output electrons follow also a Poisson distribution, this time with average output electron number $\langle n_e \rangle = \mathbf{h}\langle n_p \rangle$. This makes perfect sense intuitively, since if the input is a stream of photons such that their times of arrival are uncorrelated, and we randomly select some of them to be absorbed, the output will be a stream of electrons uncorrelated to one another.

For random input statistics, and as shown in more detail in appendix C, we may find

$$\langle n_e \rangle = \mathbf{h}\langle n_p \rangle \quad (4.26),$$

$$\langle n_e^2 \rangle = \mathbf{h}\langle n_p \rangle + \mathbf{h}^2 \left[\langle n_p^2 \rangle - \langle n_p \rangle \right] \quad (4.27),$$

from where the electron number variance may be found:

$$\mathbf{s}_{n_e}^2 = \langle n_e \rangle + \mathbf{h}^2 \left[\mathbf{s}_{n_p}^2 - \langle n_p \rangle \right] \quad (4.28).$$

Thus, if the optical input exhibits Poisson statistics, so does the electrical output, and any other input excess noise is converted into output excess noise by multiplying it by the square of the efficiency. Finally, let us mention that the Noise Figure of a photodiode can be found from (4.28) to be

$$\text{NF} = 1 + \frac{1 - \mathbf{h}}{\mathbf{h}} \frac{\langle n_p \rangle}{s_{n_p}^2} \quad (4.29).$$

Therefore, for an arbitrary optical input signal, the Noise Figure of a detector will approach the optimum limit of 1 (0dB) as the efficiency \mathbf{h} approaches 1. This also makes perfect sense intuitively, since in a photodiode with unit efficiency, all photons are detected, and there is thus no added randomness introduced by the device itself, just a direct translation of optical noise into electrical noise.

For an optical input in a coherent state, the Noise Figure is $1/\mathbf{h}$. The coupling efficiency of the optical signal into the detector may be assumed to be taken into account in the device efficiency \mathbf{h} . This results, of course, in large noise figures when the coupling efficiency is low.

Note that the noise figure will be enhanced by the additional noise contributions independent of the detection process (such as thermal noise in the load resistor or shot noise of the background current), as mentioned at the beginning of this section. These contributions to the noise figure, being *a priori* independent on the input photon number, will result in a higher noise figure for lower input optical power;

hence the importance of optical preamplification as a tool to improve the signal-to-noise ratio of the received signal in optical links.

In conclusion, in this section we have addressed the source of noise in the generation of current in photodiodes, namely the randomness in the absorption of photons. Bernoulli's sampling formula is intuitively shown to perfectly describe this phenomenon. This formula is also used to derive a mathematical description of the noise added by the photodetection process, through the electron number variance in the photocurrent, and the noise figure of photodiodes obtained from it.

Correlation between electron and photon fluctuations

In the previous sections of this chapter, noise models for SOAs and photodiodes have been briefly discussed. Neither of the two models separately has the capability of describing the effect of both amplification and detection in the noise of the final photocurrent. The combination of both may however describe the noise present in the photocurrent generated by a preamplified optical signal. First, using the photon statistics master equation, the noise in the photon stream coming out of the amplifier may be calculated, knowing the statistics of the amplifier input. The statistics of the electron number contained in the photocurrent may then be found using Bernoulli's sampling equation. However, in the presence of the distributed combination of amplification and absorption, this approach is not sufficient. In this section, the important question of the correlation between electron number and photon number fluctuations will be intuitively addressed. More detailed discussion, including

mathematical proofs of some of the ideas expressed intuitively in this section, is included in Appendix C.

Let us consider a lossless photodetector, where part of the light is absorbed, and part is transmitted. The surviving optical signal and the generated photocurrent are correlated, as expressed in figure 4.2.

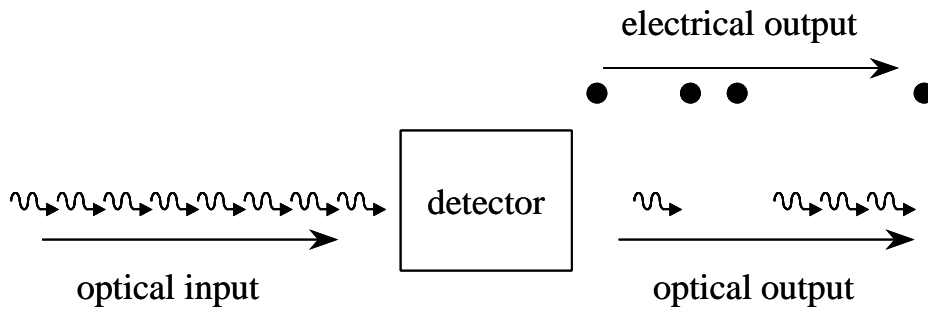


Figure 4.2: In a lossless detector where light is partially absorbed, the surviving light is correlated to the generated photocurrent. If a stream of photons, identically spaced at given time intervals, is incident, the presence of a surviving photon in one such time interval at the output of the device occurs if and only if an electron of photocurrent is not generated during that same time interval.

In Appendix C, it is shown that the covariance between the output photon and electron populations is given, in the most general case, by

$$\mathbf{s}_{n_p, n_e} = \langle n_p n_e \rangle - \langle n_p \rangle \langle n_e \rangle = \mathbf{h}(1 - \mathbf{h}) \left[\mathbf{s}_{n_{p, in}}^2 - \langle n_{p, in} \rangle \right] \quad (4.30),$$

where n_p and n_e are the output photon and electron counts, and $n_{p, in}$ is the input photon count. For arbitrary device efficiency, the covariance is identically zero only when the input photon population presents a variance equal to its average value, which is an indicator that photon arrivals are statistically uncorrelated to one another. Intuitively, if the input photons are not correlated to one another, the electrons

generated and the surviving photons will not be correlated either. However, any correlation present in the input photon stream is reflected in a cross-correlation between the two output populations.

Let us now consider two lossless, partially-absorbing photodetectors, such that the input of the second one is part of the light surviving the detection process in the first one, as shown schematically in figure 4.3. This cascading description may be used to study the behavior of a waveguide photodetector where light suffers optical loss as it propagates, by understanding that the partial coupling between both detectors is due to annihilation of part of the photons not absorbed in the first one, due to optical loss.

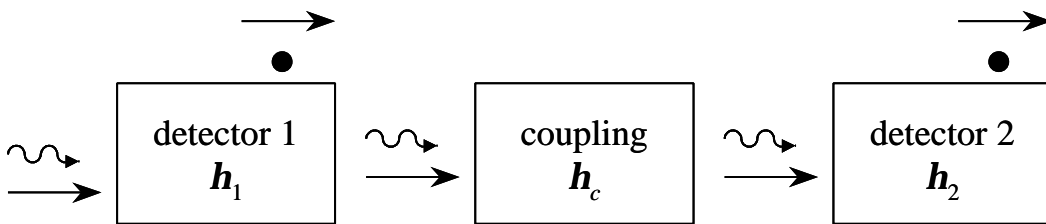


Figure 4.3: Two partially absorbing photodetectors are cascaded, so that part of the light surviving detection in the first one is coupled into the second one. The partial coupling from the first detector into the second one may be used to represent the effect of optical loss in a distributed detector. Photons are represented through wiggly arrows, electrons by full dots.

A mathematical analysis of this situation is carried out in appendix C. The conclusions of such analysis are intuitively very simple, yet of great importance.

First, there is correlation between the photon populations at different positions along the ensemble, and the electron populations generated by both detectors, as well as between both generated photocurrents. The degree of correlation (defined as the ratio between their covariance and the product of their average values) between any

two populations is, in all cases, equal to the input excess noise divided by the average input photon number squared.

Next, let us consider the total photocurrent of the ensemble, found by adding the photocurrents generated by both detectors. The statistics of this total photocurrent are identical to those generated, for the same input, by a lumped detector, whose total efficiency would be $\mathbf{h}_T = \mathbf{h}_1 + (1 - \mathbf{h}_1)\mathbf{h}_c\mathbf{h}_2$, where \mathbf{h}_1 and \mathbf{h}_2 are the efficiencies of both detectors, and \mathbf{h}_c is the fraction of optical power surviving the first detector that is coupled into the second one. \mathbf{h}_T is the efficiency of the ensemble calculated by straightforward computation, since $1 - \mathbf{h}_1$ is the fraction of input photons that survive the first detector, a fraction \mathbf{h}_c of which are coupled into the second detector. Therefore, Bernoulli's sampling formula does not only apply to lumped, lossless photodetectors, but to any photodetector not featuring optical or electrical gain, distributed or not, and even in the presence of optical loss. The correlation between the photon and electron populations is taken into account implicitly in Bernoulli's sampling formula.

Finally, the mathematical manipulations that produce the previous two conclusions are only possible because optical loss is, *per se*, a random sampling process, whose effect in the photon population statistics may be described also by Bernoulli's sampling equation. Any other non-sampling process, described by a different equation, would not, in general, result in the behavior of the ensemble being describable by Bernoulli's sampling formula with the use of an appropriated chosen

total efficiency h_T . In particular, the description of the distributed combination of amplification and absorption would require a different approach, including the explicit calculation of the correlation between the electron and photon numbers.

In summary, this section has intuitively described how photon and electron statistics in distributed photodetectors present correlations, which are implicitly taken into account in Bernoulli's sampling equation. This equation thus describes the distributed combination of photodetection and any other random sampling process, such as optical loss or non-unity coupling efficiency, provided that the adequate total efficiency is used in equation (4.24). It is also argued how the combination of amplification and absorption, the former not being a random sampling process, will result in Bernoulli's sampling equation not being valid, while the correlation between electron and photon populations needs to be still taken into account explicitly. The mathematical proofs supporting these intuitive conclusions are included in appendix C. In the next section, a new noise model will be introduced. This new model describes the joint evolution of electron and photon statistics, allowing for the description of the effect of distributed combination of amplification and absorption.

Evolution of photon and electron number statistics in the presence of distributed amplification and photodetection

In the previous section, it has been argued how the description of noise in the presence of distributed amplification and absorption requires an explicit calculation of the correlation between electron and photon statistics. A new noise model describing

the simultaneous evolution of the photon and electron number statistics, and thus fulfilling this requirement, will now be presented. Next, the results furnished by it for the limiting case of a pure SOA without photo-detection will be compared to the results from the photon statistics master equation. Finally, we will show that, when no optical amplification is present, the output electron statistics are equivalent to those given by Bernoulli's sampling formula.

Photon and electron number fluctuations and their probabilities

Both the photon statistics master equation and Bernoulli's sampling formula are based on a very simple concept: any fluctuation in the optical and electrical signals in a photodetector happens one photon and one electron at a time, respectively. In this section, we will set up the scenario for a particle-like noise model based precisely on this very concept. In order to do that, we will describe in this paragraph the changes that may happen to the populations of both electrons and holes, and assign to each of them a probability per unit length. This will be used in the next paragraph to establish the new noise model.

As described in appendix A, there are different processes that change the electron and photon number. Before beginning, we will perform a flat-band approximation, i.e., gain and spontaneous emission will be assumed to be constant over the effective bandwidth Δn_o of the amplifier. The different processes, their effect in the electron and photon populations, and their probabilities are summarized next. These

probabilities are extracted from the average values of gain and stimulated emission presented in appendix A.

Stimulated emission in the amplifier region increases by one the number of photons. If at a certain position in the device the photon count over a certain time interval is $n_p(z)$, the probability of one stimulated emission event per unit length in the vicinity of z and during that same time interval is given by $\Gamma_g(z)r_{st,em}(z)n_p(z)$, where $r_{st,em}(z)$ is the local stimulated emission rate normalized to optical intensity, as defined in appendix A, and $\Gamma_g(z)$ is the local confinement factor in the amplifier region.

Stimulated absorption in the amplifier region reduces the number of photons by one. The probability of one stimulated absorption event per unit length, in the same conditions as before, is given by $\Gamma_g(z)r_{st,ab}(z)n_p(z)$, where $r_{st,ab}(z)$ is the local stimulated absorption rate normalized to optical intensity, and the local material gain $g(z)$ is given by $g(z)=r_{st,em}(z)-r_{st,ab}(z)$.

A spontaneous emission event in the amplifier region may or may not increase the photon number by one, since the photon number considered, $n_p(z)$, takes into account only light coupled into a propagating mode of the device. The probability that a spontaneous emission event generates one photon that is indeed coupled into a guided mode, per unit time and per unit length, and in the vicinity of z , is given, as shown in appendix A, by $\Gamma_g(z)r_{st,em}(z)\Delta n_o$.

Optical loss may also reduce the number of photons by one. The probability per unit length of one photon being lost in the vicinity of z , in the time interval when $n_p(z)$

photon counts are registered at position z , is given by $n_p(z)l(z)$, $l(z)$ being the local loss per unit length in the vicinity of z .

All the previous processes leave the electron number unchanged. The only event that changes the electron number is the absorption of a photon in the detector. The probability of one electron being generated and one photon annihilated in the vicinity of z , in a time interval when $n_p(z)$ photon counts are registered at z , is given by $\Gamma_a(z)\mathbf{a}(z)n_p(z)$, where $\mathbf{a}(z)$ is the local material absorption of the detector active region and $\Gamma_a(z)$ is the local confinement factor of the mode in the absorption region.

Let us now assume that dz is a length small enough that the probability of two events to happen (i.e., the product of their probabilities per unit length and multiplied by dz^2) is much smaller than the probability of any one event to happen (i.e., the probability per unit length of each event to happen, multiplied by dz), and than the probability of no event to happen (i.e., one minus the sum of the probabilities of any event to happen). Assuming that we know that exactly $n_p(z)$ photons arrive to position z in an interval equal to one time unit, and that $n_e(z)$ electrons have been generated in that time between the device input at the device input ($z=0$) and an arbitrary position z , the possible values for the number of photons that arrive to $z+dz$ during a time unit, and the number of electrons generated in that time unit between 0 and $z+dz$, and their respective probabilities of happening, are shown in table 4.1.

$n_p(z+dz)$	$n_e(z+dz)$	Probability
$n_p(z)+1$	$n_e(z)$	$\Gamma_g(z)r_{st,em}(z)n_p(z)dz$
$n_p(z)-1$	$n_e(z)$	$\Gamma_g(z)r_{st,ab}(z)n_p(z)dz$
$n_p(z)+1$	$n_e(z)$	$\Gamma_g(z)r_{st,em}(z)\Delta n_o dz$
$n_p(z)-1$	$n_e(z)$	$l(z)n_p(z)dz$
$n_p(z)-1$	$n_e(z)+1$	$\Gamma_a(z)\mathbf{a}(z)n_p(z)dz$

Table 4.1: Possible photon and electron numbers at $z+dz$ as a function of their values at z , and their respective probabilities. The different rows describe the occurrence of (top to bottom) stimulated emission, stimulated absorption in the amplifier region, spontaneous emission, optical loss, and absorption in the detector region.

The only event not recorded in table 4.1 is the photon and electron populations remaining unchanged because no other event happens. Its probability is obviously given by one minus the sum of all probabilities expressed in table 4.1.

In conclusion, this paragraph summarizes the different events that may affect the electron and photon numbers, and their respective probabilities.

Evolution of functions depending on photon and electron numbers

In this paragraph, the events described in the previous paragraph and their respective probabilities will be used to establish the evolution, along a device featuring both amplification and absorption, of the average value of any function depending on electron and photon numbers.

Let us then assume that $f(n_p(z), n_e(z))$ is any function that depends on the photon and electron numbers. As the electron and photon numbers evolve in the device, the value of that function will also evolve. Since the electron and photon numbers cannot, in general, be known precisely, the exact value of the function f cannot be known with exactitude either. We may, however, calculate its average value, by calculating the weighted sum of all the values that f takes for all pairs of values $(n_p(z), n_e(z))$, the weights being the probability of the corresponding pairs of values to occur, which we will call $P(n_p(z), n_e(z))$, i.e.:

$$\langle f(n_p(z), n_e(z)) \rangle = \sum_{n_e(z)=0}^{\infty} \sum_{n_p(z)=0}^{\infty} f(n_p(z), n_e(z)) P(n_p(z), n_e(z)) \quad (4.31).$$

Let us now calculate the evolution of this function along the device. One possibility would be to calculate the evolution equation for the average value of f as follows:

$$\frac{d \langle f(n_p(z), n_e(z)) \rangle}{dz} = \sum_{n_e(z)=0}^{\infty} \sum_{n_p(z)=0}^{\infty} f(n_p(z), n_e(z)) \frac{dP(n_p(z), n_e(z))}{dz} \quad (4.32).$$

This approach is typically used to describe the evolution of the average value and variance of the photon population inside an SOA (see for example [6], p. 83). The inconvenient of this approach is that an equation needs to be defined for the evolution of the electron and photon probability distributions simultaneously. This may lead to complex computation. Another approach, which will be used in this new model, starts with the definition of an event probability P'_{event} . This is the probability of an

event to happen which will change the photon and electron number pair from $(n_p(z), n_e(z))$ to $(n_p(z+dz), n_e(z+dz))$, as the signal propagates from z to $z+dz$. This probability depends, obviously, on the initial and final states, and may even depend on the position along the device. For simplicity in the notation, the dependence of this probability on the initial and final states of the event, or on the position along the device, will not be shown explicitly. We can then write:

$$P(n_p(z+dz), n_e(z+dz)) = \sum_{event} \sum_{n_p=0}^{\infty} \sum_{n_e=0}^{\infty} P'_{event} P(n_p(z), n_e(z)) \quad (4.33),$$

i.e., the probability of the electron and photon numbers to be respectively $n_e(z+dz)$ and $n_p(z+dz)$ at $z+dz$ is the weighted sum of the probabilities of the electron and photon numbers to be respectively $n_e(z)$ and $n_p(z)$ at z , the weights being the probabilities of events to happen which will perform that change. Note that the sum needs to be carried out for all initial possible pairs of the electron and photon numbers, but only for those events that will result in the appropriate change of electron and photon numbers. Obviously, if no event may change the electron and photon number from the initial to the final values, the contribution of that pair of electron and photon numbers to the sum will be zero. Note that, although not expressed explicitly, the sum includes, of course, the event where nothing happens for the case where $n_p(z+dz)=n_p(z)$ and $n_e(z+dz)=n_e(z)$. Its probability will be one minus the sum of the probabilities of all other events which may happen when the initial electron and photon numbers are, respectively, $n_e(z)$ and $n_p(z)$. Note also that the sum may be carried out over “multiple events”, i.e., the combination of more than one

single event, v.g., absorption of one photon to produce an electron and simultaneous spontaneous emission of a photon. The probability of such an event will be proportional to dz to the power of the number of single events involved, and as we will soon see, the contribution of these “multiple events” is negligible.

Based on the above discussion, and using (4.33), we can write:

$$\begin{aligned} & \langle f(n_p(z+dz), n_e(z+dz)) \rangle \\ &= \sum_{event} \sum_{n_e(z)=0}^{\infty} \sum_{n_p(z)=0}^{\infty} f(n_p(z+dz), n_e(z+dz)) P'_{event} P(n_p(z), n_e(z)) \end{aligned} \quad (4.34).$$

We can now separate different terms in this sum. First, the term corresponding to “no event”, i.e., the cases where the electron and photon numbers remain unchanged because no transitions occur. Next, all processes involving exactly one transition. Finally, all events involving more than one transition. The contribution from the first term is given by

$$\begin{aligned} & \sum_0 \sum_{n_e(z)=0}^{\infty} \sum_{n_p(z)=0}^{\infty} f(n_p(z), n_e(z)) P'_{event} P(n_p(z), n_e(z)) \\ &= \sum_{n_e(z)=0}^{\infty} \sum_{n_p(z)=0}^{\infty} f(n_p(z), n_e(z)) [1 - \sum_{\geq 1} P'_{event}] P(n_p(z), n_e(z)) \\ &= \langle f(n_p(z), n_e(z)) \rangle \\ & - \sum_1 \sum_{n_e(z)=0}^{\infty} \sum_{n_p(z)=0}^{\infty} f(n_p(z), n_e(z)) P'_{event} P(n_p(z), n_e(z)) + O(dz^2) \end{aligned} \quad (4.35).$$

The subindex “0” on the sum indicates that the sum is only carried out over the event where no process happens. The subindices “ ≥ 1 ” and “1” indicate that the sum

is carried out over all single or multiple events, and over all single events, respectively, that may happen when the initial electron and photon populations at z are $n_e(z)$ and $n_p(z)$, respectively. The term indicated by $O(dz^2)$ signifies that all contributions other than the ones explicitly shown will be of an order 2 or higher on dz . The contribution from all multiple events will also be in this same order. Finally, the contribution from all single events will be given by:

$$\sum_1 \sum_{n_e(z)=0}^{\infty} \sum_{n_p(z)=0}^{\infty} f(n_p(z+dz), n_e(z+dz)) P'_{event} P(n_p(z), n_e(z)) \quad (4.36).$$

Thus, we may finally write:

$$\begin{aligned} & \langle f(n_p(z+dz), n_e(z+dz)) \rangle = \langle f(n_p(z), n_e(z)) \rangle \\ & + \sum_1 \sum_{n_e(z)=0}^{\infty} \sum_{n_p(z)=0}^{\infty} f(n_p(z+dz), n_e(z+dz)) P'_{event} P(n_p(z), n_e(z)) \quad (4.37). \\ & - \sum_1 \sum_{n_e(z)=0}^{\infty} \sum_{n_p(z)=0}^{\infty} f(n_p(z), n_e(z)) P'_{event} P(n_p(z), n_e(z)) + O(dz^2) \end{aligned}$$

Note that, since the electron and photon numbers change only by an integer (actually by 1 in the case of single events), the difference between f evaluated at z and at $z+dz$ is, in general, a finite number that does not depend on dz . However, the probability of single events to happen is a constant times dz , as shown in table 4.1. We may then subtract the average value of f evaluated at z from both sides of (4.37), divide by dz and take limits when dz tends to 0:

$$\begin{aligned} & \frac{d \langle f(n_p(z), n_e(z)) \rangle}{dz} \\ & = \sum_1 \sum_{n_e(z)=0}^{\infty} \sum_{n_p(z)=0}^{\infty} \Delta f(n_p(z), n_e(z)) \frac{P'_{event}}{dz} P(n_p(z), n_e(z)) \end{aligned} \quad (4.38),$$

where the change in the value of the function f , $\Delta f(n_p(z), n_e(z))$ is defined as:

$$\Delta f(n_p(z), n_e(z)) = f(n_p(z+dz), n_e(z+dz)) - f(n_p(z), n_e(z)) \quad (4.39).$$

Equations (4.38) and (4.39) offer, *a priori*, a way of calculating the evolution of the average value of any function that depends on the electron and photon number, for any device where both electrons and photons are generated and annihilated, as long as the probability per unit length of any event changing the electron and photon number may be calculated.

In summary, a new way of calculating the evolution along a device featuring both gain and absorption of the average value of any function depending on the electron and photon numbers has been introduced. This will constitute the basis of the new noise model which will be introduced in the next paragraph.

Evolution of the statistics of photon and electron numbers

In this paragraph, the equations describing the evolution of the statistics of the electron and photon populations in a distributed amplifier-photodetector will be drawn from results presented in the previous two paragraphs, more specifically equation (4.38) and table 4.1. The end result pursued in this paragraph will be determination of equations describing the evolution of average value, variance and

covariance of the electron and hole populations. Other intermediate results will be used to show the equivalence between this new noise model and previously existing noise models.

The statistics of a random variable may be defined by its probability distribution, as expressed at the beginning of this chapter. From this probability distribution, the average value of any function involving this random variable may be calculated. Another way of completely determining the statistics of a random variable is through the set of all its moments, i.e., the set of expectation values of all the positive natural powers of the variable. In the case of the electron and photon numbers, this complete set of moments is the average value of the set of polynomials of the form $n_p^N n_e^{N'}$, for any pair of natural numbers N and N' . The average value of each of the populations, their respective variances, and their covariance, are completely determined by the combinations such that $N+N'=1$ and $N+N'=2$. The evolution of the polynomials with these values of N and N' suffices to characterize the noise properties of amplifier-photodetectors. However, for a full description of the electron and photon population statistics, the average values of all polynomials of the form $n_p^N n_e^{N'}$ need to be calculated. Note therefore that N and N' do not have physical meaning by themselves. They correspond to different exponents for the photon and electron numbers whose averaged product we calculate in order to fully describe the joint statistics of electron and photon populations.

As shown in table 4.1, given a pair of values $(n_p(z), n_e(z))$ of the electron and photon populations at position z , the possible values of the pair $(n_p(z+dz), n_e(z+dz))$

may take after one single transition event are $(n_p(z)+1, n_e(z))$, $(n_p(z)-1, n_e(z))$ and $(n_p(z)-1, n_e(z)+1)$. In the case of stimulated emission, we may find the contribution from this event only to equation (4.38) to be described by

$$\begin{aligned} \sum_{n_e=0}^{\infty} \sum_{n_p=0}^{\infty} \left[(n_p+1)^N n_e^{N'} - n_p^N n_e^{N'} \right] \Gamma_g r_{st,em} n_p P(n_p, n_e) \\ = \Gamma_g r_{st,em} \sum_{i=0}^{N-1} \binom{N}{i} \langle n_p^{i+1} n_e^{N'} \rangle \end{aligned} \quad (4.40).$$

The contribution from the spontaneous emission term is given by

$$\begin{aligned} \sum_{n_e=0}^{\infty} \sum_{n_p=0}^{\infty} \left[(n_p+1)^N n_e^{N'} - n_p^N n_e^{N'} \right] \Gamma_g r_{st,em} \Delta \mathbf{n}_o P(n_p, n_e) \\ = \Gamma_g r_{st,em} \Delta \mathbf{n}_o \sum_{i=0}^{N-1} \binom{N}{i} \langle n_p^i n_e^{N'} \rangle \end{aligned} \quad (4.41).$$

The contributions from the terms describing the stimulated absorption in the amplifier region and the optical loss may be combined together into

$$\begin{aligned} \sum_{n_e=0}^{\infty} \sum_{n_p=0}^{\infty} \left[(n_p-1)^N n_e^{N'} - n_p^N n_e^{N'} \right] (\Gamma_g r_{st,ab} + l) n_p P(n_p, n_e) \\ = (\Gamma_g r_{st,ab} + l) \sum_{i=0}^{N-1} (-1)^{N-i} \binom{N}{i} \langle n_p^{i+1} n_e^{N'} \rangle \end{aligned} \quad (4.42).$$

And finally, the contribution from absorption and generation of photocurrent is described through

$$\begin{aligned}
& \sum_{n_e=0}^{\infty} \sum_{n_p=0}^{\infty} \left[(n_p - 1)^N (n_e + 1)^{N'} - n_p^N n_e^{N'} \right] \Gamma_a \mathbf{a} n_p P(n_p, n_e) \\
&= \Gamma_a \mathbf{a} \sum_{i=0}^{N-1} (-1)^{N-i} \binom{N}{i} \langle n_p^{i+1} n_e^{N'} \rangle \\
&+ \Gamma_a \mathbf{a} \sum_{i=0}^N \sum_{j=0}^{N'-1} (-1)^{N-i} \binom{N}{i} \binom{N'}{j} \langle n_p^{i+1} n_e^j \rangle
\end{aligned} \tag{4.43}$$

Therefore, in the case of the polynomials of the form $n_p^N n_e^{N'}$, (4.38) may be finally written as

$$\begin{aligned}
\frac{d \langle n_p^N n_e^{N'} \rangle}{dz} &= \Gamma_g r_{st,em} \sum_{i=0}^{N-1} \binom{N}{i} \langle n_p^{i+1} n_e^{N'} \rangle \\
&+ \Gamma_g r_{st,em} \Delta \mathbf{n}_o \sum_{i=0}^{N-1} \binom{N}{i} \langle n_p^i n_e^{N'} \rangle \\
&+ (\Gamma_g r_{st,ab} + l + \Gamma_a \mathbf{a}) \sum_{i=0}^{N-1} (-1)^{N-i} \binom{N}{i} \langle n_p^{i+1} n_e^{N'} \rangle \\
&+ \Gamma_a \mathbf{a} \sum_{i=0}^N \sum_{j=0}^{N'-1} (-1)^{N-i} \binom{N}{i} \binom{N'}{j} \langle n_p^{i+1} n_e^j \rangle
\end{aligned} \tag{4.44}$$

This is the central equation of the new model for noise in distributed amplifier-photodetectors. In order to find its intuitive meaning, let us first of all make $N'=0$. In other words, we will concentrate in the equations describing the evolution of the photon population statistics:

$$\begin{aligned}
\frac{d \langle n_p^N \rangle}{dz} &= \Gamma_g r_{st,em} \sum_{i=0}^{N-1} \binom{N}{i} \langle n_p^{i+1} \rangle + \Gamma_g r_{st,em} \Delta \mathbf{n}_o \sum_{i=0}^{N-1} \binom{N}{i} \langle n_p^i \rangle \\
&+ (\Gamma_g r_{st,ab} + l + \Gamma_a \mathbf{a}) \sum_{i=0}^{N-1} (-1)^{N-i} \binom{N}{i} \langle n_p^{i+1} \rangle
\end{aligned} \tag{4.45}$$

It is interesting to note that nowhere in (4.45) does the electron number appear. This is intuitively obvious, since the electron population statistics are affected by the photon population statistics through absorption, but not *vice versa*. Note also that the absorption in the detector appears in the same term as the loss and the stimulated absorption in the amplifier. This may be explained by the fact that, from the point of view of light propagation only, absorption in the detector is just another source of photon annihilation. We will later see that equation (4.45) may be deduced equivalently from the forward Kolmogorov equation. This will confirm the consistency of the new model with the model based on the photon statistics master equation. We can also make $N=0$ in (4.44), i.e., we may concentrate on the equations describing the evolution of the electron number statistics:

$$\frac{d\langle n_e^{N'} \rangle}{dz} = \Gamma_a \mathbf{a} \sum_{j=0}^{N'-1} \binom{N'}{j} \langle n_p n_e^j \rangle \quad (4.46).$$

Equation (4.46) states that the correlation between the electron population and the photon population needs to be calculated, before the actual statistical properties of the electron population may be found. This agrees perfectly with the previous discussion about the correlation between electron and photon numbers. Note that, in general, equation (4.44) shows that the evolution of the average value of $n_p^N n_e^N$ is determined by the average values of $n_p^i n_e^j$, with $i \leq N+1$, $j \leq N-1$. Eventually, this means that, in order to calculate the evolution of n_e^N , it is necessary to know the statistics of n_p^i , for all $i \leq N'$. In particular, the evolution of the electron number variance can only be

calculated once the evolution of both the photon number variance and the covariance between electron and photon numbers are known.

It can be shown from Bernoulli's sampling formula that (see appendix C):

$$\left\langle \prod_{i=0}^N (n_e - i) \right\rangle = \mathbf{h}^{N+1} \left\langle \prod_{i=0}^N (n_p - i) \right\rangle \quad (4.47).$$

Therefore, the average value of an N -th degree polynomial in the output photocurrent electron number also require in that case the knowledge of the statistics of an N -th degree polynomial of the optical input photon number. Thus, the correlation between photon and electron numbers, which is implicitly taken into account through Bernoulli's sampling formula, needs to be explicitly taken into account in this case, because of the contribution from the optical amplification to the noise. This correlation appears explicitly in the new model, as shown in equation (4.44).

In conclusion, the central equation of the new noise model, (4.44), has been deduced. It has been shown how the evolution of the photon number statistics can be determined with complete independence on the electron population, by considering the optical absorption in the detector as an added source of loss. It also shows how the correlation between electron and photon numbers make it necessary to take into account the photon statistics, and the correlation between electron and photon numbers, in order to find the electron population statistics, in perfect agreement with the intuitive picture depicted earlier in this section. In the next sub-paragraphs, the

central formula for the new noise model will be applied to the particular case of the average value, variance and covariance of the electron and photon numbers.

Evolution of the average photon and electron numbers

In order to fully characterize the evolution of the electron and photon average numbers, let us make $N=1$ in (4.45) and $N'=1$ in (4.46), which results respectively in

$$\frac{d\langle n_p \rangle}{dz} = \left[\Gamma_g (r_{st,em} - r_{st,ab}) - l - \Gamma_a \mathbf{a} \right] \langle n_p \rangle + \Gamma_g r_{st,em} \Delta \mathbf{n}_o \quad (4.48),$$

$$\frac{d\langle n_e \rangle}{dz} = \Gamma_a \mathbf{a} \langle n_p \rangle \quad (4.49).$$

Note the similarity between these equations and the DC model of traveling-wave amplifier photodetectors shown in chapter 2. Just as we did then, we will now define a net gain per unit length $\Delta g(z)$ and a cumulative gain $G(z)$ as:

$$\frac{1}{G} \frac{dG}{dz} = \Delta g = \Gamma_g (r_{st,em} - r_{st,ab}) - l - \Gamma_a \mathbf{a} \quad (4.50),$$

where the initial condition for the cumulative gain is $G(0)=1$. A cumulative efficiency $\mathbf{h}(z)$ may also be defined:

$$\frac{d\mathbf{h}}{dz} = \Gamma_a \mathbf{a} G \quad (4.51),$$

with the initial condition $\mathbf{h}(0)=0$. This definitions allow us to simplify (4.48) and (4.49) into:

$$\frac{d}{dz} \left[\frac{\langle n_p \rangle}{G} \right] = \frac{\Gamma_g r_{st,em} \Delta \mathbf{n}_o}{G} \quad (4.52).$$

$$\frac{d \langle n_e \rangle}{dz} = \frac{\langle n_p \rangle}{G} \frac{d\mathbf{h}}{dz} \quad (4.53).$$

The solution of these two equations is then given by:

$$\langle n_p(z) \rangle = G(z) \langle n_p(0) \rangle + n_{p,ASE}(z) \quad (4.54),$$

$$\langle n_e(z) \rangle = \mathbf{h}(z) \langle n_p(0) \rangle + n_{e,ASE}(z) \quad (4.55),$$

where we have defined the average photon number introduced via ASE, $n_{p,ASE}(z)$, and the average electron number generated by detection of ASE, $n_{e,ASE}(z)$, by:

$$n_{p,ASE}(z) = \Delta \mathbf{n}_o G(z) \int_0^z \frac{\Gamma_g(x) r_{st,em}(x)}{G(x)} dx \quad (4.56),$$

$$\begin{aligned} n_{e,ASE}(z) &= \Delta \mathbf{n}_o \int_0^z \Gamma_a(x) \mathbf{a}(x) G(x) \left[\int_0^x \frac{\Gamma_g(y) r_{st,em}(y)}{G(y)} dy \right] dx \\ &= \Delta \mathbf{n}_o \int_0^z \frac{n_{p,ASE}(x)}{G(x)} \frac{d\mathbf{h}(x)}{dx} dx \end{aligned} \quad (4.57).$$

Note that this description is entirely equivalent to the optical power and photocurrent formulations found in chapter 2.

In conclusion, we have used the new noise model for distributed amplifier-photodetectors to find the evolution of the average photon and electron numbers. Next, we will find the evolution of the photon number variance.

Evolution of the photon number variance

The equation describing the evolution of the photon number variance is obtained by making $N=2$ in (4.45), and using the simplifications suggested in (4.50) and (4.52):

$$\begin{aligned} \frac{d\langle n_p^2 \rangle}{dz} = & 2\frac{\langle n_p^2 \rangle}{G} \frac{dG}{dz} + 2G \frac{d}{dz} \left[\frac{\langle n_p \rangle}{G} \right] \langle n_p \rangle \\ & + (\Gamma_g r_{st,em} + \Gamma_g r_{st,ab} + l + \Gamma_a \mathbf{a}) \langle n_p \rangle + \Gamma_g r_{st,em} \Delta \mathbf{n}_o \end{aligned} \quad (4.58).$$

Subtracting from both sides of the equation the derivative of the photon number squared, we can now find

$$\frac{d\mathbf{s}_{n_p}^2}{dz} = 2\Delta g \mathbf{s}_{n_p}^2 + (\Gamma_g r_{st,em} + \Gamma_g r_{st,ab} + l + \Gamma_a \mathbf{a}) \langle n_p \rangle + \Gamma_g r_{st,em} \Delta \mathbf{n}_o \quad (4.59).$$

Note that this equation could be simplified further, but its current form allows for interesting observations. We can intuitively see from (4.50) that Δg is the rate of change for the average photon number per unit length. Therefore, since the variance has dimensions of photon number squared, it is only natural that its rate of change is $2\Delta g$. This is expressed by the first term in the RHS of (4.59). The remaining terms express the rates per unit length of all processes that alter the photon number. This description is thus completely consistent with a Langevin approach.

Equation (4.59) may be further simplified into:

$$\frac{d}{dz} \left[\frac{\mathbf{s}_{n_p}^2 - \langle n_p \rangle}{G^2} \right] = 2 \frac{\Gamma_g r_{st,em} \langle n_p \rangle}{G^2} = \frac{2}{\Delta \mathbf{n}_o} \frac{d}{dz} \left[\frac{\langle n_p \rangle^2}{G^2} \right] \quad (4.60).$$

The first equality intuitively expresses that the source of excess noise, i.e., noise not related to pure signal quantization, but introduced by some optical process, is generated by the random occurrence of the stimulated emission events which provide gain to the entire photon number, i.e, to the photons generated by amplification of the input signal and to the photons generated by amplification of the spontaneous emission coupled into guided modes. The second equality, valid only in the flat-band approximation, allows us to connect immediately the results from this model with the classical wave-like approach, since the result of the integration of the RHS will produce the so-called spontaneous-signal and spontaneous-spontaneous beat noise terms.

Note finally that the value whose derivative constitutes the LHS of (4.60) could be understood as a position-dependent “excess photon noise referred to the input”, in the sense that it is equal to the excess noise at each point in the device, divided by the square of the gain that the average photon number has experienced from the input up to that particular position. In other words, for each position in the device, it expresses the excess photon noise at the input that would produce, after the same amplification in an ideal amplifier, the same total noise at that given position.

The initial condition for (4.60) is obviously given by:

$$\left. \frac{\mathbf{s}_{n_p}^2(z) - \langle n_p(z) \rangle}{G^2(z)} \right|_{z=0} = \mathbf{s}_{n_p}^2(0) - \langle n_p(0) \rangle \quad (4.61).$$

Note that, for an input obeying Poisson statistics, this term is zero. Otherwise, it will depend on the particular probability distribution describing the optical input.

In summary, the new noise model describes the photon number variance in complete agreement with previous, well-established results. It shows how the physical origin of the photon number noise has two sources: signal quantization (responsible for the shot noise contribution) and randomness in the amplification process. Intuitive interpretations of the intermediate and final equations describing the evolution of the photon variance were also offered. The evolution of the covariance between electron and photon numbers will be calculated next.

Evolution of the covariance between photon and electron numbers

As shown in (4.46), the calculation of the evolution of the electron number variance requires the knowledge of the evolution of the covariance between electron and photon numbers. The equation describing the latter is found by making $N=N'=1$ in (4.44):

$$\frac{d\langle n_p n_e \rangle}{dz} = \Delta g \langle n_p n_e \rangle + \Gamma_{g^{st,em}} \Delta \mathbf{n}_o \langle n_e \rangle + \Gamma_{a^a} \mathbf{a} \langle n_p^2 \rangle - \Gamma_{a^a} \mathbf{a} \langle n_p \rangle \quad (4.62).$$

An intuitive interpretation of this equation from a Langevin point of view is possible. In order to do that, let us consider the following associations:

$$\left\langle n_e \frac{dn_p}{dz} \right\rangle \leftrightarrow \left\langle n_e \left[\Delta g n_p + \Gamma_{g^{st,em}} \Delta \mathbf{n}_o \right] \right\rangle = \Delta g \langle n_e n_p \rangle + \Gamma_{g^{st,em}} \Delta \mathbf{n}_o \langle n_e \rangle \quad (4.63);$$

$$\left\langle n_p \frac{dn_e}{dz} \right\rangle \leftrightarrow \left\langle n_p \Gamma_a \mathbf{a} n_p \right\rangle = \Gamma_a \mathbf{a} \left\langle n_p^2 \right\rangle \quad (4.64).$$

Note that these are just intuitive associations. The double arrow can never be substituted by an equal sign. They help, however, to understand that the first three terms in the RHS of (4.62) describe the evolution of the correlation between electron and photon numbers due to the evolution of their respective average values. The last term must therefore represent the noise source. Note that it is equal, with negative sign, to the rate at which photons are annihilated to generate electrons, i.e., to the rate of the process that couples the electron and the photon numbers, with negative sign. This is also consistent with a Langevin noise description. Regrouping terms in (4.62) produces finally the evolution equation for the covariance:

$$\frac{d\mathbf{s}_{n_p, n_e}}{dz} = \Delta g \mathbf{s}_{n_p, n_e} + \Gamma_a \mathbf{a} \left[\mathbf{s}_{n_p}^2 - \left\langle n_p \right\rangle \right] \quad (4.65).$$

In other words, the source of the increase in the covariance is the absorption of excess photon fluctuations. This equation may be further transformed into

$$\frac{d}{dz} \left[\frac{\mathbf{s}_{n_p, n_e}}{G} \right] = \frac{\mathbf{s}_{n_p}^2 - \left\langle n_p \right\rangle}{G^2} \frac{d\mathbf{h}}{dz} \quad (4.66).$$

We may recognize that the first factor in the RHS of (4.66) is what we called earlier the “excess photon noise referred to the input”. Similarly, we may call “covariance referred to the input” the value whose derivative constitutes the LHS. It is interesting to note that the source of the “covariance referred to the input” is the “excess photon noise referred to the input”. In other words, the degree of correlation

between the electron and photon populations is affected only by the excess optical noise generated during the amplification process.

The initial condition for (4.66) is trivially given by:

$$\left. \frac{\mathbf{s}_{n_p, n_e}(z)}{G(z)} \right|_{z=0} = 0 \quad (4.67),$$

since no photocurrent has been generated yet at $z=0$, and thus the electron population is identically zero.

In summary, we have discussed the intuitive interpretation and found the simplest form of the equation describing the covariance between electron and photon numbers. Proper association of terms shows that this equation is consistent with a Langevin noise description, and that the source of excess correlation between electron and photon numbers is due to the absorption of excess photon fluctuations. We will now use these results to characterize the electron variance.

Evolution of the electron number variance

Performing the substitution $N=2$ in (4.46) results in

$$\frac{d\langle n_e^2 \rangle}{dz} = 2\Gamma_a \mathbf{a} \langle n_p n_e \rangle + \Gamma_a \mathbf{a} \langle n_p \rangle \quad (4.68).$$

Similarly as in the case of the covariance between electron and photon numbers, we can perform now the following association:

$$\left\langle \frac{dn_e^2}{dz} \right\rangle \leftrightarrow 2 \left\langle n_e \frac{dn_e}{dz} \right\rangle \leftrightarrow 2 \left\langle n_e \Gamma_a \mathbf{a} n_p \right\rangle = 2 \Gamma_a \mathbf{a} \left\langle n_p n_e \right\rangle \quad (4.69).$$

The first term in the RHS of (4.68) represents thus the rate of change of the electron number squared, once the rate of change of the average electron number is known. The second term is equal to the rate at which electrons are generated, i.e., the autocorrelation of the Langevin noise source associated to the averaged-squared electron number. Rearranging terms in (4.68) allows us to find a simple equation describing the evolution of the electron number excess noise:

$$\frac{d \left[\mathbf{s}_{n_e}^2 - \langle n_e \rangle \right]}{dz} = 2 \frac{\mathbf{s}_{n_p, n_e}}{G} \frac{d\mathbf{h}}{dz} \quad (4.70).$$

The source of the electron number excess noise is thus what we have called the “covariance referred to the input”.

Since no photocurrent has been generated at $z=0$, the electron population is identically zero, and the initial condition is thus trivially given by

$$\left[\mathbf{s}_{n_e}^2(z) - \langle n_e(z) \rangle \right] \Big|_{z=0} = 0 \quad (4.71).$$

Note that the combination of (4.60), (4.66) and (4.70), with the initial conditions (4.61), (4.67) and (4.71), forms a system of equations solvable by direct integration, where the solution of one equation is inserted directly into the next.

In conclusion, it has been shown in this paragraph how, starting from the central equation (4.44) in the new noise model for distributed amplifier-photodetectors,

equations may be found that allow us, through direct integration, to find the evolution of the photon and electron number variance, and their covariance, thus describing the evolution of noise in the simultaneous or alternating presence of gain and absorption. Intermediate equations were used to find an intuitive interpretation of such evolution, showing how the excess photon noise is the source of an excess correlation between electron and photon numbers; this excess correlation is in turn the source of an excess noise in the electron number. Comparison was also made intuitively between the results from the new model and a Langevin interpretation, showing how the rates of the different processes affecting the electron and photon numbers may be understood as the autocorrelation functions of the noise sources.

Consistency of the new noise model with previous models

In the previous section, the new noise model for distributed amplifier-photodetectors has been described in detail. The equations describing the evolution of the average value, variance and covariance of the electron and photon number are intuitively sound. There is good agreement between them and the intuitive picture that one may paint by looking conceptually at the distributed combination of gain and absorption, from the points of view of noise sources and correlation between electron and photon numbers. Before this model may be admitted as a valid description, however, its consistency with previous noise models need to be established. In order to do that, it will be shown in this section how the photon statistics master equation may produce the same equations for the evolution of the photon number statistics,

provided that the absorption of photons in the detection region is considered as an additional optical loss. It will be also shown that, in the absence of optical amplification, i.e., when stimulated emission and absorption and spontaneous emission in the amplifier do not exist, the new noise model provides the same description of the evolution of the electron and photon statistics as Bernoulli's sampling formula. Part of the mathematical development necessary for this proof is included in appendix C.

Consistency with the photon statistics master equation

At the beginning of this chapter, noise in traditional SOAs was briefly addressed. The best description of the photon number statistics in a traditional SOA is probably offered by the photon statistics master equation or forward Kolmogorov equation (4.14). Note that this equation offers the description of the evolution of the photon number probability distribution, whereas the new noise model offers the description of the evolution of the moments of the photon number probability distribution through (4.45). In the photon statistics master equation, a is the probability of an amplification event happening per unit length and per incoming photon, b the probability of a photon loss event, also per unit length and per incoming photon, and c is the probability of a spontaneous emission event happening per unit length. In that sense, and for the purposes of studying the evolution of the optical signal in distributed amplifier-photodetectors, we can make the following identifications:

$$a = \Gamma_g r_{st,em} \quad (4.72).$$

$$b = \Gamma_g r_{st,ab} + l + \Gamma_a \mathbf{a} \quad (4.73).$$

$$c = \Gamma_g r_{st,em} \Delta \mathbf{n}_o \quad (4.74).$$

Note that these equalities are not mere associations, but identities that hold in a flat-band approximation. They allow us to rewrite the equations resulting from the new noise model as

$$\begin{aligned} \frac{d \langle n_p^N \rangle}{dz} = & a \sum_{i=0}^{N-1} \binom{N}{i} \langle n_p^{i+1} \rangle + b \sum_{i=0}^{N-1} (-1)^{N-i} \binom{N}{i} \langle n_p^{i+1} \rangle \\ & + c \sum_{i=0}^{N-1} \binom{N}{i} \langle n_p^i \rangle \end{aligned} \quad (4.75).$$

Using the linearity of the averaging operation, and Newton's binomial formula, we can write the following relation:

$$\begin{aligned} \sum_{i=0}^{N-1} \binom{N}{i} \langle n_p^{i+1} \rangle &= \sum_{i=0}^N \left\langle \binom{N}{i} n_p^{i+1} \right\rangle - \langle n_p^{N+1} \rangle \\ &= \langle n_p (n_p + 1)^N - n_p^{N+1} \rangle \end{aligned} \quad (4.76).$$

The other sums in (4.75) may also be rewritten in a similar way, leading to

$$\begin{aligned} \frac{d \langle n_p^N \rangle}{dz} = & a \langle n_p (n_p + 1)^N - n_p^{N+1} \rangle + b \langle n_p (n_p - 1)^N - n_p^{N+1} \rangle \\ & + c \langle (n_p + 1)^N - n_p^N \rangle \end{aligned} \quad (4.77).$$

The photon statistics master equation produces the exact same evolution equation.

In order to prove that, we may express the LHS of (4.75) as

$$\frac{d\langle n_p^N \rangle}{dz} = \frac{d}{dz} \sum_{n=0}^{\infty} n^N P_n = \sum_{n=0}^{\infty} n^N \frac{dP_n}{dz} \quad (4.78).$$

We may now insert into it the photon statistics master equation (4.14):

$$\begin{aligned} \frac{d\langle n_p^N \rangle}{dz} = & a \sum_{n=0}^{\infty} \left[n(n+1)^N - n^{N+1} \right] P_n \\ & + b \sum_{n=0}^{\infty} \left[n(n-1)^N - n^{N+1} \right] P_n + c \sum_{n=0}^{\infty} \left[(n+1)^N - n^N \right] P_n \end{aligned} \quad (4.79).$$

Obviously, the RHS of (4.79) and the RHS of (4.77) are equal, given the expression of the average value of a function that depends on a statistical variable, as shown through (4.10). This identification confirms that all the moments of the photon distribution are identically described by the photon statistics master equation and by the new noise model. Equivalently, the photon statistics described by both models are also identical, which proves their equivalence.

In conclusion, we have shown that the new noise model produces the same description of the photon statistics in a device featuring distributed amplification and absorption of light as the photon statistics master equation. The only assumption for this equivalence was the identification of light absorption in the detector region with another source of optical loss, which is intuitively perfectly valid from the point of view of light propagation and amplification.

Consistency with Bernoulli's sampling formula

For a pure photodetector, there does not exist any emission (stimulated or spontaneous), or stimulated absorption other than in the detector active region, which allows us to write $r_{st,em}=r_{st,ab}=r_{sp}=0$. The evolution equation for the average photon number and its variance can then be rewritten as:

$$\frac{d\langle n_p \rangle}{dz} = -(\Gamma_a \mathbf{a} + l)\langle n_p \rangle \quad (4.80).$$

Together with (4.35), it is then clear that we can rewrite (4.44)-(4.46) as

$$\frac{d}{dz} \left[\frac{\mathbf{s}_p^2 - \langle n_p \rangle}{\langle n_p \rangle^2} \right] = 0 \quad (4.81),$$

$$\frac{d}{dz} \left[\frac{\langle n_p n_e \rangle - \langle n_p \rangle \langle n_e \rangle}{\langle n_p \rangle} \right] = \frac{d\langle n_e \rangle}{dz} \left[\frac{\mathbf{s}_p^2 - \langle n_p \rangle}{\langle n_p \rangle^2} \right] = \frac{d}{dz} \left[\langle n_e \rangle \frac{\mathbf{s}_p^2 - \langle n_p \rangle}{\langle n_p \rangle^2} \right] \quad (4.82),$$

$$\begin{aligned} \frac{d[\mathbf{s}_e^2 - \langle n_e \rangle]}{dz} &= 2 \left[\frac{\langle n_e n_p \rangle - \langle n_e \rangle \langle n_p \rangle}{\langle n_p \rangle} \right] \frac{d\langle n_e \rangle}{dz} \\ &= \frac{d}{dz} \left[\langle n_e \rangle^2 \frac{\mathbf{s}_p^2 - \langle n_p \rangle}{\langle n_p \rangle^2} \right] \end{aligned} \quad (4.83).$$

The solution of the last equation is

$$\begin{aligned} \mathbf{s}_e^2(z) &= \langle n_e(z) \rangle + \langle n_e(z) \rangle^2 \frac{\mathbf{s}_p^2(0) - \langle n_p(0) \rangle}{\langle n_p(0) \rangle^2} \\ &= \mathbf{h}(z) \langle n_p(0) \rangle + \mathbf{h}^2(z) [\mathbf{s}_p^2(0) - \langle n_p(0) \rangle] \end{aligned} \quad (4.84),$$

where a cumulative efficiency $\mathbf{h}(z)$ has been defined, as always, by

$$\mathbf{h}(z) = \frac{\langle n_e(z) \rangle}{\langle n_p(0) \rangle} \quad (4.85).$$

The result (4.52) is the same as the variance found for a photodetector through Bernoulli's sampling formula. Note that, in order to prove the result, we have assumed the initial condition that both the average value of $n_e(z)$, and both its autocorrelation and its cross-correlation with $n_p(z)$ are zero at $z=0$, which is true since no photocurrent has been generated at that point yet.

The new model can be furthermore proved to provide exactly the same moments for the electron population statistics given any arbitrary input photon statistics. In order to do this, we define the following family of polynomials:

$$Q_N[x] = x(x-1)(x-2)\dots(x-N+1) = \prod_{k=0}^{N-1} (x-k) \quad (4.86).$$

We complete this definition with $Q_0[x]=1$. From Bernoulli's sampling formula we can find that

$$\begin{aligned} \langle Q_N[n_e] \rangle &= \sum_{m=0}^{\infty} m(m-1)\dots(m-N+1) P'_m \\ &= \sum_{n=N}^{\infty} N! \binom{n}{N} \mathbf{h}^N P_n \sum_{m=N}^n \binom{n-N}{m-N} \mathbf{h}^{m-N} (1-\mathbf{h})^{n-m} \\ &= \mathbf{h}^N \sum_{n=0}^{\infty} n(n-1)\dots(n-N+1) P_n = \mathbf{h}^N \langle Q_N[n_p] \rangle \end{aligned} \quad (4.87).$$

Note that, due to the definitions involved in Bernoulli's sampling formula, n_e and \mathbf{h} can be taken at any position z of the detector, but n_p is the initial photon number, and stands in (4.87) for $n_p(0)$.

Making again $r_{st,em}=r_{st,ab}=r_{sp}=0$ in (4.40), we find that the equation for the evolution of the electron and photon number statistics according to our new model can be written as

$$\begin{aligned} \frac{d \langle n_p^N n_e^{N'} \rangle}{dz} &= (\Gamma_a \mathbf{a} + l) \sum_{i=0}^{N-1} (-1)^{N-i} \binom{N}{i} \langle n_p^{i+1} n_e^{N'} \rangle \\ &+ \Gamma_a \mathbf{a} \sum_{i=0}^N \sum_{j=0}^{N'-1} (-1)^{N-i} \binom{N}{i} \binom{N'}{j} \langle n_p^{i+1} n_e^j \rangle \end{aligned} \quad (4.88).$$

After some mathematical development (see Appendix C), we find that this set of equations is equivalent to the following set:

$$\frac{d}{dz} \left[\frac{\langle \mathcal{Q}_N [n_p(z)] \mathcal{Q}_{N'} [n_e(z)] \rangle}{\langle n_p(z) \rangle^N} \right] = \frac{\langle \mathcal{Q}_{N+N'} [n_p(0)] \rangle}{\langle n_p(0) \rangle^{N+N'}} \frac{d \langle n_e(z) \rangle^{N'}}{dz} \quad (4.89).$$

The solution of the previous equation, assuming once more that the average electron number and any correlation product involving n_e are zero at $z=0$, is (for $N=0$)

$$\langle \mathcal{Q}_{N'} [n_e(z)] \rangle = \mathbf{h}^{N'}(z) \langle \mathcal{Q}_{N'} [n_p(0)] \rangle \quad (4.90).$$

Comparing this result to (4.55), we find it to be equal to the one obtained with Bernoulli's formula. The electron statistics for a pure photodetector found with Bernoulli's formula are thus exactly the same as those found with the new model.

In this section, we have presented the new noise model developed to describe the evolution of electron and photon population statistics in a device featuring both amplification and absorption, and we have compared it to previous, well-established models for the limiting cases of a pure SOA and a pure photodetector, finding exact agreement between their results, thus confirming the validity, in those cases, of the new model.

Fundamental noise limits for amplifier-photodetectors in a quasi-constant optical power regime

Since the concept of distributed combination of amplification and photodetection is new, it is interesting at this point to predict the fundamental limitations introduced by this technique, in terms of noise.

If the gain per unit length is negative and large in absolute value, it has already been shown that the device performance is below optimum, since the efficiency is not much greater than for traditional passive photodetectors, with the addition of a comparatively large background current. If the gain per unit length is comparable to the amplification rate $\Gamma_{g,rs,em}$, the behavior of the TAP detector is similar to that of a traditional detector with optical preamplification. Both these cases were shown to have these respective behaviors in chapter 2. We will thus restrict ourselves at this point to the case where the net gain per unit length is close to zero all along the device, i.e., the case where the cumulative gain may be approximated by one.

Under these assumptions, it was already shown in chapter 2 how both the efficiency and the ASE power generated in the active region are proportional to either the device length, in TAP detectors with transverse coupling, or to the number of sections, in devices featuring alternating gain and absorption. Therefore, from equation (4.60), and making $G=1$, we can identify the two terms in the expression for the excess noise as being either linear with position along the device or with the number of sections (for the so-called spontaneous-signal beat noise) or quadratic (for the so-called spontaneous-spontaneous beat noise). The optimum limit will be reached when the signal-spontaneous beat term dominates, since that would be a symptom that the signal power is always significantly larger than the background power. Under this condition, we can estimate to the first order that the excess optical noise will grow proportionally with either the device length, or the number of sections. This, in turn, results in the electron-photon number covariance evolving as a quadratic function of device position or number of sections (see equation (4.66) with $G=1$), and the electron number variance following a cubic law of either of these two parameters. With all these previous approximations, we can perform the following approximation for devices with transverse coupling, and of any length L , valid only when the net gain per unit length is close to zero (and thus when the device quantum efficiency is proportional to its length):

$$NF(L) = \frac{\langle n_p(0) \rangle^2 \mathbf{s}_{n_e}^2(L)}{\mathbf{s}_{n_p}^2(0) \langle n_e(L) \rangle^2} \propto \frac{L^3}{L^2} \propto \mathbf{h}(L) \quad (4.91).$$

In other words, in TAP detectors with transverse coupling, the noise figure will be proportional to the device efficiency. An equation analogous to (4.91) may be written by changing the device length L by the number of sections N in a TAP detector with alternating gain and absorption. An interesting trade-off is thus established, which will be analyzed in more detail in the next chapter, when the different noise contributions are quantified. This will allow us to set limits to the range of values of the input power and device length for which this approximation is valid, as well as quantifying the proportionality constant between the noise figure and the device efficiency.

Summary

In this chapter, a new noise model describing the evolution of electron and photon statistics in the presence of amplification and photodetection was presented. The need for this model was justified after a brief review of the most commonly used noise descriptions for amplifiers and detectors, as well as a discussion on the need to quantify the correlation between electron and photon numbers in the presence of processes not describable as random sampling. The model was then presented, showing how the evolution of the electron and photon statistics may be calculated. This new noise description was then compared with previously existing models, showing that it predicts the same results as the photon statistics master equation for conventional SOAs. In the case of traditional photodetectors, it was shown that the

new model is fully equivalent to Bernoulli's sampling equation. Finally, the new model is used to predict a trade-off between efficiency and noise figure.

References

- [1] D.G. Kendall, "On the generalized "birth-and-death" process," *Annals of Mathematical Statistics*, vol. 19, issue 1, pp. 1-15, 1948.
- [2] K. Shimoda, H. Takahasi and C.H. Townes, "Fluctuations in amplification of quanta with application to maser amplifiers," *Journal of the Physical Society of Japan*, vol. 12, n. 6, p. 686, 1957.
- [3] L.A. Coldren, S.W. Corzine, "Diode lasers and photonic integrated circuits," *John Wiley & Sons*, 1995.
- [4] E. Desurvire, "Comments on "The Noise Figure of Optical Amplifiers"," *IEEE Photonics Technology Letters*, vol. 11, no. 5, pp. 620-1, 1999.
- [5] S. Donati, G. Giuliani, "Noise in an Optical Amplifier: Formulation of a New Semiclassical Model," *IEEE Journal of Quantum Electronics*, vol. 33, no. 9, pp. 1481-8, 1997.
- [6] E. Desurvire, "Erbium-doped fiber amplifiers: principles and applications," *John Wiley & Sons*, 1994.
- [7] M.O. Scully and W.E. Lamb, "Quantum theory of an optical maser III. Theory of photoelectron counting statistics," *Physical Review*, vol. 179, n. 2, p. 368-74, 1969.

CHAPTER 5

Noise properties of TAP detectors

In order to describe the noise characteristics of Traveling-wave Amplifier Photodetectors (TAP detectors), a new distributed particle-like noise model has been developed. This model was described in detail in chapter 4. In this chapter, the results of its application to the TAP detector configurations studied in this dissertation will be presented. First, the need to take into account both forward- and backward-propagating signals, and the simplifications used to do so, will be presented. Then, the noise introduced by the coupling efficiency into the device, and the effect of the initial amplification region (whenever it exists) will be discussed. Next, the new noise model presented in the previous chapter will be applied to TAP detectors with alternating gain and absorption, and then to devices with transverse coupling. Finally, conclusions will be drawn as to the effect of noise, paying especial attention to the trade-off between efficiency and noise figure.

Forward- and backward-propagating optical signals

In the presence of distributed amplification and absorption, amplified spontaneous emission (ASE) is generated both co-propagating and counter-propagating with respect to the input signal. In chapter 2, it was shown that the effect of both needs to be taken into account when studying the background current of TAP detectors. The inclusion of both is thus necessary also to fully describe the noise characteristics of these devices.

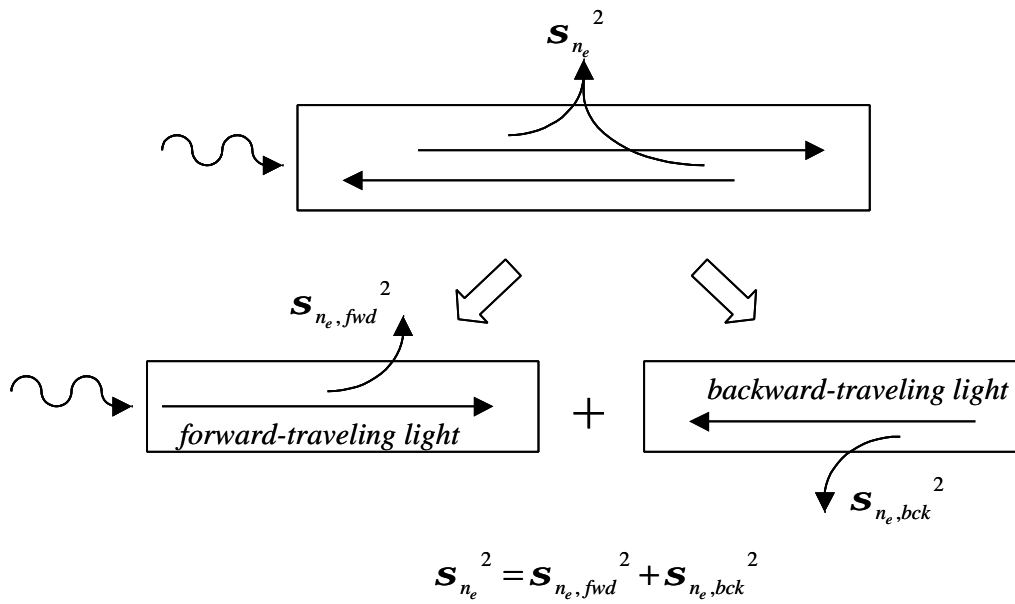


Figure 5.1: Representation of a single device with forward- and backward-propagating light as two different devices. The device representing the effect of back-propagating light presents no optical input. The electron number variances found from both devices may then be added to find the total electron number variance for the entire device. Note that this figure shows only forward- and backward-propagating light. Each one of these two will in turn generate forward- and backward-propagating photocurrent, as discussed in chapter 3.

A major simplification is however possible, since forward- and backward-propagating ASE terms are uncorrelated with one another. We may thus assume that a TAP detector is made by the juxtaposition of two fictitious devices, where light propagates only forward or backward, as shown in figure 5.1.

The photocurrent noise generated by the forward- and backward-propagating optical signals may be found separately, then added to find the total photocurrent noise. This simplification is possible due to the statistical independence between both noise components, which is in turn caused by the statistical independence between forward- and backward-propagating optical signals. This independence requires, of course, that no feedback exists between both components, i.e., no optical reflections exists at either end of the device. We may therefore analyze the noise in TAP detectors by considering only forward-propagating light in two different devices, the actual device that we are simulating and the device resulting from exchanging input and output. As shown in chapter 4, under this assumption the evolution of electron and photon number average values, and their variances and covariance, are described by the following equations:

$$\frac{d}{dz} \left[\frac{\langle n_p(z) \rangle}{G(z)} \right] = \Delta \mathbf{n}_o \frac{\Gamma_g(z) r_{st,em}(z)}{G(z)} \quad (5.1).$$

$$\frac{d \langle n_e(z) \rangle}{dz} = \frac{\langle n_p(z) \rangle}{G(z)} \frac{d\mathbf{h}(z)}{dz} \quad (5.2).$$

$$\frac{d}{dz} \left[\frac{\mathbf{s}_{n_p}^2(z) - \langle n_p(z) \rangle}{G^2(z)} \right] = \frac{\Gamma_g(z) r_{st,em}(z) \langle n_p(z) \rangle}{G^2(z)} = \frac{1}{\Delta \mathbf{n}_o} \frac{d}{dz} \left[\frac{\langle n_p(z) \rangle^2}{G^2(z)} \right] \quad (5.3).$$

$$\frac{d}{dz} \left[\frac{\mathbf{s}_{n_p, n_e}(z)}{G(z)} \right] = \frac{\mathbf{s}_{n_p}^2(z) - \langle n_p(z) \rangle}{G^2(z)} \frac{d\mathbf{h}(z)}{dz} \quad (5.4).$$

$$\frac{d \left[\mathbf{s}_{n_e}^2(z) - \langle n_e(z) \rangle \right]}{dz} = 2 \frac{\mathbf{s}_{n_e, n_p}(z)}{G(z)} \frac{d\mathbf{h}(z)}{dz} \quad (5.5).$$

The initial conditions to these equations depend on many factors. One of them is whether forward- or backward-propagating light is being considered. Another one is the presence or absence of an initial amplification section. The coupling efficiency into the device plays a role too. In order to take into account all these effects, we will introduce the coordinate system shown in figure 5.2. Let z be, as always, the direction of propagation, its value being 0 at the device input and L at the device output. However, we will define the device input and output, for the purposes of noise calculation, as the beginning and the end of the absorption sections, i.e., there is no absorption for $z < 0$ or for $z > L$, but for any value of z strictly contained between these two, photocurrent is generated at some location between 0 and z , and between z and L . Amplification may also exist for $0 < z < L$.

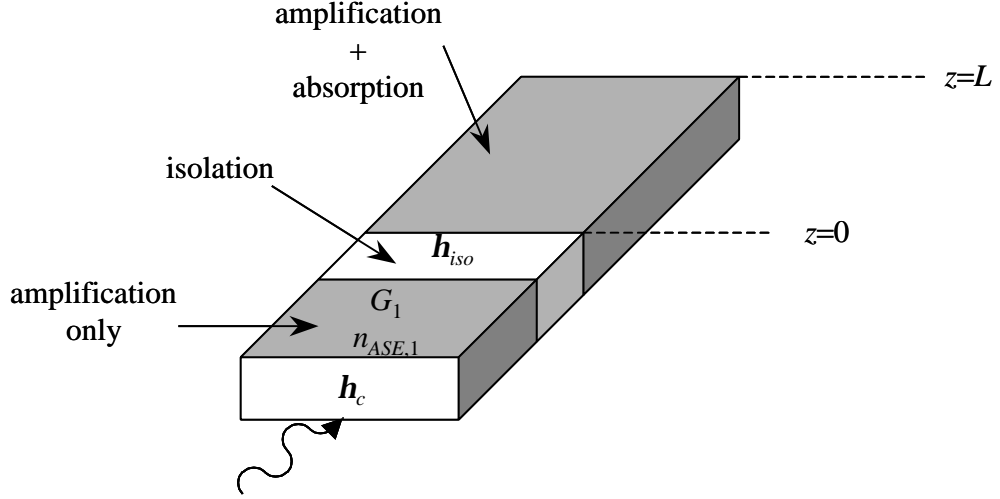


Figure 5.2: Choice of coordinates for TAP detectors for the purposes of noise calculation. The initial conditions for the backward-propagating optical signal include all average values and variances being zero at $z=L$. The initial conditions for the forward-propagating optical signal include the average electron number, the electron number variance and the covariance between electron and photon numbers being zero at $z=0$. Indicated in the figure are the coupling efficiency h_c , the gain of the initial amplification region G_1 , the average photon number $n_{ASE,1}$ generated in it in the form of forward-traveling ASE, and the fraction of photons h_{iso} that survive the isolation region between the initial gain section and the rest of the device.

With this choice of coordinates, it is obvious that no photocurrent is generated by forward-propagating light for negative values of z , resulting in

$$\mathbf{s}_{n_e}^2(0) = \mathbf{s}_{n_e, n_p}(0) = \langle n_e(0) \rangle = 0 \quad (5.6).$$

For the fictitious device that allows us to take into account the noise contribution generated by the backward-propagating light, the roles of 0 and L are reversed. Assuming that there is no further amplification for the forward-propagating light when the absorption ends, we can assume that no backward-propagating light is generated in what would be negative values of z in said fictitious device, resulting in

$$\mathbf{s}_{n_p}^2(0) = \langle n_p(0) \rangle = 0 \quad (5.7).$$

Let us now consider only forward-propagating light. As shown in figure 5.2, the most general incarnation of a TAP detector features an input with a certain coupling coefficient, followed by an initial amplification section that may or may not exist, and finally an isolation section between this one and the beginning of the absorption at $z=0$. This obviously results in the following initial conditions for the noise generated by the forward-propagating light:

$$\langle n_p(0) \rangle = \mathbf{h}_{iso} G_1 \mathbf{h}_c \langle n_p \rangle_{in} + \mathbf{h}_{iso} (n_{p,ASE})_1 \quad (5.8).$$

$$\begin{aligned} \mathbf{s}_{n_p}^2(0) = & \langle n_p(0) \rangle + \mathbf{h}_{iso}^2 G_1^2 \mathbf{h}_c^2 \left[(\mathbf{s}_{n_p}^2)_{in} - \langle n_p \rangle_{in} \right] \\ & + \frac{2}{\Delta \mathbf{n}_o} \mathbf{h}_{iso}^2 G_1 \mathbf{h}_c \langle n_p \rangle_{in} (n_{p,ASE})_1 + \frac{1}{\Delta \mathbf{n}_o} \left[\mathbf{h}_{iso} (n_{p,ASE})_1 \right]^2 \end{aligned} \quad (5.9).$$

In these equations, \mathbf{h}_c is the input coupling efficiency, G_1 the gain of the initial amplification section, $(n_{p,ASE})_1$ the average photon number per unit time generated inside it in the form of forward-propagating ASE, \mathbf{h}_{iso} the fraction of photons that survive the isolation region and $\langle n_p \rangle_{in}$ the average input photon number per unit time.

Note that the right hand side (RHS) of equation (5.9) contains several terms, expressing the contributions from shot noise (first term), the coupling and amplification or attenuation experienced by the input noise (second term), and the gain fluctuations in the initial amplification section, if this one exists (third and fourth terms). All these contributions are thus taken into account by using (5.8) and (5.9) as the initial conditions for the calculation of the noise generated by the forward-

propagating light. Note that the case where no initial amplification section exists is described simply by making $G_1=1$, $(n_{p,ASE})_1=0$ and $\mathbf{h}_{iso}=1$ in (5.8), (5.9).

In conclusion, in this section the formalism necessary to take into account the effect of both forward- and backward-propagating light has been introduced. The initial conditions necessary to take into account the effect of coupling loss and an initial amplification sections have also been described. In the next section, the effect of the coupling loss and the initial gain section will be discussed, using these initial conditions as a starting point.

Effect of coupling loss and initial amplification section

In the previous section, initial conditions for the equations describing the generation of noise in the presence of distributed amplification and photodetection were introduced. These initial conditions are affected by the coupling loss, and by the characteristics, and the presence or absence, of an initial gain section. This section will discuss these effects in the total noise generated by the device, more specifically in its noise figure.

One important characteristic of the noise figure is its dependence on both the input noise and the average value of the input signal. As an example, let us consider the noise figure NF_1 associated to the initial gain section, including the coupling efficiency into the device, and the effect of the isolation section, which may be thought of as an output coupling efficiency:

$$\begin{aligned}
NF_1 &= \frac{\langle n_p \rangle_{in}^2 \mathbf{s}_{n_p}^2(0)}{\left(\mathbf{s}_{n_p}^2\right)_{in} \left[\mathbf{h}_{iso} G_1 \mathbf{h}_c \langle n_p \rangle_{in}\right]^2} \\
&= 1 + \frac{\langle n_p \rangle_{in}}{\left(\mathbf{s}_{n_p}^2\right)_{in}} \left[2 \frac{\left(n_{p,ASE}\right)_1}{\mathbf{h}_c G_1 \Delta \mathbf{n}_o} + \frac{1}{\mathbf{h}_c G_1 \mathbf{h}_{iso}} - 1 \right] \\
&\quad + \frac{\left(n_{p,ASE}\right)_1}{\left[\mathbf{h}_c G_1\right]^2 \left(\mathbf{s}_{n_p}^2\right)_{in}} \left[\frac{1}{\mathbf{h}_{iso}} + \frac{\left(n_{p,ASE}\right)_1}{\Delta \mathbf{n}_o} \right]
\end{aligned} \tag{5.10}.$$

The average input photon number and its variance obviously affect the noise figure. Intuitively, if the input signal is very noisy, the degradation produced by the introduction of a fixed amount of additional noise is not as significant as when the input signal is close to being noise-free. Furthermore, the effect of any noise contribution independent on the input signal will become smaller as the input signal grows stronger. The combination of these two effects results in the well-known formula for a chain of amplifiers:

$$NF = NF_1 + \frac{NF_2 - 1}{G_1} + \dots + \frac{NF_n - 1}{G_1 G_2 \dots G_{n-1}} \tag{5.11},$$

where NF is the noise figure of the entire chain, which consists of n amplifiers of gains G_i , and noise figures NF_i , where i is any integer between 1 and n . This formula is strictly valid for electrical amplifiers as long as the total noise generated may be expressed as the sum of the amplified input noise and an excess noise term independent on the input signal, G_i being the power gain of the electrical amplifier, i.e., the signal (current or voltage) gain squared.

In optical amplifiers, this same equation may be obtained, but its meaning is slightly different. Equation (5.11) results after assuming that the gain provided by the first amplifier is large enough for the signal-spontaneous beat noise term to dominate for all other elements in the chain. G_i would be in this case the optical power gain, i.e., the signal gain. Equation (5.11) may not thus be applied blindly, and either assumptions need to be made about the input noise, or the resulting noise figure needs to be expressed as a function of it. It is customary, however, to consider that any optical signal will exhibit Poisson statistics after propagation over long distances, i.e.:

$$\left(\mathbf{s}_{n_p}\right)_{in} = \langle n_p \rangle_{in} \quad (5.12).$$

This assumption will be used throughout the rest of this chapter.

Let us now consider the particular case where no initial amplification section exists:

$$\langle n_p(0) \rangle = \mathbf{h}_c \langle n_p \rangle_{in} \quad (5.13).$$

$$\mathbf{s}_{n_p}^2(0) = \mathbf{h}_c(1 - \mathbf{h}_c) \langle n_p \rangle_{in} + \mathbf{h}_c^2 \left(\mathbf{s}_{n_p}^2\right)_{in} \quad (5.14).$$

Calling NF_{TAP} the noise figure describing the effect of the combination of distributed amplification and absorption (i.e., the effect of the device section contained between $z=0$ and $z=L$), and NF the noise figure for the device, including the effect of coupling efficiency, we can write:

$$NF_{TAP} = \frac{\left[\mathbf{h}_c \langle n_p \rangle_{in} \right]^2}{\mathbf{s}_{n_p}^2(0)} \frac{\mathbf{s}_{n_e}^2(L)}{\left[\mathbf{h}(L) \mathbf{h}_c \langle n_p \rangle_{in} \right]^2} = \frac{\mathbf{s}_{n_e}^2(L)}{\mathbf{h}^2(L) \mathbf{h}_c \langle n_p \rangle_{in}} \quad (5.15).$$

$$NF = \frac{\langle n_p \rangle_{in}^2}{\left(\mathbf{s}_{n_p}^2 \right)_{in}} \frac{\mathbf{s}_{n_e}^2(L)}{\left[\mathbf{h}(L) \mathbf{h}_c \langle n_p \rangle_{in} \right]^2} = \frac{NF_{TAP}}{\mathbf{h}_c} \quad (5.16).$$

In these equations, $\mathbf{h}(L)$ is the efficiency from the device from $z=0$ to $z=L$, i.e., the ratio between the photocurrent generated from $z=0$ to $z=L$ by the signal (disregarding the contribution to the current from the absorption of spontaneous emission or ASE) and the optical power coupled into the device at $z=0$, expressed in electrons per photon. It is not possible obviously to write the output signal as $\langle n_e(L) \rangle$, since this quantity includes the contribution from ASE current and spontaneous emission current, which are not part of the desired signal.

In finding equation (5.15), it has been used that, when the input signal exhibits Poisson statistics, the optical signal at $z=0$ does too, since the coupling is a random selection process.

We can therefore conclude that the noise figure of the entire device is inversely proportional to the coupling efficiency. Furthermore, this result is independent of the nature of the device into which light is coupled, as long as the input optical signal exhibits Poisson statistics. We can therefore use (5.16) to describe the effect of the input coupling efficiency when an initial amplification section exists. In this case, the noise figure of the entire device is described by the following equation:

$$NF = \frac{NF_1}{h_c} + \frac{NF_{TAP} - 1}{h_c G_1} \quad (5.17),$$

where we have used simultaneously the noise formula for an amplifier chain (5.11), and the equation describing the effect of input coupling loss (5.16). Note that the total noise figure is again inversely proportional to the input coupling efficiency, as in traditional SOAs.

Equation (5.17) expresses very powerfully an interesting trade-off that will appear in TAP detectors featuring an initial amplification section. Even if the noise generated by the distributed combination of gain and absorption is large (i.e., even if NF_{TAP} is large), its effect may be largely reduced by the introduction of an initial amplification section with strong gain. However, this would result in saturation for smaller input optical power. In other words, a trade-off between saturation power and noise figure appears in TAP detectors featuring an initial amplification section. As mentioned in chapter 2, the presence of an initial amplification section does not affect significantly the maximum unsaturated photocurrent.

In summary, in this section the effect of input coupling and an initial amplification section has been discussed. It has been shown that the noise figure of TAP detectors is inversely proportional to the input coupling efficiency, which needs thus to be as large as possible. It has also been shown how the introduction of an initial gain section may contribute to a reduction of the noise figure, barely affecting the maximum unsaturated photocurrent, though decreasing the maximum input power allowable before the device saturates.

Once the effects of the initial amplification region and the coupling efficiency have been discussed, the following sections will concentrate in the noise generation due to the distributed combination of amplification and absorption, in the particular configurations studied in this dissertation.

Noise in TAP detectors with alternating amplification and absorption

In this section, the noise generated in TAP detectors with alternating gain and absorption will be studied. First, the electron number variance will be found, using the noise model for distributed amplifier-photodetectors introduced in the previous chapter. Next, the noise figure and the different contributions to it will be discussed, giving quantitative values and establishing a trade-off between noise figure and efficiency.

Electron number variance

For the purposes of noise calculation, we will use in this paragraph the same assumptions as for the calculation of the efficiency and the ASE current, consistently with what was presented in chapter 2. In other words, all periods will be assumed identical, and inside each one of them the stimulated emission and absorption normalized to optical intensity, or the material absorption, will be assumed to be constant.

Let us now define $\langle n_p \rangle_n$ as the average photon number arriving to the n -th absorption section per unit time, and $\langle n_e \rangle_n$ as the average number of photocurrent electrons generated by the n first detection sections per unit time, as expressed schematically in figure 5.3.

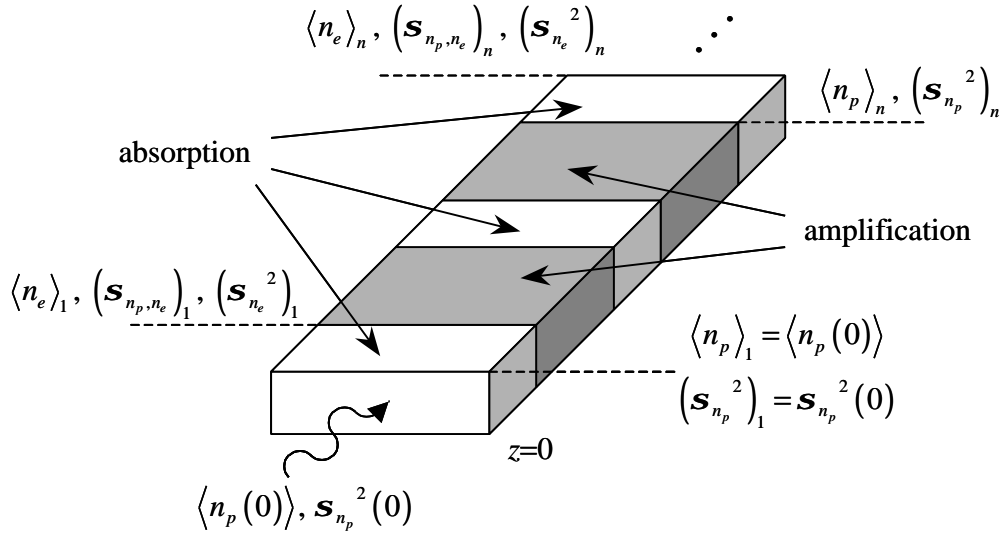


Figure 5.3: Schematic representation of a TAP detector with alternating gain and absorption for the purposes of noise calculation. The effect of the input coupling efficiency and the first gain section (when it exists) are taken into account into the signal that arrives at the beginning of the first absorption section, i.e., $z=0$. The subscript n will indicate that the corresponding value is evaluated at the n -th absorption section. Note that the average photon number and the photon number variance are evaluated at the beginning of the section, whereas the average electron number, the electron number variance and the covariance between electron and photon numbers are evaluated at the end of the same section. Given equations (5.3)-(5.5), the photon number variance referred to the input does not change in the absorption (lighter) sections, whereas the electron number variance and the covariance between the electron and photon numbers remain constant in the amplification (darker) sections.

Equations (5.1) and (5.2) are solved very similarly in the same manner used to find the optical power and photocurrent in chapter 2, yielding the following results:

$$\langle n_p \rangle_n = \Delta G^{n-1} \langle n_p(0) \rangle + \frac{\Delta G^{n-1} - 1}{\Delta G - 1} n_{ASE}^{(1)} \quad (5.18),$$

$$\langle n_e \rangle_n = \frac{\Delta G^n - 1}{\Delta G - 1} \mathbf{h}^{(1)} \langle n_p(0) \rangle + \frac{\Delta G^n - n\Delta G + n - 1}{(\Delta G - 1)^2} \mathbf{h}^{(1)} n_{ASE}^{(1)} \quad (5.19),$$

where the net gain per section ΔG and the efficiency of each detection section $\mathbf{h}^{(1)}$ have been defined identically as in chapter 2. The average number of ASE electrons generated in each amplification section that arrive to one of the immediately adjacent absorption sections, $n_{ASE}^{(1)}$, is defined as:

$$n_{ASE}^{(1)} = \mathbf{h}_{iso} \frac{\Gamma_g r_{st,em}}{\Gamma_g g - l} \left[e^{(\Gamma_g g - l)L_g} - 1 \right] \Delta \mathbf{n}_o \quad (5.20).$$

In obtaining (5.18) and (5.19), we have used the obvious initial conditions $\langle n_p \rangle_1 = \langle n_p(0) \rangle$ and $\langle n_e \rangle_1 = \mathbf{h}^{(1)} \langle n_p \rangle_1$. Equation (5.3) may be solved directly using (5.18), resulting in:

$$\begin{aligned} \left(\mathbf{s}_{n_p}^2 \right)_n - \langle n_p \rangle_n &= \Delta G^{2n-2} \left[\mathbf{s}_{n_p}^2(0) - \langle n_p(0) \rangle \right] \\ &+ 2\Delta G^{n-1} \frac{\Delta G^{n-1} - 1}{\Delta G - 1} \langle n_p(0) \rangle \frac{n_{ASE}^{(1)}}{\Delta \mathbf{n}_o} \\ &+ \left[\frac{\Delta G^{n-1} - 1}{\Delta G - 1} \right]^2 \frac{\left[n_{ASE}^{(1)} \right]^2}{\Delta \mathbf{n}_o} \end{aligned} \quad (5.21).$$

The solution of equation (5.4) can be considerably simplified in TAP detectors with alternating gain and absorption, since obviously the source terms of this equation and of (5.3) are never nonzero simultaneously. This fact produces quite trivially the following simplification:

$$\left(\frac{\mathbf{s}_{n_p, n_e}}{G}\right)_n = \left(\frac{\mathbf{s}_{n_p, n_e}}{G}\right)_{n-1} + (\mathbf{h}_n - \mathbf{h}_{n-1}) \frac{(\mathbf{s}_{n_p}^2)_n - \langle n_p \rangle_n}{\Delta G^{2n-2}} \quad (5.22),$$

where we have defined \mathbf{h}_n as the cumulative internal efficiency of the first n detection sections combined:

$$\mathbf{h}_n = \left. \frac{\langle n_e \rangle_n}{\langle n_p(0) \rangle} \right|_{n_{ASE}^{(1)}=0} = \frac{\Delta G^n - 1}{\Delta G - 1} \mathbf{h}^{(1)} \quad (5.23).$$

After some mathematical development, the following expression is found for the covariance between electron and photon numbers:

$$\begin{aligned} \left(\frac{\mathbf{s}_{n_p, n_e}}{G}\right)_n &= \mathbf{h}^{(1)} \frac{\Delta G^n - 1}{\Delta G - 1} \left[\mathbf{s}_{n_p}^2(0) - \langle n_p(0) \rangle \right] \\ &+ 2\mathbf{h}^{(1)} \frac{\Delta G^n - n\Delta G + n - 1}{(\Delta G - 1)^2} \langle n_p(0) \rangle \frac{n_{ASE}^{(1)}}{\Delta \mathbf{n}_o} \\ &+ \mathbf{h}^{(1)} \frac{(\Delta G^n - 1)(\Delta G^{n-1} + 1) - 2n\Delta G^{n-1}(\Delta G - 1) \left[n_{ASE}^{(1)} \right]^2}{\Delta G^{n-1}(\Delta G - 1)^3} \frac{1}{\Delta \mathbf{n}_o} \end{aligned} \quad (5.24).$$

The optical gain G in the denominator of the left hand side (LHS) is the gain experienced by the signal up to the end of the n -th detection section, and is therefore not equal to ΔG^{n-1} with respect to the average photon number at $z=0$, but equal to that number multiplied by the fraction of photons that survive one absorption region. If the optical loss in each of these detection regions is negligible compared to the optical absorption, and all electron-hole pairs generated are collected, this fraction is equal to $1 - \mathbf{h}^{(1)}$, resulting in:

$$\begin{aligned}
\left(\mathbf{s}_{n_p, n_e}\right)_n &= \mathbf{h}^{(1)} \left(1 - \mathbf{h}^{(1)}\right) \Delta G^{n-1} \frac{\Delta G^n - 1}{\Delta G - 1} \left[\mathbf{s}_{n_p}^2(0) - \langle n_p(0) \rangle \right] \\
&+ 2\mathbf{h}^{(1)} \left(1 - \mathbf{h}^{(1)}\right) \Delta G^{n-1} \frac{\Delta G^n - n\Delta G + n - 1}{(\Delta G - 1)^2} \langle n_p(0) \rangle \frac{n_{ASE}^{(1)}}{\Delta \mathbf{n}_o} \\
&+ \mathbf{h}^{(1)} \left(1 - \mathbf{h}^{(1)}\right) \frac{(\Delta G^n - 1)(\Delta G^{n-1} + 1) - 2n\Delta G^{n-1}(\Delta G - 1)}{(\Delta G - 1)^3} \frac{\left[n_{ASE}^{(1)}\right]^2}{\Delta \mathbf{n}_o}
\end{aligned} \tag{5.25}$$

Finally, the electron number variance may be calculated. Before doing that, equation (5.5) may also be simplified, integrating the RHS by parts and using (5.4), and profiting once more that the excess noise referred to the input is constant in the detection section, which is the only part of the device where the derivative of the efficiency is nonzero. After using (5.22) and (5.23) to provide some simplification, we find:

$$\begin{aligned}
\left[\left(\mathbf{s}_{n_e}^2\right)_n - \langle n_e \rangle_n\right] &= \left[\left(\mathbf{s}_{n_e}^2\right)_{n-1} - \langle n_e \rangle_{n-1}\right] + 2 \left(\frac{\mathbf{s}_{n_e, n_p}}{G}\right)_n \mathbf{h}_n \\
&- 2 \left(\frac{\mathbf{s}_{n_e, n_p}}{G}\right)_{n-1} \mathbf{h}_{n-1} - \frac{\left(\mathbf{s}_{n_p}^2\right)_n - \langle n_p \rangle_n}{\Delta G^{2n-2}} \left[\mathbf{h}_n^2 - \mathbf{h}_{n-1}^2\right] \\
&= \left[\left(\mathbf{s}_{n_e}^2\right)_{n-1} - \langle n_e \rangle_{n-1}\right] + 2\mathbf{h}^{(1)} \Delta G^{n-1} \left(\frac{\mathbf{s}_{n_e, n_p}}{G}\right)_n \\
&- \left[\mathbf{h}^{(1)}\right]^2 \left[\left(\mathbf{s}_{n_p}^2\right)_n - \langle n_p \rangle_n\right]
\end{aligned} \tag{5.26}$$

Using now the results obtained in (5.21) and (5.24), we may finally express the total electron number variance for a device of N absorption sections:

$$\begin{aligned}
(\mathbf{s}_{n_e}^2)_N &= \mathbf{h}_N^2 [\mathbf{s}_{n_p}^2(0) - \langle n_p(0) \rangle] \\
&+ \mathbf{h}_N \langle n_p(0) \rangle + \mathbf{k}_{sp}(\Delta G, N) \mathbf{h}_N n_{ASE}^{(1)} \\
&+ \mathbf{k}_{sig-sp}(\Delta G, N) \mathbf{h}_N^2 \langle n_p(0) \rangle \frac{n_{ASE}^{(1)}}{\Delta \mathbf{n}_o} \\
&+ \mathbf{k}_{sp-sp}(\Delta G, N) \mathbf{h}_N^2 \frac{[n_{ASE}^{(1)}]^2}{\Delta \mathbf{n}_o}
\end{aligned} \tag{5.27},$$

where the following coefficients have been defined:

$$\mathbf{k}_{sp}(\Delta G, N) = 2 \frac{\Delta G^N - N\Delta G + N - 1}{(\Delta G - 1)(\Delta G^N - 1)} \tag{5.28},$$

$$\mathbf{k}_{sig-sp}(\Delta G, N) = 2 \frac{\Delta G^{2N} - \Delta G - (2N - 1)\Delta G^N (\Delta G - 1)}{(\Delta G - 1)(\Delta G^N - 1)^2} \tag{5.29},$$

$$\mathbf{k}_{sp-sp}(\Delta G, N) = 2 \frac{\Delta G^{2N} - 4(N - 1)\Delta G^{N+1} + 4N\Delta G^N - N\Delta G^2 - 4\Delta G + N - 1}{(\Delta G - 1)^2 (\Delta G^N - 1)^2} \tag{5.30}.$$

The factor of 2 in (5.28) and (5.30) reflects the effect of both forward- and backward-propagating ASE. This is a consequence of the symmetry of the device when all periods are identical, and when the position $z=0$ is chosen at the beginning of the first detection section, as shown in figure 5.3.

For an input featuring Poisson statistics, the noise figure of a TAP detector without an amplification section, and with unity coupling efficiency, would be expressed as follows:

$$\begin{aligned}
NF_{TAP} = \frac{1}{h_N} & \left[1 + \mathbf{k}_{sp}(\Delta G, N) \frac{n_{ASE}^{(1)}}{\langle n_p(0) \rangle} \right] + \mathbf{k}_{sig-sp}(\Delta G, N) \frac{n_{ASE}^{(1)}}{\Delta \mathbf{n}_o} \\
& + \mathbf{k}_{sp-sp}(\Delta G, N) \frac{[n_{ASE}^{(1)}]^2}{\langle n_p(0) \rangle \Delta \mathbf{n}_o}
\end{aligned} \tag{5.31}.$$

The first term in the RHS shows the contribution from shot noise to the total noise figure, whereas the second and third express the contribution from what is classically called signal-spontaneous and spontaneous-spontaneous beat noise. We will call \mathbf{k}_{sp} the spontaneous emission noise coefficient, \mathbf{k}_{sig-sp} the signal-spontaneous beat noise coefficient and \mathbf{k}_{sp-sp} the spontaneous-spontaneous beat noise coefficient, following the classical interpretation for the origin of these noise contributions. These coefficients will be plotted and discussed in the next paragraph.

Contributions to the noise figure

In the previous paragraph, the electron number variance in the current generated in TAP detectors with alternating gain and absorption was calculated, allowing the noise figure to be written as given in equation (5.31). These equations show the contributions to the noise from shot noise and gain fluctuations. For simplicity in the notation and for greater intuitive clarity, coefficients \mathbf{k}_{sp} , \mathbf{k}_{sig-sp} and \mathbf{k}_{sp-sp} were defined, allowing the quantification of the noise contribution generated by shot noise due to the ASE current, gain fluctuations affecting the signal and gain fluctuations affecting the ASE, respectively. These coefficients will now be discussed.

The spontaneous emission noise coefficient k_{sp} is actually equal to the ASE current generation coefficient k_{ASE} discussed in chapter 2, and plotted for TAP detectors with alternating gain and absorption in figure 2.35. It will just be reminded here that its value tends to $N-1$ when absorption and loss dominate, to $1/\Delta G$ when gain dominates, and when gain, absorption and loss are close to cancellation, it may be approximated by the following formula:

$$k_{sp}(\Delta G, N) \Big|_{\Delta G=1} = \frac{(N-1)}{2} \left[1 - \frac{(N+1)}{6} (\Delta G - 1) \right] \quad (5.32).$$

The signal-spontaneous beat noise coefficient k_{sp-sig} is plotted in figure 5.4.

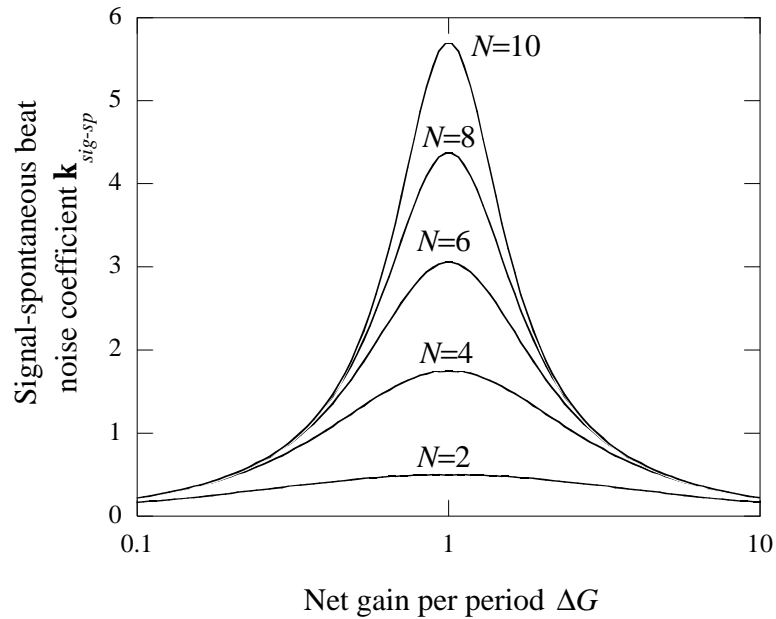


Figure 5.4: Signal-spontaneous beat noise coefficient k_{sig-sp} for a TAP detector with alternating gain and absorption as a function of the net gain per period and for different number of periods.

The signal-spontaneous beat noise coefficient reaches a maximum when the net gain per period is close to 1. Obviously, when either the absorption or the loss heavily dominate, the signal does not survive long, and neither do its random fluctuations, resulting in the shot noise component dominating the noise figure. In order to fully understand the device behavior when the net gain per period is very large, let us assume that the noise figure is so heavily dominated by the signal-spontaneous beat noise term that all other terms in (5.31) may be neglected. Furthermore, and using the traditional equations for an SOA, let us write the ASE photon number generated by each gain section as:

$$n_{ASE}^{(1)} = n_{sp} \left(G^{(1)} - 1 \right) \Delta n_o \quad (5.33),$$

where $G^{(1)}$ is the gain of each individual amplification section and n_{sp} its population inversion coefficient. When the optical loss l is neglected, and the fraction of photons \mathbf{h}_{iso} surviving each isolation sections is approximated to 1, we may write the net gain per period as:

$$\Delta G = G^{(1)} \left(1 - \mathbf{h}^{(1)} \right) \quad (5.34).$$

This would allow us to write (5.31) as:

$$NF_{TAP} \Big|_{\Delta G \gg 1} \simeq \frac{2}{\Delta G} \frac{n_{sp} \left(\Delta G - 1 + \mathbf{h}^{(1)} \right)}{1 - \mathbf{h}^{(1)}} \simeq \frac{2n_{sp}}{1 - \mathbf{h}^{(1)}} \quad (5.35).$$

This result may be understood as follows: after the first absorption region, amplification heavily dominates, and most of the photocurrent is generated in the last

sections of the device. Each amplification section has been assumed to present the same value of the population inversion coefficient n_{sp} , and since the absorption and the loss are overwhelmed by the gain, we may assume a noise figure of $2n_{sp}$ for the optical signal propagation from the end of the first absorption region to the beginning of the last one. Since the gain experienced by the optical signal is large, the additional noise introduced by the photodetection process in the last absorption region may be neglected. However, the first absorption region produces a signal attenuation of $1-h^{(1)}$, making it necessary to divide by this value the noise figure associated to the rest of the device, from the end of the first detection section up to the output. The result of this intuitive argument would result in (5.35).

Finally, when linearized around $\Delta G=1$, the signal-spontaneous beat noise coefficient becomes:

$$\mathbf{k}_{sig-sp}(\Delta G, N)|_{\Delta G=1} \simeq \frac{(2N-1)(N-1)}{3N} \left[1 - \frac{(2N+1)(N+1)}{60} (\Delta G-1)^2 \right] \quad (5.36).$$

In other words, the signal-spontaneous beat noise coefficient, in the case where the gain and the absorption are close to cancellation, is roughly linear with N , approaching $2N/3$ for a large number of sections. It is interesting to note the absence of a linear term when this coefficient is expanded around $\Delta G=1$, leading to a maximum in its value when the net gain per period is exactly 1. This is not surprising, because equation (5.36) shows how, given a certain net gain per period, the noise due to gain fluctuations affecting the signal increases with the number of periods. When the gain diverges from 1, less periods will contribute effectively to the

total photocurrent, the ones closer to the device input when the gain drops below 1, the ones closer to the end of the device when the gain grows above 1. The obvious conclusion is that the contribution of the signal-spontaneous beat noise will be greatest when the net gain per period is exactly 1.

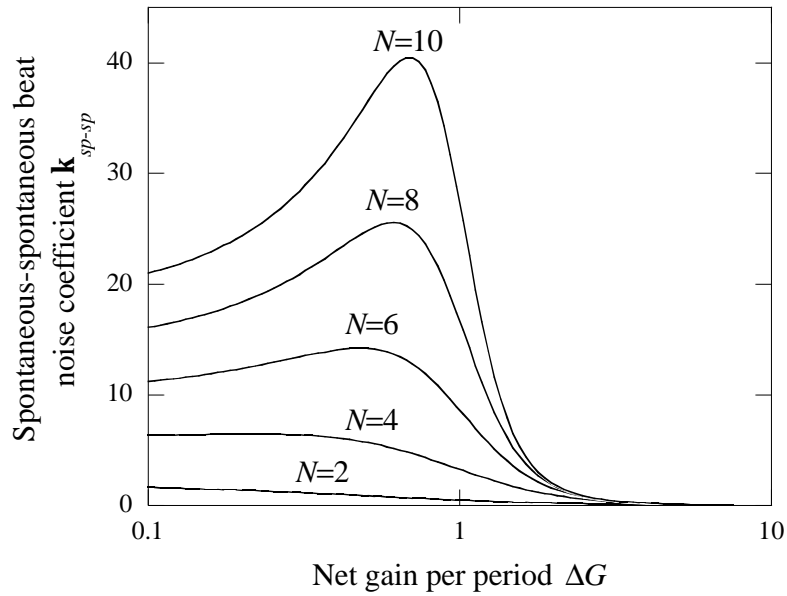


Figure 5.5: Spontaneous-spontaneous beat noise coefficient k_{sp-sp} for a TAP detector with alternating gain and absorption as a function of the net gain per period and for different number of periods.

The spontaneous-spontaneous beat noise coefficient k_{sp-sp} is plotted in figure 5.5. Same as the spontaneous emission noise coefficient k_{sp} , this coefficient tends to an asymptotic value that depends only on the photon number when absorption heavily dominates. This is due to the fact that each detector receives mostly spontaneous emission from the immediately neighboring gain sections, the contribution from the rest of the sections being negligible due to the heavy net attenuation experienced by the optical signal in each period. This behavior extends to the fluctuations in the ASE

and the current associated to its detection. The value towards which the spontaneous-spontaneous beat noise coefficient tends when absorption and loss dominate is $2(N-1)$.

When amplification dominates, the spontaneous-spontaneous beat noise coefficient tends to $2/\Delta G^2$ as the net gain per period increases. Assuming that this contribution dominates and the rest of the noise sources are negligible, we could write the noise figure for TAP detectors with alternating gain and absorption, in the limit of high net gain per period, as:

$$NF_{TAP}|_{\Delta G \gg 1} \approx \frac{2}{\Delta G^2} \frac{n_{sp}^2 (\Delta G - 1 + \mathbf{h}^{(1)})^2 \Delta \mathbf{n}_o}{(1 - \mathbf{h}^{(1)})^2 \langle n_p(0) \rangle} \approx \frac{2n_{sp}^2 \Delta \mathbf{n}_o}{(1 - \mathbf{h}^{(1)})^2 \langle n_p(0) \rangle} \quad (5.37).$$

This equation is entirely analogous to (5.35), and so is its interpretation, except this time the dominant term in the amplifier noise figure is associated to the so-called spontaneous-spontaneous beat noise. In fact, when this term dominates, the noise figure for an SOA may be approximated by:

$$NF_{SOA} \approx \frac{n_{sp}^2 \Delta \mathbf{n}_o}{\langle n_p \rangle_{in}} \quad (5.38).$$

The factor of 2 appears in (5.37) because in TAP detectors both forward- and backward-traveling ASE need to be considered. The factor $(1 - \mathbf{h}^{(1)})^2$ appears in the denominator because the spontaneous-spontaneous beat noise is independent of the input signal, and therefore equation (5.11) needs to be interpreted as in the case of a

chain of electrical amplifiers, not as in the case of a chain of optical amplifiers dominated by signal-spontaneous beat noise. Thus, the gain of the first “amplifier” of the chain, i.e., an attenuation of value $1-h^{(1)}$, needs to appear squared in the denominator.

In the case where the net gain per period is close to 1, we can use the following approximation for the spontaneous-spontaneous beat noise coefficient:

$$\mathbf{k}_{sp-sp}(\Delta G, N)\Big|_{\Delta G=1} \simeq \frac{(N-1)(N^2-N+1)}{3N} \left[1 - \frac{(N+1)(N^2+1)}{5(N^2-N+1)}(\Delta G-1) \right] \quad (5.39).$$

In other words, the spontaneous-spontaneous beat noise coefficient exhibits roughly a quadratic dependence with the number of sections, approaching $N^2/3$ for large number of sections. The previous argument used for the case of the signal-spontaneous beat noise coefficient does not apply here, since the signal and the ASE evolve differently. When the net gain per period grows, its value being in the vicinity of 1, the efficiency grows faster than the ASE current, as shown in chapter 2. This results obviously in the spontaneous-spontaneous beat noise coefficient decreasing as the net gain per period increases while having always values close to 1.

In summary, this paragraph has discussed the coefficients describing the noise contributions from different sources in TAP detectors with alternating gain and absorption. The total noise figure will be discussed in the following section, paying

special attention to the trade off that appears between this parameter and the device efficiency.

Noise figure

Once the different terms contributing to the noise figure of TAP detectors have been studied in the previous paragraph, it is important to provide some quantification for said noise figure, especially in the case where the loss is negligible and the amplifier medium is fully inverted. This case provides the fundamental limitation for the best achievable noise figure. We will assume that, whether gain and absorption exactly cancel out or not, the ASE spectral power density generated in the amplification sections may be approximated by its value when the net gain per period is exactly 1, leading to:

$$\frac{n_{ASE}^{(1)}}{\Delta n_o} \simeq \frac{\mathbf{h}^{(1)}}{1-\mathbf{h}^{(1)}} \quad (5.40),$$

where equations (5.33) and (5.34) have been used. Note that, under this approximation, the ASE spectral density depends only on the efficiency of each detection section. This is a direct consequence of assuming that the role of each amplification section is to exactly compensate for the optical power lost to the photocurrent.

We are obviously interested in the case where the total device internal efficiency \mathbf{h}_N is much larger than 1. In this case, and using (5.40), equation (5.31) may be approximated as:

$$NF_{TAP} \approx \mathbf{k}_{sig-sp}(\Delta G, N) \frac{\mathbf{h}^{(1)}}{1-\mathbf{h}^{(1)}} + \mathbf{k}_{sp-sp}(\Delta G, N) \left(\frac{\mathbf{h}^{(1)}}{1-\mathbf{h}^{(1)}} \right)^2 \frac{\Delta \mathbf{n}_o}{\langle n_p(0) \rangle} \quad (5.41).$$

The factors of $1-\mathbf{h}^{(1)}$ in the denominators have already been explained intuitively as an effect of the attenuation of the optical power introduced by each detection section (especially the first one), being squared in the case of the spontaneous-spontaneous beat noise contribution since this one does not depend on the input optical power. As discussed in chapter 4, the rates of the amplification and detection processes are the sources of fluctuations in both the photon and electron numbers. Consequently, when the gain and absorption are close to cancellation, the integration of both rates over one period is practically equal to the efficiency of each detection section. The efficiency of each detection section appears thus multiplying both contributions, reflecting in the case of the signal-spontaneous beat noise term the fluctuations in the gain experienced by the signal, and in the case of the spontaneous-spontaneous beat noise term the fluctuations both in the generation of spontaneous emission, and its subsequent amplification. In the latter case the efficiency of each detection region is thus squared in the noise contribution. The beat noise coefficients, \mathbf{k}_{sig-sp} and \mathbf{k}_{sp-sp} , reflect thus the effect of the distributed combination of amplification and absorption, in particular the mismatch between them leading to a possible net gain per period, the number of periods, and the presence of backward-propagating ASE. Note that in the case of exact cancellation between gain and absorption, leading to a device internal efficiency (not counting the effect of a possible first amplification section) of $\mathbf{h}_N = N\mathbf{h}^{(1)}$ we may write the noise figure as having the following limit:

$$NF_{TAP} \simeq \frac{2}{3} \frac{\mathbf{h}_N}{1-\mathbf{h}^{(1)}} + \frac{1}{3} \left(\frac{\mathbf{h}_N}{1-\mathbf{h}^{(1)}} \right)^2 \frac{\Delta \mathbf{n}_o}{\langle n_p(0) \rangle} \quad (5.42).$$

For a large input optical power, this results in the following limit in the case of TAP detectors with alternating gain and absorption and without an initial amplification section:

$$NF_{ext} \simeq \frac{2}{3} \frac{\mathbf{h}_N}{\mathbf{h}_c (1-\mathbf{h}^{(1)})} \quad (5.43).$$

Equation (5.43) is therefore a very important result, since it shows the optimum noise figure that may be obtained in TAP detectors with alternating gain and absorption when the net gain per period is exactly 1. The subscript “*ext*” is used to denote that the effect of the input coupling efficiency has been considered. Taking into account that the external efficiency for these devices is equal to the internal efficiency \mathbf{h}_N multiplied by the input coupling efficiency \mathbf{h}_c , we may write the optimum ratio between the total noise figure and the external quantum efficiency:

$$\frac{NF_{ext}}{\mathbf{h}_{ext}} \simeq \frac{2}{3} \frac{1}{\mathbf{h}_c^2 (1-\mathbf{h}^{(1)})} \quad (5.44).$$

Equation (5.44) thus stresses two important issues about TAP detectors. From one side, a large input coupling efficiency improves drastically the noise performance of these devices. Furthermore, total device efficiency may be increased by raising the efficiency of each individual detection section. However, not only the noise figure, but even the ratio between noise figure and device efficiency increase as the

efficiency of each detection section grows. Careful design of the efficiency of each detection section is therefore needed to achieve high efficiencies and low noise figures simultaneously.

After these considerations have been made, let us consider once more the more general case where all contributions to the noise figure are taken into account. For the remainder of this paragraph, it will be assumed that an initial amplification section does not exist. Note that in some of the contributions to the total noise figure, namely the shot noise associated to the ASE current and the spontaneous-spontaneous beat noise term, the optical power contained in the input signal is present. It is interesting to write this input power, in photons per second, normalized to the amplifier bandwidth. Let us then assume that the amplifier bandwidth is in the order of 15THz. For an emission wavelength of 860nm, typical for GaAs quantum well-based material, this corresponds to a linewidth of approximately 37nm, in the order of typical values for common GaAs-based amplifiers. At the same time, $15 \cdot 10^{12}$ photons per second correspond, for a photon energy of 1.424eV (i.e., GaAs bandgap energy) to approximately 3.4 μ W. We may then write, as a fair approximation, that:

$$\frac{\langle n_p(0) \rangle}{\Delta n_o} \simeq \frac{h_c P_{in}}{3\mu W} \quad (5.45).$$

Let us consider first the case where the net gain per period is exactly 1. Assuming that optical loss is negligible, equation (5.31) may then be approximated by:

$$\begin{aligned}
NF_{ext} = & \frac{1}{N\mathbf{h}_c\mathbf{h}^{(1)}} + \frac{N-1}{2N\mathbf{h}_c^2(1-\mathbf{h}^{(1)})} \frac{\Delta\mathbf{n}_o}{\langle n_p \rangle_{in}} \\
& + \frac{(2N-1)(N-1)}{3N} \frac{\mathbf{h}^{(1)}}{\mathbf{h}_c(1-\mathbf{h}^{(1)})} \\
& + \frac{(N-1)(N^2-N+1)}{3N} \left(\frac{\mathbf{h}^{(1)}}{\mathbf{h}_c^2(1-\mathbf{h}^{(1)})} \right)^2 \frac{\Delta\mathbf{n}_o}{\langle n_p \rangle_{in}}
\end{aligned} \tag{5.46}$$

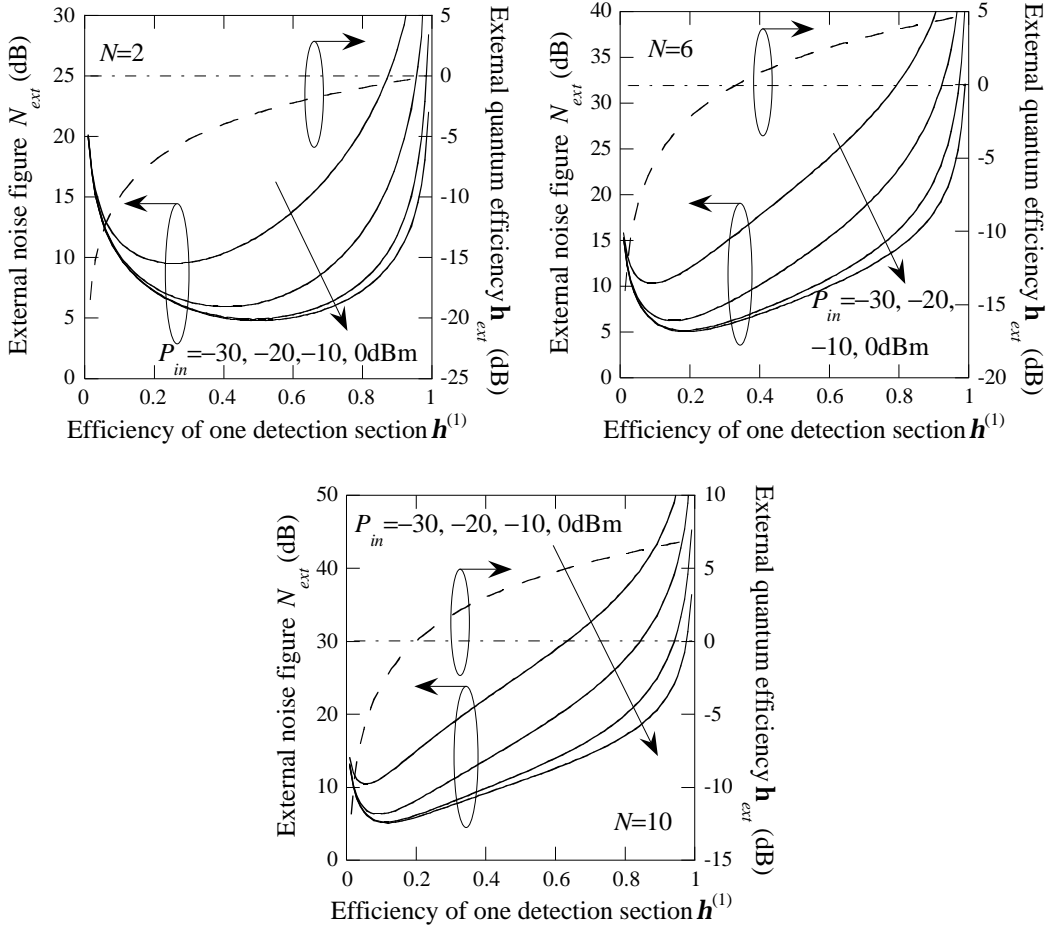


Figure 5.6: Noise figure for a TAP detector with alternating gain and absorption consisting of $N=2$ periods (top left), $N=6$ periods (top right) and $N=10$ periods (bottom) as a function of the efficiency of each detection section and for different input optical powers (full lines), when the net gain per period is 1. The total external quantum efficiency (dashed line) is also plotted. The horizontal dash-dotted line marks an external quantum efficiency of 100%. The input coupling efficiency is 50%.

The coupling efficiency will be assumed to be, as always, 50%. Figure 5.6 shows the total noise figure (expressed in dB) as a function of the efficiency of each detection section, and for different input optical powers and different numbers of periods. The external quantum efficiency is also plotted in logarithmic scale for comparison.

Several interesting features may be deduced from these plots. First, the shot noise due to the input signal dominates when the efficiency of each detection section is low. This is quite obvious since the shot noise is the only contribution that grows when the efficiency of each section decreases, and the lack of an obvious dependence with the input power shows that the effect of the shot noise due to ASE may be neglected. This is intuitively explained by considering that, if the efficiency of each detection section is very low, and the net gain per period is 1, then the gain of each amplification section, and thus the ASE generated in it, must be very small too. For a larger efficiency in each detection section, the gain of each amplification section increases in order to maintain the situation where gain and absorption cancel. This results in signal-spontaneous or spontaneous-spontaneous beat noise terms dominating. The former will dominate over the latter as the input power and as the efficiency of each detection section increases. This causes the different curves to move away from one another. It also causes different curves to start diverging for larger efficiencies when they represent the noise figure associated to larger input powers.

It may also be observed that the noise figure always reaches a minimum. Given a number of sections in the device, this minimum is obtained for similar values of the efficiency of each detection section. The minimum deviates slightly to lower efficiencies and reaches a higher value when the power decreases, indicating a larger contribution from the shot noise due to the ASE. Finally, note that the minimum is almost identical for all numbers of periods, whereas it is reached for lower efficiency in each detection section as the number of periods increases. However, these values of the efficiency of each detection section produce, for the different devices with different numbers of periods, approximately the same external efficiency, which is in the order of 50%, or equivalently an internal efficiency of 100%. As the total device efficiency grows by increasing the amount of light absorbed in each period, the gain of each amplification section increases with it, resulting in a larger production of noise due to gain fluctuations. At the minimum, the largest contribution to the noise figure is originated by the coupling loss (3dB out of the total 5dB).

Finally, let us investigate the behavior of the noise figure as the net gain per period deviates from 1. Figure 5.7 shows the noise figure for a device with 6 periods, where the efficiency of each individual detection section has been kept at 50%, and for different values of the input power.

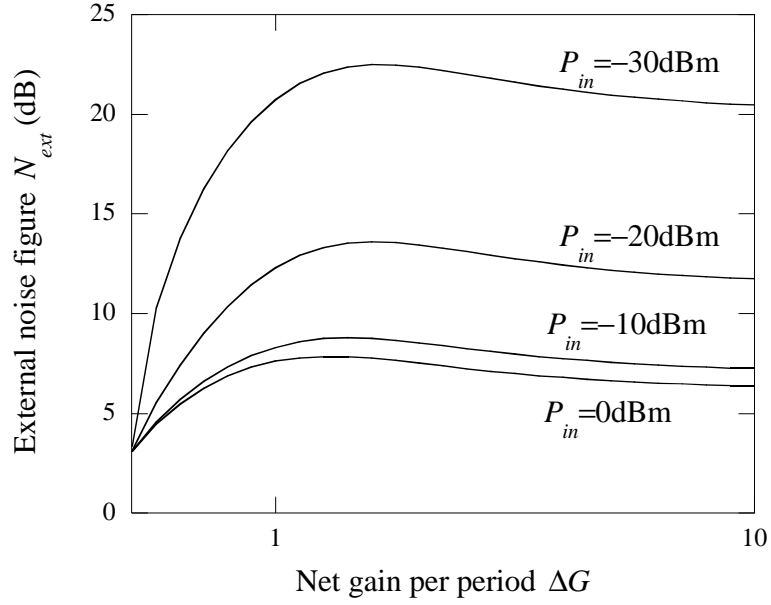


Figure 5.7: Noise figure for a TAP detector with alternating gain and absorption consisting of $N=6$ periods as a function of the net gain per period and for different input optical powers (full lines). The total external quantum efficiency (dashed line) is also plotted. The horizontal dash-dotted line marks an external quantum efficiency of 100%. The input coupling efficiency and the detection efficiency of each absorption section are assumed to be both 50%.

Since the net gain per period is now allowed to change, the approximation to the ASE power spectral density made in (5.40) is not valid anymore. We use instead

$$\frac{n_{ASE}^{(1)}}{\Delta n_o} = n_{sp} \left(G^{(1)} - 1 \right) \simeq \frac{\Delta G - 1 + \mathbf{h}^{(1)}}{1 - \mathbf{h}^{(1)}} \quad (5.47),$$

assuming once more that the population inversion factor is equal to 1. Since the efficiency of each detection section is 50%, we will furthermore assume that the net gain per period cannot be smaller than 0.5, this value being reached when the amplification regions are transparent.

The graph shows an initial onset of the noise figure when the net gain per period starts growing from its minimum value of 0.5. This value is reached when the amplifier is at transparency. We may then assume that the amount of ASE produced is very small, and the noise figure of the device is dominated in all cases by the coupling loss. As the net gain per period increases, so do the production of ASE and the gain fluctuations. However, these effects are compensated by the larger efficiency, resulting overall in relatively small variations in the noise figure for values of the net gain per period larger than 1.

Finally, note that the values for the noise figure found for these devices are rather large, especially for input powers in the order of $1\mu\text{W}$ or lower. As mentioned at the beginning of this section, an initial amplification section may contribute to a reduction in the noise figure. We can therefore conclude that this section is thus important, and should always be present in TAP detectors designed for applications where the noise properties are crucial.

In summary, the noise figure of TAP detectors with alternating gain and absorption has been discussed in this paragraph. It has been shown that a limit for ratio between the noise figure and the efficiency exists, which depends mostly on the coupling efficiency and the detection efficiency of each absorption section. Careful design has been shown to be necessary to achieve simultaneously high efficiency and low noise figure approaching this limit. Finally, it has been shown that variations in the net gain per period produce relatively small variations in the noise figure. The

noise figure in TAP detectors with alternating gain and absorption and no initial amplification section is thus mostly dominated by the design of the detection section.

This section has studied the behavior of TAP detectors with respect to noise. Intuitive explanations and quantitative calculations have been provided to describe the noise properties of these devices. The effects of the coupling loss and of a possible initial amplification section have been studied, showing the importance of a high coupling efficiency, and the possibility to reduce the overall noise figure by including a gain section at the beginning of the device, rather than having a detection section first.

Noise in TAP detectors with transverse coupling

In this section, the noise generated in TAP detectors with transverse coupling will be studied. First, the electron number variance will be found, using the noise model for distributed amplifier-photodetectors introduced in the previous chapter. Next, the noise figure and the different contributions to it will be discussed, giving quantitative values and establishing a trade-off between noise figure and efficiency.

Electron number variance

For the purposes of noise calculation, we will use in this paragraph the same assumptions as for the calculation of the efficiency and the ASE current, consistently with what was presented in chapter 2. In other words, the material gain and absorption, the stimulated emission rate normalized to the optical intensity and the

different confinement factors will be assumed to be position-independent. The device input (meaning by it the beginning of the simultaneous gain and absorption) will be located at $z=0$, and the end of the device at $z=L$. Under the aforementioned assumptions, equations (5.1) and (5.2) may be easily integrated, resulting in the following position-dependent average photon number and total electron average number:

$$\langle n_p(z) \rangle = e^{\Delta g z} \langle n_p(0) \rangle + \frac{e^{\Delta g z} - 1}{\Delta g} (\Gamma_g r_{st,em}) \Delta n_o \quad (5.48).$$

$$\begin{aligned} \langle n_e(L) \rangle &= \frac{e^{\Delta g L} - 1}{\Delta g L} (\Gamma_a \mathbf{a} L) \langle n_p(0) \rangle \\ &+ \frac{e^{\Delta g L} - 1 - \Delta g L}{(\Delta g L)^2} (\Gamma_a \mathbf{a} L) (\Gamma_g r_{st,em} L) \Delta n_o \end{aligned} \quad (5.49).$$

The position-dependent cumulative efficiency $\mathbf{h}(z)$ is then given by:

$$\mathbf{h}(z) = \frac{e^{\Delta g z} - 1}{\Delta g} (\Gamma_a \mathbf{a}) \quad (5.50).$$

The net gain per unit length Δg has been defined, as always, as the difference between gain and absorption, multiplied by their respective confinement factors, and minus the modal loss. These results are completely analogous to the equations describing the optical power, current and ASE current found in chapter 2. Using this value of the average photon number, we can calculate the excess photon noise referred to the input using equation (5.3):

$$\begin{aligned} \frac{\mathbf{s}_{n_p}^2(z) - \langle n_p(z) \rangle}{e^{2\Delta g z}} &= \mathbf{s}_{n_p}^2(0) - \langle n_p(0) \rangle + 2 \frac{1 - e^{-\Delta g z}}{\Delta g} (\Gamma_g r_{st,em}) \langle n_p(0) \rangle \\ &+ \left(\frac{1 - e^{-\Delta g z}}{\Delta g} \right)^2 (\Gamma_g r_{st,em})^2 \Delta \mathbf{n}_o \end{aligned} \quad (5.51).$$

From this result, the evolution of the covariance between electron and photon numbers is found using (5.4):

$$\begin{aligned} \frac{\mathbf{s}_{n_p, n_e}(z)}{e^{\Delta g z}} &= \frac{e^{\Delta g z} - 1}{\Delta g} (\Gamma_a \mathbf{a}) [\mathbf{s}_{n_p}^2(0) - \langle n_p(0) \rangle] \\ &+ 2 \frac{e^{\Delta g z} - 1 - \Delta g z}{\Delta g^2} (\Gamma_a \mathbf{a}) (\Gamma_g r_{st,em}) \langle n_p(0) \rangle \\ &+ \frac{e^{\Delta g z} - e^{-\Delta g z} - 2\Delta g z}{\Delta g^3} (\Gamma_g r_{st,em}) (\Gamma_g r_{st,em})^2 \Delta \mathbf{n}_o \end{aligned} \quad (5.52).$$

It is not difficult now to integrate (5.5), which allows us to write the total electron number variance as:

$$\begin{aligned} \mathbf{s}_{n_e}^2(L) &= \mathbf{h}^2(L) [\mathbf{s}_{n_p}^2(0) - \langle n_p(0) \rangle] \\ &+ \mathbf{h}(L) [\langle n_p(0) \rangle + \mathbf{k}_{sp}(\Delta g L) (\Gamma_g r_{st,em} L) \Delta \mathbf{n}_o] \\ &+ \mathbf{k}_{sig-sp}(\Delta g L) \mathbf{h}^2(L) (\Gamma_g r_{st,em} L) \langle n_p(0) \rangle \\ &+ \mathbf{k}_{sp-sp}(\Delta g L) \mathbf{h}^2(L) (\Gamma_g r_{st,em} L)^2 \Delta \mathbf{n}_o \end{aligned} \quad (5.53).$$

where the following noise coefficients have been defined:

$$\mathbf{k}_{sp}(\Delta g L) = 2 \frac{e^{\Delta g L} - 1 - \Delta g L}{(e^{\Delta g L} - 1)(\Delta g L)} \quad (5.54).$$

$$\mathbf{k}_{sig-sp}(\Delta gL) = 2 \frac{e^{2\Delta gL} - 2\Delta gL e^{\Delta gL} - 1}{(e^{\Delta gL} - 1)^2 (\Delta gL)} \quad (5.55).$$

$$\mathbf{k}_{sp-sp}(\Delta gL) = 2 \frac{e^{2\Delta gL} - 4\Delta gL e^{\Delta gL} + 4e^{\Delta gL} - 5 - 2\Delta gL}{(e^{\Delta gL} - 1)^2 (\Delta gL)^2} \quad (5.56).$$

In equations (5.54) and (5.56), the factor of 2 reflects the contributions from both forward- and backward-propagating ASE. The first term in the RHS of (5.53) represents the contribution from the noise associated to the input signal, while the second is originated by shot noise due to the detection of the input signal and of the ASE generated in the amplification region. The third term describes the contribution to the current noise from gain fluctuations associated to the input signal, while the fourth represents the fluctuations in the electron number due to random gain experienced by the ASE generated in the device.

The noise coefficients \mathbf{k}_{sp} , \mathbf{k}_{sig-sp} and \mathbf{k}_{sp-sp} have been defined in an entirely analogous way as in the case of TAP detectors with alternating gain and absorption, and we will name them also spontaneous emission noise coefficient, signal-spontaneous beat noise coefficient and spontaneous-spontaneous beat noise coefficient respectively. Note that each one of these coefficients does not depend on the net gain per unit length Δg and on the device length L independently, but only through their product. Incidentally, this value is also the natural logarithm of the amplification experienced by the input optical signal, from the beginning of the device to its end. At the same time, the only other factor in the electron number

variance that depends on the device length (apart from the efficiency) is the product of the stimulated emission rate normalized to the optical intensity, the confinement factor in the gain region and the device length. This value is actually the spectral density of the photon number per unit time generated in the entire device and traveling in one direction, when the net gain per unit length is identically zero. Indeed, making the input photon number $\langle n_p(0) \rangle$ equal to zero, and taking the limit of (5.48) when the net gain tends to zero, we find the total ASE photon number traveling in one direction generated in the entire device when gain, absorption and loss exactly cancel out to be given by the following equation:

$$\langle n_p(L) \rangle \Big|_{\substack{\Delta g=0 \\ \langle n_p(0) \rangle=0}} = (\Gamma_g r_{st,em} L) \Delta \mathbf{n}_o \quad (5.57).$$

In other words, the noise coefficients defined in (5.54)-(5.56) give us information on how much noise is generated with respect to the amount of spontaneous emission produced in a TAP detector with transverse coupling.

In the next paragraph, the noise coefficients defined above will be studied, paying special attention to their intuitive interpretation.

Contributions to the noise figure

In the previous paragraph, the electron number variance generated in a TAP detector with transverse coupling was found to be described through equation (5.53). The noise figure associated purely to the process of distributed amplification and

photodetection, i.e., the noise figure of the device without considering the effect of the input coupling efficiency or a possible initial gain section, is then easily found:

$$NF_{TAP} = \frac{1}{\mathbf{h}(L)} \left[1 + \mathbf{k}_{sp}(\Delta gL) \frac{(\Gamma_g r_{st,em} L) \Delta \mathbf{n}_o}{\langle n_p(0) \rangle} \right] + \mathbf{k}_{sig-sp}(\Delta gL) (\Gamma_g r_{st,em} L) + \mathbf{k}_{sp-sp}(\Delta gL) \frac{(\Gamma_g r_{st,em} L)^2 \Delta \mathbf{n}_o}{\langle n_p(0) \rangle} \quad (5.58).$$

The signal has been assumed to follow Poisson statistics at $z=0$ in obtaining equation (5.58). This assumption is a very good approximation in the absence of an initial gain section. The noise coefficients defined in the previous section play thus a major role in the description of the noise properties of TAP detectors with alternating gain and absorption, and will be now studied.

Figure 5.8 shows the three noise coefficients as a function of the product between the net gain per unit length Δg and the total device length L . As mentioned in the previous paragraph, these coefficients do not depend on any variable other than this product.

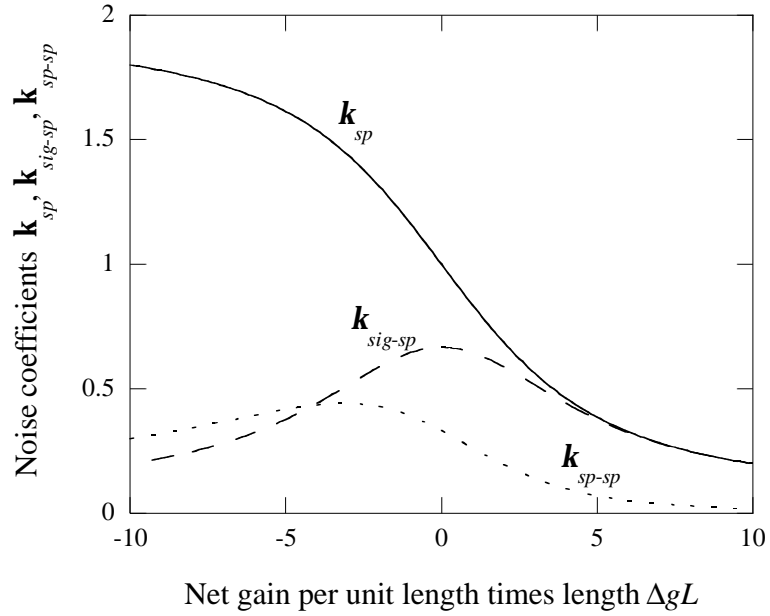


Figure 5.8: Spontaneous emission noise coefficient k_{sp} (full line), signal-spontaneous beat noise coefficient k_{sig-sp} (dashed line) and spontaneous-spontaneous beat noise coefficient k_{sp-sp} (dotted line) as a function of the product between the net gain per unit length Dg and the total device length L .

When the net gain per unit length is very small, the shot noise term dominates over the rest. This makes perfect sense intuitively, since in this case absorption clearly dominates over gain, resulting in very little noise due to gain fluctuations. The spontaneous emission coefficient k_{sp} tends to 2 as the product ΔgL is negative and grows in absolute value. This is an obvious consequence that the electron number generated by absorption of ASE in the entire device is given by $2(\Gamma_g r_{st,em} L) \Delta n_o$, a result entirely analogous to the ASE current found under these operating conditions in chapter 2. The signal-spontaneous beat noise coefficient asymptotically approaches $2/|\Delta gL|$, while the spontaneous-spontaneous beat noise coefficient tends to behave like $4/|\Delta gL|$ as the absolute value of the negative product

ΔgL grows. When the absorption heavily dominates, we may assume that the internal efficiency $h(L)$ is close to 1, and that the stimulated emission rate normalized to the optical intensity multiplied by the confinement factor in the gain region is much smaller than the material absorption multiplied by the confinement factor in the absorption region, the latter being in turn approximately equal to the absolute value of the negative gain per unit length. This results in the signal-spontaneous and the spontaneous-spontaneous beat noise terms being negligible with respect to the shot noise due to the signal, and due to the ASE, respectively. Furthermore, because of the low value presented by the stimulated emission rate normalized to the optical intensity, the total noise figure will be dominated by the shot noise associated to the signal, just like in traditional detectors, unless either the coupling efficiency or the input power are very small. This is intuitively a direct consequence of the device working very similarly to a conventional traveling-wave detector, since the gain provided by the amplification region is very small compared to the absorption.

When the product between the net gain and the device length is positive and much larger than 1, the optical signal is amplified by a factor much larger than 1 over the entire device, resulting in a behavior very similar to that of a traditional detector preceded by an optical amplifier. Indeed, since the optical power grows very rapidly, most of the photocurrent generation will happen only over the last fraction of the entire device length, the rest of it providing effectively only amplification, and a very small fraction of the total photocurrent. For this to be true, the net gain per unit

length needs to be dominated by the amplifier gain, which leads to the following approximation:

$$\Gamma_g r_{st,em} = n_{sp} \Gamma_g g \simeq n_{sp} \Delta g \quad (5.59),$$

where n_{sp} is, as always, the population inversion coefficient for the amplification region.

When the product ΔgL is much larger than 1, the spontaneous emission noise coefficient and the signal-spontaneous beat noise coefficient tend both to $2/(\Delta gL)$, whereas the spontaneous-spontaneous beat noise coefficient approaches $2/(\Delta gL)^2$, leading to the following approximate expression for the noise figure:

$$NF_{TAP} \simeq 2n_{sp} + \frac{2n_{sp}^2 \Delta \mathbf{n}_o}{\langle n_p(0) \rangle} \quad (5.60).$$

The shot noise contributions have been neglected since they appear in (5.58) divided by the internal efficiency of the device, which approaches asymptotically an exponential behavior with ΔgL when the net gain per period is large. Obviously, equation (5.60) is entirely analogous to the noise figure for a beat noise dominated SOA, except for the factor of 2 multiplying the second term in the RHS, which is introduced by the backward-propagating ASE.

When the gain and absorption are close to cancellation, the noise coefficients admit the following approximations (found by linearization around $\Delta gL=0$):

$$\mathbf{k}_{sp}(\Delta gL) \Big|_{|\Delta gL| \ll 1} \simeq 1 - \frac{\Delta gL}{6} \quad (5.61).$$

$$\mathbf{k}_{sig-sp}(\Delta gL)\Big|_{|\Delta gL|\ll 1} \simeq \frac{2}{3} - \frac{(\Delta gL)^2}{45} \quad (5.62).$$

$$\mathbf{k}_{sp-sp}(\Delta gL)\Big|_{|\Delta gL|\ll 1} \simeq \frac{1}{3} - \frac{\Delta gL}{15} \quad (5.63).$$

The same reasoning applied to the interpretation of the noise coefficients in the case of TAP detectors with alternating gain and absorption still holds here. In other words, the signal grows faster than the ASE with increasing net gain per period in the vicinity of cancellation between amplification and absorption, leading to a reduction in the spontaneous emission and in the spontaneous-spontaneous beat noise coefficients. However, when the net gain per unit length increases in absolute value, while being smaller than the inverse of the device length, the result is effectively the same as obtained for a device of shorter length, since a more and more important fraction of the photocurrent will be produced either at the beginning of the device (when absorption and loss slightly dominate) or at its end (in the case of positive net gain). This leads obviously to a maximum in the signal-spontaneous beat noise coefficient when gain, absorption and loss exactly cancel out.

In summary, this paragraph has described, both intuitively and quantitatively, the behavior of the coefficients appearing in the equation for the noise figure of TAP detectors with alternating gain and absorption. In the next chapter, the total noise figure, and its dependence on the device length and input power, will be studied.

Noise figure

This paragraph will address the noise figure of TAP detectors with alternating gain and absorption, paying especial attention to the trade-off that arises between efficiency and noise figure. The dependence of the noise figure with respect to the device length and the input optical power will also be discussed and quantified.

The optimum device behavior in all respects, including noise, will happen when the optical loss is negligible, and the amplification region is close to full inversion. The minimum noise figure will therefore be achieved when the following condition is met:

$$\Gamma_g r_{st,em} = \Gamma_g g = \Delta g + \Gamma_a \mathbf{a} \quad (5.64).$$

When no initial amplification section is present, and taking into account the input coupling efficiency \mathbf{h}_c , the external noise figure of the device NF_{ext} may be rewritten as:

$$\begin{aligned} NF_{ext} = & \frac{1}{\mathbf{h}_{ext}} + \mathbf{k}_{sp} (\Delta g L) \frac{\Gamma_a \mathbf{a} L + \Delta g L}{\mathbf{h}_c \mathbf{h}_{ext}} \frac{\Delta \mathbf{n}_o}{\langle n_p \rangle_{in}} \\ & + \mathbf{k}_{sig-sp} (\Delta g L) \frac{\Gamma_a \mathbf{a} L + \Delta g L}{\mathbf{h}_c} \\ & + \mathbf{k}_{sp-sp} (\Delta g L) \left(\frac{\Gamma_a \mathbf{a} L + \Delta g L}{\mathbf{h}_c} \right)^2 \frac{\Delta \mathbf{n}_o}{\langle n_p \rangle_{in}} \end{aligned} \quad (5.65).$$

When the net gain per unit length Δg is identically zero, it was shown in chapter 2 that the device internal efficiency was given by $\Gamma_a \mathbf{a} L$, resulting for this case in:

$$NF_{ext} = \frac{1}{\mathbf{h}_{ext}} + \frac{1}{\mathbf{h}_c^2} \frac{\Delta \mathbf{n}_o}{\langle n_p \rangle_{in}} + \frac{2\mathbf{h}_{ext}}{3\mathbf{h}_c^2} + \frac{1}{3} \frac{\mathbf{h}_{ext}^2}{\mathbf{h}_c^4} \frac{\Delta \mathbf{n}_o}{\langle n_p \rangle_{in}} \quad (5.66).$$

When the input optical power and the external quantum efficiency are large we find the following limit:

$$NF_{ext} \approx \frac{2\mathbf{h}_{ext}}{3\mathbf{h}_c^2} \quad (5.67).$$

In other words, even with no coupling loss, the noise figure of TAP detectors with transverse coupling can never be lower than 2/3 of the external quantum efficiency of the device. This result quantifies the trade-off between noise figure and efficiency that was advanced in chapter 4, when the noise model for distributed amplifier-photodetectors was presented.

These equations require some comments. First of all, a comparison of (5.66) and (5.46) shows that the factor $1-\mathbf{h}^{(1)}$ in the case of TAP detectors with alternating gain and absorption has disappeared in the case of devices with transverse coupling. Intuitively, this corresponds to the latter being physically the limit of the former when each period becomes infinitely small, resulting in a negligible “efficiency of each absorption section”. The factor $1-\mathbf{h}^{(1)}$ may be effectively substituted by 1. Next, it may be noted that there is a factor of \mathbf{h}_c^4 dividing the contribution from the spontaneous-spontaneous beat noise. A factor of \mathbf{h}_c^2 is originated by the effect of the input coupling loss, since the spontaneous-spontaneous beat noise is independent on the input optical power. Another factor of \mathbf{h}_c^2 reflects the fact that this noise term is

proportional to the internal efficiency squared, whereas the external noise figure has been written as a function of the external quantum efficiency. Similarly, the factor of h_c^2 dividing the signal-spontaneous beat noise contribution may be explained by a factor of h_c due to the effect of the input coupling loss, since this noise term is proportional to the input signal, while the actual contribution to the noise figure from the signal-spontaneous beat noise is proportional to the internal efficiency, producing the second factor of h_c when the noise figure is expressed as a function of the external quantum efficiency.

Assuming that the optical bandwidth of the amplification region may be given the same value as in the case of TAP detectors with alternating gain and absorption, we may write the relation between input photon numbers and optical bandwidth as in equation (5.45). Under this assumption, figure 5.9 shows the noise figure of TAP detectors with alternating gain and absorption for different optical powers, when the net gain per unit length is identically zero. As always, the input coupling efficiency will be assumed to be 50%.

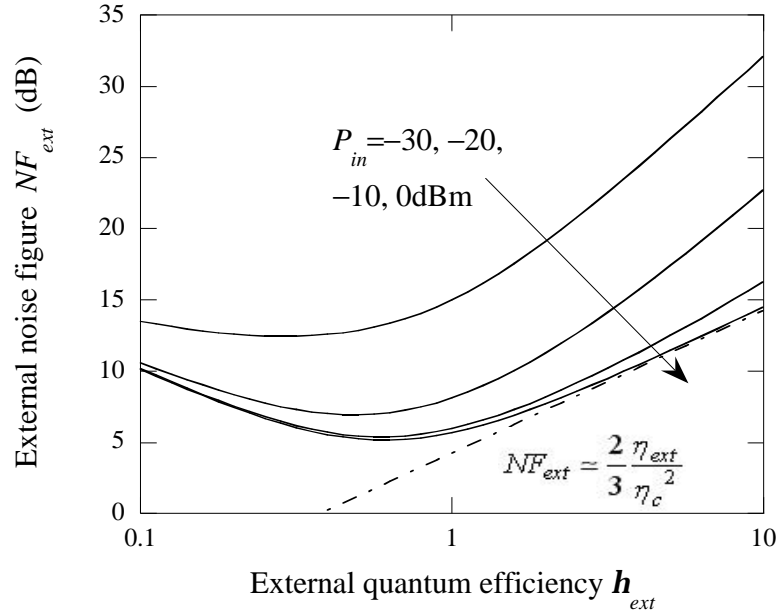


Figure 5.9: Noise figure for a TAP detector with transverse coupling as a function of the external quantum efficiency h_{ext} and for different input optical powers (full lines), when the net gain per unit length is 0. The input coupling efficiency is assumed to be 50%. The fundamental noise limit for the noise figure becomes then $NF_{ext}=8h_{ext}/3$, plotted as a dash-dotted line.

When the external efficiency is low, the noise figure is dominated by the shot noise contribution. Otherwise, the noise associated to gain fluctuations dominates. This results in a minimum for the noise figure, which happens for different values of the external quantum efficiency depending on the input optical power. In fact, for very high input optical powers (when the sum of the shot noise due to the signal and the signal-spontaneous beat noise contributions dominate), this minimum happens for the following value of the external quantum efficiency:

$$h_{ext} = \frac{h_c \sqrt{3}}{\sqrt{2}} \quad (5.68).$$

As the input optical power decreases, the efficiency for which the minimum occurs shifts to lower values, due to the effect of the spontaneous-spontaneous beat noise term.

It is also interesting to study how the noise figure evolves as the net gain per period changes. For that purpose, let us assume that the material absorption and the confinement factor in the detection region are respectively 10^4cm^{-1} and 5%. When the amplifier reaches transparency, the net gain per unit length in the absence of optical loss is $\Delta g = -500\text{cm}^{-1}$.

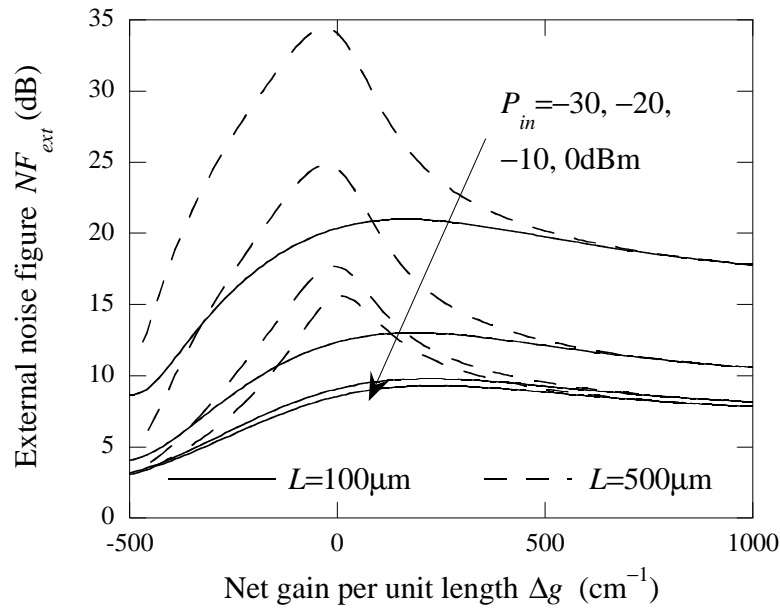


Figure 5.10: Noise figure for TAP detectors with transverse coupling as a function of the net gain per unit length Δg , for different input optical powers and for device lengths L of 100mm (full lines) and 500mm (dashed lines). The confinement factor in the absorption region is assumed to be 5%, and the material absorption 10^4cm^{-1} . The input coupling efficiency is assumed to be 50%.

Figure 5.10 shows the noise figure as a function of the net gain per period, for values larger than this one. The plots show the evolution of the noise figure for

different optical powers, and for devices 100 μm (solid lines) and 500 μm long (dashed lines). The most relevant aspects of this figure will now be discussed. First, we may notice that, given the same optical power, the noise figure for both device lengths is very similar when the net gain is large in absolute value. When loss dominates, the value reached corresponds to the shot noise due to the photocurrent and to the ASE current, the latter dominating for small input powers. The noise figure is limited to values larger than 3dB by the input coupling loss of 50%, increasing as the input power drops because of the ASE current contribution to the shot noise. As the net gain per unit length increases, more randomness due to gain fluctuations is introduced, raising the value of the noise figure. When gain dominates, the total noise figure is similar to that of a photodetector preceded by an optical amplifier. The noise figure is then limited to values larger than 6dB, the input coupling loss producing 3dB and the amplifier another 3dB. The value increases as the input power decreases, due to an increasing relative importance of the fluctuations in the gain affecting the ASE.

Next, we may see that, in perfect agreement with figure 5.9, the noise figure for the same input power becomes larger as the total device length increases. This produces, in fact, a sharp maximum in the noise figure for long devices when the net gain per unit length is close to zero. The main source of noise under these operating conditions is the fluctuations in the gain affecting the signal and the ASE. As shown in figure 5.10, the signal-spontaneous beat noise coefficient has a maximum when the net gain per unit length is identically zero, and the spontaneous-spontaneous beat

noise when the product of the net gain per unit length and the total device length is close to -2 . The combination of both produces the aforementioned feature when the device is long (as in the case when $L=500\mu\text{m}$). For short devices, the noise produced by the distributed combination of absorption and noise is not so large, and the noise figure evolves without much variation as the net gain per unit length changes.

Finally, in the case of TAP detectors with alternating gain and absorption, the efficiency of each individual detection region had a very important effect on the total noise figure, and was shown to be a critical parameter in the device design in terms of producing a desired noise figure and efficiency simultaneously. In TAP detectors with transverse coupling, this issue is bypassed thanks to the simultaneous action of amplification and absorption. However, a new concern in the device design appears, due to the effect of the population inversion in the amplification region. Figure 5.10 shows the noise figure considering that the gain region is fully inverted. If the amplification region is not close to inversion, equation (5.64) is no longer true. The correct expression in this case would be

$$\Gamma_g r_{st,em} = \Gamma_g g + \Gamma_g r_{st,ab} = \Delta g + \Gamma_a \mathbf{a} + \Gamma_g r_{st,ab} \quad (5.69).$$

Therefore, the noise figure will increase as the stimulated absorption in the amplifier increases. Consequently, we have interest in making sure that the amplifier is close to inversion at the operating point that the device is designed for, most likely for very small values for the net gain per unit length. This may be ensured by an appropriate choice of the confinement factors in the amplification and absorption

regions, achieved in its turn through careful design of the device properties in terms of optical guiding. Although the effect of inversion in the gain sections was omitted in the case of TAP detectors with alternating gain and absorption, this factor still exists there. However, the effect of the efficiency of each individual detection region in the total noise figure may be assumed to take precedence, its importance being proved by figure 5.6.

In summary, this paragraph has discussed intuitively and given quantitative values to the noise figure for TAP detectors with transverse coupling. A trade-off appears between the device efficiency and the noise figure, and it has been discussed and quantified. The distributed combination of gain and absorption has been shown to produce an increase in the noise figure as the device length grows when the net gain per unit length is relatively small in absolute value, whereas the limiting cases of very large net gain, positive or negative, have been shown to be very close to the cases of passive photodetectors, with and without a preceding optical amplifier, respectively. The importance of the ratio between the gain and absorption confinement factors in the device design has been mentioned, arguing that these parameters should be chosen so that the cancellation between gain, absorption and loss happens when the amplification region is close to inversion.

This section has discussed the noise produced in TAP detectors with transverse coupling. The different contributions to the total noise have been analyzed, both through an intuitive description and through numerical values. A trade-off existing between efficiency and noise figure has been presented and quantified. Finally,

conclusions have also been drawn in terms of an optimum device design for low noise operation.

Summary

The noise characteristics of TAP detectors have been presented and discussed in this chapter.

The foreseen trade-off between efficiency and noise figure, announced since chapter 2, has been explored and quantified. The different contributions to the noise figure, as well as the main factors affecting its value, have been studied.

The noise figure has been shown to increase with the number of periods in TAP detectors with alternating gain and absorption, and with the device length in TAP detectors with transverse coupling.

The efficiency of each individual absorption region is shown to play a major role in the noise figure of TAP detectors with alternating gain and absorption. The ratio between the gain and absorption confinement factors in TAP detectors with transverse coupling may also have a large impact in the noise figure, by determining whether the device operating point corresponds to the gain region being close to or far from inversion. The effect of these two parameters in the noise properties of TAP detectors results in careful design being needed in order to obtain simultaneously a high efficiency and a low noise figure.

CHAPTER 6

Fabrication of GaAs-based TAP detectors with vertical coupling

In this chapter, the process developed to fabricate vertically-coupled GaAs-based TAP detectors is presented. First, the epitaxial structure designed and grown to demonstrate the first TAP detectors in GaAs will be described, followed by the optimized structure that produced external quantum efficiency in excess of 200%. The different modifications included will be discussed, mainly from the point of view of their role in improving the device performance. Next, the different fabrication steps used to produce TAP detectors from the proposed structures will be described. Special emphasis will be given to the problems encountered and the solutions adopted, as well as to the on-chip test patterns that were introduced to guarantee the integrity of the devices along the fabrication process. InP-based TAP detectors were fabricated by Dr. Donato Pasquariello, and the fabrication process will thus not be addressed in this dissertation. Details on the epitaxial structure used may be found in [1].

Epitaxial structures for TAP detectors with vertical coupling

In this section, the two epitaxial structures designed to demonstrate the properties of TAP detectors will be described. The first generation of devices fabricated out of the original structure provided proof of principle of the distributed combination of amplification and absorption. Next, an optimized structure that yielded an external quantum efficiency in excess of 200% will be presented, paying special attention to the different modifications adopted to improve the device performance.

First generation

The epitaxial structure designed for the first generation of GaAs-based TAP detectors is detailed in table 6.1. The general characteristics of this structure, and the reasons for their choice, will now be discussed.

Light absorption occurs in the topmost GaAs bulk region. The main reason for using bulk is the easier carrier extraction, since carriers, especially holes, tend to get trapped in quantum wells (QWs). The top contact is evaporated directly on top of this bulk GaAs layer, providing a Schottky junction. As it will be shown through experimental results in the next chapter, and as indicated in figure 6.1 further down this section, the built-in field for this junction proves to be high enough for efficient carrier extraction, thus allowing a zero-volt operation of the absorption diode.

A highly n-doped layer beneath this absorption region allows for a low-resistance ohmic contact. This low contact resistance is necessary to avoid heating, since not

only the absorption diode current is extracted through it, but the gain diode bias current is also injected through this contact.

Layer name	Thickness	Composition	Doping (cm^{-3})
Absorption	300nm	GaAs	undoped
Contact (n)	100nm	$\text{Al}_{0.15}\text{Ga}_{0.85}\text{As}$	$5 \cdot 10^{18}$ (n)
Cladding (n)	300nm	$\text{Al}_{0.2}\text{Ga}_{0.8}\text{As}$	$1 \cdot 10^{18}$ (n)
Parabolic grade	16.5nm	graded	$1 \cdot 10^{18}$ (n)
Oxidation layers	6nm	$\text{Al}_{0.9}\text{Ga}_{0.1}\text{As}$	$1 \cdot 10^{18}$ (n)
Oxidation layers	32nm	$\text{Al}_{0.98}\text{Ga}_{0.02}\text{As}$	$1 \cdot 10^{18}$ (n)
Oxidation layers	6nm	$\text{Al}_{0.9}\text{Ga}_{0.1}\text{As}$	$1 \cdot 10^{18}$ (n)
Parabolic grade	18.2nm	graded	$1 \cdot 10^{18}$ (n)
SCH (n)	90nm	$\text{Al}_{0.15}\text{Ga}_{0.85}\text{As}$	$1 \cdot 10^{18}$ (n)
SCH	10nm	$\text{Al}_{0.15}\text{Ga}_{0.85}\text{As}$	undoped
QW (x4)	8nm	GaAs	undoped
Barrier (x3)	8nm	$\text{Al}_{0.15}\text{Ga}_{0.85}\text{As}$	undoped
SCH	60nm	$\text{Al}_{0.15}\text{Ga}_{0.85}\text{As}$	undoped
SCH (p)	20nm	$\text{Al}_{0.2}\text{Ga}_{0.8}\text{As}$	$5 \cdot 10^{17}$ (p)
Parabolic grade	18.2nm	graded	$1 \cdot 10^{18}$ (p)
Oxidation layers	6nm	$\text{Al}_{0.9}\text{Ga}_{0.1}\text{As}$	$3 \cdot 10^{17}$ (p)
Oxidation layers	32nm	$\text{Al}_{0.98}\text{Ga}_{0.02}\text{As}$	$3 \cdot 10^{17}$ (p)
Oxidation layers	6nm	$\text{Al}_{0.9}\text{Ga}_{0.1}\text{As}$	$3 \cdot 10^{17}$ (p)
Parabolic grade	16.5nm	graded	$2 \cdot 10^{18}$ (p)
Cladding (p)	200nm	$\text{Al}_{0.2}\text{Ga}_{0.8}\text{As}$	$5 \cdot 10^{17}$ (p)
Contact (p)	300nm	$\text{Al}_{0.2}\text{Ga}_{0.8}\text{As}$	$2 \cdot 10^{18}$ (p)
Cladding (p)	100nm	$\text{Al}_{0.2}\text{Ga}_{0.8}\text{As}$	$5 \cdot 10^{18}$ (p)
Sublayer	$3\mu\text{m}$	$\text{Al}_{0.5}\text{Ga}_{0.5}\text{As}$	semi-insulating
Substrate	$\sim 150\mu\text{m}$	GaAs	semi-insulating

Table 6.1: Epitaxial structure used for the fabrication of the first generation of GaAs-based TAP detectors. The layers are ordered from top to bottom, the lowermost corresponding to the growth substrate. Thickness, composition and doping are indicated for each layer. All composition-graded layers present a parabolic composition profile. The four quantum wells (QW) and the three barriers alternate.

The n-doped cladding layer provides a path for lateral conduction of the current from the common ground contact to either the gain or the absorption diode. It is therefore important that this layer presents good conductivity. This is one of the

reasons to choose this middle cladding to be n-doped. Another reason is the lower effect of the parasitic transistor when the middle cladding is n-doped. This is due to the lower diffusion length of holes with respect to electrons, as discussed in chapter 2. Finally, free-carrier absorption, a source of optical loss, is higher in heavily p-doped GaAs than in highly n-doped GaAs (see for example [2]). Thus, and given the lower mobility of holes, achieving the same resistance for this layer would result in much higher optical loss, the source of which is located between gain and detection layers. This optical loss would affect intensely all the optical modes overlapping with both regions. Reciprocally, a p-doped middle cladding featuring the same free-carrier absorption would result in added resistance to both the amplification and detection diode currents, resulting in added Joule heating.

It has been recently shown that $\text{Al}_{0.98}\text{Ga}_{0.02}\text{As}$ presents several advantages over AlAs for the purposes of selective wet oxidation, such as a higher resilience to thermal cycling, higher mechanical resistance and lower anisotropy [3]. Furthermore, the addition of $\text{Al}_{0.92}\text{Ga}_{0.08}\text{As}$ on both sides of a $\text{Al}_{0.98}\text{Ga}_{0.02}\text{As}$ has been demonstrated to produce tapering of the oxidation front, resulting in improved mechanical properties due to lower stress, as well as a more isotropic oxidation front. Based on these advantages, the oxidation layers for TAP detectors were chosen to present an intermediate $\text{Al}_{0.98}\text{Ga}_{0.02}\text{As}$ region, sandwiched between $\text{Al}_{0.9}\text{Ga}_{0.1}\text{As}$ layers. These oxidation layers were doped, using the same species as the adjacent cladding (n-type for the oxidation layers close to the middle cladding, p-type for those near the bottom

cladding). This provides two major advantages, which become apparent after considering the zero-bias band-diagram for the device structure, shown in figure 6.1.

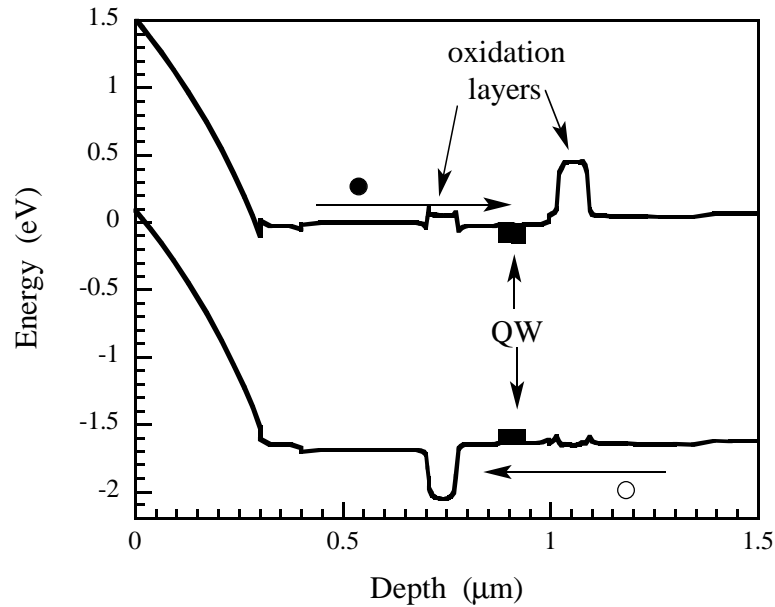


Figure 6.1: Zero-bias band-diagram for the epitaxial structure detailed in table 6.1. The zero-depth point corresponds to the top of the epitaxial structure (top of the GaAs absorption region). Note especially that the doping of the high aluminum-content oxidation layers results in easy injection of majority carriers (electrons as full dots, holes as empty dots) into the gain diode, while reducing the leakage of minority carriers out of it by the introduction of a potential barrier of $\sim 0.4\text{eV}$. Note also the built-in field generated by the metal-semiconductor Schottky junction in the absorption diode, which allows for efficient carrier extraction even in the absence of an applied bias voltage.

From one side, the doping of the oxidation layers results in the absence of a barrier to majority carrier injection when the amplification diode is forward-biased, despite the larger bandgap of higher aluminum-content material. This bandgap difference is therefore experienced nearly in its entirety by the minority carriers (electrons in the bottom cladding and holes in the middle cladding). There are two positive consequences to the presence of this barrier, since it presents an obstacle to

the leakage of carriers out of the amplification diode active region. An identical carrier concentration, and consequently the same value for the material gain, may be achieved with a lower amplifier bias current, thus reducing the effect of Joule heating. Furthermore, the leakage of holes injected into the gain diode towards the middle cladding is reduced, resulting in a smaller effect of the parasitic transistor, as described in chapter 2.

Note therefore the multiple advantages of the inclusion of oxidation layers in the device structure. From one side, lateral electrical and optical confinement is achieved through selective oxidation. The optical confinement is due both to the lower refractive index of the oxide with respect to the semiconductor, and to gain-guiding (see for example [4], p. 19), as an added advantage caused by the lateral current confinement. Furthermore, doped layers with high aluminum content produce, without being oxidized, an energy barrier for minority carriers to leave the active region, which results in an improvement in the current-gain relations, as well as a reduction in the effect of the parasitic transistor that appears in TAP detectors with vertical coupling.

A separate confinement heterostructure (SCH) provides simultaneously confinement for the electrical carriers and waveguiding for the optical mode (see for example [4], pp. 6-9). Note that part of the SCH is doped for lower resistivity, thus providing better carrier injection. The doping offset with respect to the QWs is larger on the p-doped side, to reduce the effect of the aforementioned free-carrier absorption.

A trade-off appears in the design of the bottom cladding. On one hand, the doping should be as high as possible, in order to reduce both the contact resistance and the material resistivity, since the amplifier bias current will travel both laterally from the bottom contact, and vertically through these layers, as shown in figure 6.2.

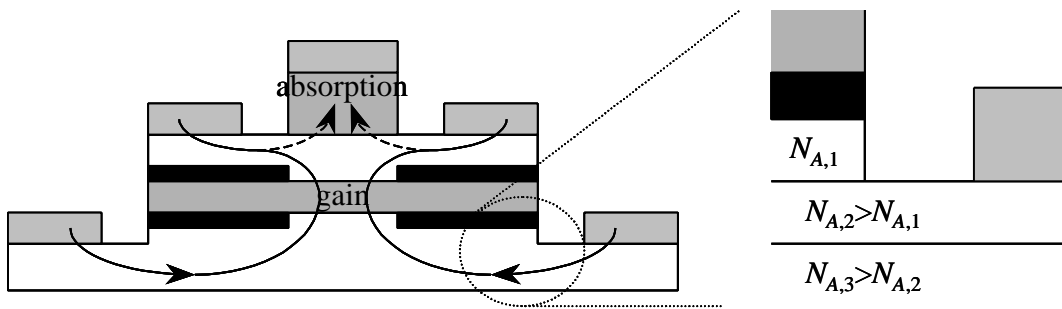


Figure 6.2: Paths followed by the currents traveling through the gain (full arrow) and absorption (dashed arrow) diodes in a TAP detector with vertical coupling. Due to the presence of the oxide (black) layers for electrical and optical confinement, both currents must travel laterally through the bottom and middle claddings, covering distances of 5-10 μm and 2-5 μm , respectively. In order to provide a low resistance while reducing the effect of free-carrier absorption, the acceptor density N_A in the bottom p-cladding increases with depth, as indicated in the detail on the right side of the figure. Active regions are shown in grey, and patterned areas indicate metal.

Note that, because of the placement of the bottom contact relatively far away ($\sim 5\text{-}10\mu\text{m}$) from the gain region in the lateral direction, a low resistivity of the bottom cladding is a necessary requirement. From this point of view, it is desirable not only that these layers present a high acceptor concentration, but that this concentration is as high as possible close to the amplifier active region. On the other hand, a high concentration of acceptor atoms increases the aforementioned free-carrier absorption, and must be removed as far as possible from the path of the optical mode, and consequently from the gain diode active region and the SCH.

The design chosen presents a relatively lower p-dopant concentration immediately adjacent to the oxidation layers separating the bottom cladding and the SCH, in order to avoid important free-carrier absorption. Another 200nm thick layer, located below this one, presents the same composition but higher doping. The bottom ohmic contact will be deposited over this layer. Finally, below this layer and far already in the vertical direction ($\sim 0.7\mu\text{m}$) from the QWs, a layer with even higher ($5 \cdot 10^{18}\text{cm}^{-3}$) acceptor concentration reduces the resistance of the lateral conduction path.

A semi-insulating $\text{Al}_{0.5}\text{Ga}_{0.5}\text{As}$ sublayer is grown first on top of the substrate, prior to the growth of any active or current-carrying layer of the device, providing a buffer to allow for surface defects from the substrate wafer to relax, thus minimizing the defect density in the actual device. Both the sublayer and the substrate are semi-insulating to reduce the microwave loss generated in the skin-effect propagation regime discussed in chapter 3.

In summary, the epitaxial structure grown for the fabrication of the first generation of GaAs-based TAP detectors with vertical coupling has been discussed in detail. The choices for the parameters of the different layers have been argued, from the point of view of obtaining a better overall device performance. In particular, the current flow has been shown to be a big concern in the design of this first generation, from the point of view of Joule heating and of current confinement. Selective oxidation in particular is argued to be a very useful tool, since the oxide produces both optical and electrical confinement, while layers with high aluminum content produce, even without being oxidized, a barrier that reduces minority carrier leakage

out of the gain active region. A trade-off is described between optical loss induced through free-carrier absorption and resistance to the amplifier bias current. The effect of this trade-off is reduced through a design incorporating acceptor concentration increasing with depth away from the active region. The goal of this design is to provide low resistance to lateral conduction, while minimizing the effect of free-carrier absorption in the guided optical signal.

The effect of the epitaxial structure on the optical guiding, and more specifically on the vertical mode distribution, has not been addressed as of yet. This issue will be discussed in detail in the next paragraph, since it was the main reason behind the changes in the epitaxial structure from the first to the second generation of GaAs-based TAP detectors.

Second generation

In the previous paragraph, a detailed description is given of the epitaxial structure out of which the first generation of TAP detectors was fabricated. Experimental results obtained from them resulted in the first demonstration of distributed amplification and photodetection. These experimental results will be shown in the next chapter. Although this represents in itself an important success, the theory developed for TAP detectors, presented in previous chapters of this dissertation, promised higher external quantum efficiencies than those achieved by this first generation. A second generation was then designed and fabricated. In this paragraph,

the epitaxial structure designed for this second generation will be presented, motivating and paying special attention to the changes with respect to the first one.

The main concern in the design of the first generation of TAP detectors was the creation of a structure where lateral current confinement would produce an effective amplification region extending laterally over the same range as the absorption region, while at the same time presenting low resistance to the flow of current (especially for the current injected into the gain diode), low optical loss due to free-carrier absorption, and low leakage of minority carriers out of the gain diode in order to minimize the effect of the parasitic transistor. Optical simulations of this structure were performed with BeamPROP, a commercial software based on the beam propagation method [5]. The main motivation behind these simulations was an optimization of the thickness of the SCH, middle cladding and absorption region. It was believed at the time when these simulations were performed that these were the main parameters affecting the vertical distribution of the optical power, and consequently these parameters alone would determine the confinement factors of the optical modes in the gain and absorption regions. It was however found that the $\text{Al}_{0.5}\text{Ga}_{0.5}\text{As}$ sublayer plays a major role in this optical power distribution, as shown in figure 6.3. In fact, the presence of this sublayer of lower index of refraction is enough to support an optical mode that overlaps mostly with the bottom cladding, partially with the amplifier and only marginally with the detection region. This mode, or any other mode presenting similar characteristics, will be hereafter referred to as “cladding mode”. Two other main modes exist, one overlapping mostly with the

gain region, and partially with the detector region (referred to as “amplifier mode”), and one that overlaps mostly with the absorption region, presenting a very small confinement factor with the amplification region (“detector mode”). These modes were found independently using BeamPROP and a Helmholtz equation solver, contained in the semiconductor optoelectronic device simulator APSYS [6]. The cladding mode, however, disappears in both cases when the simulated structure does not include the $\text{Al}_{0.5}\text{Ga}_{0.5}\text{As}$ sublayer.

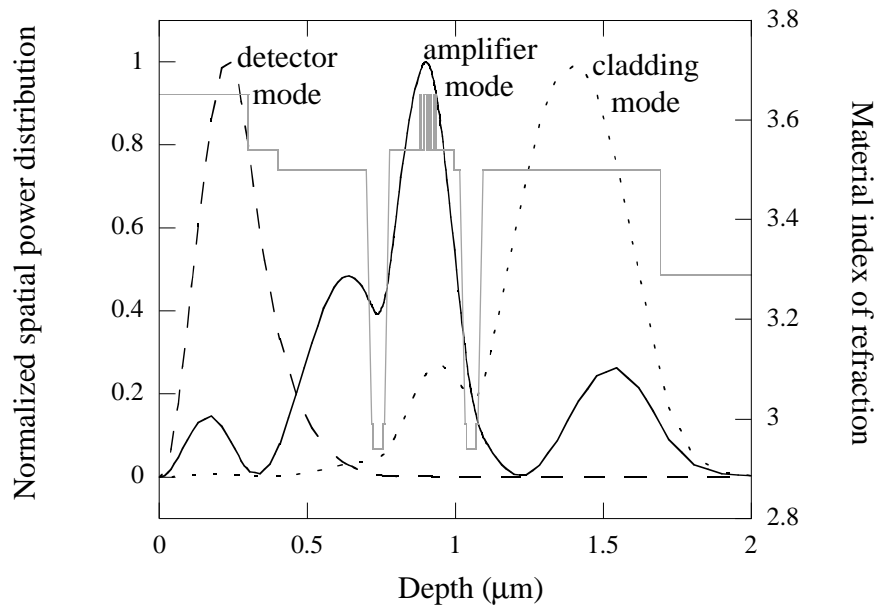


Figure 6.3: Schematic representation of the modes supported by TAP detectors with vertical coupling fabricated using the epitaxial layer structure detailed in table 6.1. The plot shows the laterally integrated optical intensity, as a function of depth. $z=0$ indicates the top of the absorption region. Only the three main modes are represented. The “cladding mode” (dotted line) overlaps partially with the amplification region, only marginally with the absorption region. The “amplifier mode” (full line) overlaps mostly with the amplification region, and partially with the detection region. Finally, most of the optical power contained in the “detector mode” (dashed line) travels along the detection region, and only a small part of it overlaps with the gain region. The gray line shows the material index of refraction as a function of position.

The optimum coupling efficiency (defined as the situation where maximum power is transferred to the three modes simultaneously) from a fiber mode produces the following input coupling coefficients: 42.3% into the cladding mode, 16.5% into the amplifier mode, 23.1% into the detector mode. These values assume the absence of reflection at the input facet. Note that most of the input power gets coupled either into the detector mode, where absorption heavily dominates, or into the cladding mode, which produces only a small amount of photocurrent because of its poor overlap with the absorption region. The presence of the cladding mode is therefore an important obstacle to achieve optimum TAP detector performance. Not only it “steals” power from the other two modes, especially from the amplifier mode, but it experiences large net gain per unit length, thus contributing to saturation, without producing a considerable amount of photocurrent in exchange. The design of the second generation of GaAs-based TAP detectors was consequently directed to the suppression of this mode, while maintaining the electrical characteristics obtained in the first generation. This was achieved by assuming the composition of the sublayer and of the bottom cladding to be identical. This way, the optical confinement due to the index difference between these two layers disappears.

BeamPROP simulations showed that the minimum index of refraction necessary to eliminate the cladding mode while providing enough waveguiding to sustain an amplifier mode corresponded to a slightly lower than 25% aluminum composition, although *a priori* better results could be achieved with higher aluminum content. However, a high aluminum content is not a practical solution, since the electrical

carrier mobility in $\text{Al}_x\text{Ga}_{1-x}\text{As}$ greatly decreases for intermediate values of the aluminum fractional composition x ($0.3 < x < 0.8$) [7]. At the same time, a high aluminum content would make the exposed bottom cladding material more susceptible to changes during the wet oxidation than a low aluminum content. Thus, the composition of the bottom cladding and of the sublayer was chosen to be $\text{Al}_{0.25}\text{Ga}_{0.75}\text{As}$. Simultaneously, the thickness of the SCH was increased, to compensate for the loss of the additional confinement to the amplifier mode provided by the $\text{Al}_{0.5}\text{Ga}_{0.5}\text{As}$ sublayer.

The target of the simulations was obtaining confinement factors in the gain and absorption regions of 15-20% and 4-5%, respectively. This double target was achieved after reducing the absorption region thickness to 200nm, while increasing the number of QWs to seven, and increasing the thickness of the middle cladding to 600nm. The optimized epilayer structure, including the aforementioned changes, is shown in detail in table 6.2. With this epitaxial layer structure, the guided cladding mode disappears. The confinement factors in the gain and absorption regions for the amplifier mode become 16% and 3.7%, respectively, while the input coupling coefficient for this mode is 46%. The coupling efficiency into the detector mode is 18%. Both coupling coefficients assume the absence of a reflection at the input facet. The gain confinement factor for the detector mode is small enough that the effect of the amplification region in this mode can be neglected.

Layer name	Thickness	Composition	Doping (cm ⁻³)
Absorption	200nm	GaAs	undoped
Contact (n)	100nm	Al _{0.15} Ga _{0.85} As	5 10 ¹⁸ (n)
Cladding (n)	600nm	Al _{0.2} Ga _{0.8} As	1 10 ¹⁸ (n)
Parabolic grade	16.5nm	graded	1 10 ¹⁸ (n)
Oxidation layers	6nm	Al _{0.9} Ga _{0.1} As	1 10 ¹⁸ (n)
Oxidation layers	32nm	Al _{0.98} Ga _{0.02} As	1 10 ¹⁸ (n)
Oxidation layers	6nm	Al _{0.9} Ga _{0.1} As	1 10 ¹⁸ (n)
Parabolic grade	18.2nm	graded	1 10 ¹⁸ (n)
SCH (n)	140nm	Al _{0.15} Ga _{0.85} As	1 10 ¹⁸ (n)
SCH	10nm	Al _{0.15} Ga _{0.85} As	undoped
QW (x7)	8nm	GaAs	undoped
Barrier (x6)	8nm	Al _{0.15} Ga _{0.85} As	undoped
SCH	60nm	Al _{0.15} Ga _{0.85} As	undoped
SCH (p)	90nm	Al _{0.15} Ga _{0.85} As	5 10 ¹⁷ (p)
Parabolic grade	18.2nm	graded	1 10 ¹⁸ (p)
Oxidation layers	6nm	Al _{0.9} Ga _{0.1} As	3 10 ¹⁷ (p)
Oxidation layers	32nm	Al _{0.98} Ga _{0.02} As	3 10 ¹⁷ (p)
Oxidation layers	6nm	Al _{0.9} Ga _{0.1} As	3 10 ¹⁷ (p)
Parabolic grade	16.5nm	graded	2 10 ¹⁸ (p)
Cladding (p)	300nm	Al _{0.25} Ga _{0.75} As	5 10 ¹⁷ (p)
Contact (p)	200nm	Al _{0.25} Ga _{0.75} As	5 10 ¹⁸ (p)
Cladding (p)	200nm	Al _{0.25} Ga _{0.75} As	2 10 ¹⁸ (p)
Sublayer	3μm	Al _{0.25} Ga _{0.75} As	semi-insulating
Substrate	~150μm	GaAs	semi-insulating

Table 6.2: Epitaxial structure used for the fabrication of the second (optimized) generation of GaAs-based TAP detectors. The layers are ordered from top to bottom, the lowermost corresponding to the growth substrate. Thickness, composition and doping are indicated for each layer. All composition-graded layers present a parabolic composition profile. The seven quantum wells (QW) and the six barriers alternate.

One additional change was the inversion of the two bottom cladding layers with higher acceptor concentration, in order to improve the contact resistance, which was bound to be negatively affected by the increase in the aluminum content of the bottom cladding alloy.

In summary, two different epitaxial structures have been described in detail and discussed in this section. The first one produced the first reported demonstration of distributed amplification and photodetection, while the second one was designed specifically to improve the performance observed in the first generation. The second structure was designed after careful simulations, whose main goal was the optimization of the optical guiding properties of the device without affecting negatively the current transport properties observed in the first generation.

In the next section, the fabrication process itself will be described, paying special attention to some of the difficulties encountered and the solutions developed to overcome them.

Fabrication process

In this section, the process developed in order to fabricate GaAs-based TAP detectors with vertical coupling will be described. First, this process will be outlined, providing a brief description of the different steps involved. Next, some of the critical steps, the difficulties that they presented, and their optimization, will be discussed. Finally, the on-chip test patterns included to guarantee the integrity of the devices during the fabrication process will be described. These test patterns were extremely important in determining which steps were critical, and in identifying possible failure mechanisms.

Outline of the fabrication process

This paragraph will describe the process developed to fabricate TAP detectors with vertical coupling in the GaAs material system, starting with the epitaxial structures described in the previous section. The different steps involved will be briefly discussed.

First, the top metal contact for the detection diode is deposited over the GaAs absorption region. A Ti/Au metal scheme may be used, but Ti/Pt/Au usually results in lower dark current, due to the added barrier to gold diffusion into the semiconductor introduced by the platinum. The first generation of TAP detectors featured the former, whereas the second generation was fabricated using the latter. No significant difference was though appreciated in the dark current of the absorption diode. The metal is patterned via lift-off. Prior to the metal deposition, and in both cases, a surface cleaning dip in an $\text{H}_2\text{SO}_4:\text{H}_2\text{O}_2:\text{H}_2\text{O}$ (1:1:40) solution is performed. Together with a previous O_2 plasma descum, this ensures the top surface being clean of impurities. This precaution is necessary to produce a detection diode with rectifying characteristics, since impurities create surface states that tend to pin the Fermi level, resulting in large dark currents.

The top contact described above is used as a mask for a wet etch that defines the detection region. A $\text{HCl}:\text{H}_2\text{O}_2:\text{H}_2\text{O}$ (1:4:40) solution is used for this chemical attack. The etch rate ($\sim 300\text{nm}/\text{min.}$) is very repeatable. The chemical attack is stopped 10 seconds before the GaAs/ $\text{Al}_{0.15}\text{Ga}_{0.85}\text{As}$ interface would be reached under normal etch rate. The final etch depth is measured by Dektak, and etching continues at 5 second

intervals until the contact layer is reached. This precaution is necessary since this solution attacks $\text{Al}_{0.15}\text{Ga}_{0.85}\text{As}$ at a faster rate ($\sim 500\text{nm}/\text{min.}$), and a reduction in the thickness of the contact layer would result in larger resistance to lateral current conduction.

The ground contact, i.e., the common contact for amplifier and detector diodes, is required to present low dark current. Typically, good ohmic contacts to n-type $\text{Al}_x\text{Ga}_{1-x}\text{As}$ are obtained by depositing Ni/AuGe/Ni/Au, then annealing at $420\text{-}440^\circ\text{C}$. In test samples, optimum contact resistances in the low $10^{-6}\Omega\text{cm}^2$ were obtained for an anneal temperature of 430°C . However, this temperature was suspected to create gold spikes through the middle cladding, reaching even into the amplifier active region, resulting in catastrophic failure of the gain diode. For this reason, during TAP detector fabrication, the n-contact anneal was performed at a temperature of 420°C , resulting consistently in characteristic contact resistances of $4\text{-}5 \cdot 10^{-6}\Omega\text{cm}^2$. The metal is patterned via lift-off, its deposition being preceded by descum and chemical cleaning as in the case of the top contact for the detector diode.

After the ground contact is evaporated and annealed, the sample is covered with SiN_x via chemical vapor deposition. The SiN_x is patterned via reactive ion etching (RIE), using a $\text{CF}_4\text{:O}_2$ gas mixture. This dielectric is then used as a mask for a Cl_2 RIE attack that defines the amplifier diode and the optical waveguide. This step is monitored via normal-incidence interferometry, producing a very distinctive, repeatable pattern when different samples from the same wafer are etched. Monitoring the etch stop is a necessary precaution. Stopping the etch too early would

result in the bottom contact being deposited over a low-doped $\text{Al}_{0.25}\text{Ga}_{0.75}\text{As}$ or $\text{Al}_{0.15}\text{Ga}_{0.85}\text{As}$ layer, producing a high contact resistance, whereas stopping too late could result in a thinner doped channel for the lateral conduction of the amplifier bias current injected from the bottom contact. The surface damage produced by this RIE Cl_2 attack is reduced via a short dip in an $\text{NH}_4\text{OH}:\text{H}_2\text{O}_2:\text{H}_2\text{O}$ (1:1:40) solution. The sample with the SiN_x mask deposited and patterned, prior to the Cl_2 RIE attack is shown in figure 6.4.

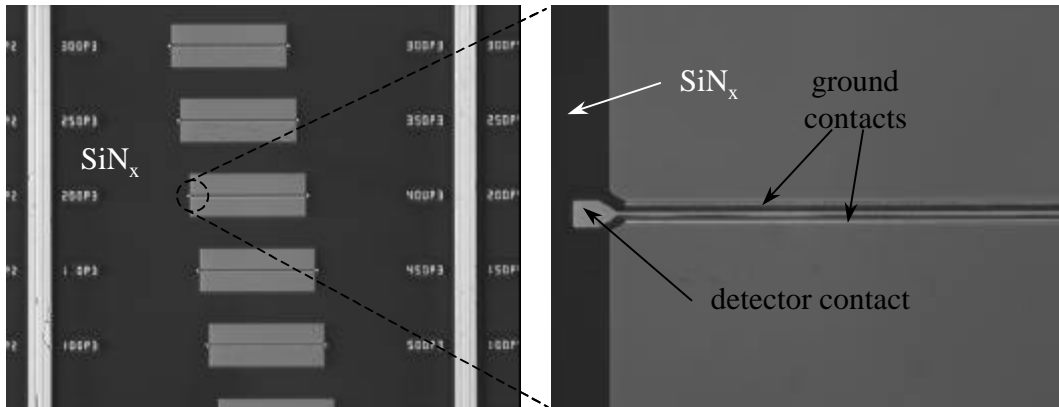


Figure 6.4: Optical microscope picture (left) and detail (right) taken during TAP detector fabrication, prior to the Cl_2 RIE chemical attack performed to define the amplifier ridge. The picture shows the SiN_x (darker area) deposited via PECVD and patterned via CF_4/O_2 RIE that serves as a mask for the Cl_2 -based etch. Note that the gap between ground and detector contacts is covered by the SiN_x mask.

Next, the amplifier contact is deposited on the p-type $\text{Al}_x\text{Ga}_{1-x}\text{As}$ bottom cladding, where $x=0.15$ for the original design, and $x=0.25$ for the optimized design. Ohmic contacts to p-type GaAs are usually feasible using Ti/Pt/Au. However, this same metal scheme does not provide good ohmic contacts in the presence of Al-containing contact layers, resulting in all test samples exhibiting a residual rectifying

behavior. Better results were typically obtained using Zn, introduced via the evaporation of either Cr/AuZn/Cr/Au or Pd/Zn/Pd/Au. In test samples, the former produced contact resistances in the mid $10^{-6}\Omega\text{cm}^2$ after annealing at 410°C . The latter produced, as evaporated, ohmic contacts with similar contact resistance; a 380°C anneal further reduced this contact resistance to $1\text{-}2 \cdot 10^{-6}\Omega\text{cm}^2$. During the fabrication of TAP detectors, Pd/Zn/Pd/Au was thermally evaporated, and patterned via lift-off. Immediately after this deposition, and before lift-off, SiO_2 is evaporated on the sample. This creates an insulating layer on top of the bottom metal, preventing possible short circuits between it and the ground plane of the coplanar waveguide (CPW).

After lift-off, the sample is oxidized at 400°C for 45 minutes in a wet environment, by feeding the furnace with 10l/min of N_2 that previously passes through a bubbler where water is heated at 90°C . This produces an oxide depth of $4\mu\text{m}$. Since the ground contact is $2\mu\text{m}$ wide and there are $2\mu\text{m}$ of spacing between this contact and the absorption region, this procedure results in the aperture in the amplification diode being aligned vertically to the detection region. Prior to the oxidation, and in order to remove any native oxide, the sample is dipped in undiluted NH_4OH for $\sim 5\text{sec}$, being kept in isopropanol from that moment until being blown dry with a N_2 gun and inserted into the oxidation furnace. The oxidation is performed after the bottom contact deposition to prevent any change in the bottom cladding that may degrade the characteristics of the bottom ohmic contact to the amplification diode. Figure 6.5 shows a cross-section of a finished and cleaved device, where the oxide

depth may be appreciated to confine the current injection into the amplifier to a region with about the same width, and directly below, the detection diode.

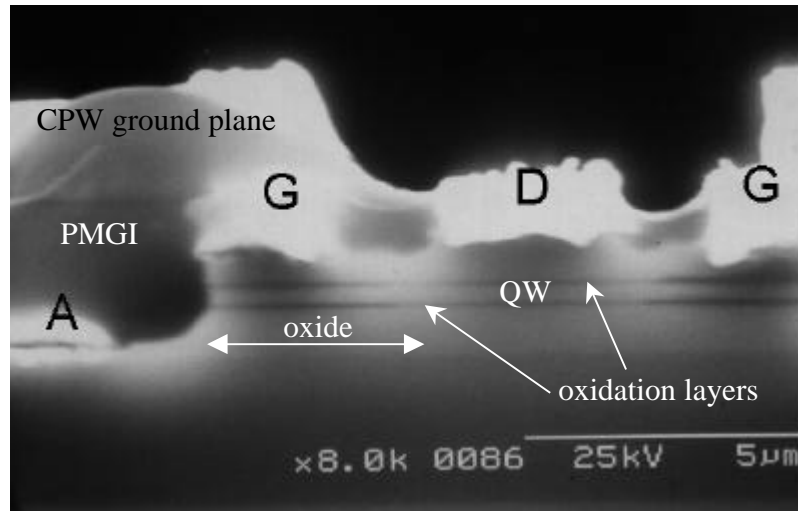


Figure 6.5: SEM micrograph of the input facet of a finished TAP detector. Note that the oxide depth is calibrated to confine the current flow into the amplifier to a region of the same width as, and directly below, the top absorption diode; the thicker region in the dark, horizontal line actually indicates the oxidized $\text{Al}_{0.9}\text{Ga}_{0.1}\text{As}$. The quantum well-based amplification active region is confined, as shown, between the two oxide layers. The different metal contacts are also indicated (A for amplifier, G for ground, D for detector), as well as the PMGI for planarization and the CPW ground plane.

At this time, the TAP detectors themselves are finished. All the rest of the steps are used to provide the interconnections necessary to test the devices.

After the oxidation, a new lithography is used to selectively remove the SiO_2 from the areas where the contact pad used to inject current into the amplifier will come in touch with the bottom contact metal. Subsequently, and using the same photoresist for lift-off, a thick layer of gold is deposited to make the bottom contact available for interconnection after planarization.

The first step in the planarization consists on spinning polymethylglutarimide (PMGI) on the sample, baking it at 240°C for 20min and patterning it via deep-UV exposure and development, using AZ4330 photoresist as the mask. The PMGI chosen was MicroChem SF-15. Two layers were spun at 5Krpm, resulting in a thickness of ~5µm. After the PMGI is spun and baked, the photoresist is spun and patterned using traditional lithography. Later, deep-UV exposure hardens the photoresist, while making soluble in SAL-101 developer the PMGI not covered by it. After the PMGI has been selectively developed, the photoresist is removed by spraying the sample with acetone. Subsequently, the PMGI is etched back to expose the top of the detector, ground and amplifier contacts (the later through the metal pillar deposited after oxidation). Finally, the PMGI is caused to reflow by heating the sample at 240°C for 10min. This provides smooth height transitions so that the final CPW metal deposition is continuous even at locations where the sample height varies. Prior to the spinning of the first layer of PMGI, a surface oxide clean is performed to improve the dark current characteristics of the detection diode. This oxide clean consists on a 10sec dip in a H₂SO₄:H₂O₂:H₂O (1:1:40) solution. The sample is kept in isopropanol after this clean and until blown dry right before the spinning of the first layer of PMGI.

After a final lithography, the CPW and the pad allowing access to the bottom contact of the amplifier are evaporated. A thin layer of Ti is deposited first for adhesion, followed by a thick (~2µm) layer of gold. The fabrication process as described above is schematically represented in figure 6.6.

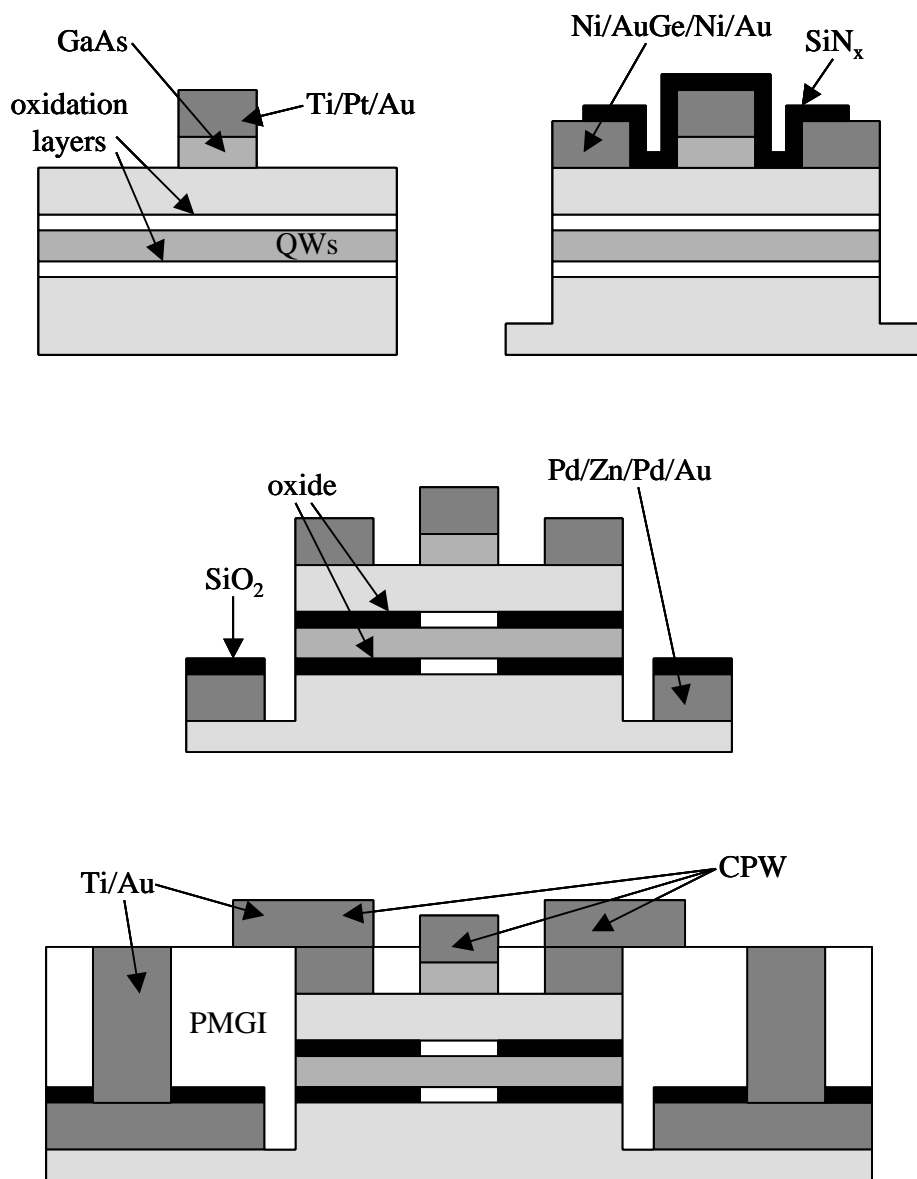


Figure 6.6: Schematic representation of the different steps involved in the fabrication of TAP detectors. The following steps are represented: top left: deposition of Schottky contact to the absorption region and wet etch to define the absorption diode width. Top right: ground contact deposition and Cl_2 -based RIE attack defining the amplifier ridge - the figure shows the SiN_x mask protecting the region in between detector and ground contacts during this attack. Middle: Bottom contact deposition and lateral oxidation. The figure shows the SiO_2 layer deposited to prevent short-circuits caused by PMGI punch-through. Bottom: Protective SiO_2 layer etch, followed by pillar deposition for interconnection, PMGI planarization and passivation, and CPW deposition.

At this point, the current-voltage (I-V) characteristics of the fabricated TAP detectors are measured. Next, the devices need now to be made ready for testing. As shown in figure 6.7, the last metal evaporation (CPW and amplifier contact pad) is also used to deposit marks allowing precise cleaving of the devices to produce, due to their strategic placement, TAP detectors of different lengths in the same sample and with one single cleave. Prior to cleaving, the sample is thinned. After cleaving, the devices are ready to be tested. Preliminary optical characterization is interesting at this point in order to ascertain the wavelength for which the optical gain inside the device is highest. Next, SiO_x deposition on the facet provides an anti-reflection coating (AR-coating) at the desired wavelength, which makes the devices ready for complete characterization of their properties. The refractive index of SiO_x depends on the ratio of silicon to oxygen, which in turn is a function of the evaporation rate. A 1220Å-thick layer, evaporated at a rate of 8-9Å/sec, was estimated after calibration to produce residual reflections under 1% at a wavelength of 855nm.

After summarizing the fabrication process, some of the critical steps will be discussed in more detail.

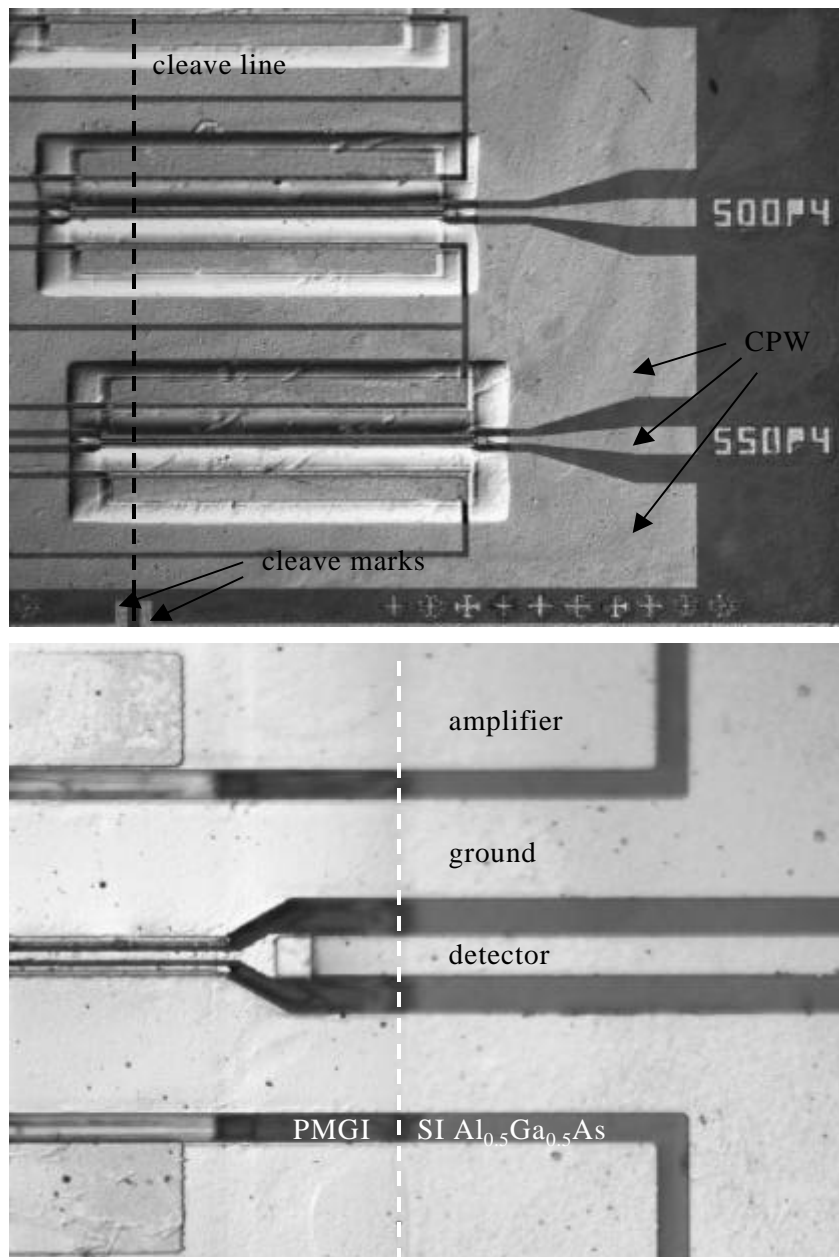


Figure 6.7: Optical microscope picture of fabricated TAP detectors prior to cleaving (top) and detail (bottom). A symmetric placement allows the creation of two sets of devices at both sides of the cleave line. The staggering between them produces different lengths in the same sample with one single cleave. Note how the contact pad and CPW lie mostly on the semi-insulating substrate instead of PMGI. This significantly increases the device robustness in order to sustain the cleaving and characterization process, as well as reducing the microwave loss due to propagation in the CPW. Note also the cleave marks deposited simultaneously to the CPW.

Temperature budget

Prior to the first successfully fabricated generation of TAP detectors with vertical coupling, one of the early attempts exhibited no optical gain in the amplification region, while the turn-on voltage of the gain diode was $\sim 0.5\text{V}$, much lower than the expected value, which should be similar to the GaAs bandgap divided by the charge of an electron (1.424V). This was believed to be caused by gold spiking from the ground contact and into the active region, as shown in figure 6.8.

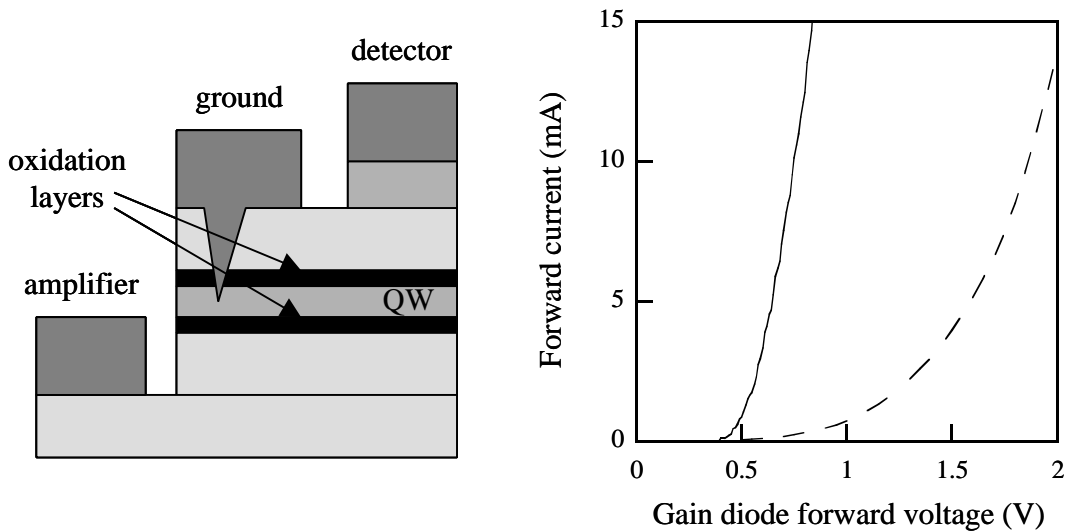


Figure 6.8: Schematic representation of the formation of gold spikes from the ground contact and into the gain region (left). This was believed to be the cause of failure in early attempts to fabricate TAP detectors with vertical coupling. The device failure showed itself through the nearly absence of optical emission, and a much lower turn-on voltage of the gain diode than expected given the bandgap of GaAs. Right: the forward I-V characteristics of gain diodes in early attempts (full line) and successfully fabricated devices (dashed line) are compared.

Since AuGe reaches a eutectic point at 430°C , which was believed to be the mechanism triggering the spike formation, the strategy to solve this problem was to try to avoid this temperature in any step of the process after the AuGe deposition. All

anneals were thus performed at 420°C or lower, which resulted in an n-contact resistance slightly higher than its optimum value (reached for the annealing temperature of 430°C). The p-contact resistance using a Pd/Zn/Pd/Au metal scheme was found to be optimum for an annealing temperature 380°C, and was thus not affected by this limitation. Oxidation, initially performed at 420°C for 12min, was recalibrated and performed at 400°C. Whether the cause of the problem described in early attempts was indeed gold spiking or not, and whether it was caused by the n-contact anneal or by the oxidation is still unclear, but changing the temperature budget eliminated the problem, which did not appear again.

PMGI punch-through

Another source of failure in early fabrication attempts was the short-circuiting of the gain diode. This problem was known to occur after planarization and CPW deposition. All pointed to PMGI punch-through being the cause, as schematically represented in figure 6.9.

It is still unclear whether this was caused by the more porous nature of PMGI with respect to other insulators (such as SiN_x or SiO₂), or by local variations in the thickness. However, introducing a 200nm thick SiO₂ layer on top of the bottom contact, removed selectively to allow for contact of the gain diode p-type cladding, caused this problem not to reappear. The implementation of this solution is also schematically represented in figure 6.9.

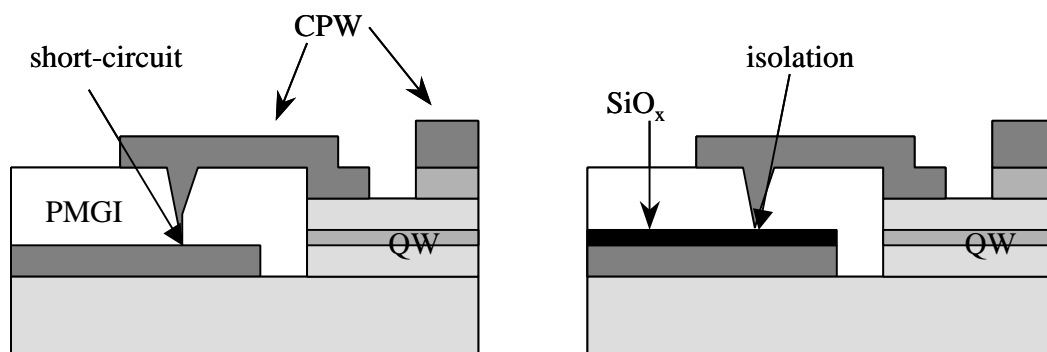


Figure 6.9: Left: schematic representation of the PMGI punch-through leading to a short-circuit of the gain diode. Right: this problem was solved by evaporation of a 200nm thick layer of SiO_2 directly on top of the bottom contact, and patterned via lift-off with the same photoresist mask as the metal itself. This SiO_2 layer was selectively removed via CF_4/O_2 RIE etch immediately before the deposition of the pillar facilitating the connection between the gain pad and the bottom contact.

In summary, the fabrication process used to produce TAP detectors with vertical coupling has been outlined, and the main problems encountered and the solutions adopted have been discussed in detail. In the next paragraph, some of the test patterns used to guarantee device integrity through the fabrication process, as well as allowing early failure detection and troubleshooting will be presented.

On-chip test patterns

In this paragraph, the test patterns included on-chip in order to monitor the characteristics of the devices during fabrication will be presented. Because of the device design featuring small contact dimensions, the actual TAP detectors could not be probed at different stages of their creation, only after the final CPW is deposited. Thus, on-chip test patterns became very useful to detect eventual failures during the fabrication process, as well as identifying at what stage they happened. The

information provided by these test patterns was used to optimize the fabrication process and overcome the problems outlined in the previous section.

Gain and absorption diodes

Due to the small dimensions of the detector and ground contacts in TAP detectors, it is not possible to measure the integrity of gain and absorption diodes during fabrication. After initial attempts where it was believed that gold spiking from the ground contact was disabling the gain diodes, not only all temperatures involved in the device fabrication were reduced to 420°C or lower, but large area (50-90µm wide) square-shaped diodes were introduced as test patterns easily accessible at all moments during fabrication. Such diodes were fabricated simultaneously as the gain and absorption diodes in the TAP detectors. Figure 6.10 shows a top view optical microscope picture, identical for both gain and absorption diodes.

After the inception of this test pattern, it was possible to test the integrity of the gain diodes as soon as their bottom contact was deposited and between the different subsequent fabrication steps. Special emphasis was made on testing these diodes before and after oxidation, trying to ascertain whether this particular step was the cause of the degradation observed in early fabrication attempts, and shown in figure 6.8. Since the problem was not reproduced after the adoption of these test patterns, a definitive answer cannot be provided on this issue. However, the confirmation that the gain and absorption diodes was not degraded during fabrication once the annealing and oxidation temperatures were reduced was extremely valuable.

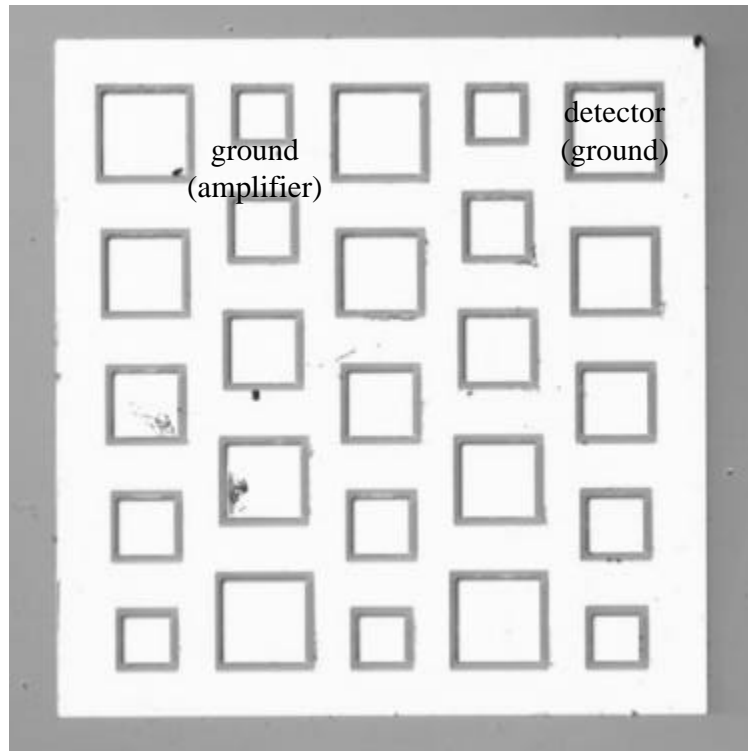


Figure 6.10: Microscope picture of gain or absorption diode test patterns. As indicated in the figure, the Au squares constitutes the detector contact in absorption diodes or the ground contact in gain diodes, while the bottom Au plane serves as the ground contact in the former, or as the amplifier contact in the latter.

The detection diodes never experienced such a problem, but these test patterns were deemed useful in order to determine the origin of their dark current. In fact, the test diodes being square-shaped with variable side lengths, a dark current depending linearly on the square side length for a given voltage would indicate a surface leakage source (the sidewall surface of the absorption test diode is given by $4Lt_i$, t_i being the intrinsic detection region thickness and L the square side length), while bulk leakage would cause a quadratic dependence (the absorption test diode area being L^2). Furthermore, any step significantly increasing the dark current could be easily identified by using these test patterns. It was concluded through monitoring along the

fabrication process that, after the planarization and prior surface oxide clean, most of the dark current was caused by bulk leakage. The dark current would however increase with time if the detector sidewalls were left uncovered. Hence the importance of the PMGI, not only for planarization, but also as a passivation agent.

Oxidation depth test

Although the oxidation rate for the parameters used during fabrication had been previously calibrated, it was deemed important to be able to determine as precisely as possible the oxide depth achieved in TAP detectors. Since the amplifier waveguide ridge is partially covered in metal by the time of oxidation (ground and detector contacts have already been deposited), a direct measurement of this depth is not possible. Test patterns were thus introduced, defining stripes uncovered by metal during the Cl₂-based amplifier waveguide etch. The sidewalls of these stripes are thus identical to those of the amplification diode in the TAP detectors, barring the presence of metal, which is not known to be an important factor in the oxidation rate. Stripes oriented along, perpendicularly and at a 45° angle with respect to the longitudinal direction of TAP detector waveguides were defined, as shown in figure 6.11. The combination of these features may also be used to test the isotropy of the oxidation.

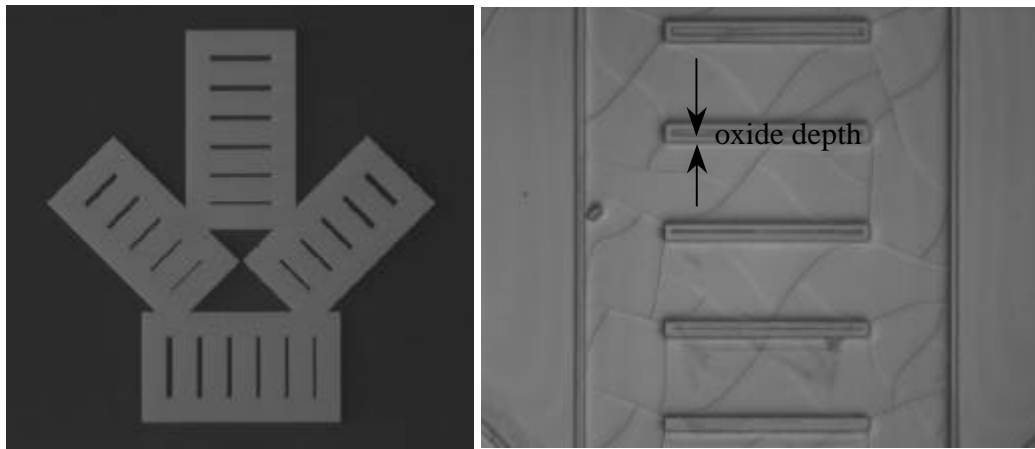


Figure 6.11: Oxidation depth test pattern. Top view with SiNx mask and prior to etching (left) and detail after oxidation (right). The different stripe orientations are used to confirm the isotropy of the oxidation. The different stripe widths allow for a quick estimation of the oxide depth before a more accurate measurement.

PMGI punch-through test pattern

After the initial fabrication attempts resulting in short-circuited amplification diodes, the process was changed as outlined in the previous section. However, in order to confirm the cause of this problem should it repeat itself, test patterns were introduced in the shape of parallel-plate capacitors, as shown in figure 6.12.

The bottom plate is defined by the p-contact metal, while the top plate is deposited at the same time as the CPW. All the bottom plate, except for an opening to allow testing, is covered with SiO₂ at the same time as the bottom contact in the actual devices.

These test patterns would have, in the case of the gain diodes being again short-circuited, allowed us to determine whether the probable cause of PMGI punch-

through was indeed behind this behavior. However, after the fabrication process was changed, introducing the SiO_2 deposition, this problem did not reappear.

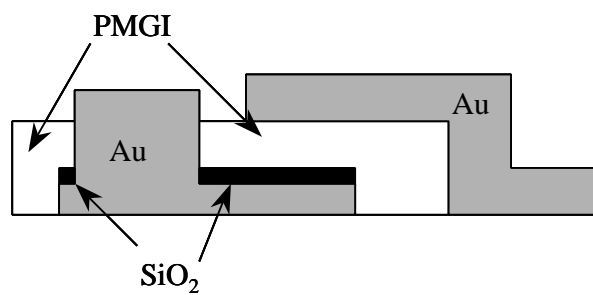
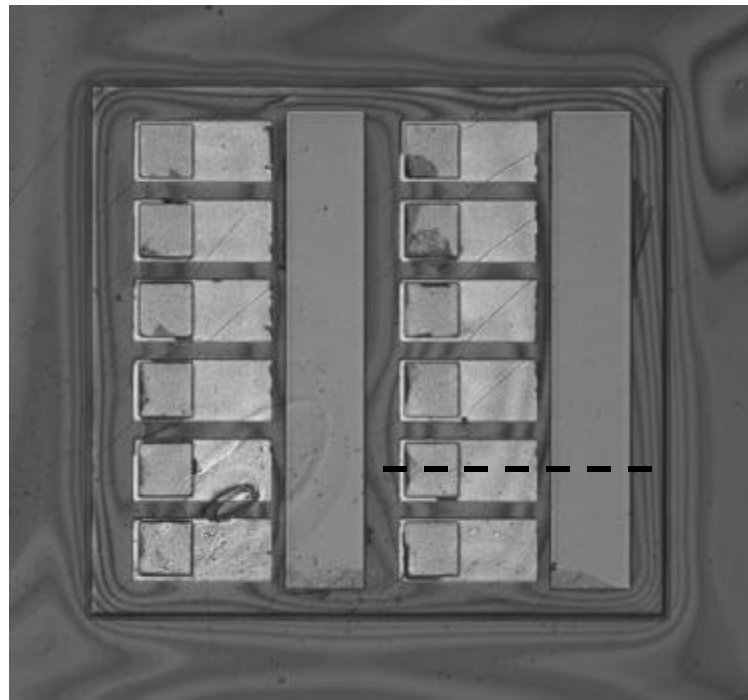


Figure 6.12: PMGI punch-through test pattern. Top view before CPW metalization (top) and schematic cross-section along the dashed line after completion (bottom). The structure shown presents the same cross-section as the ensemble formed by the bottom contact, SiO_2 , PMGI and CPW in actual TAP detectors.

Devices equipped with test pads

As shown in figure 6.7, the placement by default of TAP detectors in the sample is such that with one cleave two sets of devices are formed, at either side of the cleave line, and with different lengths. This makes it impossible to access these devices during the fabrication process. The previously described test patterns allow for general testing of the integrity of “magnified” device parts, v.g., gain and absorption diodes of large width to facilitate their on-chip probing prior to the deposition of the interconnection CPW. However, it is possible to encounter problems during fabrication that appear only when device sizes are small (v.g., short-circuit of detector and ground contacts due to the small separation between them). In order to identify early this sort of problems, one test pattern was devised as follows: for one set of devices, instead of fabricating TAP detectors at both sides of the cleave line, wide contact pads are fabricated at one side, which allowed access to the device located at the other side of the cleave line, as shown in figure 6.13. This way, at least some of the devices on the sample may be probed during fabrication, with a minimum waste of useful space. Note that these devices may also be cleaved to produce one set of TAP detectors at one side of the cleave line.

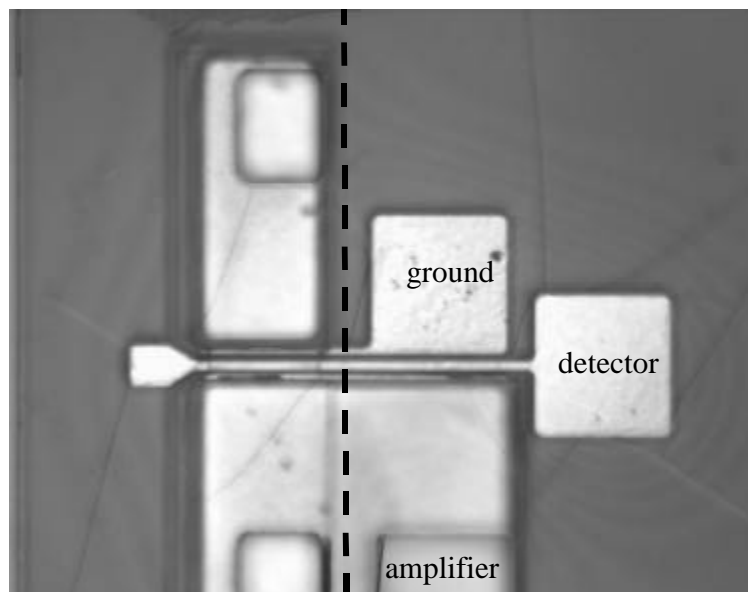


Figure 6.13: Optical microscope picture of TAP detectors equipped with large contact pads allowing their probing during fabrication. The devices are cleaved along the dashed line between their active half (left) and the probe pads (right), thus making it possible to test these devices optically after the fabrication process is complete. The role of each of the contact pads is indicated in the figure.

This concludes the description of the most important test patterns embedded in the sample during TAP detector fabrication.

In summary, the fabrication process of TAP detectors in GaAs has been described and discussed, paying special attention to the problems encountered, the solutions adopted and the on-wafer test patterns designed to detect and help correct these problems.

References

[1] J. Piprek, D. Pasquariello, D. Lasoasa, J.E. Bowers, "Novel waveguide photodetectors on InP with integrated light amplification," *Proceedings of the Electro-Chemical Society International Symposium*, pp. 1-8, 2003.

- [2] H.C. Casey Jr., F. Stern, "Concentration-dependent absorption and spontaneous emission of heavily doped GaAs", *Journal of Applied Physics*, vol. 47, no. 2, pp. 641-43, 1976.
- [3] K.D. Choquette, K.M. Geib, C.I.H. Ashby, R.D. Twisten, O. Blum, H.Q. Hou, D.M. Follstaedt, B.E. Hammons, D. Mathes, R. Hull, "Advances in selective wet oxidation of AlGaAs alloys", *IEEE Journal of Selected Topics in Quantum Electronics*, vol. 3, no. 3, pp. 916-26, 1997.
- [4] L.A. Coldren, S.W. Corzine, "Diode lasers and photonic integrated circuits," *John Wiley & Sons*, 1995.
- [5] BeamPROP 5.0, *RSoft Design Group*, 2001 (<http://www.rsoftdesign.com>).
- [6] APSYS 4.3.3, *Crosslight Software*, 2001 (<http://www.crosslight.com>).
- [7] S. Adachi, "GaAs, AlAs and $\text{Al}_x\text{Ga}_{1-x}\text{As}$: Material properties for use in research and device applications", *Journal of Applied Physics*, vol. 58, no. 3, pp. R1-29, 1985.

(This page is intentionally left blank)

CHAPTER 7

Experimental characterization of TAP detectors with vertical coupling

In this chapter, the results of the experimental characterization of TAP detectors with vertical coupling will be presented. Conclusions about the validity of the modeling presented in previous chapters will be drawn, paying special attention to the factors limiting the performance of TAP detectors fabricated to date. Before cleaving the devices, they were characterized electrically, by measuring both independently and simultaneously the response of the gain and absorption diodes. After cleaving, an initial optical measurement allowed us to find the peak of the optical gain. An anti-reflection coating (AR-coating) was then deposited on the input facet of the device before proceeding to fully characterize their optoelectronic response. The results from these measurements will be presented and discussed in this chapter. Most of the experimental results shown, as well as most of the discussion, will be centered around GaAs-based TAP detectors, since the experimental characterization of InP-based TAP detectors was performed by Dr. Donato Pasquariello. However, and since the

analysis of those experimental results and their comparison with the theoretical predictions was performed jointly with the author of this dissertation, a brief summary of the characteristics measured in InP-based TAP detectors, as well as the conclusions supported by those data, will also be presented.

Electrical characterization of TAP detectors

The electrical measurements performed on TAP detectors had two main goals: ascertaining the electrical properties of gain and absorption diodes in order to be able to relate them to the optoelectronic performance of the device, and measuring the effect of the parasitic transistor that appears in TAP detectors with vertical coupling. The forward-biased current-voltage (I-V) characteristics of the gain diodes will be presented first in this section. Then, the effect of the parasitic transistor and the reverse-biased I-V characteristics of the absorption diodes will be presented simultaneously, by studying the dependence of the reverse current in the detection diode on both the reverse bias applied to it, and on the forward bias applied to the gain diode. These measurements were performed using an HP4145 semiconductor parameter analyzer.

Figure 7.1 shows the forward I-V characteristics of the amplification diodes in the two generations of successfully fabricated GaAs-based TAP detectors with vertical coupling. These results were taken before cleaving, resulting in all devices having the same length (600 μm). Very little deviation may therefore be expected for

different devices, as confirmed by the plots. There is however a change in the dynamic forward resistance from one generation to the next. The larger resistance exhibited by devices from the second generation may without a doubt be related to a larger resistance of the $\text{Al}_{0.25}\text{Ga}_{0.75}\text{As}$ p-doped cladding with respect to the $\text{Al}_{0.2}\text{Ga}_{0.8}\text{As}$ p-doped cladding present in devices from the first generation, and to the larger characteristic resistance of the contacts deposited on this cladding. Transfer length method (TLM) measurements confirmed this hypothesis, showing how the p-doped cladding resistance had increased from the first to the second generation from $\sim 800\Omega$ per square to $\sim 6000\Omega$ per square, while the characteristic contact resistance had risen from $\sim 2 \cdot 10^{-6}\Omega\text{cm}^2$ to $\sim 1.5 \cdot 10^{-5}\Omega\text{cm}^2$.

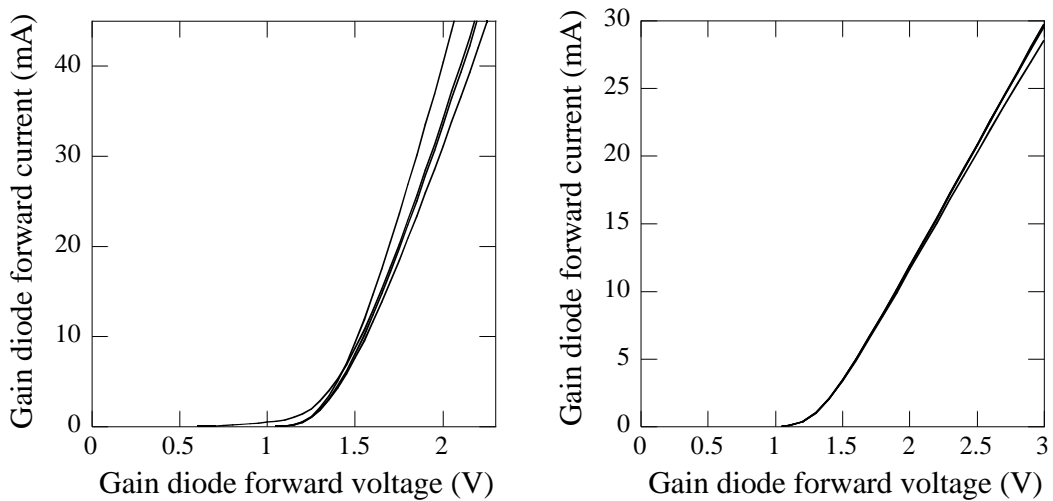


Figure 7.1: Typical current-voltage (I-V) characteristics of the forward-biased amplification diodes in GaAs-based TAP detectors with vertical coupling. The results shown correspond to several different devices from the first (left) and second (right) generations. The increase in the forward differential resistance is due mostly to an increase in the p-layer resistance and p-contact characteristic resistance because of the increase in the aluminum content in the bottom cladding ($\text{Al}_{0.2}\text{Ga}_{0.8}\text{As}$ to $\text{Al}_{0.25}\text{Ga}_{0.75}\text{As}$). The measurements were taken before cleaving, and correspond to the equivalent of 600mm long devices.

The natural consequence of these results is that more Joule heating was produced in devices from the second generation. The effect of the ensuing increase of temperature will need to be taken into account when explaining the difference in performance between these two generations.

The characteristics of the absorption diode and the parasitic transistor will now be described. These are shown in figure 7.2, through the plot of the current of the reverse-biased absorption diode as a function of the voltage applied to its terminals and of the current injected into the forward-biased amplifier diode. Note that, although the devices were not cleaved at the point in time where these measurements were taken, spontaneous emission and ASE are produced in the device. The total current in the absorption diode is thus the sum of its dark current, the current generated by the effect of the parasitic transistor, and the contribution produced by the absorption of spontaneous emission and ASE.

The reverse current in the absorption diode seems to have two very different regimes. For low applied reverse voltages ($<1.5\text{V}$), the total reverse current is virtually independent on the applied voltage, being determined nearly exclusively by the current injected into the amplification diode.

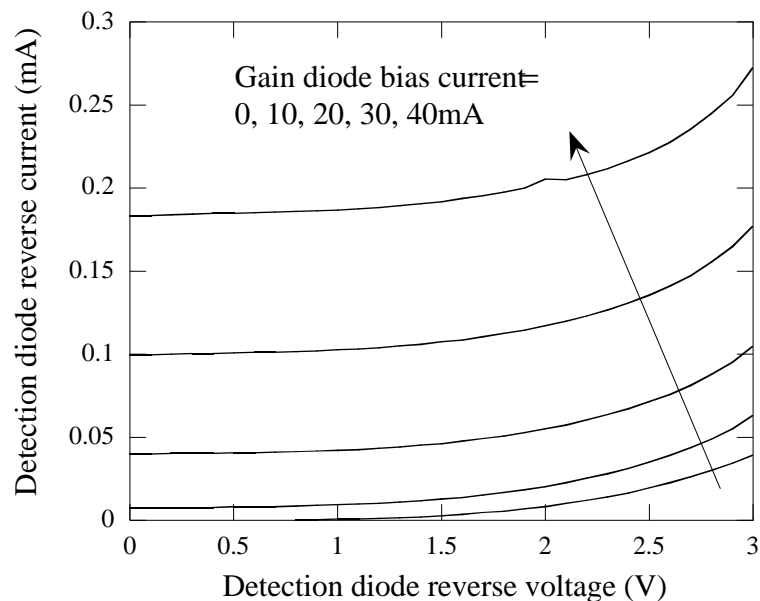


Figure 7.2: Typical current-voltage (I-V) characteristics of the reverse-biased absorption diodes in GaAs-based TAP detectors with vertical coupling, for different values of the amplification diode bias current. The results shown correspond to the first generation of successfully fabricated devices. Little qualitative difference was found between the characteristics of both generations.

We may expect the reverse current across the absorption diode to have mostly two origins: the absorption of ASE and spontaneous emission generated in the amplification region, and the collector current from the parasitic transistor. In the first case, the reverse voltage applied to the detector may help extract the generated electron-hole pairs more efficiently. In the second case, this applied voltage corresponds to the base-collector voltage, and would generate changes in the transistor behavior due to modulation of the base width. However, the base of the parasitic transistor (middle cladding) is thick and highly doped (see tables 6.1 and 6.2). We may therefore expect the effect of the modulation of the base thickness to be negligible. Likewise, due to the built-in field of the detection Schottky diode, the

carrier extraction is already efficient at zero applied bias. Therefore, both current contributions may be assumed to depend very little on the reverse voltage applied to the absorption diode. Thus, whether the main mechanism generating this quasi-constant reverse current in the detection diode is only absorption of spontaneous emission and ASE, or an important contribution to it is generated through the effect of the parasitic transistor, may not be explained using only the plot shown in figure 7.2. Comparison between electrical and optical properties will be necessary to distinguish between these different contributions.

In a second regime, for higher reverse voltages, we may see how the reverse current generated does depend indeed on the applied voltage, while simultaneously the plots for different amplifier bias currents are not parallel anymore and start diverging. Obviously, when no current is injected in the gain diode, we may assume that all the current measured corresponds to the dark current of the detection diode. The divergence between the plots for different amplifier bias currents may be explained as follows: due to the non-zero resistance between the region of the n-cladding immediately below the detection diode and the ground contacts, a positive voltage, increasing with the amplifier bias current, will appear at the anode of the absorption diode, resulting in an absolute value V_{eff} of the effective reverse applied voltage given by

$$V_{eff} = V_{rev} + I_{bias} R_{lat} \quad (7.1),$$

where V_{rev} is the absolute value of the reverse bias applied between detector and ground contacts, I_{bias} is the current injected into the amplifier and R_{lat} the lateral conduction resistance. The result is thus a larger absolute value of the reverse voltage applied to the detection diode for larger values of the bias current injected into the gain active region. The detector being already close to breakdown, as evidenced by the curve obtained when the gain diode is not biased, these small changes in the effective voltage applied to the detection diode (in the order of 0.1V for gain diode current variations in the order of 10mA) cause measurable variations in the background current of the detection diode.

In the next section, the comparison between the electrical and the optical characteristics of the device will determine the relative importance of the contributions of absorption of spontaneous emission and ASE, and the effect of the parasitic transistor, to the total background current. One main conclusion however may be pointed out of the results shown in figure 7.2: the changes that we may expect in the carrier collection efficiency through changes in the reverse bias applied to the absorption diode are not bound to be significant, making it possible to operate the device with an external bias of 0V applied between ground and detector contacts.

Optical characterization of TAP detectors

In this paragraph, the optical characteristics extracted through measurement from GaAs-based TAP detectors with vertical coupling will be presented. First, the setup used to measure said characteristics will be briefly described. Next, the device

behavior in the absence of an optical input will be presented. Using the measured spontaneous emission, ASE and background current, we will establish how important the effect of the parasitic transistor really is. Similar measurements extracted from InP-based devices will be presented too, in order to determine the main factors affecting the contribution of this transistor to the background current for generic TAP detectors with vertical coupling. Finally, the measured photocurrent will be presented, and its dependence on various factors will be described.

Measurement setup

Given the relative complexity of TAP detectors, and the various phenomena of different nature that are present in them, several different measurements are necessary in order to accurately characterize their behavior and the processes involved. The measurable photocurrent may be extracted by measuring the total current collected in the absorption diode, both in the presence and absence of an input optical signal, and subtracting both quantities. Expressing this amount in units of electrons per second, and dividing it by the known input optical power, expressed in units of photons per second, we obtain the measurable external quantum efficiency. In order to optimize the coupling efficiency, a lensed fiber was used. Its working distance was $\sim 4\mu\text{m}$, while a typical spot size was $\sim 2\mu\text{m}$. Measuring the optical power present in the fiber allows for the characterization of the true external quantum efficiency. Precision translation stages are used to optimize the coupling. The criteria used for this optimization will be described in detail later in this chapter.

The measurements presented in the previous section characterize the background current of the device, including its dependence on the amplifier bias current. However, in order to fully determine its origin, and what factors may be significant to its generation, it is also necessary to measure the ASE and spontaneous emission generated. The former is obtained by substituting the lensed fiber by a broad area detector, allowing the measurement of the ASE power coupled out through the device input facet. The latter may be measured by adding a second broad area detector, positioned at an angle with respect to the direction of propagation of light inside the device. This feature was added for the measurements performed on the second generation of TAP detectors. Figure 7.3 shows a schematic representation and a photograph of the described measurement setup. An HP4145 semiconductor parameter analyzer was used as current and voltage source, and current meter for the detection diode and external broad area diodes. The experimental results obtained with this setup will be presented and discussed in the following sections.

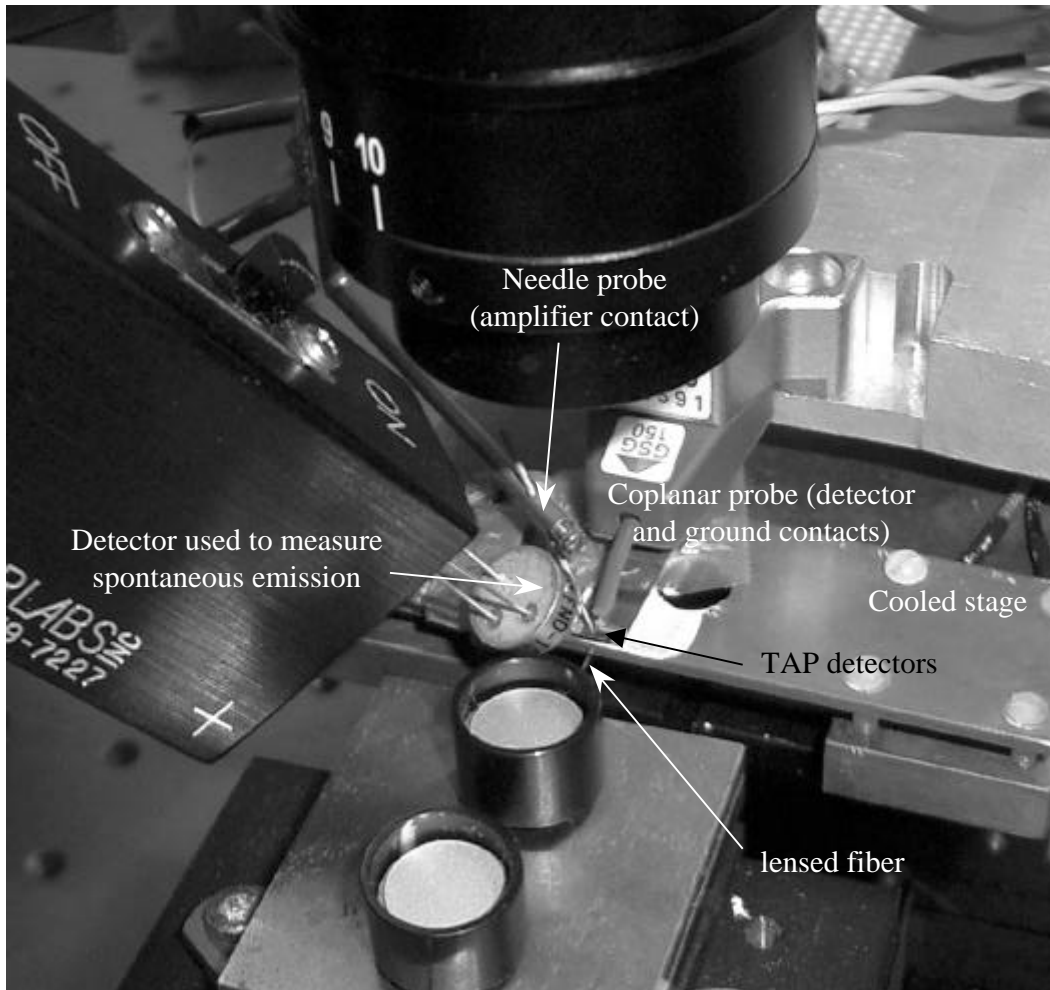


Figure 7.3: Photograph of the measurement setup used to characterize the behavior of TAP detectors with vertical coupling: photograph. The lensed fiber may be exchanged by a broad area detector, allowing the measurement of the ASE produced in the amplifier region. A second broad area detector, shown in the photograph, is used to measure the spontaneous emission produced.

Spontaneous emission, ASE and background current

The importance of the different contributions to the background current in TAP detectors may be determined by the simultaneous measurement of the spontaneous emission and ASE produced in the device, together with the total background current.

Figure 7.4 shows the measured ASE produced in the device and background current for four different cases. These two quantities are normalized to their maximum values in the range of amplifier bias current considered. Two of the plots shown correspond to measurements performed on InP-based TAP detectors, with p-n-p and n-p-n configurations. The third and fourth plots correspond to devices from the first and second generations, respectively, of GaAs-based TAP detectors. In the plot corresponding to devices from the second generation of GaAs-based TAP detectors, the spontaneous emission generated in the device is shown. This spontaneous emission was measured using a broad area detector at an angle with the direction of propagation of light inside the device. A quantitative relationship between the measured spontaneous emission and the actual spontaneous emission per unit volume and time inside the gain region of the TAP detector is, at best, extremely difficult to estimate, due to the effect of reflections in the multiple semiconductor layer boundaries and interconnection metal present in fully fabricated devices. Normalized values of the spontaneous emission, expressed in arbitrary units, provide however enough information to deduce the relative importance and respective behavior of the contributions to the total background current from absorption of spontaneous emission and ASE.

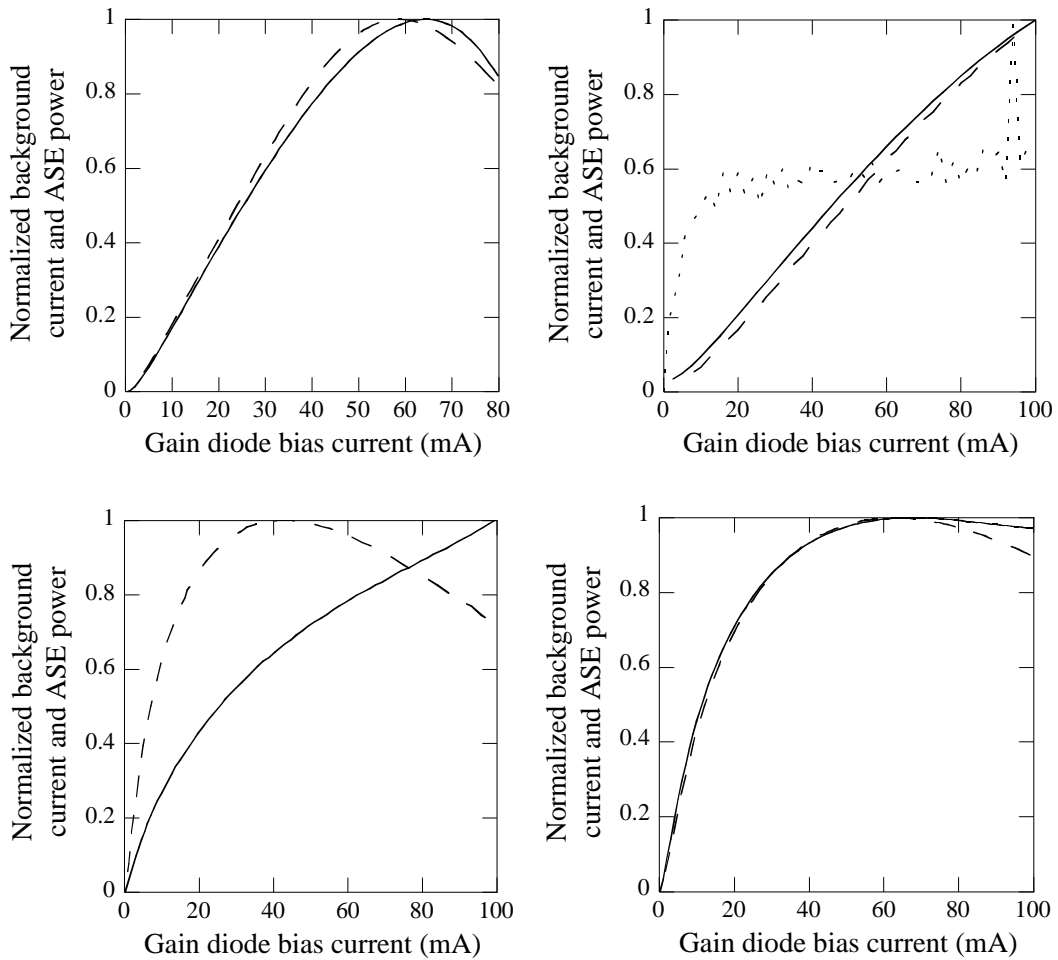


Figure 7.4: Simultaneous measurement of ASE generated in TAP detectors (dashed line) and total background current (full line) as a function of the bias current in the gain diode. Results are shown for four different devices: GaAs-based TAP detectors from the first (top left) and second (top right) generations, and InP-based TAP detectors with n-p-n (bottom left) and p-n-p (bottom right) configurations. The spontaneous emission generated in the GaAs-based TAP detector from the second generation, and captured in a broad-area detector at an angle with the direction of propagation of light inside the device (dotted line) is also shown in the corresponding plot. Current and power values are normalized to their maximum value in the amplifier bias current range considered. The applied reverse voltage to the detection diode is 3V for the InP-based devices, and 0V for GaAs-based devices. All devices whose behavior is shown in this figure are approximately 200mm long, and the widths of their detection and amplification regions are 3mm.

Note that, since the absorption diode in InP-based TAP detectors is not a Schottky diode, a reverse bias may be necessary for efficient carrier extraction. A reverse

applied voltage of 3V was shown to produce this efficient extraction, while minimizing any possible effects on other contributions to the dark current. The bias applied to the absorption diode in GaAs-based TAP detectors is 0V. The use of plots from devices with the same length ($\sim 200\mu\text{m}$) and active region width ($3\mu\text{m}$) makes a fair comparison between the different cases possible.

Figure 7.4 allows for very valuable conclusions. First, a very important qualitative difference may be found between InP-based n-p-n TAP detectors and TAP detectors with a p-n-p configuration. In the device with n-p-n configuration, the background current increases monotonically, independently on the roll-off experienced by the ASE produced in the device, showing a very significant contribution from the parasitic transistor. In devices with a p-n-p configuration, however, the ASE and the background current evolve much more similarly, rolling-off nearly simultaneously. The absorption of ASE may then be assumed to be the origin of most of the background current. As discussed in chapter 2, the reason for this difference in behavior is most likely the lower mass and higher diffusion length of electrons with respect to holes. In n-p-n devices, this results in a worse confinement of carriers injected from the bottom cladding into the amplification diode, i.e., a larger flow of minority carriers into the middle cladding. Furthermore, these carriers diffuse more easily through this middle cladding, being collected in the form of a current through the detection diode much more easily than holes in the case of devices with a p-n-p configuration. Apart from the doping type of the different layers, there was not a significant difference in the design of n-p-n and p-n-p InP-

based TAP detectors, which strongly supports that the latter is a much better configuration for minimizing the effect of the parasitic transistor. This conclusion, reached through observation of the measured characteristics of InP-based devices, may be in principle extrapolated to any material system where electrons are lighter and present higher diffusion lengths than holes.

Slight differences exist also between the results shown in figure 7.4 for GaAs- and InP-based devices with a p-n-p configuration. When the ASE rolls off, the background current seems to remain pretty much constant in the latter case, whereas it starts decreasing rapidly in the first case. In other words, the contribution from other origins other than the absorption of spontaneous emission and ASE may be assumed to be of little significance in GaAs-based TAP detectors, while a small contribution of a different origin, most likely stemming from the parasitic transistor, appears in InP-based devices for high amplifier bias currents. As discussed in chapter 2, this difference in the behavior may be explained through the better confinement of carriers in the amplification region in GaAs-based devices, due to the presence of the doped, higher aluminum content (and thus higher bandgap) layers used to provide lateral current confinement through selective wet oxidation.

A difference is also observed between the first and second generations of TAP detectors. We may expect that the second generation would roll-off more quickly due to the additional Joule heating, but the plots show the opposite. This is due to the fact that, in the first generation, saturation is much more important than in the second, for two different reasons: first, the presence of the cladding mode described in chapter 6

(see figure 6.3), and second, the larger (nearly double) cross-sectional area of the active region in devices from the second generation, due to the additional quantum wells (QWs) (compare tables 6.1 and 6.2). In other words, a smaller amount of heating produces in the first generation roll-off of the ASE at lower amplifier bias currents due to the combination of a much smaller saturation power and the presence of modes experiencing net gain for smaller values of the carrier density. In the range of amplifier bias values considered, both devices produce roughly similar values of total background current ($\sim 1\text{mA}$), while the device from the first generation produced higher ASE power ($\sim 150\mu\text{W}$) than the device from the second generation ($\sim 70\mu\text{W}$). In other words, the ASE produced in devices from the first generation grows faster with the amplifier bias current (consistent with a smaller amplification volume to be pumped and with the presence of supported modes experiencing net gain for smaller values of the carrier density), while devices from the second generation convert more efficiently optical power generated in the amplifier into current in the detector (consistent with the presence of supported modes with significant simultaneous overlap with both gain and absorption regions). In other words, a much more dramatic effect of the distributed combination of amplification and detection may be expected from the second generation. So far, the changes introduced from the first to the second generation of GaAs-based devices seem to produce the desired results.

Finally, let us address the issue of spontaneous emission and ASE in the case of GaAs-based devices from the second generation. As the ASE and background current start to increase, the spontaneous emission initially increases, and then seems

to quickly saturate, remaining close to constant. This is not surprising given the simulation results and discussion about the effect of competition between signal and ASE presented in chapter 2 (see figure 2.34). As a result of the stimulated emission rate due to the presence of ASE increasing much more quickly than the spontaneous emission rate, the carrier density inside the gain region grows sublinearly with the injected bias current, resulting actually in a behavior similar to the carrier clamping experienced in semiconductor lasers. This accounts for the quick saturation in the value of spontaneous emission collected, while the ASE produced, and background current collected, continue to increase.

In summary, the measured ASE and background current produced in TAP detectors in the absence of an input signal have been presented and discussed. It has been shown that in GaAs-based TAP detectors (all with n-p-n configuration) the contribution to the total background current from the effect of the parasitic transistor is negligible. In InP-based TAP detectors with a p-n-p configuration, this contribution may be considered residual, while it is very important in InP-based devices with an n-p-n configuration. This strongly supports the validity of the discussion and conclusions presented in chapter 2, i.e., an n-p-n configuration is undesirable due to the higher mobility of electrons resulting in a larger effect of the parasitic transistor, while the doped, higher aluminum content layers used for selective lateral oxidation in GaAs-based TAP detectors add carrier confinement in the vertical direction, reducing the effect of the transistor action in the device. The additional Joule heating expected in the second generation of GaAs-based devices is

shown to be, *a priori*, less important than the saturation in the first generation. This is argued to be a consequence of the optimization of the optical mode overlap with gain and absorption regions, geared towards the elimination of the cladding mode supported by devices from the first generation, while modes presenting significant overlap with both active regions are supported in devices from the second generation. This is consistent with the faster growth of ASE power with amplifier bias current, the smaller background current produced by the same amount of ASE, and the earlier onset of saturation in devices from the first generation. Thus, despite the additional Joule heating, the distributed combination of gain and absorption may be expected to have a more dramatic effect in devices from the second generation. This will be shown to be true in the next section, when the device response in the presence of input power is presented and discussed.

Photocurrent

In this section, the photocurrents measured in GaAs-based TAP detectors are presented. The meaning of “optimum coupling” will be discussed, especially as far as the first generation of devices is concerned. Finally, the effects of temperature and saturation are intuitively compared based on the experimental results obtained. This allows us to evaluate the device performance and establish the main performance limiting factors in both generations.

First generation

According to the optical simulations presented in chapter 6 (see figure 6.3), three main modes or types of modes are supported in TAP detectors with vertical coupling, overlapping chiefly with the claddings, the amplification and the absorption region, respectively. The three types of modes are predicted to exist in the first generation of successfully fabricated GaAs-based TAP detectors. This, of course, results in complications when the optimum position of the fiber lens for maximum coupling is sought. One way to look for this optimum position is by reverse-biasing both gain and absorption diodes, and looking for the maximum detected photocurrent for a given input optical power under these conditions, either in the amplification or in the detection diodes. Maximizing the sum of both photocurrents is also a viable strategy. Once the optimum position for the lensed fiber is found, the amplifier is forward-biased and the measurement of the photocurrent in the presence of simultaneous gain and absorption may be performed. In order to compare how these three criteria do or do not produce an optimum response, a vertical scan was performed, moving the lensed fiber at 1 μ m intervals with the help of a precision translation XYZ stage. Prior to this scan, the sum of the photocurrents in gain and absorption diodes was maximized by translating the fiber in the three orthogonal directions. It was assumed that this alignment produced the optimum fiber position in the lateral (x) and longitudinal (z) directions. The results of the scan in the vertical (y) direction are shown in figure 7.5, taking as $y=0$ the lowest point scanned (closest to the device substrate). The input optical wavelength was set at 855nm. This value coincides with

the maximum power density in the output ASE spectrum measured in the absence of an input signal.

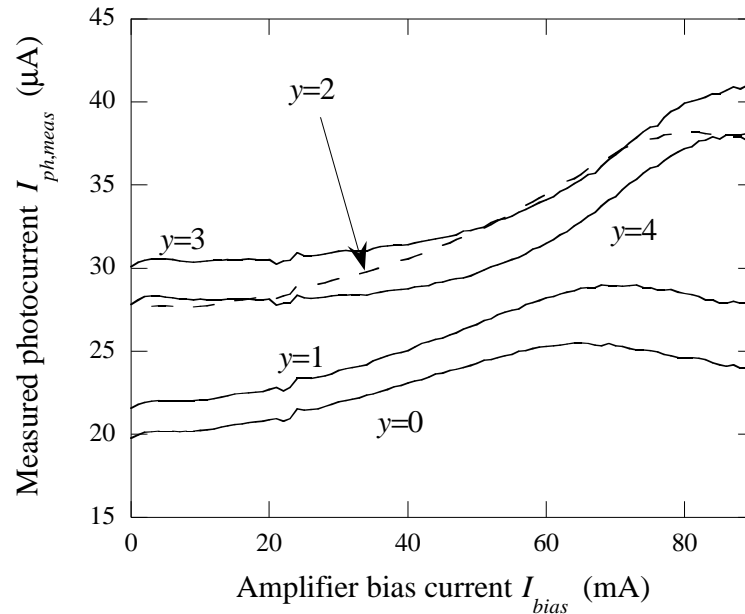


Figure 7.5: Measured photocurrent (difference between total current in the presence and absence of an optical input) in GaAs-based TAP detectors from the first generation as a function of the amplifier bias current and for different vertical positions of the lensed fiber y . The coordinate $y=0$ is taken at the lowest point in the scan performed. For clarity, the curve for coordinate $y=2$ (closest to the maximum photocurrent detected in the gain diode when both diodes are reverse-biased) is dashed. The closest position to the maximum current detected in the absorption diode when both diodes are reverse-biased corresponds to $y=3$. The device length is 300mm, while the width of gain and absorption active regions is 3mm. The incident optical power is 200mW. The device measured was not AR-coated.

Figure 7.5 corroborates most of the assumptions that have been developed about the inner working of the first generation of TAP detectors. In order to substantiate this statement, let us focus on the evolution of three characteristics of the curves shown in this figure with the position of the lensed fiber: the value of the measured photocurrent at low amplifier bias current, the initial slope of the measured

photocurrent with respect to the amplifier bias current, and the value of the amplifier bias current for which the measured photocurrent reaches a maximum.

Obviously, the measured photocurrent for small values of the amplifier bias current corresponds to what we could call “direct detection in the absorption region”. The carrier injection into the gain diode being very low, this diode is highly absorptive. Most of the photocurrent will be thus originated by absorption of light coupled into detector modes. In this region of the curves, the distributed combination of amplification and absorption does not show its effects yet. The maximum value of the photocurrent in this regime corresponds to the highest photocurrent generated in the absorption region when both diodes are reverse-biased, in perfect agreement with this interpretation.

The initial slope may be related to the effect of the distributed combination of amplification and detection when the saturation has not yet set in, or when its effect is small. Consequently, this slope should be largest when the coupling into the amplifier mode is optimized. When both diodes are reverse biased, this would correspond to the maximum photocurrent value detected in the amplifier, i.e., a situation close to the curve shown in figure 7.5 for $\gamma=2$. As the coupling shifts towards detector modes ($\gamma>2$) or cladding modes ($\gamma<2$), the value of this slope should drop, since detector modes do not experience the benefits from the distributed gain, while cladding modes overlap very little with the absorption region, and generate thus very small amounts of photocurrent.

Finally, the roll-off in the measurable efficiency indicates the onset of saturation in the gain region. Since the chief cause of amplifier saturation is the presence of a large amount of power in the cladding mode, which is the only one experiencing net gain, we would expect a more dramatic effect of saturation when the coupling into the cladding mode is optimized. In perfect agreement with this hypothesis, the roll-off shifts to lower amplifier bias currents as the fiber is moved downward, i.e., as most of the light is incident on the lower cladding.

It is interesting to note that, as a consequence of the different effects mentioned in the previous discussion, the highest measurable photocurrent corresponds to positions of the fiber that maximize the coupling into the detector, and not into the amplifier. This is not, however, the behavior that we would expect from TAP detectors with an optimum design. It is important to realize, however, that when $\gamma=2$, the slope of the measured photocurrent with the amplifier bias current is maximum for the cases considered. In that sense, the effect of the distributed combination of gain and absorption is most dramatic, coinciding with the optimum coupling into the amplifier mode. In other words, it is the saturation of the amplifier due to the presence of the cladding mode that limits the performance of TAP detectors in this generation. Furthermore, with the simulated values for the confinement factors in the gain and absorption regions, the amplifier mode still suffers net attenuation, or an even more dramatic effect of the combination of gain and absorption may be possible if cancellation between them becomes possible, and cladding modes are inhibited.

In terms of the absolute values of the measured efficiency, the maximum value of photocurrent corresponds to roughly 35% external quantum efficiency. Due to the lack of an anti-reflection coating for these devices at the time when these measurements were taken, approximately 30% of the optical power is lost to reflection at the front facet. Considering therefore that only 70% of the input power has a possibility of being coupled into the device, we may estimate the external quantum efficiency of an identical device with a perfect AR-coating at 50%. This number is still below the expectations for TAP detectors. The maximum efficiency actually found for this generation of devices corresponded to coupling in between positions $y=2$ and $y=3$, after optimizing again the alignment in the longitudinal z direction, and for a device $300\mu\text{m}$ in length. The measured external quantum efficiency is shown in figure 7.6, for an input optical power of $268\mu\text{W}$. The device was still not AR-coated.

Consistently with previous measurements, the photocurrent changes slowly with the amplification diode bias current. In fact, more than half of the total photocurrent measured seems to be due to the detector mode. Thus, even though an external quantum efficiency of 56% is shown in figure 7.6 (corresponding to ~80% external quantum efficiency if a perfectly matched AR-coating was deposited in the front facet), and this figure, together with figure 7.5 do indeed constitute proof of principle of the effect of the distributed combination of gain and absorption, this effect is still relatively small.

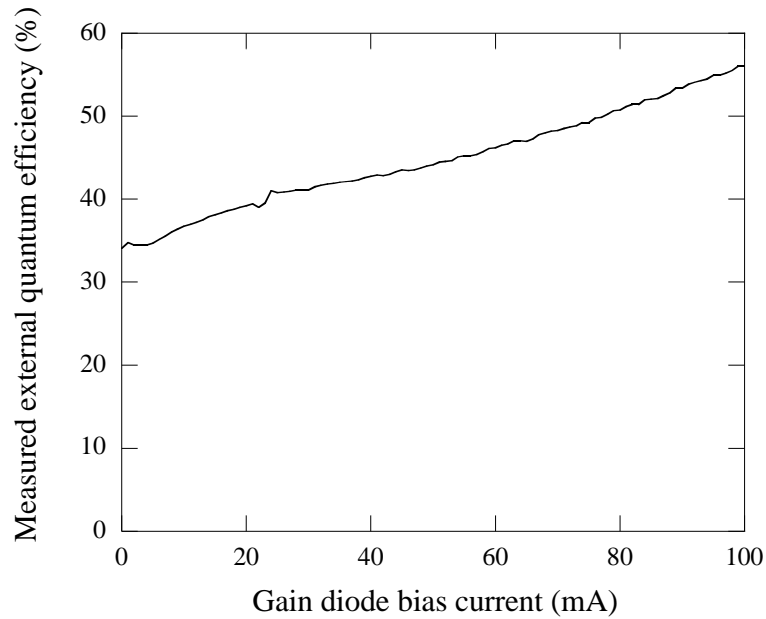


Figure 7.6: Maximum measured external quantum efficiency in GaAs-based TAP detectors from the first generation as a function of the amplifier bias current. The device length is 300mm, while the width of gain and absorption active regions is 3mm. The incident optical power is 268mW. The device measured was not AR-coated.

All the experimental results presented up to now in this chapter strongly suggest that the main factor limiting the TAP detector response is gain saturation affecting both the signal and the ASE. The optimum efficiency presented in figure 7.6 was indeed obtained by optimizing the coupling in order to produce a maximum photocurrent in the detection region when both diodes were reverse-biased, i.e., close to the minimum coupling into the cladding mode while keeping close to its maximum the sum of power coupled into the detector and amplifier modes, consistently with this hypothesis.

Devices from the first generation were AR-coated and measured again. The device whose response is shown in figures 7.5 and 7.6 failed before the AR-coating was deposited, due most probably to having its front facet scratched by the lensed

fiber in an effort to improve the coupling efficiency. Other AR-coated devices exhibited an increase in their external quantum efficiency of about 40%, consistent with a close to optimum coating being deposited on their front facet. However, the absolute value of their measured efficiency was not higher than the optimum value shown in figure 7.6. A device length of 300 μ m seems therefore to be the best compromise between longer devices for higher efficiency and shorter devices for smaller effect of saturation.

In summary, proof of principle of the effect of the distributed combination of amplification and absorption has been offered. A maximum external quantum efficiency of 56% has been demonstrated for the first generation of GaAs-based TAP detectors with vertical coupling, without the deposition of an AR-coating. The observed behavior (dependence on the amplifier bias current and input optical power) is fully consistent with the modeling performed, strongly supporting the conclusion that gain saturation due to the presence of a cladding mode is the chief limiting factor for this generation of devices.

In the next paragraph, results obtained through measurements performed on the second generation of GaAs-based TAP detectors will be presented and discussed.

Second generation

The measurements performed on the second generation of GaAs-based TAP detectors are analogous to those performed in the first generation. The measured

external quantum efficiency for a 200 μm long device is shown in figure 7.7, as a function of the amplifier bias current and for different input optical powers.

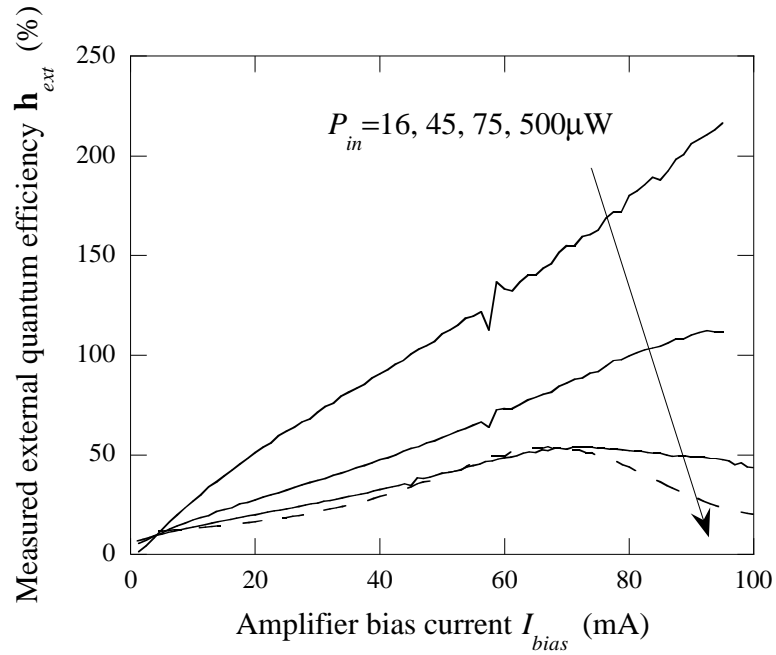


Figure 7.7: Measured external quantum efficiency in GaAs-based TAP detectors from the second generation as a function of the amplifier bias current, and for different values of the input optical power. The device length is 200 μm , while the width of gain and absorption active regions is 3 μm . The device measured was AR-coated. For clarity, the response for 0.5mW input power is shown in a dashed line.

The optimization of the coupling was performed by reverse-biasing the amplification region, and maximizing the photocurrent detected in it. As opposed to the first generation, only two main modes exist *a priori* in the second generation of GaAs-based devices, a detector mode and an amplifier mode. The photocurrent extracted from the former will not depend heavily on the amplifier bias current, due to the much larger confinement factor in the absorption region for this mode. The latter will experience the effect of the distributed combination of amplification and

photodetection, and overlaps mostly with the amplifier. Thus, maximizing the optical power coupled into this mode is nearly equivalent to the procedure used.

The first characteristic that we may notice in figure 7.7, apart from the much larger value of the measured external quantum efficiency, is the difference in the response for different input optical powers. For relatively small input optical powers ($16\mu\text{W}$), the efficiency increases nearly linearly with the amplifier bias current, reaching values in excess of 200% for an amplifier bias current of 100mA. This was the maximum value provided by the HP4145 semiconductor parameter analyzer. The external quantum efficiency does not seem to saturate yet for this value of the input optical power. As the input optical power grows, the efficiency decreases, showing clear signs of saturation when the input is 0.5mW. This trend may be understood intuitively as an effect of the competition between the signal and ASE for the available optical gain, as discussed in chapter 2. In other words, as the input optical power increases, the additional recombination necessary to sustain this optical power inside the device results in a reduction of the carrier density present in the amplification region, in turn producing a reduction of the background current, resulting in a lower measurable external efficiency. This is fully consistent with the interpretation of TAP detector behavior outlined in this dissertation.

In order to continue carrying this comparison, let us focus on the behavior for small values of the amplifier bias current, shown in figure 7.8. Comparing this plot with figure 2.36, we may immediately see similarities and differences. The slope obviously changes, decreasing as the input optical power increases. The curves

shown in figure 7.8 for input optical powers of 16, 45 and 75 μ W intersect at one point, as all the curves do in figure 2.36. The measured curve for an input optical power of 0.5mW was not obtained simultaneously with the other three, so a change in the coupling efficiency (although the optimization procedure was the same) may be expected.

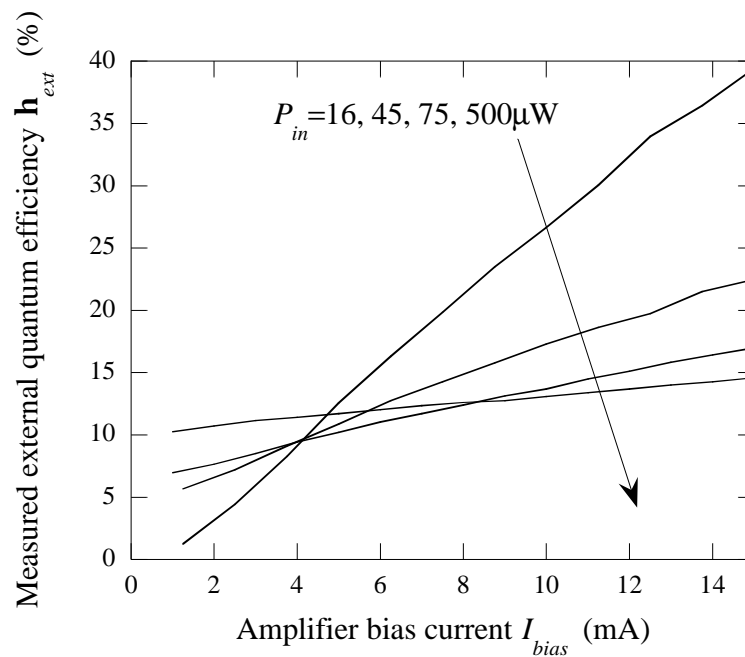


Figure 7.8: Measured external quantum efficiency in GaAs-based TAP detectors from the second generation as a function of the amplifier bias current, and for different values of the input optical power. The plot is a detail of figure 7.7, showing the behavior of the same device for small values of the amplifier bias current. The device length is 200mm, while the width of gain and absorption active regions is 3mm. The device measured was AR-coated.

The previous observations will now be interpreted. First, the amplifier bias current for which all curves in figure 2.36 meet is intuitively understood as the point where the amplification region becomes transparent. Under this condition, the amplification region produces no effect in the incoming light, and *vice versa*. It is

therefore just natural to assume that, as long as the coupling efficiency is constant, the measured efficiency should be the same for all input optical powers. This is indeed consistent with the results shown in figure 7.8. For lower bias currents, stimulated absorption in the amplifier region dominates, resulting on one hand in net attenuation for the input optical power, and on the other hand on a net generation of electron-hole pairs which increases as the input optical power grows. This excess number of electron hole pairs will contribute to the generation of ASE and spontaneous emission, i.e., to the background current. Therefore, for amplifier bias currents below the common point in figure 7.8, the apparent larger external quantum efficiency for larger input optical power is actually a result of the increase in the background current. The simulations presented in chapter 2 seem to indicate that the most important reason for this increase is the change in the current generated in the detection region as a result of the absorption of spontaneous emission produced in the gain region. The theory developed for TAP detectors with vertical coupling and the experimental results obtained therefore agree at this point, at least qualitatively.

Assuming that the previous conclusion is true, as evidenced by the experimental results shown in figures 7.7 and 7.8, we may also conclude that the roll-off shown in the response for the highest input power considered (0.5mW) is due to a reduction in the current generated through absorption of the ASE produced in the gain region. This effect shows itself in the modeling presented in chapter 2 when the net gain per unit length is very large, as evidenced by the values of the measurable efficiency (~ 100) that may be reached before the competition between signal and ASE produces

a roll-off in the device response. The importance of this effect increases with the input optical power. It is therefore not surprising that the response clearly exhibits this roll-off for an input optical power of 0.5mW, while it is less important for 75 μ W. Saturation may be observed for 45 μ W, and the response for 16 μ W is nearly linear in all the measured range of values of the amplifier bias current.

Therefore, a direct comparison between the simulated values shown in figures 2.35 and 2.36 and figures 7.7 and 7.8, allows us to conclude that the experimental results obtained agree qualitatively with the behavior of TAP detectors as we have described it in previous chapters of the dissertation starting from known aspects of the physics of traditional amplifiers and photodetectors. Quantitative differences exist, as evidenced by the following facts: the difference in the slopes of the measurable efficiency with the amplifier bias current for different input optical powers is much more severe in the experimental data. Furthermore, device saturation is recorded to happen experimentally for lower values of the external quantum efficiency. In other words, in real, fabricated devices, the effects of saturation are more important than in the simulated results shown in chapter 2. This disagreement will be discussed and reconciled in the following paragraph, where the approximations made in producing said simulated values will be considered, together with the effect of changes in temperature as a consequence of Joule heating. The latter will be argued to be an important factor in the experimental results obtained for the second generation of GaAs-based TAP detectors with vertical coupling, in agreement with the increase in the gain diode resistance shown in figure 7.1.

In summary, the measured external quantum efficiency in GaAs-based TAP detectors with vertical coupling has been presented and discussed in this paragraph. These results show a very good qualitative agreement with the modeling performed and conclusions reached in previous chapters of this dissertation.

Effect of temperature

In the previous paragraph, the measured external quantum efficiency in GaAs-based TAP detectors with vertical coupling was presented. The values obtained, and specifically their dependence on the input optical power and the gain diode bias current were discussed, showing very good qualitative agreement with the theory developed for these devices and presented in previous chapters of this dissertation. However, quantitative differences still exist. In this paragraph, the effect of the device temperature and the approximations introduced in chapter 2 when calculating the effect of competition between signal and ASE will be discussed. It will be argued that these effects are the source of these quantitative differences.

In order to study the effect of temperature in the devices, let us recall that, as the temperature of an optical amplifier increases, two effects occur. One of them is the broadening of the electron-hole pair distribution with energy, as a consequence of an increase in the Fermi energy of the carrier reservoir. Another one is the lower injection efficiency, due to the increase of thermionic emission of electrons and holes, which escape from the quantum wells and the SCH (see for example [1], Appendix 2). Other effects are also caused by an increase in the device temperature, but these

two are the only ones for which clear evidence exists in the recorded data, so all other effects of temperature will be neglected in the following discussion. The two effects considered may be intuitively understood to affect the gain in the following way: due to the broadening of the electron-hole pair occupancy as a function of energy, a broadening of the gain and spontaneous emission spectra may be expected. Therefore, and since the input signal is monochromatic, smaller and smaller changes in the gain experienced by that signal may be expected as the carrier density increases by fixed amounts, due to a larger range of electron-hole pair energies being populated by the added carriers. Furthermore, carriers are less and less efficiently confined in the gain region as the temperature increases, resulting in larger bias current variations needed to obtain the same carrier density increase. As a larger bias current is injected, the temperature will increase through Joule heating, requiring a larger bias current change for the same change in the gain, and so and so forth, leading to the optical gain for a fixed wavelength saturating with increasing amplifier bias current. This effect is indeed observed in TAP detectors with vertical coupling, as evidenced by figure 7.9, where the ASE spectrum measured for different bias currents for the amplification region is shown.

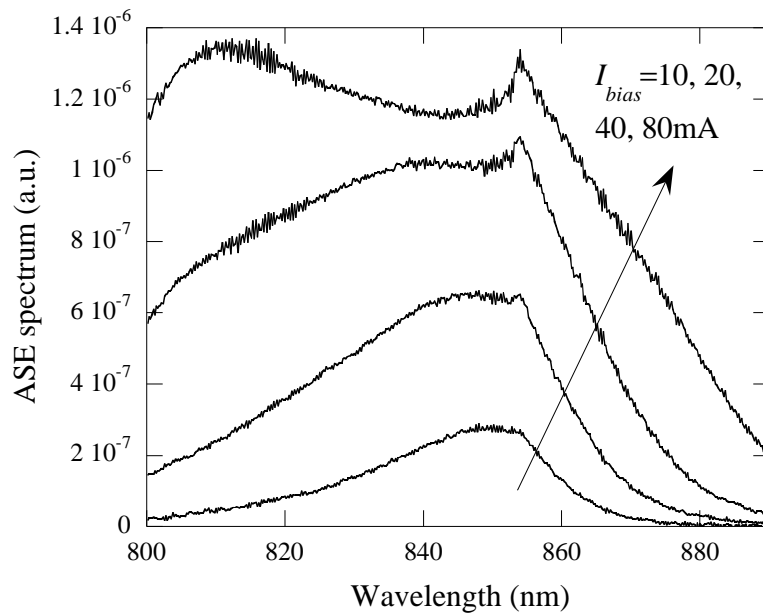


Figure 7.9: Measured spectrum of the ASE produced in the absence of an input signal for the GaAs-based TAP detector whose response to an input optical signal is shown in figures 7.7 and 7.8.

As the amplifier bias current keeps doubling, the effect of this increase in the gain recorded for the wavelength of interest (855nm) is smaller and smaller. On the other hand, the ASE spectrum becomes larger and larger. In other words, for bias currents around or above 40mA, the increase in the background current shown in Figure 7.4 (top right plot) is a consequence of the spectral broadening of the ASE power at least as much as by the increase in the amplification experienced by the ASE. Similarly, we may argue that in real devices, the rather linear behavior of the measurable efficiency with the gain diode bias current, instead of the highly superlinear dependence shown in chapter 2 (even when competition between signal and ASE is taken into account) is partly caused by the increase in temperature. The effect of saturation is also further enhanced by the increase in temperature, supplying the

second cause for the linear behavior at low input power, and for the dramatic dependence of the device response on the input power, both shown in figure 7.7. The temperature-enhanced carrier leakage results in a variable injection efficiency, decreasing with increasing temperature, and thus with increasing amplifier bias current. In other words, the ratio between the actual bias current and the recombination current (neglecting leakage) needed for the same increase in the carrier density increases with increasing temperature. Figure 2.35 shows the dependence of the device external efficiency as a function of the recombination current, assuming a constant injection efficiency, while figure 2.31 shows the dependence of the gain on the carrier concentration for a fixed temperature (room temperature or 300°K). In real devices, the actual bias current needed to produce the same response would be much larger than the recombination current shown in figure 2.35, the ratio between both increasing as they increase, as a result of added Joule heating. This also results on the actual gain for the input signal wavelength being smaller than the one shown in figure 2.31, as a result of the broadening of the electron-hole pair distribution with energy. The combination of these two effects results in saturation of the device performance being reached for much lower values of the external quantum efficiency. It is noteworthy, however, that the qualitative features of the result of competition between signal and ASE shown in figures 2.35 and 2.36 are still present in the measurements despite the aforementioned simplifications (constant injection efficiency and constant temperature) used in obtaining the simulated results.

One final quantitative difference between simulations and measurement is explained due to the quasi-constant power approximation made in the modeling of competition between signal and ASE presented in chapter 2. When the optical modes suffer large variations along the device, whether net gain or net attenuation, the local maximum optical power will be much larger than the average used in the simulations, resulting in an underestimation of the effect of saturation in the model used. This explains the much larger variations in the slope of the external quantum efficiency as a function of the amplifier bias current when the latter presents small values. Indeed, we may consider a device biased so that the amplifier is at transparency. Now, when the amplifier bias current decreases from this value, the gain region becomes absorptive, leading to the eventual disappearance of the input optical power at the end of the device. The average optical power in the device becomes thus much smaller than the input optical power, resulting in small changes in the carrier density induced by the absorption of the input signal. Although these changes occur (in the model) along the entire device, due to the non-linear dependence of the gain with the carrier density, larger changes in the carrier density over a smaller region (as would happen in a real device) would have a more dramatic effect in the device performance. An analogous discussion shows that this underestimation of the effect of saturation in the model presented in chapter 2 applies also when the gain region becomes amplifying.

In summary, the effect of an increase of the device temperature due to Joule heating, coupled with the underestimation of the effect of saturation due to the quasi-constant power approximation performed in chapter 2, are intuitively shown to be

behind the quantitative differences between modeled and experimental results for GaAs-based TAP detectors with vertical coupling.

This section has thus presented the optical characterization of GaAs-based TAP detectors with vertical coupling. Different measurements (ASE produced, external quantum efficiency and ASE spectrum) have been presented and discussed, showing very good qualitative agreement between the model presented and the results obtained from fabricated devices. The quantitative differences between them may be tracked to the effect of temperature and to the simplifications made in the model. The experimental results presented are therefore important evidence that the theory of TAP detectors presented in this dissertation indeed holds, and that the only differences between the results modeled using this theory and the measured data may be tracked to simplifications performed in the model at the time of actual computation (constant temperature, quasi-constant optical power).

Measured efficiency in InP-based TAP detectors

The measured external quantum efficiency obtained in InP-based TAP detectors will now be briefly presented and discussed. Figure 7.10 shows this efficiency as a function of the gain diode bias current, for a 300 μm long device, and an input optical power of 2.1 μW . The device absorption region was 3 μm wide.

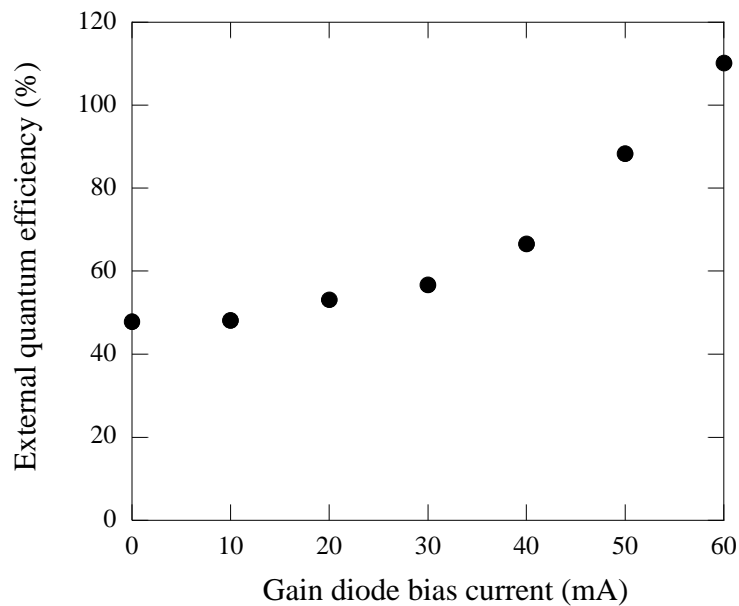


Figure 7.10: External quantum efficiency measured in a 300mm long InP-based TAP detector with vertical coupling, featuring a 3mm wide absorption region, for an input optical power of 2.1mW.

These devices were fabricated and measured by Dr. Donato Pasquariello, based on a joint design by him, grower Yae Okuno and the author of this dissertation. The experimental results were analyzed between Dr. Pasquariello and the author, with contributions from Associate Adjunct Professor Joachim Piprek on simulations of material gain and mode properties. Further details on the design, fabrication and analysis of this device may be found in [2].

The device, as shown in [2], presents two main modes, one detector mode and one amplifier mode, each one of them overlapping marginally with the other active region. The low bias current efficiency may therefore be assigned almost exclusively to the detector mode, while the amplifier mode experiences large net gain as it propagates. This results in a rapidly increasing efficiency with the gain diode bias

current for small optical powers ($2.1\mu\text{W}$ in figure 7.10), but also on saturation due to the large signal power when the input power increases (not shown in the figure). These features are, once more, in complete agreement with the theory developed for TAP detectors.

It is noteworthy that over 100% external quantum efficiency was also obtained in InP, as a result of adapting the device design to the characteristics of this material system. Figure 7.10 is therefore evidence pointing to the applicability of the theory for TAP detectors developed in this dissertation to other material systems than GaAs, and the possibility to obtain, using these devices, large efficiency and bandwidth may be obtained at the wavelengths used in fiber-optic communication systems, which is ultimately the main reason that motivated this work.

Summary

In this chapter, the experimental results obtained from fabricated TAP detectors with vertical coupling have been presented and discussed, paying special attention to GaAs-based devices. The results obtained support the theoretical model presented in earlier chapters of this dissertation, showing at all times good qualitative agreement. Quantitative differences may be explained as a result of the Joule heating-induced temperature changes and the approximations performed during computation, namely the quasi-constant optical power approximation used during the calculation of the effect of the competition between signal and ASE. Supported both theoretically and

experimentally, we may conclude that it is this competition between signal and ASE, related to amplifier saturation, which currently limits the performance of TAP detectors demonstrated up to date. Evidence is also presented that this limitation is worsened by the effect of temperature increase due to Joule heating. Results obtained from InP-based devices are also presented. Both GaAs- and InP-based devices show behaviors that constitute, to the best of our knowledge, the first demonstrations of the effect of the distributed combination of gain and absorption. Devices fabricated in both material systems exhibited external quantum efficiencies in excess of 100%, with GaAs-based devices exceeding 200%. The fact that the original design for the GaAs material system could be adapted into the InP system, producing comparable results, is an important step in TAP detector research, since it shows that these devices may also be designed and fabricated to operate at telecommunication wavelengths. The overall experimental evidence discussed, and its support of the model developed for TAP detectors and presented in earlier chapters of this dissertation, is another important advance, since this theory may be accepted as a solid starting point for future work in these devices.

References

- [1] L.A. Coldren, S.W. Corzine, "Diode lasers and photonic integrated circuits," *John Wiley & Sons*, 1995.
- [2] D. Pasquariello, J. Piprek, D. Lasoosa, J.E. Bowers, "InP-based waveguide photodetector with integrated photon multiplication," *Proceedings of the SPIE-ITCom International Symposium*, vol. 5248, 2003.

CHAPTER 8

Conclusions

In this chapter, the contents of this dissertation will be summarized, stressing the main contributions made by the research described in it, and suggesting future directions for research on traveling-wave amplifier photodetectors (TAP detectors). First, the main theoretical results will be briefly summarized and discussed. This discussion includes the description of the general behavior of TAP detectors, as well as a brief comparison between the different structures proposed, stressing their advantages or disadvantages over one another. Next, conclusions will be drawn from the experimental results, stressing the main limitations to TAP detectors performance observed to date. Finally, and based on both theoretical and experimental conclusions, possible improvements will be suggested for future TAP detector research.

Theoretical conclusions

In this dissertation, a thorough theoretical investigation of TAP detectors is performed. To the best of my knowledge, this constitutes the first theoretical study of the implications and possible advantages of the distributed combination of optical amplification and photodetection. In order to simulate the operating characteristics of TAP detectors, previously existing models have been combined, and a new noise model has been developed. Throughout the dissertation, equations are drawn from first principles, avoiding typical simplifications that may not be valid in the presence of simultaneous or alternating optical amplification and photodetection. The result of this theoretical study is a set of equations that may be used in the most general case of amplifier-photodetectors with arbitrary geometry, which is next applied to three particular configurations proposed in this dissertation, and used to simulate their efficiency and bandwidth, as well as saturation and noise characteristics. From this theoretical study, the main results are the description of the general behavior of TAP detectors, as well as the particular characteristics of the different configurations proposed in this dissertation. The former is described and the latter are compared in the following two paragraphs, respectively.

General behavior of TAP detectors

This paragraph outlines the main characteristics of TAP detectors, based on the common features presented by all configurations proposed in this dissertation. The

following characteristics are a direct consequence of the distributed combination of amplification and photodetection:

- 1) TAP detectors are capable of producing a larger photocurrent for the same peak optical power inside the device. This fact justifies the potential of TAP detectors in producing large, unsaturated photocurrents.
- 2) The simultaneous action of gain and absorption results in a trade-off between efficiency and noise characteristics, resulting, under ideal circumstances, in a constant ratio between noise figure and device efficiency when the optical power propagates without changes. The device overall noise figure may however be reduced by means of an initial amplification section, resulting in a noise figure similar to that of traditional semiconductor optical amplifiers (SOAs).
- 3) The presence of spontaneous emission and amplified spontaneous emission (ASE) introduces limitations to the device performance, through the generation of an undesired background current and larger uncertainty (noise) in the detected signal. When the noise contribution from spontaneous emission and ASE is negligible, the aforementioned ratio between noise figure and device efficiency may be reached.
- 4) Furthermore, the fluctuations in the background current induced by the presence of an input optical power results in a measurable efficiency which is lower than the actual device efficiency. Gain saturation in the amplifier

region, due to either signal or ASE, increases this effect. The origin of the reduction in the measurable efficiency and the gain saturation lays on the competition between existing photons (either belonging to the signal or being originated through spontaneous emission) for the available gain.

Note that all of the above, except for the first characteristic, result in limitations to TAP detector performance. Because of the nature of optical amplification and the inherent spontaneous emission of photons, these limitations cannot be eliminated, but their effect may be reduced. In order to do so, it is important to minimize the ASE build-up and the generation of spontaneous emission that may be absorbed in the detection region.

In the next paragraph, the TAP detector configurations proposed in this dissertation will be compared.

Comparison of the proposed TAP detector configurations

To the best of my knowledge, only TAP detectors with vertical coupling have been successfully demonstrated up to date. An experimental comparison between the different configurations proposed in this dissertation is therefore not yet possible. The theory contained in this dissertation is however complete enough to allow the prediction of the unique characteristics of each configuration.

It is important to realize that the differences between TAP detectors with lateral and vertical coupling will be *a priori* minimal, the performance of both configurations being mostly determined by the modal confinement factors in the gain

and absorption regions. Both configurations will have a loss-limited high-speed performance, because of the continuous interaction of the signal electrode in the interconnection coplanar waveguide (CPW) and semiconductor layers. Unless careful design is applied, both configurations are prone to present modes interacting mostly with the amplification region, leading to device saturation, and suffering strongly from the competition between signal and ASE for the optical gain, resulting in a strong dependence of the measurable efficiency on the input optical power.

The main advantages of TAP detectors with lateral coupling is a consequence of the smaller angle of spontaneous emission from the gain region that will be absorbed in the detection region, as well as the absence of a parasitic transistor. However, TAP detectors with vertical coupling present several two very important advantages in return:

- 1) Fabrication is simpler, without the need of ion implantation and/or intermixing for electrical isolation.
- 2) The vertical stacking of gain and absorption region allows for single-epitaxy grown, separately optimized active regions.

As shown in this dissertation, however, the effect of the parasitic transistor may be minimized by appropriate bandgap engineering, while the effect of absorption of spontaneous emission is secondary to absorption of ASE, leading to an overall advantage of TAP detectors with vertical stacking, based on much simpler device fabrication and better performance of each active region.

TAP detectors with alternating gain and absorption present two very important advantages when compared to a configuration presenting vertical coupling:

- 1) TAP detectors presenting alternating gain and absorption may be impedance- and velocity-matched, presenting furthermore low attenuation, resulting in excellent microwave propagation characteristics, and hence high potential bandwidths (>100GHz).
- 2) The absence of a parasitic transistor, together with the minimal angle of spontaneous emission that is coupled into the absorption regions limits the main contribution to the background current to absorption of ASE.

TAP detectors with alternating gain and absorption are however more difficult to fabricate, requiring ion implantation and/or regrowth for electrical isolation, and as shown in this dissertation, good noise performance requires appropriate design of the efficiency of each absorption region. However, the additional device complexity is rewarded with much higher possible efficiency-bandwidth products.

The overall conclusion to be drawn from this paragraph may be then expressed as follows: TAP detectors have, theoretically, the potential of presenting simultaneously high efficiency, bandwidth and saturation power, with little or no change in noise figure with respect to traditional photodetectors with optical preamplification. The optimum configuration to achieve these results simultaneously would present alternation between gain and absorption sections, the first section in the device providing amplification. Lower bandwidth values may be expected in TAP detectors

with transverse coupling. The reduction of the production of spontaneous emission and ASE may be key in achieving optimum performance.

The conclusions supported by the experimental results obtained will be outlined next.

Experimental conclusions

This dissertation presents the, to the best of my knowledge, first experimental demonstration of the distributed combination of optical amplification and photodetection. External quantum efficiency over 200% was demonstrated in GaAs-based devices. In a parallel effort, InP-based devices were also fabricated, reaching over 100% external quantum efficiency. However, the experimental contribution of this dissertation goes beyond a proof of principle, or a certain performance value. Indeed, the combination of experimental data and theoretical simulations points out the most important factors limiting TAP detector performance up to date. The following conclusions may be drawn from the experimental results and their comparison with the theory developed for TAP detectors:

- 1) The presence of modes suffering large net gain may result in saturation, due to either the signal or the ASE. In particular, all evidence points to these modes as being the main limiting factor in the first generation of successfully fabricated GaAs-based TAP detectors.

- 2) The competition between signal and spontaneous emission for the available gain reduces the measurable efficiency in TAP detectors. This effect is also linked with optical gain saturation, and depends largely on the input optical power. Experimental evidence points to this effect being the main limiting factor in the external quantum efficiency measured for the second generation of successfully fabricated GaAs-based TAP detectors.

It is therefore clear from the previous two conclusions that optimum TAP detectors performance may only be obtained when all modes suffering large net gain are eliminated, while at the same time the absorption of ASE in the detection regions is minimized. Based on the previous theoretical and experimental conclusions, a possible future line of research on TAP detectors will be next outlined. In my opinion, this line of research has the best possibilities of obtaining optimum TAP detector performance.

Future work

Based on the conclusions obtained from both theoretical and experimental results shown in this dissertation, I will now outline the, in my opinion, best procedure for obtaining optimum TAP detector performance, as a proposed future work direction.

Obviously, and due to loss-limited performance of configurations featuring transverse coupling, it is clear that achieving optimum efficiency-bandwidth product requires the use of alternating gain and absorption. This configuration presents the

additional advantage of minimizing the percentage of spontaneous emission that is absorbed in the detection regions of the device. These two advantages are obtained at the price of higher device fabrication complexity, requiring ion implantation, intermixing or both. The separate optimization of amplification and detection regions requires at least one regrowth, so that the gain sections feature a quantum well-based active region, while absorption sections feature bulk active material. However, an additional, extremely important advantage, may be obtained at little additional cost: a second regrowth would allow the definition of filtering sections, with an active region providing absorption at energies above the peak gain energy, i.e., slightly above the energy for which the net gain per period is maximum. The photocurrent obtained from absorption in these filtering regions is discarded, resulting effectively in high optical loss for wavelengths shorter than the range of input wavelengths for which the device performance is optimum.

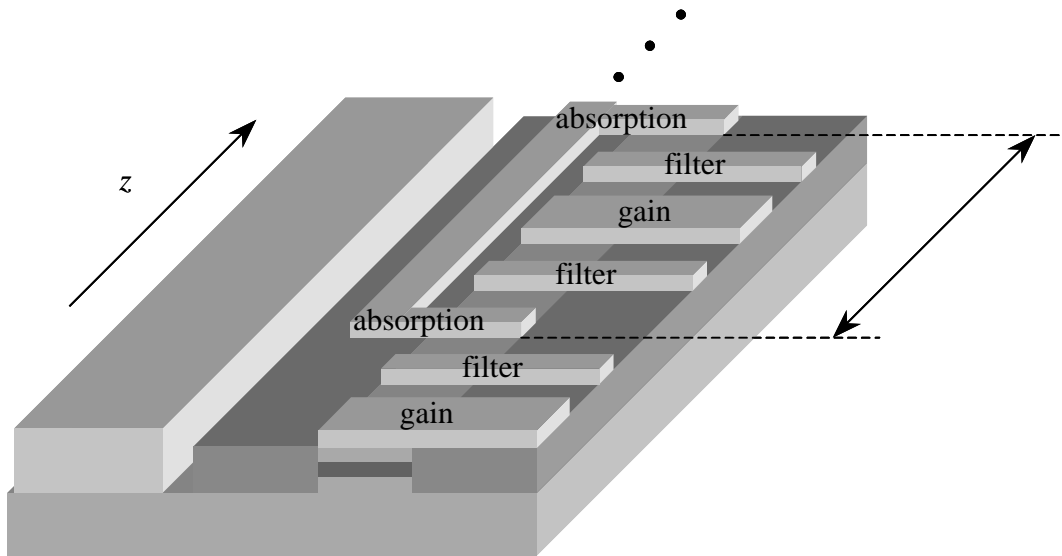


Figure 8.1: TAP detector with alternating gain and absorption and integrated filtering sections. This configuration prevents ASE build-up, while taking advantage of velocity- and impedance- matching, and low microwave propagation loss, for high efficiency-bandwidth products and better linearity over a larger range of input optical power. The initial amplification section ensures lower noise figure, as well as higher external quantum efficiency. The double-sided arrow indicates the extent of one full period.

This scheme, shown in figure 8.1, presents the following advantages:

- 1) The ASE build-up inside the device is inhibited for wavelengths other than those in the close neighborhood of the input wavelength for which device performance is optimum.
- 2) As a consequence, the background current produced by absorption of ASE is greatly diminished. Furthermore, the photocurrent noise term classically called “spontaneous-spontaneous beat noise term” becomes also much smaller, leading to the noise figure approaching the theoretical limit for a larger range of input optical powers.

- 3) Since the background current is much smaller, so are its variations induced by changes in the input optical power. This results in a much better device linearity, namely in a smaller dependence of the measurable efficiency on the input optical power.

Note that it is important that filtering sections are included at both sides of the absorption regions, in order to reduce also the build-up of backward-traveling ASE. It is also important to include an initial amplification section, not only to obtain larger external quantum efficiencies, but also to reduce the overall device noise figure.

In conclusion, we have presented in this chapter the conclusions obtained from both theoretical and experimental results shown in this dissertation. A future line of TAP detector research is also proposed, in the form of TAP detectors with alternating gain and absorption featuring an initial amplification section for low-noise performance, and integrated optical filtering for higher linearity through minimization of the effects of ASE build-up.

(This page is intentionally left blank)

APPENDIX A

Gain and spontaneous emission in Semiconductor Optical Amplifiers

The concepts of optical amplification and spontaneous emission of photons in semiconductor optical amplifiers (SOAs) cannot be separated. This fact becomes very important at different levels. First, the spontaneous recombination of electron-hole pairs subtracts from the total available gain that the input signal may experience. Next, the spontaneous emission of photons, being random in nature, and independent of the input signal, generates an inconvenient background level of optical power, and becomes an important source of noise. Finally, as some of the spontaneously generated photons may couple into guided modes, the amount of amplified spontaneous emission (ASE) in the SOA may become important enough to saturate the gain, thus becoming the source of non-linear behavior. In this Appendix, equations are given linking gain and spontaneous emission. These relations are used widely throughout the dissertation to describe the phenomena of saturation and noise in TAP detectors.

Emission and absorption of photons in semiconductors

In this section, the concepts of spontaneous emission and stimulated emission and absorption of photons by semiconductors, as well as their mathematical description, are briefly addressed. Although these concepts or their expressions are not new, it is important to establish a consistent notation at this point that will allow us to build a strong model for gain, spontaneous emission of photons and noise throughout the dissertation.

Semiconductors may be used to emit, amplify and detect light. The mechanisms via which this may happen are summarized in figure A.1.

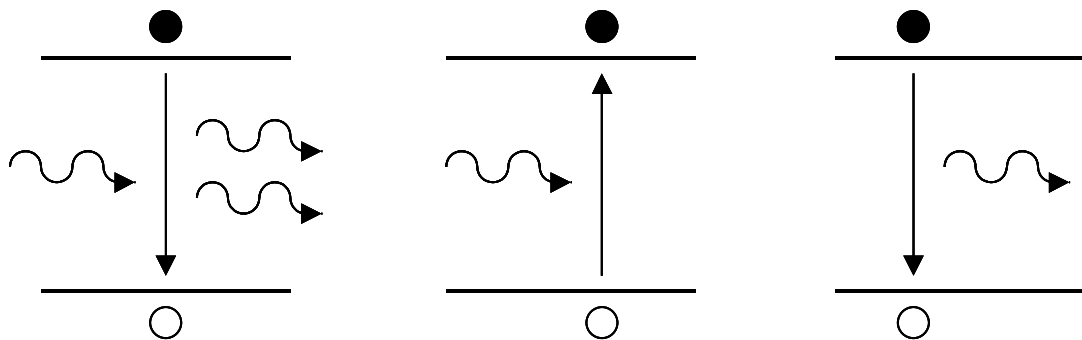


Figure A.1: Stimulated emission (left), stimulated absorption (center) and spontaneous emission (right). Full dots represent electrons in the conduction band, empty dots holes in the valence band, wiggly arrows represent photons and straight arrows electronic transitions.

From left to right, it shows stimulated emission, stimulated absorption and spontaneous emission of photons. In stimulated emission, a second photon identical to one that already exists is generated. The energy of that photon is given by an electron in the conduction band that recombines with a hole in the valence band. An

electron-hole pair may also recombine independently of already existing light, generating in this case a photon with random momentum, via spontaneous emission. Finally, an electron hole pair may also be generated via the stimulated absorption of a photon. Conservation of energy requires that the photon frequency $\boldsymbol{\nu}$ is equal to the difference in the energies of the electron in the conduction band and the hole in the valence band divided by Planck's constant h . Since photons have negligible momentum compared to electrons, direct bandgap semiconductors, where the minimum energy in the conduction band and the maximum energy in the valence band coincide in momentum space, are much more efficient light emitters than indirect gap semiconductors.

The following paragraphs will show the mathematical description of the relation between spontaneous and stimulated emission of photons in semiconductors.

Density of optical modes and spontaneous emission coupling coefficient

Resonant modes in an optical cavity must satisfy the requirement that, after a round-trip, their phase changes by an integer multiple of $2\boldsymbol{p}$. Calling n the refractive index inside said cavity, the condition of resonance may be used to find the total number of modes that may be emitted in it. The density of optical modes per unit frequency and volume, $\boldsymbol{r}_0(\boldsymbol{\nu})$, will then be given by the derivative of the number of modes with respect to frequency, and divided by the cavity volume (see, for example, [1], pp. 441-443):

$$\mathbf{r}_0(\mathbf{n}) = \frac{8\mathbf{p}n^2n_g\mathbf{n}^2}{c^3} \quad (\text{A.1}),$$

where $n_g = n + \mathbf{n}(\partial n / \partial \mathbf{n})$ is the group index.

Since frequency \mathbf{n} and wavelength \mathbf{l} are related through $\mathbf{n}\mathbf{l} = c$, we can write the density of optical modes per volume and per unit wavelength as

$$\mathbf{r}_0(\mathbf{l}) = \mathbf{r}_0(\mathbf{n}) \left| \frac{d\mathbf{n}}{d\mathbf{l}} \right| = \frac{8\mathbf{p}n^2n_g}{\mathbf{l}^4} \quad (\text{A.2}).$$

The spontaneous emission coupling coefficient \mathbf{b}_{sp} represents the fraction of spontaneously emitted photons that will couple into a particular mode. We can assume that the probability of a spontaneously emitted photon to couple to each mode is identical. Integrating (A.2) over the linewidth of the spontaneous emission and multiplying by the mode volume, we would therefore obtain the inverse of \mathbf{b}_{sp} for a semiconductor laser. However, for traveling wave SOAs longitudinal resonance is not a requirement. There is however confinement of the optical power in the lateral and vertical directions. This results in a spontaneous emission coupling coefficient of [2], [3]

$$\mathbf{b}_{sp} = \frac{\Gamma \mathbf{l}^2}{8\mathbf{p}n^2S} \quad (\text{A.3}),$$

where S is the cross-section surface of the active region and Γ the transverse modal confinement factor. Intuitively, this means that the number of available modes in each of the transverse directions is proportional to the number of times that we can fit

a wavelength in the waveguide dimension in that direction. This value is much larger than the spontaneous emission factor in the case of a semiconductor laser, which may be calculated as mentioned above from (A.2), and is given by (see, for example, [1] pp. 444-445)

$$\mathbf{b}_{sp} = \frac{\Gamma I^4}{8pn^2n_g\Delta I_{sp}V} \quad (\text{A.4}),$$

where V is the active region volume and ΔI_{sp} is the spontaneous linewidth. The following paragraphs will make use of the relations shown here to describe the transition rates that produce gain and spontaneous emission in SOAs.

Emission and absorption rates

Stimulated emission and absorption may be understood as the coupling of a electron state and a hole state via an external optical field. Spontaneous emission can then be understood as the coupling of the same states in the absence of an external field, or in the presence of a vacuum field. This is probably best represented through Einstein's approach to emission and absorption of light by atoms (see, for example, [1] pp. 462-465). According to Einstein's theory, the stimulated emission rate $R_{st,em}$, stimulated absorption rate $R_{st,ab}$ and spontaneous emission rate R_{sp} , expressed in units of inverse of volume and time, are given respectively by

$$R_{st,em}(\mathbf{h}\mathbf{n}) = W(\mathbf{n})B_{21}\mathbf{r}_r(\mathbf{h}\mathbf{n})f_c(1-f_v)h\mathbf{d}\mathbf{n} \quad (\text{A.5}),$$

$$R_{st,ab}(\mathbf{h}\mathbf{n}) = W(\mathbf{n})B_{12}\mathbf{r}_r(\mathbf{h}\mathbf{n})f_v(1-f_c)h\mathbf{d}\mathbf{n} \quad (\text{A.6}),$$

$$R_{sp}(\hbar\mathbf{n}) = A_{21} \mathbf{r}_r(\hbar\mathbf{n}) f_c (1 - f_v) \hbar d\mathbf{n} \quad (\text{A.7}),$$

where $W(\mathbf{n})$ is the radiation energy density per unit volume and per unit energy, $\mathbf{r}_r(\hbar\mathbf{n})$ is the semiconductor reduced density of states or density of state pairs at energy difference $\hbar\mathbf{n}$, f_c is the probability of occupancy of a state in the conduction band and f_v the probability of occupancy of a state in the valence band. Note that (A.5)-(A.7) express the emission and absorption rates for photons whose energies lie in an interval $\hbar d\mathbf{n}$ centered at $\hbar\mathbf{n}$. The total emission and absorption rates are calculated by integration over the amplifier bandwidth of (A.5)-(A.7). The spontaneous emission rate is usually expressed as a spectral density of spontaneous emission, in units of inverse time, inverse volume and inverse energy, i.e., what is sometimes given as the spontaneous emission rate is actually $R_{sp}(\hbar\mathbf{n})/(\hbar d\mathbf{n})$.

The coefficients A_{21} , B_{21} and B_{12} are referred to as Einstein's A and B coefficients. Assuming thermal equilibrium in the material, they are found to satisfy the following relations:

$$B_{12} = B_{21} \equiv B \quad (\text{A.8});$$

$$A_{21} = \mathbf{r}_0(\mathbf{n}) \hbar \mathbf{n} B \equiv A \quad (\text{A.9}).$$

For a monochromatic input field at frequency \mathbf{n}_0 , and with a spatial photon density N_p , the radiation density can be written as

$$W(\mathbf{n}) = \hbar \mathbf{n}_0 N_p \mathbf{d}(\nu - \mathbf{n}_0) \quad (\text{A.10}),$$

which results in a photon generation and absorption rates via stimulated transitions of

$$R_{st,em}(\hbar\mathbf{m}_0) = \hbar\mathbf{m}_0 N_p h B \mathbf{r}_r(\hbar\mathbf{m}_0) f_c (1 - f_v) \quad (\text{A.11}),$$

$$R_{st,ab}(\hbar\mathbf{m}_0) = \hbar\mathbf{m}_0 N_p h B \mathbf{r}_r(\hbar\mathbf{m}_0) f_v (1 - f_c) \quad (\text{A.12}).$$

The spontaneous emission rate per unit volume and time, for an energy interval of width $h d\mathbf{n}$ around $\hbar\mathbf{m}_0$ is given by:

$$\begin{aligned} R_{sp}(\hbar\mathbf{m}_0) &= \mathbf{r}_0(\mathbf{n}_0) \hbar\mathbf{m}_0 h B \mathbf{r}_r(\hbar\mathbf{m}_0) f_c (1 - f_v) d\mathbf{n} \\ &= \frac{\mathbf{r}_0(\mathbf{n}_0)}{N_p} R_{st,em}(\hbar\mathbf{m}_0) d\mathbf{n} \end{aligned} \quad (\text{A.13}).$$

The spontaneous emission rate is then equal to the stimulated emission rate that would occur when the input radiation present be equal to the blackbody radiation. This allows for a simple representation of the spontaneous emission contribution to the total radiation, which will be described in the next section.

Finally, note that we can write the optical intensity (power arriving per unit of cross-sectional surface) as $N_p v_g$, in units of photons per unit time and area. This allows us to normalize both stimulated transition rates to the optical intensity, by defining

$$r_{st,em}(\mathbf{n}) = \frac{R_{st,em}(\hbar\mathbf{m})}{N_p v_g} = \frac{h^2 \mathbf{n} B}{v_g} \mathbf{r}_r(\hbar\mathbf{m}) f_c (1 - f_v) \quad (\text{A.14}),$$

$$r_{st,ab}(\mathbf{n}) = \frac{R_{st,ab}(\hbar\mathbf{m})}{N_p v_g} = \frac{h^2 \mathbf{n} B}{v_g} \mathbf{r}_r(\hbar\mathbf{m}_0) f_v (1 - f_c) \quad (\text{A.15}).$$

Note that $r_{st,em}$ and $r_{st,ab}$ depend only on the material characteristics, the electrical carrier concentration and the frequency of the incoming radiation, but not on its

power. Using (A.13), we can rewrite the stimulated emission rate normalized to optical intensity as

$$r_{st,em}(\mathbf{n}) = \frac{R_{st,em}(h\mathbf{n})}{v_g N_p} = \frac{R_{sp}(h\mathbf{n})}{v_g \mathbf{r}_0(h\mathbf{n}) d\mathbf{n}} = \frac{hc^2}{8\mathbf{p}n^2} \frac{R_{sp}(h\mathbf{n})}{hd\mathbf{n}} \quad (\text{A.16}).$$

As we will show in the next paragraph, $r_{st,em}(\mathbf{n})$ can be used to fully describe the spontaneous emission power density added per unit length in an SOA. Equation (A.16) is also important since it allows us to find the stimulated emission rate normalized to optical intensity from the spontaneous emission rate. The latter may be calculated from first principles for amplifier active regions.

The relations drawn in this paragraph between stimulated and spontaneous emission rates will be next used to find the relations between optical gain and added spontaneous emission in SOAs.

Optical gain and amplified spontaneous emission power

In this paragraph, we will show the relations existing between the optical gain that an input signal will experience in an SOA, and the optical power that is generated in the same SOA, in the form of amplified spontaneous emission (ASE).

Let us consider a semiconductor region of length Δz and cross-section surface S . Let us assume that, during a time interval Δt , monochromatic radiation at frequency \mathbf{n}_0 , with constant optical power P_{in} , is coupled into this semiconductor region, traveling longitudinally, as shown in figure A.2.

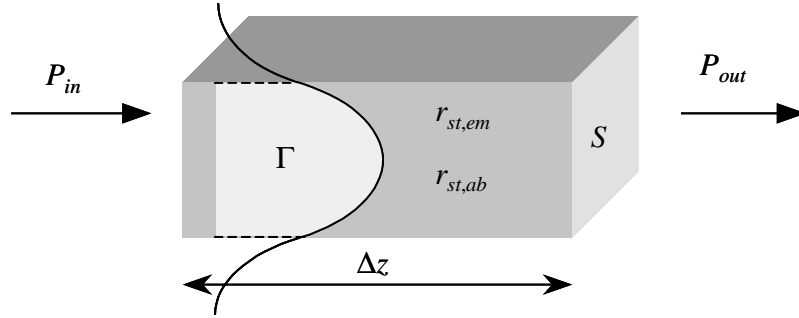


Figure A.2: Schematic representation of a semiconductor active region in an SOA of cross-sectional surface S and length Δz . P_{in} and P_{out} are the input and output optical powers. The effect of the semiconductor in terms of gain and ASE generation is determined by the stimulated emission and absorption rates normalized to optical intensity, $r_{st,em}$ and $r_{st,ab}$, in that region, and by the overlap Γ of the guided mode with the active region.

Let us assume that the time interval Δt is chosen such that $\Delta z = v_g \Delta t$, v_g being the group velocity of light. The photon density present in the semiconductor region is then given by:

$$N_p = \frac{1}{S \Delta z} \frac{\Gamma P_{in} \Delta t}{h \mathbf{m}_0} = \frac{\Gamma P_{in}}{h \mathbf{m}_0 v_g S} \quad (\text{A.17}).$$

The transverse gain confinement factor Γ is introduced to account for the fact that only a fraction Γ of the total photon number from the guided radiation actually overlaps with the amplification region. If Δz is small enough that each photon may participate in at most one stimulated transition, the total net variation of the optical power due to stimulated emission and absorption will be given by

$$P_{out} - P_{in} = h \mathbf{m} \left[R_{st,em} (h \mathbf{m}_0) - R_{st,ab} (h \mathbf{m}_0) \right] S \Delta z \quad (\text{A.18}).$$

Defining the material gain $g(\mathbf{n})$ as the relative optical power variation per unit length, and letting Δz tend to zero, we find that

$$\begin{aligned} g(\mathbf{n}_0) &= \lim_{\Delta z \rightarrow 0} \frac{P_{out} - P_{in}}{\Gamma P_{in} \Delta z} = \frac{R_{st,em}(\hbar \mathbf{n}_0) - R_{st,ab}(\hbar \mathbf{n}_0)}{N_p v_g} \\ &= r_{st,em}(\mathbf{n}_0) - r_{st,ab}(\mathbf{n}_0) \end{aligned} \quad (\text{A.19}).$$

The confinement factor in the denominator is introduced to obtain a result that depends only on the material, independently on the amount of overlap that a particular mode may have with the semiconductor active material.

Let us now consider the spontaneous emission power generated in the same semiconductor region during the same time interval, and in a frequency interval $d\mathbf{n}$ around a given frequency \mathbf{n} . The fraction of this spontaneous emission power that will be coupled into a mode propagating along the amplifier is given by

$$\hbar \mathbf{b}_{sp} R_{sp}(\hbar \mathbf{n}) S \Delta z = \hbar \mathbf{n} \Gamma r_{st,em}(\mathbf{n}) \Delta z d\mathbf{n} \quad (\text{A.20}),$$

where we have made use of (A.1), (A.3), (A.13) and (A.14). The spectral density of spontaneous emission coupled into an amplifier waveguide mode per unit length will be denoted by $p_{SE}(\mathbf{n})$, and can therefore be expressed as

$$p_{ASE}(\mathbf{n}) = \hbar \mathbf{n} \Gamma r_{st,em}(\mathbf{n}) \quad (\text{A.21}).$$

Let us furthermore denote the position-dependent optical power spectral density at frequency \mathbf{n} as $p_{opt}(z, \mathbf{n})$. Its evolution along an SOA may be calculated by combining

the amplification of already existing power, together with the spontaneous emission of new power:

$$\frac{dp_{opt}(z, \mathbf{n})}{dz} = \Gamma g(\mathbf{n}) p_{opt}(z, \mathbf{n}) + p_{SE}(\mathbf{n}) \quad (\text{A.22}).$$

This equation is obviously valid even if the gain, the spontaneous emission and the confinement factor are position-dependent along the amplifier. The initial condition for this equation is obviously given by

$$p_{opt}(0, \mathbf{n}) = \mathbf{h}_c P_{in} \mathbf{d}(\mathbf{n} - \mathbf{n}_0) \quad (\text{A.23}),$$

where we assume that the input is a monochromatic field, with an incident power P_{in} at frequency \mathbf{n}_0 . \mathbf{h}_c is the fraction of the incident power that gets effectively coupled into the mode propagating along the SOA. When gain, spontaneous emission and confinement factor are position-independent, the solution of (A.22) is written as

$$p_{opt}(z, \mathbf{n}) = e^{\Gamma g(\mathbf{n})z} \mathbf{h}_c P_{in} \mathbf{d}(\mathbf{n} - \mathbf{n}_0) + \mathbf{h}_m \frac{r_{st,em}(\mathbf{n})}{g(\mathbf{n})} \left[e^{\Gamma g(\mathbf{n})z} - 1 \right] \quad (\text{A.24}).$$

The first term in the right hand side (RHS) of (A.24) is obviously the result of the amplification of the input signal. The second term describes the ASE power generated by the amplifier. The total gain $G(\mathbf{n}_0)$ experienced by a monochromatic signal of frequency \mathbf{n}_0 inside an SOA of length L , neglecting input and output coupling coefficients, is

$$G(\mathbf{n}_0) = e^{\Gamma g(\mathbf{n}_0)L} = e^{\Gamma [r_{st,em}(\mathbf{n}_0) - r_{st,ab}(\mathbf{n}_0)]L} \quad (\text{A.25}).$$

The total ASE power P_{ASE} produced by the same amplifier can be found by integrating the ASE spectral power density:

$$P_{ASE} = \int h\nu \frac{r_{st,em}(\mathbf{n})}{g(\mathbf{n})} [G(\mathbf{n}) - 1] d\mathbf{n} \quad (\text{A.26}).$$

At this point, it is interesting to define the spontaneous emission factor or population inversion factor n_{sp} , as

$$n_{sp} = \frac{R_{st,em}}{R_{st,em} - R_{st,ab}} = \frac{r_{st,em}}{g} \quad (\text{A.27}).$$

Note that, a priori, n_{sp} is frequency dependent. We may assume, however, that the amplifier gain is flat and n_{sp} is constant across its optical bandwidth $\Delta\mathbf{n}_o$ centered around \mathbf{n}_o (flat-band approximation), which allows us to rewrite (A.26) as

$$P_{ASE} \simeq h\nu_o n_{sp} (G - 1) \Delta\mathbf{n}_o \quad (\text{A.28}).$$

This result is a widely used approximation.

In the previous analysis, we have neglected optical loss due to phenomena such as scattering, free-carrier absorption or stimulated absorption other than in the active region. When loss is included, (A.22) needs to be rewritten as

$$\frac{dp_{opt}(z, \mathbf{n})}{dz} = [\Gamma g(\mathbf{n}) - l] p_{opt}(\mathbf{n}) + p_{SE}(\mathbf{n}) \quad (\text{A.29}),$$

where l is the optical loss per unit length. It is, in general, close to frequency-independent in the bandwidth of typical SOAs. In most cases, amplification as high as possible is desired. The loss is therefore kept at a minimum, and (A.28) is a good

approximation. However, in the case of TAP detectors, where the optical power is kept close to constant along the device (i.e., $G-1$ is much smaller than one and $(\Gamma g-l)$ is much smaller than $r_{st,em}$), that approximation is not valid. This consideration will be important when analyzing the properties of TAP detectors.

In conclusion, this paragraph has shown how the material gain and the spontaneous emission added to the amplifier guided modes are related between them and to the stimulated emission and absorption rates per unit length normalized to optical intensity. These relations are widely used throughout this dissertation to calculate the efficiency and noise characteristics of TAP detectors.

Competition between signal and amplified spontaneous emission

Amplification of optical radiation results in the annihilation of electrical carriers through stimulated recombination. In an SOA with constant pumping, an increase in the input optical power results in a lower carrier density, and thus in a lower gain. In that sense, given an SOA with constant pump current, i.e., a constant electrical carrier generation rate, there is a maximum available optical gain. The input signal and the ASE compete for this available gain, in the sense that every stimulated emission reduces the probability of other photons to be amplified. This results in a lower ASE generation in the presence of a higher input signal. In TAP detectors, this effect proves to be very important, as discussed theoretically in chapter 2, and shown experimentally in chapter 7. In this section, the competition between signal and ASE

for the available optical gain will be discussed. First, the dependence of the carrier concentration on the optical power will be established. As the optical signal evolves in an SOA, this results on the need to define a position-dependent carrier concentration, and therefore position-dependent optical gain and spontaneous emission. Moreover, the carrier concentration will be shown to depend also on the input optical power. The saturation of the gain will be found to be a consequence of the mutual dependence between carrier concentration and optical power. Next, a method used successfully in the past to model this phenomenon will be presented. A variation of this method is used in this dissertation to treat the effect of competition between gain and ASE. Finally, the competition between the signal and the spontaneous emission for the available gain is described in terms of the saturation power of the amplifier.

Carrier density and local optical power

The optical gain in the active region of an SOA is known to depend on the carrier density. Reciprocally, the local optical power may affect the carrier concentration at a given position of the amplifier. This is best understood when the different processes that affect the carrier concentration are considered. They are schematically represented in Figure A.3.

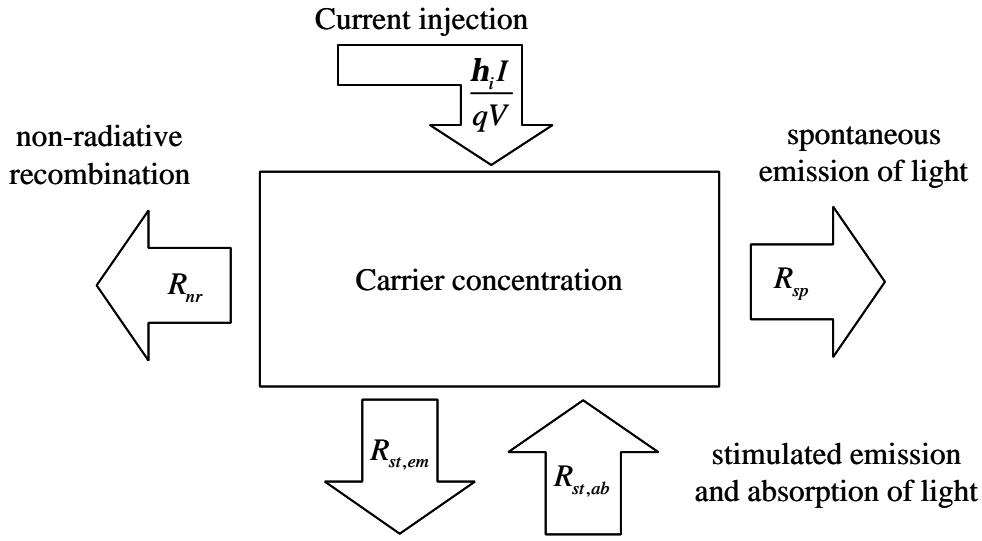


Figure A.3: Processes affecting the carrier concentration in the active region of an electrically pumped SOA.

The condition for equilibrium between the different processes may be deduced from the classical carrier density rate equation (see, for example, [1], pp. 186-187):

$$\frac{h_i I}{qV} = R_{nr} + R_{sp} + (R_{st,em} - R_{st,ab}) \quad (\text{A.30}).$$

In (A.30), I is the current pumped into the active region of volume V . h_i is the injection efficiency, i.e., the fraction of current carriers that arrive into and recombine in the active region. Other current carriers will either leak through it, or be captured into the active region and then thermionically emitted. The spontaneous and stimulated emission rates have been discussed previously in this appendix. Finally, the non-radiative recombination rate may be written as

$$R_{nr} = AN + CN^3 \quad (\text{A.31}),$$

where N is the carrier density in the active region, and A and C are phenomenological coefficients. The first term in the RHS of (A.31) accounts for defect-assisted carrier recombination. The second term accounts for recombination due to Auger processes.

Let us now assume that the carrier concentration N is known at a given position in the amplifier when a certain optical power is present at that position. As this power increases, the stimulated emission term in (A.30) will increase. If the current injected remains constant, the spontaneous emission rate and the non-radiative recombination rate must be lower so that the equality still holds. Therefore, the carrier concentration must be lower. As a consequence, larger input optical signals will experience a reduced gain, leading to saturation of the amplifier. Moreover, the carrier concentration will be position-dependent along the amplifier, being lower where the local optical power is higher. This situation is expressed schematically in figure A.4.

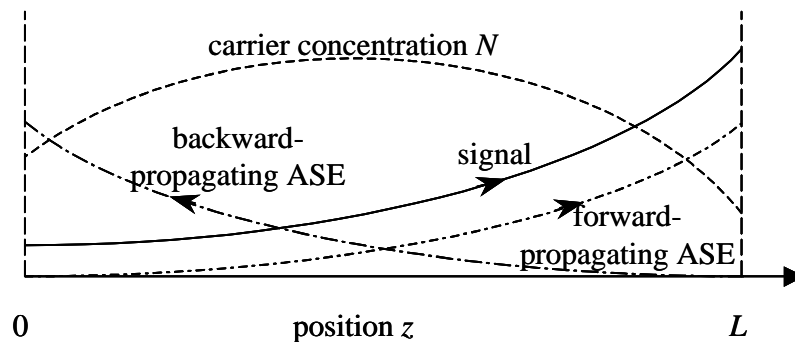


Figure A.4: Carrier density (dashed line), amplified input signal power (full line) and ASE (dash-dotted line) in an SOA. The spatial evolution of the optical power results in position-dependent carrier density and gain. Higher local optical power results in lower local carrier density, because of a faster electron-hole pair recombination rate.

Position-dependent gain and spontaneous emission rate must therefore be defined in (A.22). This equation and (A.30) form a system that needs to be self-consistently solved. Note that this system needs to include also the effect of the back-propagating ASE, so in fact there are two equations of the form of (A.22) that need to be satisfied: one for the signal and forward-propagating ASE, one for the backward-propagating ASE.

The fact that the gain may locally be depleted due to a decrease in the carrier concentration is usually referred to as spatial hole burning. There is an additional complication, which appears when the local optical power reaches very high values. The stimulated recombination rate may be high enough that the carrier lifetime approaches the carrier relaxation time. The electron population or the hole population will be out of equilibrium in such a situation. Strong monochromatic radiation may deplete the occupied electron-hole pairs that would produce emission in the neighborhood of its frequency, leading to a more drastic reduction in the gain for a certain range of wavelengths. This phenomenon is called spectral hole burning. All throughout the dissertation this effect will be neglected, and the electron population and the hole population will be assumed to be, each one of them separately, always in equilibrium.

In conclusion, it has been shown in this paragraph how the accurate description of the effect of the saturation in the behavior of an SOA requires the definition of position-dependent carrier concentration. This results obviously in the gain and spontaneous emission depending on position too. As a consequence, two equations

need to be solved consistently together. One of them, which needs to be satisfied for all positions in the amplifier, expresses the equilibrium between carrier injection and annihilation processes. The second one is the equation describing the evolution of the optical power, but using this time position-dependent gain and spontaneous emission rate. In the next paragraph, we will describe a method successfully used in the past to solve these equations.

Calculation of the amplifier gain in the presence of saturation

As discussed in the previous paragraph, the carrier density at a given position in an SOA depends on the local optical power. Two equations need to be solved together, one expressing the evolution of the optical power, another the equilibrium in the local carrier density. The latter needs to be solved for all positions in the amplifier. In general, the system formed by both cannot be solved self-consistently in a closed form, and numerical computation is necessary. In this section, one method successfully used in the past to solve this system will be presented. This method is based on dividing the amplifier in a number of longitudinal sections, and assuming that the carrier concentration, and thus the gain and spontaneous emission, are constant in each section, as expressed in figure A.5.

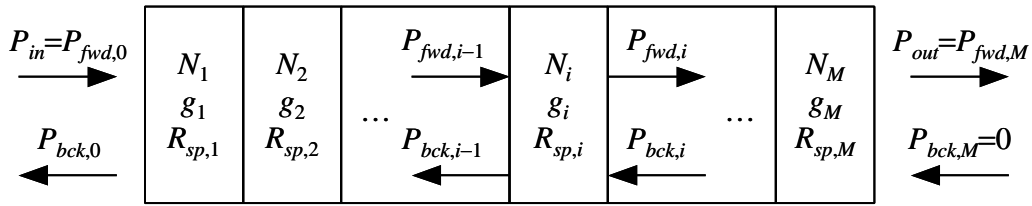


Figure A.5: A semiconductor optical amplifier may be divided into a number M of sections. The carrier concentration may be assumed to be constant in each section. The gain and spontaneous emission rate are therefore constant in each section too.

Using this constant gain and spontaneous emission, the evolution of the signal and the forward- and backward-propagating ASE may be expressed as a function of the carrier density vector (N_i) and the input power P_{in} . The system of equations to be solved becomes a system of $3M$ equations, where M is the number of sections. For each section, one equation expresses the equilibrium in the carrier concentration, one the evolution of the forward-propagating optical power (taking into account both signal and ASE) and one the evolution of the backward-propagating optical power (ASE only in most cases). The pump current for each section may be assumed to be I/M if all sections have the same length. This method shows quick convergence as the number of section increases (see [3]), and constitutes a great simplification from the original problem, where the carrier concentration equilibrium equation needed to be solved for all positions.

A numerical method that allows the competition of ASE and signal for the available gain to be taken into account quantitatively has been briefly presented. A variation of this method is used in chapter 2 of this dissertation to describe the effect of this competition in TAP detectors.

Saturation power

The competition for the available gain is usually described in terms of the saturation power P_{sat} of the amplifier, as an alternative formulation not requiring the use of the carrier density rate equation. Let us consider equation (A.30) under the assumption that the pump current is constant, and variations in the carrier density are produced only through changes in the local optical power. We may therefore assume that the gain is a function of the local optical power only, the carrier density being an intermediate variable that depends on the photon density. Under these conditions, the derivative of the RHS of equation (A.30) with respect to the carrier density will be zero, since we are assuming a constant pump current:

$$\frac{1}{\mathbf{t}_{\Delta N}} + v_g a N_p + v_g g \left(\frac{dN}{dN_p} \right)^{-1} = 0 \quad (\text{A.32}),$$

where the differential carrier lifetime $\mathbf{t}_{\Delta N}$ and the differential gain a are defined by

$$\frac{1}{\mathbf{t}_{\Delta N}} = \frac{d(R_{nr} + R_{sp})}{dN} \quad (\text{A.33}),$$

$$a = \frac{dg}{dN} \quad (\text{A.34}).$$

Note that, in principle, these quantities are carrier density-dependent, since neither the gain nor the non-radiative and spontaneous recombination rates are perfectly linear with the carrier density. Applying the chain rule, we may now describe the variations in the optical gain induced by changes in the local optical power:

$$\frac{dg}{dN_p} = \frac{dg}{dN} \frac{dN}{dN_p} = \frac{dN}{dN_p} = - \frac{g}{N_p + \frac{1}{v_g a \tau_{\Delta N}}} \quad (\text{A.35}).$$

Equation (A.35) may be integrated by separating the terms containing the gain and those containing the photon density:

$$\ln(g) - \ln(g_0) = \ln\left(\frac{1}{v_g a \tau_{\Delta N}}\right) - \ln\left(N_p + \frac{1}{v_g a \tau_{\Delta N}}\right) \quad (\text{A.36}),$$

where g_0 is the unsaturated value of the optical gain, valid for very small optical powers. Using now equation (A.17), we may write

$$g = \frac{g_0}{1 + v_g a \tau_{\Delta N} N_p} = \frac{g_0}{1 + \frac{P_{opt}}{P_{sat}}} \quad (\text{A.37}),$$

where the power for which the local gain falls to half of its unsaturated value is

$$P_{sat} = \frac{h\nu_0 S}{\Gamma_g a \tau_{\Delta N}} \quad (\text{A.38}).$$

This saturation power depends thus on the characteristics of the amplification material (through the differential carrier lifetime and the differential gain), on the dimensions of the active region (through its cross-sectional surface) and on the overlap of the mode with it (through the confinement factor). Note that, in principle, the saturation power depends on the local bias point of the amplifier, since as mentioned earlier, and though treated as constants in the integration of (A.35), the differential carrier lifetime and the differential gain depend on the carrier density.

Equations (A.37) and (A.38) provide therefore a phenomenological description of the amplifier saturation without the use of the rate equation.

In summary, this appendix has discussed the background necessary for the analysis of optical gain and ASE generation in SOAs, both conceptually and mathematically. The information contained in this appendix is used widely throughout the dissertation as a starting point to describe the behavior of TAP detectors.

References

- [1] L.A. Coldren, S.W. Corzine, “Diode lasers and photonic integrated circuits,” *John Wiley & Sons*, 1995.
- [2] L. Thylén, “Amplified spontaneous emission and gain characteristics of Fabry-Perot and traveling wave type semiconductor laser amplifiers,” *IEEE Journal of Quantum Electronics*, vol. 24, pp. 1532-1537, 1988.
- [3] G. Giuliani, D. D’Alessandro, “Noise analysis of conventional and gain-clamped semiconductor optical amplifiers”, *IEEE Journal of Lightwave Technology*, vol. 18, n. 9, pp. 1256-1263, 2000.

APPENDIX B

Representations of the propagation characteristics of a microwave transmission line

The propagation characteristics of a microwave transmission line may be described mathematically through several different formalisms. In this dissertation, two of such formalisms are used: the current-voltage transmission matrix or ABCD matrix, and a description that uses both the characteristic impedance and the microwave propagation coefficient \mathbf{g} . In this appendix, the relations between the two representations will be shown. Special attention will be given to the current-voltage transmission matrix in the case of periodic transmission lines, which is used in the dissertation to describe the high-speed behavior of TAP detectors with alternating gain and absorption.

Propagation in microwave transmission lines

High-speed electrical signals are affected through several phenomena as they travel in microwave transmission lines. The effects of these phenomena may be grouped in three different results, namely attenuation, delay, and reflections at discontinuities or at transitions between lines of different characteristics. The characteristics of the transmission line may be represented in different ways. A more direct representation of the actual attenuation and delay is provided by the microwave propagation coefficient \mathbf{g} . Together with the characteristic impedance Z , this fully describes a homogeneous transmission line. When the complexity of the transmission line increases, different approaches may be used. A transmission line may be viewed as a junction with two ports, both serving simultaneously as input and an output. Its characteristics may then be represented by a scattering matrix, i.e., a matrix that relates the outgoing electrical signals at each port to the incoming excitations (see for example [1], pp. 248-57). Transmission matrix formalisms are also possible. Their main virtue is that the physical juxtaposition of transmission lines may be represented mathematically by the ordered product of their corresponding transmission matrices (see for example [1], pp. 257-60). This allows for easy calculations of the characteristics of complex transmission lines. In this section, two different formalisms used to describe the characteristics of microwave transmission lines will be briefly introduced, as well as the relations between them.

Propagation coefficient and characteristic impedance

Let us consider a homogeneous transmission line of length L along the z direction, extending from $z=0$ to $z=L$. Electrical signals traveling in it may be described as forward- and backward-propagating voltage and current waves. An analysis of a transmission line, using Maxwell's equations, allows us to write the relations between such voltage and current waves as (see, for example, [1] chapter 3)

$$\frac{V_{fwd}(z)}{I_{fwd}(z)} = \frac{V_{bck}(z)}{I_{bck}(z)} = Z_{car} \quad (\text{B.1}),$$

$$\frac{V_{fwd}(z)}{V_{fwd}(0)} = \frac{V_{bck}(L-z)}{V_{bck}(L)} = e^{-\mathbf{g}z} \quad (\text{B.2}).$$

Z_{car} is the characteristic impedance, and $\mathbf{g}=\mathbf{a}+j\mathbf{b}$ the complex microwave propagation coefficient, where \mathbf{a} and \mathbf{b} are real numbers. In general, both Z_{car} and \mathbf{g} are frequency-dependent.

The loss coefficient \mathbf{a} describes the attenuation per unit length that a current or voltage wave traveling along the transmission line will suffer. The dispersion coefficient \mathbf{b} is related to the phase velocity v_p via

$$v_p = \frac{\mathbf{w}}{\mathbf{b}} \quad (\text{B.3}),$$

where \mathbf{w} is the angular frequency. In general, this parameter will also be frequency-dependent. The group velocity v_g , defined as the velocity at which a pulse consisting

of a very narrow band of frequency components propagates, is found to be related to the dispersion coefficient \mathbf{b} through the equation

$$v_g = \left(\frac{d\mathbf{b}}{d\omega} \right)^{-1} \quad (\text{B.4}),$$

The microwave propagation coefficient describes thus the attenuation and delay suffered by an electrical signal propagating in a transmission line. The reflections between different transmission lines are related to the characteristic impedance. Let us now consider the boundary between two transmission lines of respective characteristic impedances $Z_{car,1}$ and $Z_{car,2}$, as shown in figure B.1. Let us assume that an electrical signal travels from the former to the latter. The incoming current wave will be represented by $I_{fwd,1}$, the reflected current wave by $I_{bck,1}$, and the transmitted current wave by $I_{fwd,2}$.

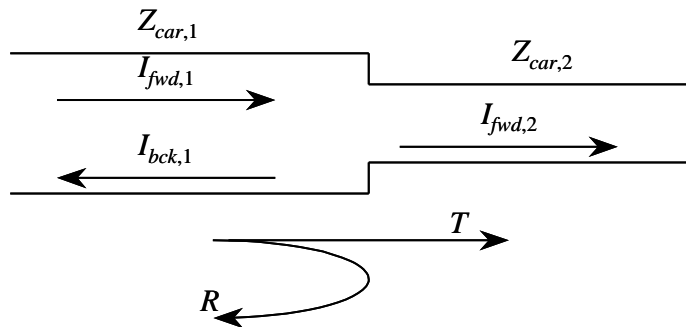


Figure B.1: Interface between two transmission lines of different characteristic impedance. Incoming and outgoing current waves are shown.

Conservation of voltage and current at the interface between two different transmission lines of characteristic impedance $Z_{car,1}$ and $Z_{car,2}$, respectively, ensures that the current transmission and reflection coefficients, T and Γ , are given by

$$T = \frac{I_{fwd,2}}{I_{fwd,1}} = \frac{2Z_{car,1}}{Z_{car,2} + Z_{car,1}} \quad (\text{B.5}),$$

$$\Gamma = \frac{I_{bck,1}}{I_{fwd,1}} = \frac{Z_{car,2} - Z_{car,1}}{Z_{car,2} + Z_{car,1}} \quad (\text{B.6}).$$

The reflection coefficient for the voltage wave is the same as the current wave reflection coefficient, but the transmission coefficient for the voltage wave is given by

$$T = \frac{V_{fwd,2}}{V_{fwd,1}} = \frac{2Z_{car,2}}{Z_{car,2} + Z_{car,1}} \quad (\text{B.7}).$$

In this dissertation, the main concern is the propagation of the photocurrent generated in TAP detectors. Hence, equation (B.5) will be used.

Thus, between the microwave propagation coefficient g and the characteristic impedance Z_{car} , attenuation, delay and reflections in transmission lines may be described. As the complexity of the transmission line increases, and different sections with different characteristics are present, the calculations shown above become quite cumbersome. Other formalisms may be then more useful, as it will be shown in the next section.

Voltage-current transmission matrix (ABCD matrix)

Transmission matrix-based formalisms have the advantage of allowing easy calculation of the characteristics of a complex transmission line presenting several different sections. One example is the voltage-current transmission matrix or ABCD matrix (see, for example, [1], pp. 257-259). Figure B.2 shows the ABCD matrix representation of a transmission line. The matrix elements describe the relation between voltage and current waves at the input as a function of current and voltage waves at the output.

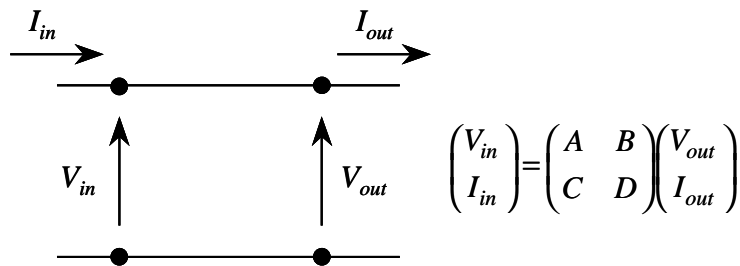


Figure B.2: Current-voltage matrix representation of a transmission line, showing voltage V_{in} and incoming current I_{in} at the input and voltage V_{out} and outgoing current I_{out} at the output.

The voltage-current transmission matrix is then defined as

$$\begin{pmatrix} V_{in} \\ I_{in} \end{pmatrix} = \begin{pmatrix} A & B \\ C & D \end{pmatrix} \begin{pmatrix} V_{out} \\ I_{out} \end{pmatrix} \quad (\text{B.8}).$$

Note that both currents are taken in the same direction, i.e., incoming at the input, outgoing at the output. Thus, the ABCD matrix of two transmission lines is the product of the ABCD matrices of both transmission lines, ordered from the input to the output of the ensemble. Let us now consider a homogeneous transmission line of

length L along the z direction, with input at $z=0$, output at $z=L$. As before, we can define forward- and backward-propagating voltage and current waves. Their relation to the input and output current and voltage are given by

$$V_{in} = V_{fwd}(0) + V_{bck}(0) \quad (\text{B.9}),$$

$$V_{out} = V_{fwd}(L) + V_{bck}(L) \quad (\text{B.10}),$$

$$I_{in} = I_{fwd}(0) - I_{bck}(0) \quad (\text{B.11}),$$

$$I_{out} = I_{fwd}(L) - I_{bck}(L) \quad (\text{B.12}).$$

Using (B.1) and (B.2), we can readily find the relation between the ABCD parameters and the propagation characteristics of the transmission line:

$$\begin{pmatrix} A & B \\ C & D \end{pmatrix} = \begin{pmatrix} \cosh(\mathbf{g}L) & Z_{car} \sinh(\mathbf{g}L) \\ \frac{1}{Z_{car}} \sinh(\mathbf{g}L) & \cosh(\mathbf{g}L) \end{pmatrix} \quad (\text{B.13}).$$

Note that, independently on the characteristics of the line, this matrix always has a determinant equal to 1, and its inverse is trivially found to be

$$\begin{pmatrix} A & B \\ C & D \end{pmatrix}^{-1} = \begin{pmatrix} \cosh(\mathbf{g}L) & -Z_{car} \sinh(\mathbf{g}L) \\ -\frac{1}{Z_{car}} \sinh(\mathbf{g}L) & \cosh(\mathbf{g}L) \end{pmatrix} \quad (\text{B.14}).$$

The voltage-current transmission matrix has thus been introduced, and when describing a homogeneous transmission line of length L , its value has been related to the propagation characteristics of said line.

In conclusion, we have introduced in this section two different formalisms to describe the properties of microwave transmission lines. The relation between these formalisms has also been shown.

Voltage-current transmission matrix for periodic transmission lines

In this section, the voltage-current transmission matrix formalism used in the dissertation to model the behavior of TAP detectors with alternating gain and absorption will be introduced. Since such devices present a periodic geometry, the particular case of periodic transmission lines will be studied. We will show how, knowing the ABCD matrix of a unit cell, the characteristics of the transmission line may be calculated (see, for example, [1] pp. 522-557).

Let us consider a periodic transmission line of period length Λ . Figure B.3 shows how the voltage and current at a given node in between periods may be related to the voltage and current at an adjacent node. This allows us to treat the problem of finding the characteristics of the full transmission line as an eigenvalue problem.

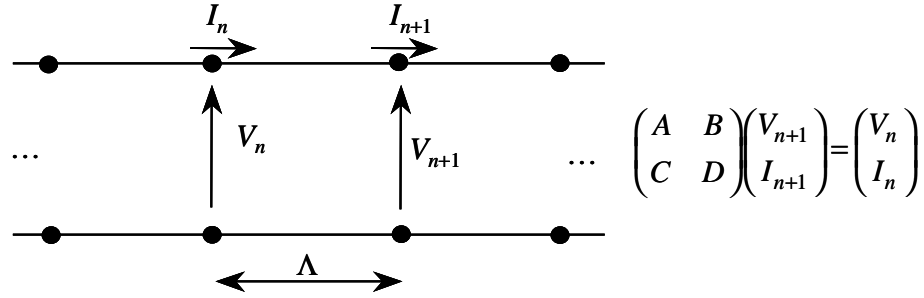


Figure B.4: Schematic representation of a periodic transmission line, showing voltages and currents at two adjacent nodes. The relation between these voltages and currents is given by the equation that accompanies the figure.

We will make no *a priori* assumptions about the transmission matrix of each period. As such, if each period is not homogeneous, writing the ABCD matrix associated to each one of them in the form (B.13) may not be possible. Using from one side the relations between voltage and current through the ABCD matrix, and from another the fact that, if a propagating wave exists, then an effective propagation coefficient g exists such that $V_{n+1}=V_n e^{-g\Lambda}$ and $I_{n+1}=I_n e^{-g\Lambda}$, we can write

$$\begin{pmatrix} A & B \\ C & D \end{pmatrix} \begin{pmatrix} V_{n+1} \\ I_{n+1} \end{pmatrix} = \begin{pmatrix} V_n \\ I_n \end{pmatrix} = \begin{pmatrix} e^{g\Lambda} & 0 \\ 0 & e^{g\Lambda} \end{pmatrix} \begin{pmatrix} V_{n+1} \\ I_{n+1} \end{pmatrix} \quad (\text{B.15}).$$

It becomes obvious that $r=e^{g\Lambda}$ is an eigenvalue of the transmission matrix. For non-trivial (non-zero voltage and current) solutions to exist, such eigenvalue needs to satisfy

$$r^2 - (A+D)r + AD - BC = r^2 - (A+D)r + 1 = 0 \quad (\text{B.16}).$$

We have used that, for reciprocal transmission lines, regardless of any other consideration, the determinant of the voltage-current transmission matrix is always 1.

The product of the two roots of (B.16) is 1. Therefore, if one of them represents $e^{g\Lambda}$, the other one will be $e^{-g\Lambda}$, and half their sum will be in any case equal to $\cosh(g\Lambda)$. But the sum of both roots is $A+D$, and it is then obvious that

$$\cosh(g\Lambda) = \frac{A+D}{2} \quad (\text{B.17}).$$

The characteristic impedance may be found to be

$$Z_{car} = \frac{V_{n+1}}{I_{n+1}} = \frac{B}{e^{g\Lambda} - A} = \frac{e^{g\Lambda} - D}{C} \quad (\text{B.18}).$$

Note at this point that, if $A=D=\cosh(g\Lambda)$, then

$$Z_{car} = \frac{B}{\sinh(g\Lambda)} = \frac{\sinh(g\Lambda)}{C} = \sqrt{\frac{B}{C}} \quad (\text{B.19}).$$

But since the transmission line is reciprocal, $BC=AD-1=\sinh^2(g\Lambda)$ is ensured, and there is no uncertainty about the value of the characteristic impedance. However, if $A \neq D$, two possible values exist for $e^{g\Lambda}$, and therefore for Z_{car} :

$$e^{g\Lambda} = \frac{A+D}{2} \pm \sqrt{\left(\frac{A+D}{2}\right)^2 - 1} \quad (\text{B.20}).$$

$$Z_{car} = \frac{A-D}{2C} \pm \frac{1}{C} \sqrt{\left(\frac{A+D}{2}\right)^2 - 1} \quad (\text{B.21}).$$

In a passive waveguide, $|e^{g\Lambda}| \leq 1$. This allows us to choose the correct pair of values from the previous two equations. Since A and D are complex, it cannot be

known *a priori* whether the correct sign will be plus or minus. Indeed, the correct choice may depend on frequency.

It is therefore convenient that $A=D$ in order to avoid that uncertainty, and this is always true for any geometrically symmetric waveguide. This condition for $A=D$ is sufficient, but not necessary. We will choose the starting and ending point of the period such that the period is geometrically symmetric whenever possible, and in that case, use (B.17) and (B.19) to calculate the characteristics of the transmission line.

It has thus been shown how the microwave propagation coefficient and the characteristic impedance of a periodic transmission line may be calculated knowing the voltage-current transmission matrix associated to one period, and that in order to avoid uncertainties in the values found, unit cells presenting a voltage-current transmission matrix satisfying $A=D$ are helpful.

This concludes the presentation of the voltage-current transmission matrix or ABCD matrix as a useful tool to analyze non-homogeneous, periodic waveguides.

References

- [1] R.E. Collin, "Foundations for microwave engineering," 2nd edition, *McGraw-Hill*, 1992.

(This page is intentionally left blank)

APPENDIX C

Noise properties of photodetectors

Photodetection in semiconductor materials is a quantized process, where a photon is absorbed, generating a free electron-hole pair. This electron-hole pair is then collected by the application of an external or a built-in field, generating a current, generally across a diode. The nature of the absorption process directly relates the statistical properties of the photocurrent thus generated to those of the incident light. Probably the best way to describe the relation between the statistical distributions of light and current is Bernoulli's sampling formula. Using this formula, the repercussions of the nature of the photodetection process in the statistics of the generated photocurrent will be presented in this appendix. Furthermore, the description provided by the noise model for distributed amplifiers photodetectors will be shown to be, in the limiting case where no light amplification processes are present, fully equivalent to the description provided by Bernoulli's sampling formula. This is relevant since the new noise model in the presence of distributed amplification

and photodetection needs to be consistent with previously existing, well established noise models.

Bernoulli's sampling formula

Light absorption in semiconductor-based photodetectors is a quantized process. The photodetection quantum efficiency h may be used to relate the statistical properties of the generated photocurrent and the incident light. This is best described by Bernoulli's sampling formula. In this section, this equation and its intuitive meaning will be presented, as well as its description of the noise properties of photodetectors.

The source of noise in photodetectors is related to the quantized nature of the absorption process, as illustrated in figure C.1.

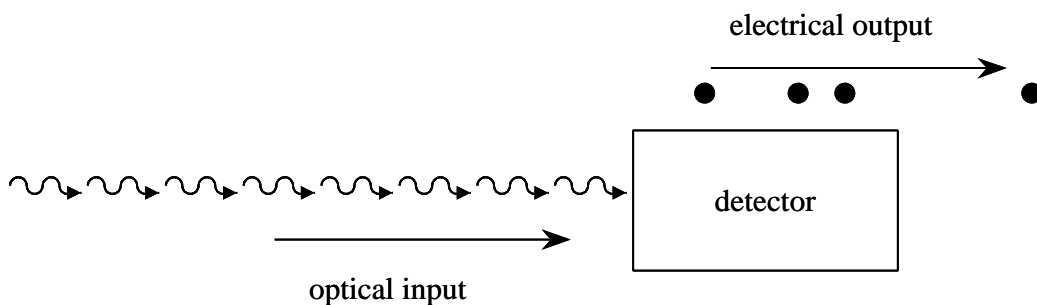


Figure C.1: Representation of the noise added by a photodetector. A “quiet” stream of photons produces a “noisy” output current due to the randomness in the absorption process. The input photons are represented by wiggly arrows, and the output electrons by dots.

Figure C.1 shows how, even if there is very little noise in the optical input, if the detector efficiency is less than 1, noise will be added, because of the random selection

of the photons that produce photocurrent electrons. Moreover, even if the average efficiency is known, there is a probability that the actual efficiency for a given photon stream will be different. For example, even if exactly half of the photons depicted in figure C.1 produced an electron, the average efficiency could be different than 50%. Therefore, noise is added both by the uncertainty in the number of output electrons given a certain number of input photons, and by the random selection of photons that generate a contribution to the output photocurrent. These two effects are direct consequences of the quantized nature of the photodetection process.

Let us now consider a photodetector with quantum efficiency \mathbf{h} . Intuitively, this means that a photon of incident light has a probability \mathbf{h} of generating one electron-hole pair that will be collected, adding to the total device current, and a probability $1-\mathbf{h}$ not to. The latter case may happen, for example, when the photon is not coupled into the device or is victim of optical loss, when it exits the device without being absorbed or generates an electron-hole pair that is not collected.

During a given time interval, let us call P_n the probability of exactly n photons arriving to the detector, and P'_m the probability of exactly m electrons being contributed by these photons to the output photocurrent. These probabilities are related through Bernoulli's sampling equation (see, for example, [1], p. 156)

$$P'_m = \sum_{n=m}^{\infty} \binom{n}{m} \mathbf{h}^m (1-\mathbf{h})^{n-m} P_n \quad (\text{C.1}),$$

where

$$\binom{n}{m} = \frac{n!}{m!(n-m)!} \quad (\text{C.2})$$

is the number of ways in which we can choose m elements out of a set of n identical ones.

Intuitively, (C.1) describes that, when n photons enter the device, m electrons of photocurrent will be generated if exactly $n-m$ photons do not generate electron-hole pairs that are collected. The combinatorial number expresses that any subset of exactly m photons (out of the incoming n) are suitable to generate electron-hole pairs with equal probability. The sum is carried out for all photon numbers larger than the expected electron number, since obviously in detectors without gain no more electron-hole pairs may be generated than input photons. It is noteworthy that, when the efficiency is 1, the output electron statistics are identical to the input photon statistics. Obviously, there is no added uncertainty introduced by an ideal detector where every photon generates an electron-hole pair, if the latter is always collected. Another property of passive photodetectors, i.e., light with Poisson statistics produces photocurrent following also Poisson statistics, can be easily proved from (C.1). Input light with Poisson statistics is described by:

$$P_n = e^{-\langle n_p \rangle} \frac{\langle n_p \rangle^n}{n!} \quad (\text{C.3}).$$

The output electron statistics are then described by:

$$\begin{aligned}
P'_m &= \sum_{n=m}^{\infty} \binom{n}{m} \mathbf{h}^m (1-\mathbf{h})^{n-m} e^{-\langle n_p \rangle} \frac{\langle n_p \rangle^n}{n!} \\
&= \frac{e^{-\langle n_p \rangle} \mathbf{h}^m \langle n_p \rangle^m}{m!} \sum_{n=m}^{\infty} \frac{[(1-\mathbf{h}) \langle n_p \rangle]^{n-m}}{(n-m)!} \\
&= \frac{e^{-\langle n_p \rangle} \mathbf{h}^m \langle n_p \rangle^m}{m!} e^{(1-\mathbf{h}) \langle n_p \rangle} = e^{-\mathbf{h} \langle n_p \rangle} \frac{[\mathbf{h} \langle n_p \rangle]^m}{m!}
\end{aligned} \tag{C.4},$$

i.e., the output photocurrent presents also Poisson statistics, with average an electron number \mathbf{h} times the average of the input photon number.

This makes perfect sense intuitively, since the Poisson distribution describes the statistics of a stream of photons whose arrivals are independent on one another. Random detection of a fraction of those photons will therefore produce also a stream of electrons whose arrival instants will be independent on one another.

Let us now consider a light input with arbitrary, but known, statistics, and a photodetector with quantum efficiency $\mathbf{h} < 1$. The full statistics of the generated photocurrent may be calculated using (C.1). It may be, however, a tedious process. Possibly, the best way to breach the gap between photon and electrons statistics is by means of the following polynomials:

$$Q_N[x] = \prod_{k=0}^{N-1} (x-k) = x(x-1)\dots(x-N+1) \tag{C.5}.$$

We may think of them as the eigenfunctions of the probability distribution transformation expressed by Bernoulli's sampling formula. Indeed, the expectation value of these polynomials, expressed as a function of the electron number, is equal to

a constant times the expectation value of the same polynomial, expressed this time as a function of the photon number:

$$\begin{aligned}
\langle Q_N [n_e] \rangle &= \sum_{m=0}^{\infty} Q_N [m] P'_m = \sum_{n=0}^{\infty} \sum_{m=N}^n Q_N [m] \binom{n}{m} \mathbf{h}^m (1-\mathbf{h})^{n-m} P_n \\
&= \mathbf{h}^N \sum_{n=0}^{\infty} Q_N [n] P_n \sum_{m=N}^n \binom{n-N}{m-N} \mathbf{h}^{m-N} (1-\mathbf{h})^{n-m} \\
&= \mathbf{h}^N \sum_{n=0}^{\infty} Q_N [n] P_n = \mathbf{h}^N \langle Q_N [n_p] \rangle
\end{aligned} \tag{C.6}$$

In the previous derivation, we have used the following obvious relations:

$$n! = Q_N [n] (n-N)! \tag{C.7};$$

$$\sum_{m=N}^n \binom{n-N}{m-N} \mathbf{h}^{m-N} (1-\mathbf{h})^{n-m} = [\mathbf{h} + (1-\mathbf{h})]^{n-N} = 1 \tag{C.8}.$$

Using (C.6), the average value and the variance of the input photon population and of the output electron population are found to be related through the following equations:

$$\langle n_e \rangle = \langle Q_1 [n_e] \rangle = \mathbf{h} \langle Q_1 [n_p] \rangle = \mathbf{h} \langle n_p \rangle \tag{C.9};$$

$$\begin{aligned}
\mathbf{s}_{n_e}^2 &= \langle n_e^2 \rangle - \langle n_e \rangle^2 = \langle Q_2 [n_e] \rangle + \langle n_e \rangle - \langle n_e \rangle^2 \\
&= \mathbf{h}^2 \langle Q_2 [n_p] \rangle + \mathbf{h} \langle n_p \rangle - \mathbf{h}^2 \langle n_p \rangle^2 = \mathbf{h}^2 \mathbf{s}_{n_p}^2 + \mathbf{h}(1-\mathbf{h}) \langle n_p \rangle
\end{aligned} \tag{C.10}$$

The noise figure NF of a photodetector can therefore be expressed as:

$$NF = \frac{SNR_{in}}{SNR_{out}} = \frac{\langle n_p \rangle^2 \mathbf{s}_{n_e}^2}{\langle n_e \rangle^2 \mathbf{s}_{n_p}^2} = 1 + \frac{(1-\mathbf{h}) \langle n_p \rangle}{\mathbf{h} \mathbf{s}_{n_p}^2} \tag{C.11}.$$

In conclusion, Bernoulli's sampling formula has been presented in this section, showing its mathematical description and its intuitive meaning. As an example, two of the common properties of photodetectors (output photocurrent statistics are identical to input light statistics for ideal detectors with unit quantum efficiency, and light with Poisson statistics produces photocurrent with Poisson statistics) have been shown by means of this formula. Furthermore, the use of suitably defined polynomials has been shown to simplify finding the output current statistics as a function of the input light statistics.

In the next section, the correlations existing between electron and photon numbers in a distributed photodetector will be explored. It will be shown that Bernoulli's sampling formula implicitly takes these correlations into account. It will also be shown that, on the other hand, these correlations need to be explicitly considered in a noise model for devices presenting a distributed combination of optical gain and absorption.

In the final section, and using the polynomials $Q_N[x]$ introduced above, it will be shown that the noise model for distributed amplifier-photodetectors presented in this dissertation, in the absence of light amplification, is equivalent to Bernoulli's sampling formula.

Correlation between photon and electron numbers in photodetectors

The generation of photocurrent is produced by the absorption of light, one photon at a time. This intuitively involves that a correlation will exist between the electron count in the produced photocurrent and the photon count in the remaining optical signal. Optical loss reduces the photon count without adding to the photocurrent. Other processes, such as the absorption of a photon generating an electron-hole pair that is not collected, may create the same effect. We may therefore think that these processes may alter this correlation existing between the electron number generated and the surviving photon population. However, it will be shown in this section that Bernoulli's sampling formula implicitly takes into account the effect of all the phenomena above, from the correlation between electrons and photons due to the nature of the absorption, to the processes that alter the photon number but not the electron number. Intuitively, this may be explained by the fact that optical loss and photodetection are in nature random selection processes, and thus their combination in any order results also in a random selection. Other processes of different nature would however introduce changes in the correlation between electron and photon statistics. As a consequence, the effect of additional, non-sampling processes (such as optical gain) needs to be explicitly taken into account in a model describing the noise properties of a device featuring other than absorption and loss.

In order to show all of the above, we will consider the sequential action of two lumped, lossless photodetectors, such that the input of the second one is comprised of the photons remaining after absorption in the first one, after these have suffered optical loss between both detectors. The resulting effect of the ensemble may be described by Bernoulli's sampling equation, where the total efficiency is appropriately chosen. This situation is expressed schematically in figure C.2.

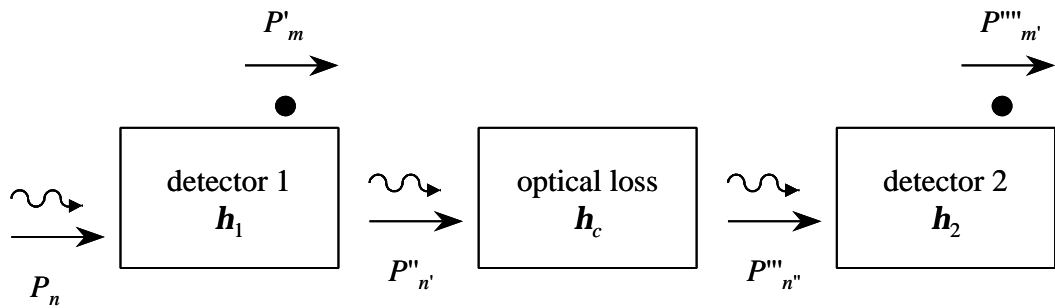


Figure C.2: Evolution of photon and electron numbers through two photodetectors of efficiencies h_1 and h_2 , with optical loss between them. The wiggly arrows represent photon streams, and the dots electron streams. The probability distribution for particle counts at each point is indicated.

Figure C.2 shows two photodetectors, with efficiency h_1 and h_2 , respectively. In between, optical loss exists, so that each photon that is not absorbed in the first detector has a probability h_c of being coupled into the second detector. We will assume that a photon stream presenting a known but arbitrary probability distribution is the input of the ensemble. We will denote by P_n, P''_n the statistics of the optical input, and by P'_m, P''''_m' the statistics of the electrical output, of the first and second detectors, respectively. Bernoulli's sampling formula may be applied to each of these detectors:

$$P'_m = \sum_{n=m}^{\infty} \binom{n}{m} h_1^m (1-h_1)^{n-m} P_n \quad (\text{C.12});$$

$$P'''_{m'} = \sum_{n''=m'}^{\infty} \binom{n''}{m'} h_2^{m'} (1-h_2)^{n''-m'} P'''_{n''} \quad (\text{C.13}).$$

Furthermore, let us call $P''_{n'}$ the statistics of the optical output of the first photodetector. If any photon has a probability h_1 of being absorbed, then it has a probability $1-h_1$ of not being absorbed, and thus

$$P''_{n'} = \sum_{n=n'}^{\infty} \binom{n}{n'} (1-h_1)^{n'} h_1^{n-n'} P_n \quad (\text{C.14}).$$

Finally, the effect of the loss is described again as a sampling process of efficiency h_c :

$$P'''_{n''} = \sum_{n'=n''}^{\infty} \binom{n'}{n''} h_c^{n''} (1-h_c)^{n'-n''} P''_{n'} \quad (\text{C.15}).$$

The probability that, simultaneously, m electrons are absorbed in the first detector and n' photons exit it is given by the probability of m electrons being generated in the first detector when its input is exactly equal to $m+n'$ photons:

$$\binom{m+n'}{m} h_1^m (1-h_1)^{n'} \quad (\text{C.16}).$$

The expectation value of the product mn' of the photon number surviving the first detector and the electron number generated in this detector is given by

$$\begin{aligned}
\langle mn' \rangle &= \sum_{m=0}^{\infty} \sum_{n'=0}^{\infty} mn' \binom{m+n'}{m} \mathbf{h}_1^m (1-\mathbf{h}_1)^{n'} P_{m+n'} \\
&= \mathbf{h}_1 (1-\mathbf{h}_1) \sum_{n=0}^{\infty} n(n-1) P_n \sum_{n'-1=0}^{n-2} \binom{n-2}{n'-1} \mathbf{h}_1^{n-n'-1} (1-\mathbf{h}_1)^{n'-1} \quad (\text{C.17}). \\
&= \mathbf{h}_1 (1-\mathbf{h}_1) [\langle n^2 \rangle - \langle n \rangle]
\end{aligned}$$

We can also find the expectation value of m and n' , given obviously by $\langle m \rangle = \mathbf{h}_1 \langle n \rangle$ and $\langle n' \rangle = (1-\mathbf{h}_1) \langle n \rangle$. The covariance between m and n' may then be easily calculated:

$$\mathbf{s}_{m,n'} = \langle mn' \rangle - \langle m \rangle \langle n' \rangle = \mathbf{h}_1 (1-\mathbf{h}_1) [\mathbf{s}_n^2 - \langle n \rangle] \quad (\text{C.18}).$$

In other words, unless the variance of the optical input of the ensemble presents a variance equal to its average (which is a symptom of the input photons arriving independently of one another), there will be a correlation between the electrons generated in the first detector, and the photons surviving the absorption process, as we intended to prove. This means, obviously, that the probability distributions P'_m and $P''_{n'}$ are not in general independent on one another. Thus, neither will be P'_m and $P'''_{n'}$, or consequently P'_m and $P''''_{m'}$. Let us now calculate the covariance of m and m' , and the statistics of the current flow resulting from adding the photocurrents from both detectors, i.e., the statistics of $m+m'$.

The probability that the second detector will put out m' electrons may be calculated as a function of the probability distribution of n' photons surviving the first detector by combining (C.13) and (C.15):

$$\begin{aligned}
P_{m'}^{m''} &= \sum_{n''=m'}^{\infty} \sum_{n'=n''}^{\infty} \binom{n'}{n''} \binom{n''}{m'} \mathbf{h}_2^{m'} (1-\mathbf{h}_2)^{n''-m'} \mathbf{h}_c^{n''} (1-\mathbf{h}_c)^{n'-n''} P_n^{n''}, \\
&= \sum_{n'=m'}^{\infty} \binom{n'}{m'} (\mathbf{h}_2 \mathbf{h}_c)^{m'} (1-\mathbf{h}_2 \mathbf{h}_c)^{n'-m'} P_n^{n'}.
\end{aligned} \tag{C.19}.$$

In other words, the ensemble of the loss and the second detector behave as a single detector of efficiency $\mathbf{h}_2 \mathbf{h}_c$. This makes perfect intuitive sense, since the probability of each photon that survives the first detector to generate an electron in the second detector is equal to the product of the probability of a photon that exits the first detector surviving the loss, \mathbf{h}_c , and the probability of a photon arriving to the second detector actually generating an electron, \mathbf{h}_2 , both events being independent of one another.

Let us now assume that the input of the ensemble consists of exactly n photons. The probability of generating m electrons in the first detector and simultaneously m' electrons in the second is then equal to the probability of generating m electrons in the first detector given that the input consists on exactly n photons, multiplied by the probability of generating m' electrons in the second detector when the number of photons that survive the first detector n' is exactly equal to $n-m$:

$$\binom{n}{m} \binom{n-m}{m'} \mathbf{h}_1^m (1-\mathbf{h}_1)^{n-m} (\mathbf{h}_2 \mathbf{h}_c)^{m'} (1-\mathbf{h}_2 \mathbf{h}_c)^{n-m-m'} \tag{C.20}.$$

Equations (C.12) and (C.19) were used to find this value. In the case where the optical input for the ensemble follows a probability distribution P_n , the previous result expressed in (C.20) needs to be multiplied by said distribution, and added over all

values of n larger than $m+m'$. This produces the joint probability of the first detector producing m electrons of photocurrent while the second one produces m' , for any arbitrary input statistics. We can use this value to calculate the expectation value of the product mm' :

$$\begin{aligned}
\langle mm' \rangle &= \sum_{m=0}^{\infty} \sum_{m'=0}^{\infty} mm' \sum_{n=m+m'}^{\infty} \binom{n}{m} \binom{n-m}{m'} \mathbf{h}_1^m (1-\mathbf{h}_1)^{n-m} (\mathbf{h}_2 \mathbf{h}_c)^{m'} (1-\mathbf{h}_2 \mathbf{h}_c)^{n-m-m'} P_n \\
&= \mathbf{h}_2 \mathbf{h}_c \sum_{n=0}^{\infty} P_n \sum_{m=1}^{n-1} \binom{n}{m} m(n-m) \mathbf{h}_1^m (1-\mathbf{h}_1)^{n-m} \\
&= \mathbf{h}_1 (1-\mathbf{h}_1) \mathbf{h}_2 \mathbf{h}_c \sum_{n=0}^{\infty} n(n-1) P_n = \mathbf{h}_1 (1-\mathbf{h}_1) \mathbf{h}_2 \mathbf{h}_c \left[\langle n^2 \rangle - \langle n \rangle \right]
\end{aligned} \tag{C.21}.$$

The average value of m' may also be calculated, yielding $\langle m' \rangle = (1-\mathbf{h}_1) \mathbf{h}_2 \mathbf{h}_c \langle n \rangle$. Using this result, the average value of m calculated earlier, and (C.21), the covariance of the photocurrents generated by both detectors may be found:

$$\mathbf{s}_{m,m'} = \langle mm' \rangle - \langle m \rangle \langle m' \rangle = \mathbf{h}_1 (1-\mathbf{h}_1) \mathbf{h}_2 \mathbf{h}_c \left[\mathbf{s}_n^2 - \langle n \rangle \right] \tag{C.22}.$$

Note that (C.22) and (C.18) together make perfect intuitive sense, since both electron numbers, and the electron and photon numbers, are both uncorrelated if and only if the input variance is equal to the input average. Otherwise, the degree of correlation is the same in both cases:

$$\frac{\mathbf{s}_{m,n'}}{\langle m \rangle \langle n' \rangle} = \frac{\mathbf{s}_{m,m'}}{\langle m \rangle \langle m' \rangle} = \frac{\mathbf{s}_n^2 - \langle n \rangle}{\langle n \rangle^2} \tag{C.23}.$$

In other words, excess noise in the input of the ensemble results in correlation between the electron number generated in the first detector and electron and photon numbers further down the ensemble. This result is only possible to obtain since all the processes encountered were of a random sampling nature, i.e., they could all be understood as random selection processes. If instead of loss, a different, non-sampling process were to take place between both detectors, the previous mathematical manipulations would not be possible.

Let us finally calculate the statistics of the photocurrent resulting of adding the electron streams generated by both photodetectors, which we will call P_M^T , where $M=m+m'$. Obviously, if the input of the ensemble consists of exactly n photons, the probability of the total photocurrent consisting of M electrons may be found by adding (C.20) over all possible values of m (i.e, between 0 and M), after performing the substitution $m'=M-m$:

$$\begin{aligned} & \sum_{m=0}^M \binom{n}{m} \binom{n-m}{M-m} \mathbf{h}_1^m (1-\mathbf{h}_1)^{n-m} (\mathbf{h}_2 \mathbf{h}_c)^{M-m} (1-\mathbf{h}_2 \mathbf{h}_c)^{n-M} \\ &= \binom{n}{M} \left[1-\mathbf{h}_1 - (1-\mathbf{h}_1) \mathbf{h}_2 \mathbf{h}_c \right]^{n-M} \left[\mathbf{h}_1 + (1-\mathbf{h}_1) (\mathbf{h}_2 \mathbf{h}_c) \right]^M \end{aligned} \quad (\text{C.24}).$$

Multiplying by the probability of the input consisting of n photons and adding over all possible input photon numbers, we find:

$$P_M^T = \sum_{n=M}^{\infty} \binom{n}{M} \left[\mathbf{h}_1 + (1-\mathbf{h}_1) \mathbf{h}_2 \mathbf{h}_c \right]^M \left[1-\mathbf{h}_1 - (1-\mathbf{h}_1) \mathbf{h}_2 \mathbf{h}_c \right]^{n-M} P_n \quad (\text{C.25}).$$

In other words, the total photocurrent has the same statistics as those generated from the optical input by a photodetector of efficiency $\mathbf{h}_1+(1-\mathbf{h}_1)\mathbf{h}_2\mathbf{h}_c$. Now, this is of course the total probability of any input photon producing a contribution to the total photocurrent. Therefore, we can calculate the average efficiency for the ensemble, being equal to the efficiency suggested by (C.25). The statistics of the total photocurrent generated by the ensemble are then found by using this efficiency in Bernoulli's sampling formula.

We can then conclude that, as shown in this section, there is indeed correlation between the photocurrent generated and the optical signal that survives the detection process. These correlations are, however, taken into account implicitly in Bernoulli's sampling formula. The addition of loss, which is in nature a random sampling process, just like absorption of light in detectors, preserves this correlation. The distributed combination of absorption and loss generates thus photocurrent with statistics that may be calculated using the DC efficiency value by means of Bernoulli's sampling formula, once the statistics of the input light are known. The addition of a process of a different nature (e.g., optical gain from an SOA), would result in Bernoulli's sampling formula not being valid anymore. Thus, in the presence of distributed amplification and photodetection, the correlation between electron and photon numbers along the device need to be explicitly taken into account in order to accurately calculate the statistics of the output photocurrent.

The noise model presented in chapter 4 expresses explicitly those correlations and their evolution along a distributed amplifier-photodetector. However, when the

optical gain and spontaneous emission are turned off, this new model should provide the same results as Bernoulli's sampling formula. This will be proved in the next section.

Noise model for amplifier-photodetectors and its equivalence with Bernoulli's sampling formula

In chapter 4, a new particle-like noise model describing the effect of distributed amplification and detection is presented. In the same chapter, it is shown that the evolution of the photon statistics described by that model is exactly the same as the evolution described using the photon statistics master equation. It will now be shown that the new model presented is also equivalent, when light amplification is turned off, to Bernoulli's sampling formula. This concludes the proof that the new model is consistent with well-established noise models for both amplifiers and photodetectors. In order to do that, we will first demonstrate some properties of the $Q_N[x]$ polynomials, which will be used throughout the proof. Next, we will use those properties to find, from the new noise model, the evolution of the photon statistics in a passive photodetector. This will be later used to find the evolution of the photocurrent electron statistics. These electron statistics will then be compared with the ones obtained through Bernoulli's sampling formula.

Properties of the polynomials $Q_N[x]=x(x-1)\dots(x-N+1)$

The polynomial $Q_N[x]$ is an N -th degree polynomial without a constant term. It can therefore be written as

$$Q_N[x] = \prod_{k=0}^{N-1} (x-k) = \sum_{u=1}^N (-1)^{N-u} a_{N,u} x^u \quad (\text{C.26}).$$

It is trivial to verify that all $a_{N,u}$ thus defined are positive, and equal to the sum of the products of all possible subsets of $N-u$ different elements taken from $\{0, \dots, N-1\}$. For example, for all N , $a_{N,N-1}=N(N-1)/2$, and $a_{N,1}=(N-1)!$.

It is also obvious that, since $Q_{N+1}[x]=(x-N)Q_N[x]$, the coefficient of $u+1$ -th degree in $Q_{N+1}[x]$ is equal to the sum of the u -th degree coefficient, and N times the $u+1$ -th degree coefficient, both taken in $Q_N[x]$, or

$$a_{N+1,u+1} = a_{N,u} + Na_{N,u+1} \quad (\text{C.27}).$$

Let us now consider the $v+1$ -th ($v \leq N$) derivative of $Q_{N+1}[x]$:

$$\begin{aligned} \frac{d^{v+1}Q_{N+1}[x]}{dx^{v+1}} &= \sum_{u=1}^{N+1} (-1)^{N+1-u} a_{N+1,u} \frac{d^{v+1}x^u}{dx^{v+1}} \\ &= (v+1)! \sum_{u=v+1}^{N+1} (-1)^{N+1-u} \binom{u}{v+1} a_{N+1,u} x^{u-v-1} \end{aligned} \quad (\text{C.28}).$$

Since $Q_{N+1}[x]=xQ_N[x-1]$, we can also write this derivative in the following form:

$$\frac{d^{v+1}Q_{N+1}[x]}{dx^{v+1}} = x \frac{d^{v+1}Q_N[x-1]}{dx^{v+1}} + (v+1) \frac{d^v Q_N[x-1]}{dx^v} \quad (\text{C.29}),$$

where we have used that

$$\frac{d^n [f(x)g(x)]}{dx^n} = \sum_{m=0}^n \binom{n}{m} \frac{d^m f(x)}{dx^m} \frac{d^{n-m} g(x)}{dx^{n-m}} \quad (\text{C.30}).$$

Evaluating (C.28) at $x=0$, $x=-1$ and $x=1$ produces

$$\left. \frac{d^{v+1} Q_{N+1}[x]}{dx^{v+1}} \right|_{x=0} = (-1)^{N-v} (v+1)! a_{N+1,v+1} \quad (\text{C.31}),$$

$$\left. \frac{d^{v+1} Q_{N+1}[x]}{dx^{v+1}} \right|_{x=-1} = (-1)^{N-v} (v+1)! \sum_{u=v+1}^{N+1} \binom{u}{v+1} a_{N+1,u} \quad (\text{C.32}),$$

$$\left. \frac{d^{v+1} Q_{N+1}[x]}{dx^{v+1}} \right|_{x=1} = (v+1)! \sum_{u=v+1}^{N+1} (-1)^{N+1-u} \binom{u}{v+1} a_{N+1,u} \quad (\text{C.33}).$$

We can write the following equality, using (C.29), (C.31) and (C.32):

$$\begin{aligned} (-1)^{N-v} v! a_{N+1,v+1} &= \frac{1}{v+1} \left. \frac{d^{v+1} Q_{N+1}[x]}{dx^{v+1}} \right|_{x=0} = \left. \frac{d^v Q_N[x-1]}{dx^v} \right|_{x=0} \\ &= \left. \frac{d^v Q_N[x]}{dx^v} \right|_{x=-1} = (-1)^{N-v} v! \sum_{u=v}^N \binom{u}{v} a_{N,u} \end{aligned} \quad (\text{C.34}),$$

from where we can conclude:

$$a_{N+1,v+1} = \sum_{u=v}^N \binom{u}{v} a_{N,u} \quad (\text{C.35}).$$

We can also find, using (C.29), (C.31) and (C.33):

$$\begin{aligned}
(v+1)! \sum_{u=v+1}^{N+1} (-1)^{N+1-u} \binom{u}{v+1} a_{N+1,u} &= \left. \frac{d^{v+1} Q_{N+1}[x]}{dx^{v+1}} \right|_{x=1} \\
&= \left. \frac{d^{v+1} Q_N[x-1]}{dx^{v+1}} \right|_{x=1} + (v+1) \left. \frac{d^v Q_N[x-1]}{dx^v} \right|_{x=1} \\
&= \left. \frac{d^{v+1} Q_N[x]}{dx^{v+1}} \right|_{x=0} + (v+1) \left. \frac{d^v Q_N[x]}{dx^v} \right|_{x=0} \\
&= (-1)^{N-1-v} (v+1)! a_{N,v+1} + (-1)^{N-v} (v+1)! a_{N,v}
\end{aligned} \tag{C.36}$$

and so we can finally write:

$$\sum_{u=v}^N (-1)^{N-u} \binom{u}{v} a_{N,u} = (-1)^{N-1-v} a_{N-1,v} + (-1)^{N-v} a_{N-1,v-1} \tag{C.37}.$$

This concludes the demonstration of those properties of the $Q_N[x]$ polynomials that will be used in the following proofs. We will now use these properties to show that the new noise model for amplifier-photodetectors in the absence of light amplification is consistent with Bernoulli's sampling formula.

Photon number statistics in a photodetector

In chapter 4, it is shown how the noise model for distributed amplifier-photodetectors yields the following equation describing the evolution of the photon number statistics:

$$\frac{d \langle n_p^N \rangle}{dz} = (\Gamma_a \mathbf{a} + l) \sum_{i=0}^{N-1} (-1)^{N-i} \binom{N}{i} \langle n_p^{i+1} \rangle \tag{C.38},$$

where $\Gamma_a \mathbf{a}$ and l are the coefficients describing the absorption in the detector and the optical loss, respectively, both expressed in units of inverse of distance. Both of these

coefficients may depend on the longitudinal propagation position z , but any such dependence will not be shown explicitly, in order to lighten the notation. Using (C.38), we will next show that

$$\frac{d}{dz} \left[\frac{\langle Q_N [n_p(z)] \rangle}{\langle n_p(z) \rangle^N} \right] = 0 \quad (\text{C.39}).$$

When $N=1$,

$$\frac{d \langle n_p \rangle}{dz} = -(\Gamma_a \mathbf{a} + l) \langle n_p \rangle \quad (\text{C.40}).$$

Using (C.38) and (C.40) allows us to write:

$$\begin{aligned} \frac{d}{dz} \left[\frac{\langle Q_N [n_p] \rangle}{\langle n_p \rangle^N} \right] &= -\frac{N}{\langle n_p \rangle^{N+1}} \frac{d \langle n_p \rangle}{dz} \sum_{u=1}^N (-1)^{N-u} a_{N,u} \langle n_p^u \rangle \\ &\quad + \frac{1}{\langle n_p \rangle^N} \sum_{u=1}^N (-1)^{N-u} a_{N,u} \frac{d \langle n_p^u \rangle}{dz} \\ &= -\frac{N}{\langle n_p \rangle^{N+1}} \frac{d \langle n_p \rangle}{dz} \sum_{u=1}^N (-1)^{N-u} a_{N,u} \langle n_p^u \rangle \\ &\quad - \frac{1}{\langle n_p \rangle^{N+1}} \frac{d \langle n_p \rangle}{dz} \sum_{u=1}^N \sum_{i=0}^{u-1} (-1)^{N-i} \binom{u}{i} a_{N,u} \langle n_p^{i+1} \rangle \end{aligned} \quad (\text{C.41}).$$

But using (C.35) and (C.27) yields

$$\begin{aligned} \sum_{u=1}^N \sum_{i=0}^{u-1} (-1)^{N-i} \binom{u}{i} a_{N,u} \langle n_p^{i+1} \rangle &= \sum_{i=0}^{N-1} (-1)^{N-i} \langle n_p^{i+1} \rangle \sum_{u=i+1}^N \binom{u}{i} a_{N,u} \\ &= -N \sum_{i+1=1}^N (-1)^{N-(i+1)} a_{N,i+1} \langle n_p^{i+1} \rangle \end{aligned} \quad (\text{C.42}),$$

which when inserted in (C.41) obviously produces (C.39). Integrating (C.39) produces the following equivalent result:

$$\langle \mathcal{Q}_N [n_p(z)] \rangle = \frac{\langle n_p(z) \rangle^N}{\langle n_p(0) \rangle^N} \langle \mathcal{Q}_N [n_p(0)] \rangle \quad (\text{C.43}).$$

Note that this is equivalent to a random selection process, whose “efficiency” is the ratio of surviving photons at position z to incoming photons at position 0. This is in perfectly good agreement with the intuitive picture painted all throughout this appendix. We will now find how the new noise model describes the evolution of the electron number statistics in a photodetector.

Electron number statistics in a photodetector

Earlier in this appendix, the need to take into account the correlation between electron and photon numbers in distributed amplifier-photodetectors was discussed. In chapter 4, the general equation describing the evolution of said correlation in distributed amplifier-photodetectors was found. In the particular case of a detector without optical amplification, no spontaneous emission or stimulated transitions occur. The equation describing the evolution of the correlation between electron and photon numbers can then be simplified into

$$\begin{aligned} \frac{d \langle n_p^N n_e^{N'} \rangle}{dz} &= (\Gamma_a \mathbf{a} + l) \sum_{i=0}^{N-1} (-1)^{N-i} \binom{N}{i} \langle n_p^{i+1} n_e^{N'} \rangle \\ &+ \Gamma_a \mathbf{a} \sum_{i=0}^N \sum_{j=0}^{N'-1} (-1)^{N-i} \binom{N}{i} \binom{N'}{j} \langle n_p^{i+1} n_e^j \rangle \end{aligned} \quad (\text{C.44}).$$

When $N=0, N'=1$,

$$\frac{d\langle n_e \rangle}{dz} = \Gamma_a \mathbf{a} \langle n_p \rangle \quad (\text{C.45}).$$

Making use of (C.40), (C.44) and (C.45), we can write the following relation involving the $Q_N[x]$ polynomials:

$$\begin{aligned} & \frac{d}{dz} \left[\frac{\langle Q_N[n_p] Q_{N'}[n_e] \rangle}{\langle n_p \rangle^N} \right] \\ &= -N \frac{1}{\langle n_p \rangle^{N+1}} \frac{d\langle n_p \rangle}{dz} \sum_{u=1}^N \sum_{u'=1}^{N'} (-1)^{N+N'-u-u'} a_{N,u} a_{N',u'} \langle n_p^u n_e^{u'} \rangle \\ & \quad - \frac{1}{\langle n_p \rangle^{N+1}} \frac{d\langle n_p \rangle}{dz} \sum_{u=1}^N \sum_{u'=1}^{N'} \sum_{i=0}^{u-1} (-1)^{N+N'-i-u'} \binom{u}{i} a_{N,u} a_{N',u'} \langle n_p^{i+1} n_e^{u'} \rangle \\ & \quad + \frac{1}{\langle n_p \rangle^{N+1}} \frac{d\langle n_e \rangle}{dz} \sum_{u=1}^N \sum_{u'=1}^{N'} \sum_{i=0}^u \sum_{j=0}^{u'-1} (-1)^{N+N'-i-u'} \binom{u}{i} \binom{u'}{j} a_{N,u} a_{N',u'} \langle n_p^{i+1} n_e^j \rangle \end{aligned} \quad (\text{C.46}).$$

This relation may be written in a simpler way:

$$\begin{aligned} & \frac{d}{dz} \left[\frac{\langle Q_N[n_p] Q_{N'}[n_e] \rangle}{\langle n_p \rangle^N} \right] \\ &= - \frac{1}{\langle n_p \rangle^{N+1}} \frac{d\langle n_p \rangle}{dz} \sum_{u=1}^N \sum_{u'=1}^{N'} (-1)^{N+N'-i-u'} a_{N',u} b_{N,u} \langle n_p^u n_e^{u'} \rangle \\ & \quad - \frac{1}{\langle n_p \rangle^{N+1}} \frac{d\langle n_e \rangle}{dz} \sum_{u=1}^{N+1} \sum_{u'=0}^{N'-1} (-1)^{N+N'-u-u'} c_{N,u} d_{N',u'} \langle n_p^u n_e^{u'} \rangle \end{aligned} \quad (\text{C.47}),$$

where the following definitions apply:

$$b_u = Na_{N,u} - \sum_{i=u}^N \binom{i}{u-1} a_{N,i} \quad (\text{C.48});$$

$$c_{N,u} = \sum_{i=u-1}^N \binom{i}{u-1} a_{N,i} = a_{N,u-1} + Na_{N,u} - b_u \quad (\text{C.49}).$$

$$d_{N',u'} = \sum_{j=u'+1}^{N'} (-1)^{u'-j} \binom{j}{u'} a_{N',j} \quad (\text{C.50}).$$

Now, using (C.27), (C.35) and (C.37) allows some simplification:

$$b_u = Na_{N,u} + a_{N,u-1} - a_{N+1,u} = 0 \quad (\text{C.51});$$

$$c_{N,u} = a_{N,u-1} + Na_{N,u} = a_{N+1,u} \quad (\text{C.52}).$$

$$d_{N',u'} = -a_{N'-1,u'} + a_{N'-1,u'-1} - a_{N',u'} = -N' a_{N'-1,u'} \quad (\text{C.53}).$$

When inserted into (C.47), these relations produce the following result:

$$\frac{d}{dz} \left[\frac{\langle \mathcal{Q}_N [n_p] \mathcal{Q}_{N'} [n_e] \rangle}{\langle n_p \rangle^N} \right] = N' \frac{\langle \mathcal{Q}_{N+1} [n_p] \mathcal{Q}_{N'-1} [n_e] \rangle}{\langle n_p \rangle^{N+1}} \frac{d \langle n_e \rangle}{dz} \quad (\text{C.54}).$$

We will now use this result to prove by induction the following hypothesis:

$$\frac{d}{dz} \left[\frac{\langle \mathcal{Q}_N [n_p] \mathcal{Q}_{N'} [n_e] \rangle}{\langle n_p \rangle^N} \right] = \frac{\langle \mathcal{Q}_{N+N'} [n_p] \rangle}{\langle n_p \rangle^{N+N'}} \frac{d \langle n_e \rangle^{N'}}{dz} \quad (\text{C.55}).$$

This hypothesis is obviously true for $N'=0$ and for all N because of (C.39). If (C.55) were true, then integrating it we find that

$$\frac{\langle \mathcal{Q}_N [n_p] \mathcal{Q}_{N'} [n_e] \rangle}{\langle n_p \rangle^N} = \frac{\langle \mathcal{Q}_{N+N'} [n_p] \rangle}{\langle n_p \rangle^{N+N'}} \langle n_e \rangle^{N'} \quad (\text{C.56}).$$

If (C.55), and thus (C.56), is valid for $N'=0, \dots, u'$, and for all N , then with the help of (C.54), we can find for $N'=u'+1$:

$$\begin{aligned} \frac{d}{dz} \left[\frac{\langle \mathcal{Q}_N [n_p] \mathcal{Q}_{u'+1} [n_e] \rangle}{\langle n_p \rangle^N} \right] &= (u'+1) \frac{d \langle n_e \rangle}{dz} \frac{\langle \mathcal{Q}_{N+u'+1} [n_p] \rangle}{\langle n_p \rangle^{N+u'+1}} \langle n_e \rangle^{u'} \\ &= \frac{\langle \mathcal{Q}_{N+(u'+1)} [n_p] \rangle}{\langle n_p \rangle^{N+(u'+1)}} \frac{d \langle n_e \rangle^{u'+1}}{dz} \end{aligned} \quad (\text{C.57}).$$

The result is therefore valid for all N' and for all N . In particular, when $N=0$,

$$\frac{d \langle \mathcal{Q}_{N'} [n_e] \rangle}{dz} = \frac{\langle \mathcal{Q}_{N'} [n_p] \rangle}{\langle n_p \rangle^{N'}} \frac{d \langle n_e \rangle^{N'}}{dz} \quad (\text{C.58}).$$

Integration of (C.58) over the entire device yields

$$\langle \mathcal{Q}_{N'} [n_e] \rangle = \frac{\langle n_e \rangle^{N'}}{\langle n_p \rangle^{N'}} \langle \mathcal{Q}_{N'} [n_p] \rangle = \mathbf{h}^{N'} \langle \mathcal{Q}_{N'} [n_p] \rangle \quad (\text{C.59}),$$

which is exactly the result obtained from Bernoulli's sampling formula. Obviously, the new noise model for distributed amplifier-photodetectors is thus consistent with it.

In conclusion, Bernoulli's sampling formula and the noise model for distributed amplifier-photodetectors produce the same results when applied to classical detectors. This confirms that the latter is consistent with the former.

In this appendix, Bernoulli's sampling formula has been introduced. It is possibly the most accurate noise model for classical photodetectors. It has been shown how the electron and photon populations evolving along a detector are correlated. This correlation and its effect in the photocurrent statistics are taken into account through Bernoulli's sampling formula, when all processes affecting the light are of a random sampling nature. It has finally been shown that the new noise model presented in this dissertation is, in the absence of amplification and spontaneous emission, consistent with Bernoulli's sampling formula.

References

- [1] E. Desurvire, "Erbium-doped fiber amplifiers: principles and applications," *John Wiley & Sons*, 1994.

(This page is intentionally left blank)